

# Electronic and Optical Properties of Silicon Nanowires: Theory and Modeling

by

Daryoush Shiri

A thesis  
presented to the University of Waterloo  
in fulfillment of the  
thesis requirement for the degree of  
Doctor of Philosophy  
in  
Electrical and Computer Engineering

Waterloo, Ontario, Canada, 2012

© Daryoush Shiri 2012

## **AUTHOR'S DECLARATION**

I hereby declare that I am the sole author of this thesis. This is a true copy of the thesis, including any required final revisions, as accepted by my examiners. I understand that my thesis may be made electronically available to the public.

Daryoush Shiri

## Abstract

Narrow silicon nanowires host a rich set of physical phenomena. Understanding these phenomena will open new opportunities for applications of silicon nanowires in electronic and optical devices and importantly adds more functionality to silicon especially in those realms that bulk silicon may not operate remarkably. Compatibility of silicon nanowires with the mainstream fabrication technology is also advantageous. The main theme of this thesis is finding the possibility of using silicon nanowires in light sources; laser and light emitting diodes. Using 10 orbital ( $sp^3d^5s^*$ ) Tight Binding (TB), Molecular Dynamic (MD) with classical many-body potential and ab-initio Density Functional Theory (DFT) methods it was shown that axial strain can induce significant changes in the effective mass, density of states and bandgap of silicon nanowires. Generality of the observed effects was proven by investigating nanowires of different crystallography, diameter and material (e.g. germanium nanowires). The observed direct to indirect bandgap conversion suggests that strain is able to modulate the light emission properties of silicon nanowires.

To investigate this possibility, spontaneous emission time is formulated using the first and second order perturbation theory including Longitudinal Optical (LO) and Longitudinal Acoustic (LA) phonons. It was observed that corresponding to direct to indirect bandgap conversion, the spontaneous emission time can be modulated by more than one order of magnitude. This emanates from direct to indirect bandgap conversion and symmetry change of wave function in response to axial strain. Furthermore a mechanism for lasing and population inversion was proposed in the thesis which is based on the study of carrier statistics in direct and indirect conduction sub bands of a strained nanowire. By calculating all possible electron-phonon scattering mechanisms which may deplete the already populated indirect subband, it was shown that at different temperatures and under different electric fields there is a factor of 10 difference between the population of indirect and direct sub bands in a strained nanowire. This suggests that population inversion can be achieved by biasing an already strained nanowire in its indirect bandgap state. The light emission is possible then by releasing or inverting the strain direction. A few ideas of implementing this experiment were proposed as a patent application.

The carrier population dynamic was studied with Ensemble Monte Carlo (EMC) simulator which uses the scattering data calculated in this thesis. All scattering events including intra- and inter-subband scatterings including LA and LO phonons were taken into account. The effects of strain on the symmetry of wave functions in nanowires promise strain-modulated photo absorption in silicon nanowires. Photo absorption of silicon nanowires was calculated using TB method and the role of diameter, optical anisotropy and strain were investigated on the band edge absorption. Modulation of absorption also suggests new applications for silicon nanowires. Furthermore the formulation and the codes developed in this thesis provide the basis for further investigation of non-radiative processes in silicon nanowires e.g. Auger Recombination as well as effects of strain on the nonlinear optics of silicon nanowires.

## Acknowledgements

There are many who have helped me to decrease the burden of paving the path of life, work, research and of course writing this thesis, and to whom many thanks are due. Most particularly I am greatly indebted to my dear parents who sacrificed a lot to let their son pursue his big and seemingly unreachable dreams. I am ashamed that I could not serve them better in return and I greatly thank my dear brothers Darab, Davood and Ebrahim for doing what I was supposed to do and I didn't.

I thank Master Mohammad Jafar Tahvildari (Sharif and AmirKabir Universities of Technology) whose enthusiastic teaching style, high morale standard and humbleness inspired me and ignited my passion for teaching and being a good and caring teacher. He was always available to listen to my problems, helped me to believe in myself and see a glimpse of hope in those murky days.

I am indebted to my PhD advisor and guru, Professor M. P. (Anant) Anantram (now at University of Washington), who taught me how to think deeply, see the big picture in each problem, how to learn and never sacrifice high quality understanding with anything else. I treasure his advices and his brotherly supports won't be forgotten. Also his respectful family deserves a lot of appreciation due to their kindness and hospitality when they were here in Waterloo and when I was visiting Seattle.

I thank Professor C. R (Selva) Selvakumar for his supports and brotherly advices during the last years of my PhD research. Professor Dayan Ban and Professor Simarjeet Singh Saini were very helpful and supportive during these years and I sincerely thank them both. I thank Professor Shirley Tang and Professor Ash Parameswaran (Simon Fraser University) who accepted to be in my PhD thesis examination committee.

I thank Professor Frank Wilhelm-Mauch (now at Universität des Saarlandes) who was helpful in a few occasions that I needed help. I also appreciate Professor Jonathan Baugh for giving me a job at his lab in IQC and his patience regarding my absence due to my workload and thesis deadlines.

I also acknowledge Waterloo Institute for Nanotechnology (WIN) for providing generous nano-fellowship awards during 2008-2010. Professor Arthur Carty, the Executive Manager of WIN, always made encouraging remarks about my research whenever we met and I thank him a lot.

I was helped a lot by Dr. Andrei Buin and Professor Amit Verma (Texas A&M University-Kingsville) during my PhD research and I sincerely thank them both for teaching me whatever they knew. I also thank Yifan Kong, Keving Chien, Jie Liu and Jianqing qi (both at University of Washington) for their helps during my research. My friend KM Azizur Rahman (McMaster University) helped me in proof reading my thesis although he had a busy schedule.

My stay in Canada has been a sweet memory thanks to my remarkable and honest friends like Arash Tabibiazar, Mohammad Neshat, Mohsen Baratvand, Mohsen Keshavarz Akhlaghi, Golam Md. Rabbani and Mohammad H. Ansari and their respectful families. I would like to add that Golam (now at University of Washington) is one of the best colleagues and classmates that I have ever had during my academic life.

At last but not the least I thank my beloved wife, colleague and classmate, Anita Fadavi Roudsari, for her support, help, smart suggestions and solutions when they were vitally needed.



## **Dedication**

I would like to dedicate my thesis to my beloved wife

*Anita*

## Table of Contents

AUTHOR'S DECLARATION.....	ii
Abstract.....	iii
Acknowledgements.....	iv
Dedication.....	v
Table of Contents.....	vi
List of Figures.....	ix
List of Tables.....	xvi
List of Abbreviations.....	xvii
Chapter 1 Introduction.....	1
1.1 Silicon Nanowire Fabrication Methods.....	3
1.1.1 Bottom-up Methods.....	3
1.1.2 Top-down Methods.....	5
1.2 Optical Properties of SiNWs.....	8
1.2.1 Studies of Optical Emission.....	8
1.2.2 Studies of Optical Absorption.....	18
1.3 Organization of the Thesis.....	19
1.4 Sources of Strain in SiNWs.....	20
1.4.1 Intrinsic sources of strain.....	21
1.4.2 Extrinsic sources of strain.....	22
1.4.3 Strain Measurement.....	24
Chapter 2 Strain Effects on the Electronic Properties of Silicon Nanowires.....	26
2.1 Tight Binding (TB) Calculation of the Band Structure.....	26
2.2 Strain Effects on the Band Structure of [110] and [100] SiNWs.....	28
2.2.1 Effective mass and Density of States.....	34
2.2.2 Strain Effects on the Bulk Silicon.....	37
Chapter 3 Strain Effects on the Electronic Properties of Germanium Nanowires.....	40
3.1 Energy Minimization in DFT.....	40
3.2 Band Structure of [110] and [100] GeNWs.....	41
3.3 Strain Effects.....	43
3.3.1 Effective Mass.....	46
3.3.2 DFT and the Value of Bandgap.....	47

3.4 Effect of strain on the band structure of bulk germanium .....	48
Chapter 4 Spontaneous Emission Time in Silicon Nanowires: <i>Computational Methods</i> .....	50
4.1 Energy Minimization .....	50
4.2 Position and Momentum Matrix Element .....	51
4.2.1 Slater Orbitals .....	55
4.2.2 Visualization of Wave functions and Matrix Elements .....	56
4.3 First Order Spontaneous Emission Process .....	60
4.4 Second Order Spontaneous Emission Process .....	63
4.4.1 LA Phonons .....	64
4.4.2 LO Phonons .....	69
4.5 First Order Electron-Phonon Scattering Rates .....	71
4.5.1 Electron-LA phonon scattering .....	71
4.5.2 Electron-LO phonon scattering .....	75
4.5.3 Post processing of scattering data for EMC simulation .....	77
Chapter 5 Spontaneous Emission Time in Silicon Nanowires: <i>Results</i> .....	81
5.1 Outline .....	81
5.2 Introduction .....	81
5.3 Results .....	83
5.3.1 Direct bandgap regime .....	83
5.3.2 Direct to indirect bandgap conversion .....	87
5.4 Discussions .....	92
5.5 Methods .....	99
5.6 Addendum .....	101
5.6.1 Local Field Effects (LFE) on the spontaneous emission time .....	101
5.6.2 Sub band exchange due to strain .....	103
5.6.3 Semi-analytic equation for 2nd order spontaneous emission .....	105
5.6.4 DFT vs. TB (band structure calculation) .....	108
5.6.5 Many-body (exciton) effects .....	109
Chapter 6 Photo absorption in Silicon Nanowires .....	110
6.1 Methods .....	111
6.1.1 Numerical Method .....	114
6.1.2 Semi-analytic Method to Calculate Absorption .....	117

6.1.3 Direct Absorption in Bulk Silicon .....	118
6.2 Results & Discussions.....	121
6.2.1 Absorption in bulk Silicon .....	121
6.2.2 Comparison of Fully Numerical and Semi-analytic Methods.....	122
6.2.3 Anisotropy, Diameter and Strain .....	123
6.2.4 Bulk silicon vs. SiNW .....	126
6.2.5 [100] SiNW .....	127
6.3 Conditions for optical gain.....	128
6.4 Measurement of the Absorption.....	130
Chapter 7 Conclusions .....	133
7.1 Summary .....	133
7.2 Future Work .....	135
7.2.1 Auger Recombination .....	135
7.2.2 Two Photon Absorption .....	138
7.2.3 Surface Effects .....	141
Appendices.....	142
Appendix A: Density of States (DOS) Calculation using Surface Green Function.....	142
Appendix B: TB calculation of bandstructure of bulk silicon .....	144
Appendix C: Simplification of the momentum matrix element.....	146
Appendix D: Matrix element of $e^{iq \cdot r}$ .....	149
Appendix E: Electron-LO phonon scattering rate in Effective Mass Approximation .....	153
Permissions .....	155
Bibliography .....	168

## List of Figures

Figure 1.1 (a) Band structure of bulk silicon showing an indirect bandgap. (b) Band structure of a 2.2nm [100] SiNW shows a direct bandgap. ....	2
Figure 1.2 VLS mechanism of silicon nanowire growth which starts from silicon and metal catalyst droplet.....	4
Figure 1.3 (a) TEM image of grown SiNW using laser ablation of Si <sub>6</sub> Fe <sub>1-x</sub> target (scale bar is 100nm). (b) 10nm thick SiNW covered with amorphous oxide sheath. Reprinted with permission from [30]. Copyright 1998 AAAS.....	5
Figure 1.4 (a) Floating SiNW. (b) floating pentagonal. (c) Non-floating (body-tied) omega-shaped SiNW with diameters of 208nm, 197nm and 372 nm, respectively. (d) Top-view of GAA_FET of type (a) SiNW. Reprinted with permission from [33]. Copyright 2007 IEEE. ....	6
Figure 1.5 Oxide-assisted narrowing of a floating SiNW before (a) and after (b) gate metallization. (c) Cross section of oxide covered SiNW. Reprinted with permission from [34][2]. Copyright 2007 IEEE. ....	6
Figure 1.6 (a), (b) and (c) peeling off the SNAP nanowires from the SOI substrate using PDMS glue. (d), (e) and (f) Pattern transfer on SU-8 epoxy coated plastic (mylar) substrate. Reprinted with permission from [6]. Copyright 2007 Macmillan Publishers Ltd.....	8
Figure 1.7 Six models proposed to explain the visible PL emission from porous silicon. Reprinted with permission from [50]. Copyright 1997 American Institute of Physics.....	10
Figure 1.8 (a) An array of 50nm SiNWs. Inset shows the TEM image of a 4nm thick SiNW narrowed by thermal oxide. (b) Diameter dependence of the PL peak is compared with TB method with (solid line) and without (dashed line) radial strain. Reprinted with permission from [37]. Copyright 2010 American Chemical Society. ....	14
Figure 1.9 (a) A model for oxidation-assisted narrowing of SiNW. The bandgap energy initially decreases due to radial strain and then the role of QC gets stronger in narrower diameters. (b) Comparison of TB calculations with the measured values of the PL peak shift. Reprinted with permission from [67]. Copyright 2011 American Physical Society.....	16
Figure 1.10 (a) Direct radiative recombination. Direct AR of (b) eeh type and (c) hhe type. (d) Indirect phonon assisted AR process. CB and VB stand for conduction band and valence band, respectively.....	17
Figure 1.11 (a) PL decay curves versus optical pump intensity at T=10k for Au-catalyzed SiNWs. Reprinted with permission from [57]. Copyright 2009 American Chemical Society. (b) AR lifetime	

( $\tau_a$ ) versus excitation intensity at three different temperatures for TiSi <sub>2</sub> -catalyzed SiNWs. Reprinted with permission from [66]. Copyright 2008 American Physical Society. ....	17
Figure 1.12 (a) Residual strain vs. TaN film thickness and sputtering power. Two parallel floating HfO <sub>2</sub> /TaN covered SiNW (b) before and (c) after TaN deposition. Reprinted with permission from [2]. Copyright 2007 IEEE. ....	21
Figure 1.13 A four point bending apparatus to bend the wafer containing the SiNW-based FET. Reprinted with permission from [99]. Copyright 2009 American Institute of Physics. ....	23
Figure 2.1 (a) Cross section of a [110] SiNW in <i>xy</i> plane with 6 Si atoms and 8 H atoms. (b) Three unit cells of [110] SiNW along <i>z</i> direction [Sideview of (a)]. The unit cell length is 3.83959 Å. ....	27
Figure 2.2 Cross sections (left) and side views (right) of three unit cells of (a) 1.7nm [110] and (b) 2.2nm [100] SiNW terminated with hydrogen atoms. For [110] SiNW, the diameter is defined as the average value of large and small diameters. ....	29
Figure 2.3 (a) Bandgap vs. strain for 1.7nm [110] SiNW and (b) the band structure at +1% and -5% strains. Blue (dark) curves show that the band structure is indirect at -5% and heavy bands (H) determine the bandgap and effective mass of electrons. Red (light) curves show that at +1% strain, the band structure becomes direct and light band (L) determines the effective mass. Reprinted with permission from [117]. Copyright 2008 American Institute of Physics. ....	30
Figure 2.4 Bandgap versus strain for 2.2nm [100] SiNW (square ■). Direct-to-indirect transition occurs at -1% strain. Circles (●) show the same data for the 2.6 nm [100] SiNW with bandgap transition point now at 0% strain. Reprinted with permission from [117]. Copyright 2008 American Institute of Physics. ....	31
Figure 2.5 The square (■), circle (●) and diamond (◆) show bandgap versus strain for 1.7, 2.3 and 3.1 nm [110] SiNWs, respectively. Arrows indicate the strain value at which the bandgap becomes indirect. Reprinted with permission from [117]. Copyright 2008 American Institute of Physics. ....	32
Figure 2.6 (a) Energy of heavy (CBM2) and light (CBM1) conduction band minima and valence band maximum (VBM1) versus strain in a 1.7nm [110] SiNW. (b) $\Delta_2$ and $\Delta_4$ correspond to the bonding states of CBM2 and CBM1, respectively. Panel b was adapted with permission from [118]. Copyright 2008 American Chemical Society. ....	33
Figure 2.7 (a) Energy of heavy (CBM2) and light (CBM1) conduction band minima and direct (VBM1) and indirect (VBM2) valence band maxima vs. strain in a 2.2nm [100] SiNW. (b) Band structure of the unstrained nanowire as (a). (c) Anti-bonding p orbitals corresponding to VBM2. (d)	

Anti-bonding $sp^3$ orbitals corresponding to VBM1. Panels (c) and (d) were adapted with permission from [118]. Copyright 2008 American Chemical Society. ....	34
Figure 2.8 (a) The normalized effective mass ( $m^*/m_0$ ) vs. strain ( $m_0$ is the free mass of electron) for 1.7, 2.3 and 3.1nm [110] SiNW. (b) Effective density of states ( $N_c$ ) in versus strain. Reprinted with permission from [117]. Copyright 2008 American Institute of Physics. ....	35
Figure 2.9 (a), (b) and (c) shows the strain induced band structure change in tensile strain regime, bandgap transition point and compressive strain regime, respectively. ....	37
Figure 2.10 (a) Band structure of bulk silicon showing indirect bandgap (1.17eV) at off- $\Gamma$ point $0.85\pi/a$ . $\Gamma$ corresponds to $k=[000]$ i.e. BZ center. (b) Constant energy surface corresponding to 6 conduction valleys. ....	38
Figure 2.11 Biaxial [110] (lines) and uniaxial [100] (dots) strain effects on the energy of conduction sub bands at three different points in the BZ of the bulk silicon. ....	39
Figure 3.1 (a) Cross section of a 1.9nm [110] GeNW and (b) its side view showing three unit cells with canted $GeH_2$ groups. ....	41
Figure 3.2 Band structure of a 1.97nm [110] GeNW shows direct bandgap. Reprinted with permission from [130]. Copyright 2009 Wiley-VCH. ....	42
Figure 3.3 (a) Constant energy surface corresponding to conduction band minimum of bulk germanium at L point in BZ. (b) Band structure of bulk germanium showing indirect (0.66eV) and direct (0.8eV) bandgap values at L and $\Gamma$ (BZ center) respectively. ....	42
Figure 3.4 Band structure of a 2.5nm unstrained [100] GeNW with indirect bandgap. Inset: Cross section of the nanowire in $xy$ plane. Reprinted with permission from [130]. Copyright 2009 Wiley-VCH. ....	43
Figure 3.5 Bandgap values vs. strain for a 1.97nm [110] GeNW. Symbols $\circ$ and $*$ denote indirect and direct bandgap. (b) Symbols ( $\blacksquare$ ), $(-)$ and ( $\blacktriangle$ ) represent the band structure at +5%, 0 and -5% strains, respectively. Reprinted with permission from [130]. Copyright 2009 Wiley-VCH. ....	44
Figure 3.6 (a) Bandgap vs. strain for a 2.5nm [100] GeNW. Symbols of ( $\blacksquare$ ), $(-)$ , ( $\blacktriangle$ ) correspond to band structure at +5%, 0 and -5% strain values, respectively. Symbols $\circ$ and $*$ denote indirect and direct bandgap. Reprinted with permission from [130]. Copyright 2009 Wiley-VCH. ....	45
Figure 3.7 Effective mass of electrons and holes vs. strain in a 1.97nm [110] GeNW. Values are normalized to the rest mass of the electron ( $m_0$ ). Reprinted with permission from [130]. Copyright 2009 Wiley-VCH. ....	46

Figure 3.8 Biaxial [110] (line) and uniaxial [100] (dots) strain effects on the energy of conduction sub bands at three different points in BZ of bulk germanium. ....	49
Figure 4.1 The contributions of atomic orbitals in the value of $\Psi(x,y,z)$ are added at point P which is inside the cross sectional plane of ( $z=z_p$ ). ....	57
Figure 4.2 An energy minimized 2.2nm [100] SiNW.....	58
Figure 4.3 (a) Conduction band (CB) and (b) valence band (VB) states at BZ center. CB and VB have even and odd symmetry, respectively. ....	59
Figure 4.4 Normalized momentum matrix element ( $P_{cv}^2/2m$ in terms of eV) along the BZ $[-\pi, \pi]$ of a 2.2nm [110] SiNW for z, y and x polarizations, respectively .....	59
Figure 4.5 Photon polarization vectors are in a plane which is normal to the photon wave vector ( $k$ ). .....	62
Figure 4.6 Schematic of an indirect bandgap SiNW band structure. Difference between direct and indirect conduction sub band minima is shown as $\Delta\Omega$ . This quantity determines the order of light emission process in an indirect bandgap nanowire. There are two possible transitions from indirect conduction minimum ( $i$ ) to the valence band maximum ( $f$ ): (1) via intermediate states ( $m$ ) within the valence band (ADC) or (2) via intermediate states ( $m$ ) within the conduction band (ABC). ....	64
Figure 4.7 Available LA phonons with a common $q_z$ and transversal vectors which span <b><math>qt\_min = 0</math></b> to <b><math>qt\_max</math></b> .....	68
Figure 4.8 Inter-sub band electron-LA phonon scattering events starting from $k_z$ . ....	72
Figure 4.9 Flowchart of saving individual rates for e-LA phonon scattering events. ....	78
Figure 4.10 Grouping and sorting individual LA phonon absorption (a) and emission (e) rates according to intra- or inter-sub band nature of the event. ABS and EM represent absorption and emission of phonons, respectively. A subscript like 12 means scattering from band1 to band2. ....	80
Figure 4.11 Algorithm of grouping and sorting individual LA/LO phonon absorption and emission rates. ....	80
Figure 5.1 (a: left) Cross section of a [110] SiNW with the diameter ( $d$ ) of 1.7nm in xy plane. Diameter ( $d$ ) is defined as average of large ( $D1$ ) and small ( $D2$ ) diameters. Right panel shows the side view of two unit cells along the length of nanowire ( $z$ ) with unit cell length of $U_c$ . Dark and bright atoms represent Si and H atoms, respectively. (b) Electronic structure of the 1.7nm diameter [110] SiNW, which shows direct bandgap i.e. conduction/valence band minimum/maximum reside on the BZ center ( $K=0$ ). Band offset, $\Delta E_{cmin}$ , is smaller for larger diameter nanowires. (c) Normalized	



momentum matrix element, $P_{cv}^2/2m$ (in eV) between conduction and valence band along BZ. Red, Blue and green correspond to Z, Y and X polarizations of emitted photon. ....	84
Figure 5.2 (a) Effect of compressive strain on second valence sub band (V2) which results in the change of wave function symmetry. From left to right, it can be seen that compressive strain raises the energy of V2 faster than it lowers the energy of C2. (b) Normal ized squared value of wave function ( $ \Psi ^2$ ) in the cross sectional plane of a 1.7nm [110] SiNW. From left to right strain values are -2%, 0% and +2%, respectively. Valence and conduction band states (VB and CB) are at BZ center. As can be seen in the left panel (for -2% strain) the change of symmetry is more pronounced for valence sub band. ....	86
Figure 5.3 (a) Mechanism of bandgap conversion in response to compressive strain is due to lowering of C2 sub band. Electronic structure of (b) unstrained and (c) -5% strained 3.1nm [110] SiNW. The indirect conduction band minimum of strained case (c) is lower than the direct conduction band minimum by $\Delta\Omega=80$ meV. This quantity determines the order of phonon mediated process for light emission. ....	88
Figure 5.4 (a) Top: Two serial 1st order processes which model the light emission calculation in indirect bandgap nanowires with $\Delta\Omega < E_{LO/LA}$ . Bottom: A model based on a 2nd order process presented for calculation of light emission in indirect nanowires with $\Delta\Omega > E_{LO/LA}$ . (b) Inter-sub band (direct to indirect) electron-phonon scattering rate ( $s^{-1}$ ) versus the energy starting from the bottom of direct conduction band ( $E-E_{cmin}$ ). As can be seen scattering times for electron-LO phonon and electron-LA phonon scattering events are in the order of 1ps and 100ps, respectively. (c) Possible second order transitions from indirect conduction sub band to the valence band maximum. As it is discussed in the <b>Results</b> section the $A \rightarrow D \rightarrow C$ event is less probable than $A \rightarrow B \rightarrow C$ . Initial, intermediate and final states are represented by $i$ , $m$ and $f$ , respectively. ....	90
Figure 5.5 (a) Occupancy of indirect and direct sub bands vs. electric field for a 3.1nm [110] SiNW at -5% strain (indirect bandgap). Inset shows the positive half of the BZ (i.e. $k$ spans $[0,\pi]$ ) with two conduction sub bands used in the EMC simulation. (b) Time evolution of the electron distribution function under different electric fields. (c) The total LA and LO electron-phonon scattering rates. In the legend, C1 and C2 show the initial sub band from which the electron starts to be scattered by emission/absorption of LA and LO phonons. ....	94
Figure 5.6 Time evolution of electron distribution function under different electric fields at low temperature ( $T=77K$ ). The distribution function is calculated by Professor Amit Verma [149] using the scattering data calculated by the author. ....	95

Figure 5.7 Direct to indirect transition through LO phonon emission (AB and AC transitions) followed by LA emission to reach to the indirect sub band bottom. ....	96
Figure 5.8 (a) Injecting current in a compressively strained nanowire (top) which has an indirect bandgap (bottom) can generate an initial population in SiNW. Although non-radiative processes may deplete this sub band of most of those injected carriers, there will still be a factor of 10 difference in the electron occupancy between the indirect and direct sub bands. (b) During strain release or when applying tensile strain (top), the initial population can scatter into the direct sub band via electron-phonon scattering processes within picosecond time scale. Thereafter (bottom) the inverted population can initiate lasing (coherent stimulated emission) if the nanowire is already embedded in a suitable mode enhancing cavity. In the case of incoherent (spontaneous) emission the light has a broader spectrum suitable for light emitting diode (LED) applications. Similar set up can be devised for light absorption (i.e. photocurrent) modulation using strain. ....	98
Figure 5.9 Effect of external field on the local (internal) electric field when it is parallel (a) and perpendicular (b) to the nanowire. ....	101
Figure 5.10 Imaginary part of dielectric function for a 2.2nm [110] SiNW. Reprinted with permission from [155]. Copyright 2005 American Physical Society. ....	102
Figure 5.11 Valence subbands of a 1.7nm [110] SiNW at -2% (right) and -3% (left) strains. ....	103
Figure 5.12 Right panel: Normalized probability density plot of (V1) and optical matrix element of C1-V1 transition for z, y and x polarizations. Left panel: Normalized probability density plot of (V2) and optical matrix element of C1-V2 transition. ....	104
Figure 5.13 Right panel: Normalized probability density plot of (V1) and optical matrix element of C1-V1 transition for z, y and x polarizations. Left panel: Normalized probability density plot of (V2) and optical matrix element of C1-V2 transition. ....	105
Figure 5.14 (a) Summation over transversal phonon wave vector, $S_{qt}$ . Blue and red curves correspond to analytic and numerical calculation of form factor at each iteration of $k_f$ . Summation is confined to [-0.5,05] interval for the sake of visibility. (b) Multiplying by Fermi factor confines the previous summation in the region close to $k_z=0$ . This calculation is for a 3.1nm [110] SiNW in -5% strain. .	107
Figure 5.15 (a) Diameter dependence of bandgap value for [110] SiNWs. (b) Band structure of a 13nm [110] SiNW (first conduction band and the last valence band are shown only). ....	108
Figure 6.1 Method of finding the number of available transitions (c and v combinations) corresponding to each given photon energy $\hbar\omega$ . ....	115

Figure 6.2 The first BZ of the reciprocal lattice with emphasis on the first octant (solid line) which carries: (b) the first irreducible wedge (dashed line). .....	119
Figure 6.3 Format of saving the states and energies found for $N_w$ triplets of $(k_x, k_y, k_z)$ within the irreducible wedge. ....	120
Figure 6.4 The absorption spectrum of bulk silicon was calculated by DFT and TB. A comparison was made with experimental data provided in [184]. Inset: Imaginary part of dielectric function of bulk silicon, $(\epsilon_2(\omega))$ , calculated by TB and DFT methods .....	121
Figure 6.5 Comparison of the absorption spectra for 0.5nm and 1.1nm [110] SiNWs, calculated by fully numerical and semi-analytic methods. ....	122
Figure 6.6 The absorption spectrum of a 1.7nm [110] SiNW for three different polarizations of the incoming photon. ....	124
Figure 6.7 The absorption spectra of three SiNWs with different diameters (photon polarization is along the z axis). ....	124
Figure 6.8 The magnified section of the absorption spectra around the bandgap energy which was shown in Figure 6.7. (Incoming photons are z polarized). ....	125
Figure 6.9 Absorption spectra for -2%, 0% and +2% strained 1.7nm [110] SiNW. (Incoming photons are z polarized). ....	126
Figure 6.10 Comparison of the bulk silicon absorption spectrum (experimental) with that of a 2.3nm [110] SiNW at +5% strain (tight binding calculation) .....	127
Figure 6.11 The absorption spectrum of a 2.2nm [100] SiNW. Inset shows that the band edge absorption is nonzero for x and y polarized photons while it is zero for z polarized photons. ....	128
Figure 6.12 Measured reflectance of GaN nanowires (Inset). The boundaries of the maximum reflectance portion of the spectrum correspond to LO and TO phonon energies. The minima are used to extract the information regarding plasma frequency. Reprinted with permission from [187]. Copyright 2001 American Institute of Physics. ....	132
Figure 7.1 The flowchart of computational study of AR in SiNWs using tight binding and DFT methods. ....	137

## List of Tables

Table 1.1 Summary of the most recent PL experiments on SiNWs in which the role of quantum confinement is better dissociated from the other effects i.e. models (b) to (f) in Figure 1.7. ....	15
Table 1.2 Summary of the methods with which strain can be generated in a 1D nanostructure e.g. SiNW or CNT. (*) The Young modulus of bulk silicon (150GPa) is used here [119]. (**) Alumina= $\text{Al}_2\text{O}_3$ . (***) PE= Poly Ester. (#) SPM= Scanning Probe Microscopy. ....	25
Table 3.1 Summary of bandgap calculations for bulk Si and Ge. Reprinted with permission from Table I & II of [132]. Copyright 1995 American Physical Society. ....	47
Table 4.1 Components of eigenvectors (basis coefficients) for conduction and valence states of a Si atom within a unit cell. ....	54
Table 4.2 Nonzero overlapping integrals and their corresponding weights in terms of eigenvector entries i.e. $[\alpha_1 \dots \alpha_{10}]$ and $[\beta_1 \dots \beta_{10}]$ . These are used to build the first term in the right hand side of equation 4.8. ....	55
Table 4.3 Slater type orbitals of Si atom. ....	56
Table 4.4 Non-zero overlapping integrals for Salter type orbitals in Si. ....	56
Table 5.1 Average spontaneous emission time, $\tau_{\text{avg}}$ (s) vs. diameter (nm) of [110] SiNWs. Although all nanowires in these strain values have direct bandgap, the change of $\tau_{\text{avg}}$ with compressive strain is mainly due to valence sub band exchange. ....	87
Table 5.2 Spontaneous emission time (s) in a 3.1nm [110] SiNW (at -5% strain with indirect bandgap). (*) Role of LO phonons is more significant than LA phonons (100 times more) in determining the emission times. ....	92
Table 5.3 Electron-LO phonon scattering rates for direct to indirect sub band transitions at two different temperatures. A, B and C states are introduced in Figure 5.7. Note that the transitions through LO phonon emission ( $A \rightarrow B$ and $A \rightarrow C$ ) are almost unchanged at both temperatures. ....	96

## List of Abbreviations

AFM	Atomic Force Microscopy
AR	Auger Recombination
APD	Avalanche Photo Diode
BFGS	Broyden-Fletcher-Goldfarb-Shanno method
BZ	Brillouin Zone
CB	Conduction Band
CBM	Conduction Band Minimum
CG	Conjugate Gradient
CGS	Centimeter-Gramm-Second
CL	Cathodoluminescence
CNT	Carbon Nano Tube
CMP	Chemical Mechanical Polishing
DC	Direct Current
DFT	Density Functional Theory
DOS	Density of States
DZP	Double-zeta type with polarization
EBL	Electron Beam Lithography
EEH	Electron-Electron-Hole
EHL	Electron Hole Liquid
EL	Electro Luminescence
EMA	Effective Mass Approximation
EMC	Ensemble Monte Carlo
EMT	Effective Medium Theory
EPS	Empirical pseudo-potential
FET	Field Effect Transistor
FF	Fill Factor
GAA	Gate All Around
GeNW	Germanium Nano Wire
GGA	Generalized Gradient Algorithm
GW	Green function and screened interaction (W)
HF	Hydrofluoric
HHE	Hole-Hole-Electron
HMS	Hexagonal meso-porous silica
IR	Infrared
JDOS	Joint Density of States

LA	Longitudinal Acoustic
LED	Light Emitting Diode
LDA	Local Density Approximation
LFE	Local Field Effect
LO	Longitudinal Optical
LPCVD	Low Pressure Chemical Vapor Deposition
LTO	Low Temperature Oxidation
MBE	Molecular Beam Epitaxy
MG	Maxwell-Garnett
NC	Nano Cone
PA	Phonon Assisted
PC	Purely Collisional
PDMS	Poly(dimethylsiloxane)
PE	PolyEster
PL	Photoluminescence
PMMA	Poly(methyl methacrylate)
PSM	Phase Shift Mask
RIE	Reactive Ion Etching
RPA	Rapid Phase Approximation
SCF	Self-Consistent Field
SI	Système international
SIMOX	Separation by Implanted Oxygen
SiNW	Silicon Nano Wire
SOI	Silicon On Insulator
SNAP	Super lattice NANowire Pattern transfer
SPM	Scanning Probe Microscopy
SRV	Surface Recombination Velocity
STS	Scanning Tunneling Spectroscopy
STM	Scanning Tunneling Microscopy
TB	Tight Binding
TDDFT	Time Dependent DFT
TEM	Transmission electron Microscopy
TIDFT	Time Independent DFT
TO	Transverse Optical
TPA	Tow Photon Absorption
TRPL	Time Resolved Photoluminescence
UV	Ultraviolet

VB	Valance Band
VBM	Valance Band Maximum
VLS	Vapor Liquid Solid
XEOL	X-ray excited optical luminescence
XES	X-ray emission spectroscopy

# Chapter 1

## Introduction

Interest in Silicon nanowires (SiNW) never stops growing. Potential advantages of SiNWs, such as quantum confinement, large surface-to-volume ratio, adjustable bandgap, sensitivity of electronic properties to surface ligands and mechanical excitation and compatibility with mainstream silicon technology have resulted in a flurry of experimental and theoretical investigations of these nano-structures. Over the years SiNWs have been also explored for use in transistors [1][2], logic circuits [3] and memory [4], spin-based quantum computing [5], chemical [6] and biological [7] sensors, piezo-resistive sensor [8], nano mechanical resonator [9] and thermoelectric converters [10][11]. We are also witnessing the utilization of SiNWs in optoelectronic applications, such as in solar cells [12][13], photo-transistors [14][15], and avalanche photodiodes [16][17].

Efficient light emission from SiNWs makes the idea of single chip Silicon optoelectronics possible. Integrating silicon with photonics has been always favorable due to low cost and matured fabrication technology of silicon chips. Over the years researchers have been trying to observe the signature of quantum confinement induced light emission from SiNWs. Availability of new fabrication and characterization methods has made it possible to reduce the non-radiative and surface recombination and carrier trap effects on the radiation spectrum of a nanowire. However after excluding the non-idealities the efficient light emission in SiNWs requires direct bandgap and symmetry allowed optical transition between conduction and valence states. In other word to have a nonzero optical transition matrix element, which is defined as

$$\langle \Psi_c(\mathbf{r}) | \mathbf{r} | \Psi_v(\mathbf{r}) \rangle = \int \Psi_c^*(\mathbf{r}) \cdot \mathbf{r} \cdot \Psi_v(\mathbf{r}) d\mathbf{r} \quad (1.1)$$

the integrand should have an even symmetry.  $\Psi_c$ ,  $\Psi_v$  and  $\mathbf{r}$  represent conduction band state (wave function), valence band state and position operator, respectively. In bulk silicon and large diameter SiNWs the conduction band minimum and valence band maximum have different values of momentum within the Brillouin Zone (BZ) of the crystal (Figure 1.1a). Since electron-hole recombination should be momentum conserving process (and photon cannot provide the momentum difference), the indirect transition is possible via a second order process containing phonon absorption and emission. On the other hand narrow diameter SiNWs can have direct bandgap due to the folding of the off center energy states of bulk silicon into the BZ center (Figure 1.1b).

For the aforesaid reasons, in the reported experiments that involve large SiNWs in a hybrid light emitting device, the photon emission process is efficiently occurring in the direct



bandgap nanowire which is made from III-V materials and SiNW plays the biasing and carrier injection role. For example nano-lasers and Light Emitting Diodes (LEDs) reported in [18][19] are based on the combination of top-down grown SiNWs and bottom-up III-VI and Cd-VI nanowires, respectively. Hayden et al [20] have also reported a core/shell p-Si/n-CdS nanowire working as a LED.

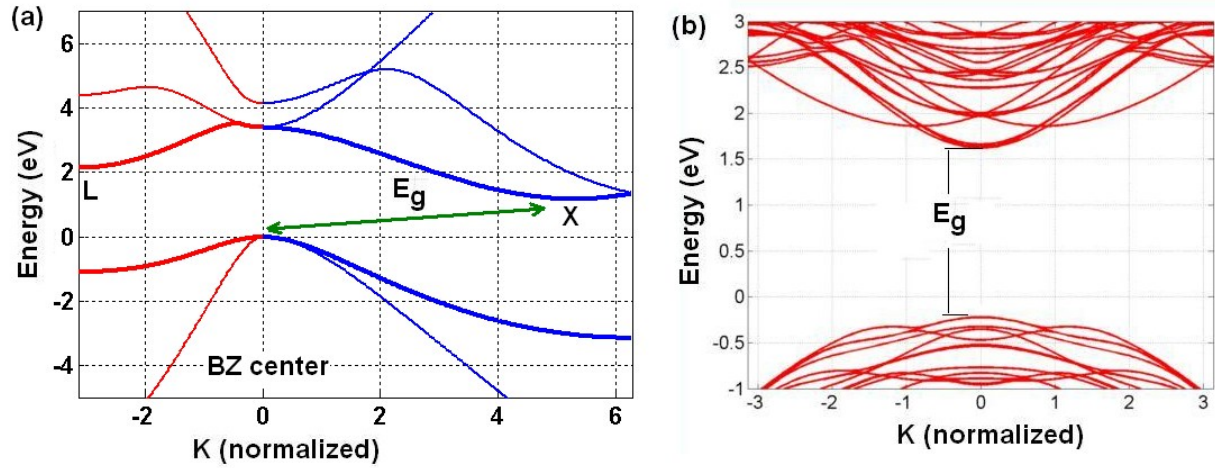


Figure 1.1 (a) Band structure of bulk silicon showing an indirect bandgap. (b) Band structure of a 2.2nm [100] SiNW shows a direct bandgap.

The main theme of this thesis is computational study of strain effects on the electronic and optical properties of SiNWs i.e. photon emission and absorption. The results and underlying physics can build a foundation on which novel applications for SiNWs could be proposed. For this reason the introductory chapter primarily reviews the experimental studies of optical emission in SiNWs. After an introductory section devoted to nanowire fabrication methods, we present how the progress of technology made it possible to understand the light emission mechanism in SiNWs better. This is followed by a short review of how absorption in SiNW array makes them attractive for solar cell applications. Electronic, thermal and mechanical properties and applications of SiNWs and other nanowire materials have been extensively reviewed in [21][22][23][24].

The organization of the thesis is introduced in the third section and the main problems of this thesis are stated there. Finally the methods of strain generation in SiNWs are summarized. These methods are promising the possibility of using strain as a degree of freedom to modulate the optical properties of SiNWs.

## 1.1 Silicon Nanowire Fabrication Methods

Methods of SiNW growth and fabrication can be divided into two main groups: bottom-up, and top-down. As its name suggests, bottom-up method is based on the preferential deposition of reactants on silicon substrate to induce a chemical reaction which results in the crystallization and growth of Si nanowire in a specific direction. The top-down method is based on the standard lithography, oxidation and etching of a silicon layer in which the oxide removal helps in narrowing down the diameter. Although the bottom-up approach can result in narrow diameter nanowires however it lacks the controllability, reproducibility and compatibility with the main stream silicon technology. On the other hand, the minimum achievable size in top-down methods is limited by the resolution of standard lithography and etching processes. But in recent days both methods have demonstrated significant progress in circumventing their limitations. Nowadays generating narrow diameter ( $d \sim 3\text{nm}$ ) SiNWs is possible using either bottom up or top-down methods.

### 1.1.1 Bottom-up Methods

Generally there are three different kinds of bottom-up nanowire growth methods. They are (1) Vapor-Liquid Solid (VLS), (2) Laser-ablated VLS and (3) Oxide-assisted growth. Each of these methods is briefly explained in the following sections.

#### 1.1.1.1 Vapor-Liquid-Solid (VLS) Method

Most of the bottom-up growth techniques of SiNWs are based on the VLS method. In this method a liquid droplet of a catalyst metal (Au, Pt) absorbs silicon atoms from the vapor precursor like silane ( $\text{SiH}_4$ ) or disilane ( $\text{Si}_2\text{H}_6$ ) which is being carried by an inert gas e.g. Ar. Controlling the temperature ( $\sim 440^\circ\text{C}$ ) and pressure (100mTorr), bring the Si-Au droplet into super-saturation [25]. Therefore silicon atoms nucleate on the silicon wafer epitaxially and a nanowire is formed on the substrate with a diameter which is determined by the metallic nano-particle size. The nano-particle remains in liquid form on the tip of the nanowire during the growth process (Figure 1.2). Nanowires with [110] and [111] orientation have been grown using this method. The diameters span between 6nm-20nm and the wires are covered by 1-3nm oxide. It was observed that diluting the  $\text{SiH}_4$  reactant with  $\text{H}_2$  inhibits the oxide formation on the SiNW surface hence SiNWs as thin as 3nm were grown without any oxide coverage [26]. The preferred crystallographic growth direction for nanowires with diameters of 3nm-10nm is [110], while for diameters between 10nm-20nm and above is [112] and [111]. This growth preference can be understood from solid nanowire-liquid catalyst interface and SiNW surface energy. Theoretical studies based on DFT (Density Functional Theory) confirmed the diameter-dependent growth preference [27].

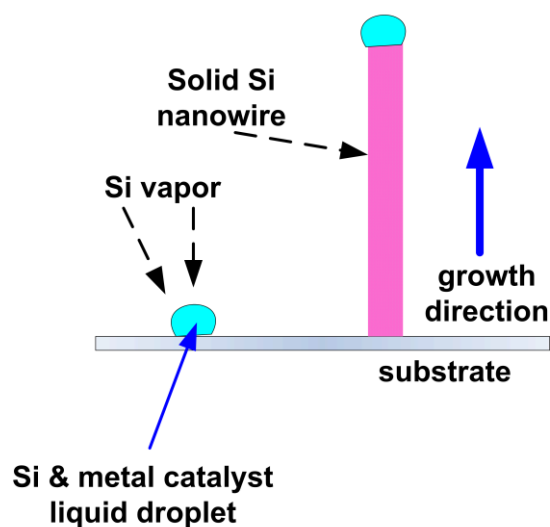


Figure 1.2 VLS mechanism of silicon nanowire growth which starts from silicon and metal catalyst droplet.

It was observed that diluting the  $\text{SiH}_4$  reactant with  $\text{H}_2$  inhibits the oxide formation on the SiNW surface hence SiNWs as thin as 3nm were grown without any oxide coverage [26]. The preferred crystallographic growth direction for nanowires with diameters of 3nm-10nm is [110], while for diameters between 10nm-20nm and above is [112] and [111]. This growth preference can be understood from solid nanowire-liquid catalyst interface and SiNW surface energy. Theoretical studies based on DFT (Density Functional Theory) confirmed the diameter-dependent growth preference [27].

Review of all types of VLS method is beyond the scope of this introductory chapter. Interested readers can refer to recent extensive review articles for example [28] [29] which give details of different growth processes and corresponding pros and cons.

#### 1.1.1.2 Laser Ablated VLS Method

Since the size of nanowire is limited by the size of liquid catalyst-Si droplet in equilibrium phase, growing the nanowire from non-equilibrium cluster will result in smaller diameters. This is achieved by a laser with the wavelength of  $\lambda = 532\text{nm}$  which ablates silicon and metal catalyst ( $\text{Si}_{0.9}\text{Fe}_{0.1}$ ) targets in a quartz furnace [30]. This subsequently leads to the formation of dense and hot plasma ( $1200^\circ\text{C}$ ). Once the vapor condenses into liquid droplets, silicon atoms which are being cooled due to collision with Ar carrier atoms enter into the droplet and nucleation begins after the super-saturation. Figure 1.3 shows the Transmission Electron Microscopy (TEM) image of [111] SiNWs in 6nm-20nm diameter range. The oxide sheath on each nanowire is formed due to the reaction with residual oxygen in the growth chamber.

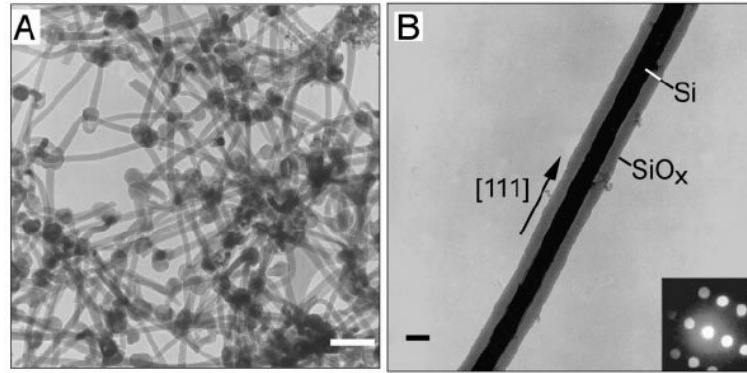


Figure 1.3 (a) TEM image of grown SiNW using laser ablation of  $\text{Si}_{1-x}\text{Fe}_x$  target (scale bar is 100nm). (b) 10nm thick SiNW covered with amorphous oxide sheath. Reprinted with permission from [30]. Copyright 1998 AAAS.

#### 1.1.1.3 Oxide Assisted Catalyst Free Method

The smallest SiNW reported ever (1.3-7nm) has been synthesized by this high yield and catalyst-free method [31]. This method is based on the decomposition of SiO into Si core and  $\text{SiO}_2$  sheath. The process starts with heating of SiO in an alumina furnace up to  $1200^\circ\text{C}$ . At  $900^\circ\text{C}$ , SiNW starts to nucleate under a flow of  $\text{H}_2$  and Ar gas mixture. The observed growth directions are mainly [112] and [110]. The oxide sheath on the nanowires is removed by Hydro Fluoric (HF) acid and as a result the surface silicon atoms are terminated with hydrogen atoms. Scanning Tunneling Spectroscopy (STS) and Microscopy (STM) images confirm the formation of stable  $\text{SiH}_2$  and  $\text{SiH}_3$  groups on SiNW surfaces [31]. Importantly the relationship of bandgap value and diameter of the nanowire confirms the quantum confinement in this experiment [31]. Other alternative of catalyst free method is using laser ablation and powder mixture of pure Si and  $\text{SiO}_2$ . It has been confirmed that  $\text{SiO}_2$  plays an important role in high yield catalysis of SiNW formation [32].

### 1.1.2 Top-down Methods

There are many variants of top-down methods in the literature however they can be categorized according to their capability in creating a single nanowire or an array of nanowires. An example of each category is presented here.

#### 1.1.2.1 Single Nanowire

Figure 1.4a-c shows three different process flows for SiNW Gate-All-Around (GAA) Field Effect Transistor (FET) fabrication. Starting from a highly piezoresistive, low doped p-type silicon wafer ( $10^{15} \text{ cm}^{-3}$ ), three types of SiNW can be fabricated depending on the oxidation time and isotropic etching rate (Figure 1.4a-c). The first and the second steps of Figure 1.4a-c show the Low Pressure Chemical Vapor Deposition (LPCVD) of  $\text{Si}_3\text{N}_4$  layer (etching mask),

isotropic etching (HF acid) and oxidation. The third step consists of Low Temperature Oxidation (LTO) followed by Chemical-Mechanical Polishing (CMP). Thinning the oxide (10-20nm) followed by LPCVD Polysilicon growth results in an oxide-surrounded SiNW gate in three different forms: (a) floating triangular SiNW, (b) floating pentagonal SiNW and (c) a body-tied omega shaped SiNW [33].

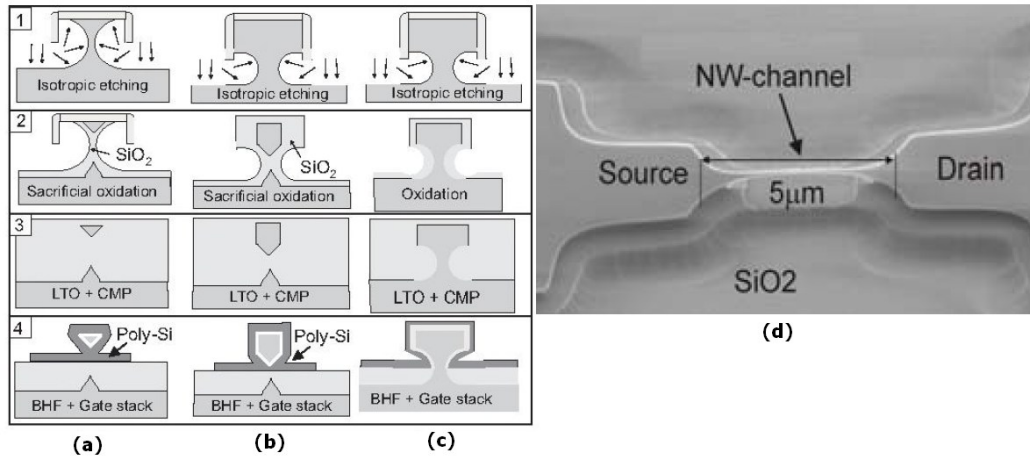


Figure 1.4 (a) Floating SiNW. (b) floating pentagonal. (c) Non-floating (body-tied) omega-shaped SiNW with diameters of 208nm, 197nm and 372 nm, respectively. (d) Top-view of GAA\_FET of type (a) SiNW. Reprinted with permission from [33]. Copyright 2007 IEEE.

Since silicon is etched from the bulk material, the minimum thickness of SiNW is limited by the resolution of lithography which is defined by the etch-stop layer ( $\text{Si}_3\text{N}_4$  in this case). This limitation is circumvented by a more precise lithography techniques e.g. employing Phase-Shift-Mask (PSM) [34][2]. Starting from a Silicon On Insulator (SOI) wafer as above, a 30nm-40nm silicon fin can be defined by KrF PSM lithography. The subsequent etching and self-limited oxidations result in a floating SiNW as thin as 3nm (Figure 1.5).

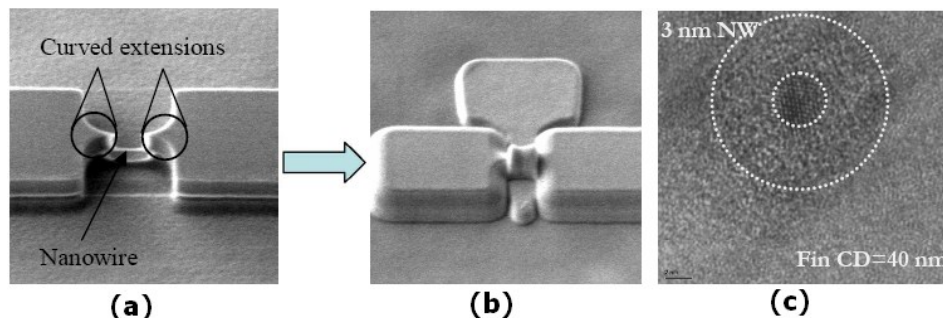


Figure 1.5 Oxide-assisted narrowing of a floating SiNW before (a) and after (b) gate metallization. (c) Cross section of oxide covered SiNW. Reprinted with permission from [34][2]. Copyright 2007 IEEE.

Different SiNW-based GAA-FETs can be implemented by covering the SiNW with SiO<sub>2</sub> or HfO<sub>2</sub> (as gate dielectric) and Polysilicon or TaN (as gate contact) [34][2].

#### 1.1.2.2 Array of Silicon Nanowires

**Horizontal Array:** Arrays of silicon nanowires are of interest in memory, crossbar switch, biosensors and logic circuit applications. Reproducibility and uniformity of an array is an important requisite which can be met by top-down method. However there is one example of mixing top-down and bottom-up approach reported in [35]. In [35] a long bottom-up grown (2mm) SiNW serves as a common channel of a FET array. Superlattice Nanowire Pattern transfer (SNAP) is a method which circumvents the resolution limit of optical lithography or low throughput Electron Beam Lithography (EBL) using high precision Molecular Beam Epitaxy (MBE) [36]. In SNAP method a GaAs/Al<sub>0.8</sub>Ga<sub>0.2</sub>As super lattice is grown on a [100] GaAs wafer. Selective etching dissolves the AlGaAs layers as deep as 30nm. Different metals like Pt, Al, Au and Cr are evaporated on to the etched edge of MBE grown layers while tilted at 36°. The pattern of metallic nanowires can be transferred on a 10nm thick epoxy film which is grown on the SOI wafer. After curing the epoxy layer and etching the GaAs layers away the remaining patterns on epoxy layer form a metallic nanowire array. Interestingly the metallic nanowire array can be used as an etch stop mask to transfer the patterns of nanowires on the semiconductor substrate. The area between the metallic nanowires can be etched away using Reactive Ion Etching (RIE) and the remaining area under the metallic layers forms a SiNW array on the oxide layer. The diameters can be as small as 18-20nm with pitches of 30-60nm. The metallic or semiconductor nanowire array which is obtained in SNAP method can be transferred to a Poly(dimethylsiloxane) (PDMS) stamp or a soluble glue layer. As shown in Figure 1.6, the adhesive PDMS layer peels off the SNAP nanowire array from the SOI wafer. Bringing PDMS stamp into conformal contact with epoxy coated plastic (mylar) substrate, followed by UV curing and peeling off the PDMS, result in a SiNW array on plastic substrate [6].

Transferring electronic circuits on plastic substrate is always interesting because it makes the implementation of low cost, light weight, flexible, implantable, wearable and bio-compatible sensors and circuits possible. Importantly it was observed that stretching and deforming the plastic substrate does not cause any breakage or bundling of SiNWs which is very useful in studying the strain induced changes in electronic and optical properties of nanowires.

**Vertical Array:** While previous methods are useful to generate horizontal arrays, recent experiments are promising for highly repetitive uniform array of SiNWs. As an example in [37] a vertical array of 50nm thick SiNWs are formed by etching a crystalline <100> silicon wafer. An array of 30-50nm disks is patterned in a 75nm Poly-(methyl methacrylate) PMMA layer followed by direct current (DC) sputtering of 25nm Al<sub>2</sub>O<sub>3</sub> layer. This layer serves as an etch mask for further fluorine etching with 60:1 aspect ratio. Finally thermal oxidizing the

nano pillars at 850-950°C reduces the diameter of silicon cores down to 2.5nm. The narrowing of diameter is due to the growth of oxide layer thickness. This growth is however self-limited due to the increase of strain energy at the Si/oxide core/shell interface [38].

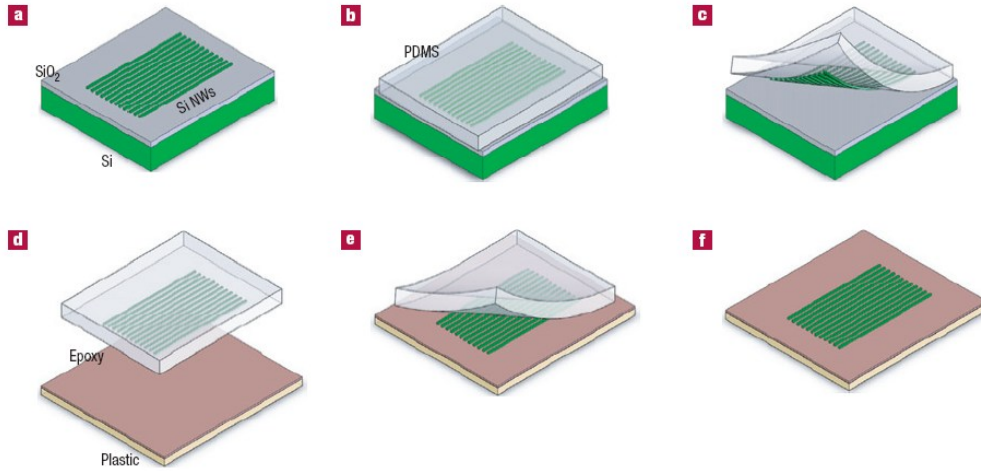


Figure 1.6 (a), (b) and (c) peeling off the SNAP nanowires from the SOI substrate using PDMS glue. (d), (e) and (f) Pattern transfer on SU-8 epoxy coated plastic (mylar) substrate. Reprinted with permission from [6]. Copyright 2007 Macmillan Publishers Ltd.

## 1.2 Optical Properties of SiNWs

The review of the all experimental works related to SiNWs is not straightforward since in the literature the diameter of nanowire spans 3nm to 900nm. To discriminate between large and small diameter nanowires, the Bohr radius of free excitons in bulk Si ( $a=4.9\text{nm}$ ) [39] is used as a criteria to define a one dimensionally confined nanowire. However there are reported experiments with large diameter nanowires ( $d>a$ ) which reveal interesting physical effects and they help us in general understanding of surface, strain and local field effects. Additionally they reveal the trend of technology and experimental studies of light emission in SiNWs during the last decade.

### 1.2.1 Studies of Optical Emission

The first experiments that stimulated intensive study of SiNW as a potential light source were reported by [40][41]. It was suggested that quantum confinement in the silicon filaments is responsible for visible red peak in photoluminescence (PL) spectrum. The thickness of these filaments was less than 5nm and they were formed by anisotropic etching of porous silicon. Further theoretical ab-initio studies [42], Time Resolved (TR) PL spectroscopy [43] approved the confinement-based model. Also Lu et al [44] observed a visible PL from Si/SiO<sub>2</sub> super lattice made by MBE. They showed that PL emission is detectable from

samples in which the thickness of silicon layers is less than 3nm. Later on more theoretical works based on tight binding (TB) [45], empirical pseudo-potential (EPS) [46][47] and ab-initio DFT methods [48][49] attempted to identify the source of visible PL spectra and blue shift by using idealized 1D silicon nanostructures.

In addition to the above-mentioned studies alternative models have been proposed to explain the visible PL from porous silicon. Figure 1.7 represents six models to which the visible PL has been attributed [50]. The proposed models are:

(a) *Crystalline silicon* (i.e. bulk or quantum confinement): In this model the bandgap enlargement due to 1D confinement results in visible luminescence.

(b) *Hydrogenated amorphous silicon*: which attributes the PL emission to amorphous a-Si:H phase. TEM studies however rejected this idea by showing that in porous silicon there is no a-Si:H phase.

(c) *Surface Hydrides*: In this model SiH<sub>2</sub> surface Hydration are proposed as a source of PL emission. This is based on the observation of blue peak bleaching after surface treatment with HF. However the following observations rejected this model by showing that:

(i) Reducing H coverage by high quality oxidation has increased the PL intensity rather than decreasing it.

(ii) There are samples of porous silicon with high SiH<sub>x</sub> coverage which showed no PL emission.

(iii) Loss of PL after removing SiH<sub>x</sub> from the surface in some experiments can be due to non-radiative recombination in oxide defects, not due to SiH<sub>x</sub> removal.

(d) *Defects*: PL peaks which are diameter independent can be due to electron-hole recombination in these vacancies. Any diameter dependent peak in PL spectrum cannot be due to this model though. Change of diameter could be the result of changing oxidation process, temperature and etching conditions.

(e) *Molecules*: Siloxane molecules (polymers of Si/O/H) which are formed during porous silicon formation can be the source of PL according to this model. Since PL peaks are not removed by increasing the temperature, this indicates that in porous silicon the Siloxane model could not be the source of the PL emission. This is because Siloxane molecules melt at elevated temperatures and PL peaks are expected to be wiped out.

(f) *Surface states*: Depending on how deep the surface trap potential is, they can be categorized as follows:

(i) *Deep or strongly localized*: In this case the wave function is highly localized on an atomic site hence the momentum conservation condition for indirect exciton recombination is relieved. Therefore many phonons with different momentum and energy are available to make the light emission possible. This will in turn lead to a broad PL emission spectrum.



(ii) *Shallow or weakly localized*: In this model the wave function is spread on a few atomic sites and it is weakly localized. Hence the recombination takes place with the help of one phonon with exact momentum difference which exists between initial and final electronic states. If the PL emission is attributed to this process then the PL spectrum width change with temperature is less than that of deep surface state. In the case of deep surface state the temperature effect is more pronounced on the broad skirts of the PL spectrum.

As it can be seen in all the following works the common trend is an attempt to dissociate the quantum confinement and other effects from which PL features may have been induced.

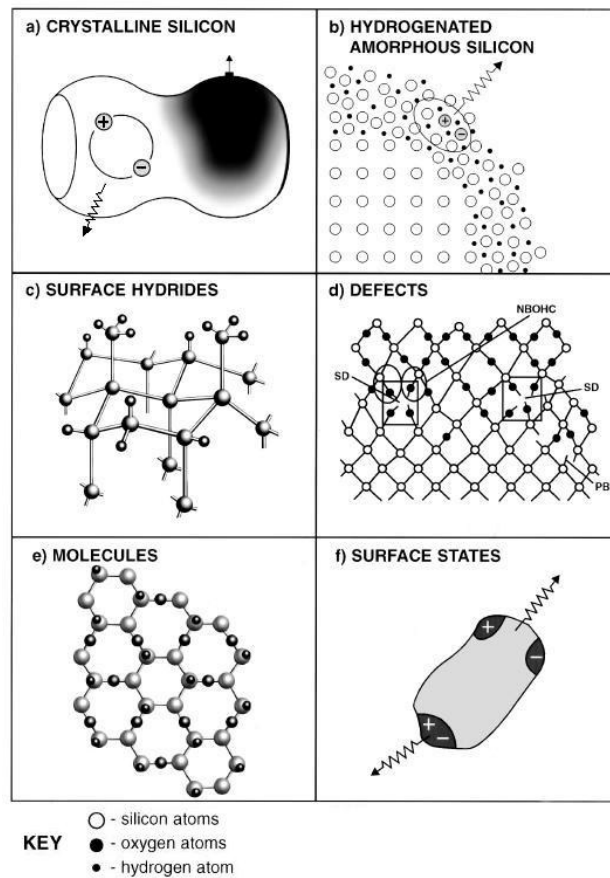


Figure 1.7 Six models proposed to explain the visible PL emission from porous silicon. Reprinted with permission from [50]. Copyright 1997 American Institute of Physics.

In accordance with this trend we observe how the better surface quality and controlled diameter of SiNWs through advanced fabrication and characterization have reduced the role of (b)-(f) processes and let the remaining mechanism of (a) be the major source of visible

light emission in SiNWs. Cullis et al showed that their first observation of PL does not fit into any of (b)-(f) models and can be explained by model (a) in Figure 1.7 [50].

#### 1.2.1.1 Evidences in support of Models (b)-(f)

Looking at the experiments using large diameter nanowires, reveals that defects, surface effects and surface Hydrides play an important role in determining the PL spectrum of these nanowires. Also they may obscure the visible PL which is arising from quantum confinement in silicon nano-crystallites within oxide layers (if there are any). Discriminating between the surface and confinement induced PL features is done by: first measuring the whole PL spectrum; then performing surface treatment by removing oxide/nitride from the surface of SiNW by suitable liquid or gaseous etchants and finally measuring the PL spectrum for the second time. If there is any feature in the PL spectrum after this stage, it can be due to pure confinement induced PL emission i.e. direct recombination of electron and holes within the core of SiNW.

As an example the *top-down* process which starts with a low quality Separation by Implanted Oxygen (SIMOX) wafer resulted in a large number of non-radiative traps in Si-SiO<sub>2</sub> interface on a SiNW [51] similar to model (d) of Figure 1.7d. As the energy levels within these defects are insensitive to the diameter of nanowires, the PL spectrum in these nanowires should be diameter independent; otherwise the source must be something else rather than defects. After subtracting PL emission due to oxide as well as nitride layer in those samples that were passivated by amorphous a-Si<sub>x</sub>N<sub>y</sub>:H, there is no PL peak which can be attributed to the SiNW core (quantum confinement). This suggests that top-down fabrication of narrow SiNWs requires precise control of the number of non-radiative centers on the surface of SiNW.

The importance of surface effects is also observable in the *bottom-up* grown SiNWs. The PL spectrum of 15±3 nm <111> SiNWs surrounded by a 2 nm thick amorphous Si oxide layer [52] shows two blue peaks at 2.40 eV and 2.95 eV. Since the diameter of SiNWs is larger than the Bohr radius of free excitons (4.9 nm) [39], the peaks are attributed to the amorphous Si oxide coverage layer. Macro-PL measurements [52][53] reveals a similar blue peak and proves that it results from the recombination in oxide related defects. Although SiNWs in [53] are thinned to 4 nm using oxide assisted narrowing, still the PL is obscured by low quality oxide defects.

Blue PL emission has also been observed in Si<sub>1-x</sub>Ge<sub>x</sub> oxide nanowires grown on epitaxial SiGe alloys using VLS method [54]. The PL spectrum of these nanowires have a peak at  $\lambda = 415$  nm which is shorter than the peak at wavelength of  $\lambda = 470$  nm observed for SiNWs with oxide layer. The increased number of O<sub>3</sub>=Si-Ge=O<sub>3</sub> and O<sub>3</sub>=Ge-Ge=O<sub>3</sub> bonds is responsible for the increased emitted PL energy i.e. a shorter wavelength. On the contrary the Si-SiO<sub>2</sub> system has lower energy due to oxygen deficit O<sub>3</sub>=Si-Si=O<sub>3</sub> bonds. This notion that radiative

centers in the cladding layer and interface states are responsible for luminescence features has been also confirmed by [55] and [56]. Through X-ray excited optical luminescence (XEOL) with X-ray emission spectroscopy (XES) [55] and Cathodoluminescence (CL) spectroscopy [56] it was observed that in SiNWs with diameters between 20 nm and 50 nm which have oxide cladding, the CL spectrum has blue and red line emissions. Since the blue CL line disappears after treating the surface with HF acid, this means that oxide layer defects are the source of the blue peak with PL decay of 1 msec. The red color wavelength peak with faster PL decay of 10  $\mu$ sec is due to faster dynamics associated with Si-H and Si-H<sub>2</sub> bonds that replace the Si-O bonds in the core-cladding interface [56] after HF treatment. This is the evidence of surface Hydride model which is shown in Figure 1.7c.

It was demonstrated that thermal oxidation followed by precursor gas annealing can reduce the surface trap density of SiNWs by up to  $5 \times 10^9 \text{ cm}^{-2}$  [57] which is three orders of magnitude less than the previously reported values [58]. Using TRPL spectroscopy at T=10K and fitting the measured data to the surface recombination model shows that surface recombination velocity (SRV) of SiNWs can be reduced to the record value of 20cm/sec. Furthermore it is observed that gold nanoparticle has negligible role in the PL spectrum of Au-catalyzed Vapour Liquid Solid (VLS) grown SiNWs. This is proved by showing that the bulk recombination time of thick (d~200nm) SiNWs is close to the same value for bulk silicon and mainly arises from surface effects [57].

#### 1.2.1.2 Quantum Confinement: Model (a)

Study of quantum confinement and PL in SiNWs was revived again by observing the diameter dependent PL spectrum of SiNWs in [59] and [31]. Also with the availability of advanced methods of generating porosity like: (1) electro-less etching, (2) metal-assisted electrochemical etching, (3) wet etching, (4) porous silica template, and (5) oxide-assisted narrowing, it is now possible to observe more evidences in favor of the quantum confinement model [model (a) in Figure 1.7].

***Electro-less etching:*** Crystalline porous SiNW arrays was fabricated using electro-less etching of p-type <100> silicon wafers [60]. The PL spectrum of p-type nanowires with average pore diameter of 9.7 nm shows a peak centered at 680 nm (visible orange red). Although the role of surface oxide/defect cannot be ruled out, this peak is attributed to quantum confinement within 3-4nm thick Si nano pillars which are formed around the electro-less etched pores [60].

***Metal-assisted electrochemical etching:*** Similarly a PL spectrum centered at 650 nm is observed for n-type SiNWs which formed in the pores of an n-type <100> silicon wafer. The pores are created by metal-assisted electrochemical etching [61]. Optical micrograph has shown that PL emission has a uniform intensity along the length of the SiNW [61]. The

visible red orange light emission ( $\lambda=600\text{nm}$ ) also exists in the PL spectrum of 4nm thick SiNWs which are excited capacitively with a 3kHz  $\pm 70\text{V}$  pulse [62]. The nanowires were covered with  $\text{HfO}_2$  and the Electro Luminescence (EL) spectrum resembles those PL spectra which were observed in [60] and [61]. Although there is no peak due to surface defects ( $\lambda=800\text{nm}$ ), however authors could not dissociate direct recombination and the recombination in deep centers due to Au impurities which results from VLS growth.

**Wet etching:** Similar visible (red orange) PL spectrum was observed at room temperature for SiNWs fabricated by wet etching of both n-type and p-type  $\langle 111 \rangle$  Si wafers [63]. According to the authors, HF-treatment of SiNWs removes  $\text{SiO}_x$  surface states and causes a red shift in the PL spectrum. But this change is only significant at wavelengths corresponding to Si–O vibration frequencies. Therefore it is suggested that visible PL spectrum is partly due to surface state and mainly due to quantum confinement in periodically rough sidewall structures of SiNWs. While the diameter of nanowires is between 30nm and 200nm, the size of the side wall non uniformities is in the 2.5-3.5nm range in which quantum confinement effect is believed to occur.

**Porous silica template:** Fabrication of 2D arrays of silicon [64] and germanium [65] nanowires have been reported using a hexagonal meso-porous silica (HMS) template. The SiNWs with diameters of 2.2nm, 4.5nm, 5nm and 7.3nm can be encased in this template using a method called supercritical fluid inclusion-phase [64]. The following observations were made in these works. Firstly the UV-absorption spectrum shows that all nanowires start to absorb at 3.5eV which is the direct bandgap value of bulk silicon. Secondly there is a strong and temperature independent PL signal for all nanowires within visible and ultraviolet (UV) range (2.5eV-4.5eV). Temperature independent peak and corresponding wavelength (at both  $T=300\text{K}$  and  $T=15\text{K}$ ) shows that the recombination process is not of indirect phonon-assisted type. Thirdly the blue shift with decreasing diameter is the signature of quantum confinement. And finally since the UV-PL peaks are diameter dependent they cannot be due to the electron-hole recombination at oxygen defect centers in SiNW/silica interface [according to the model (d) in Figure 1.7].

Further crystallography studies proved that as the diameter of nanowires decrease the curvature between nanowire surface and surrounding template material (silica) causes radial lattice expansion. This was also confirmed from germanium nanowire studies [65].

**Oxide-assisted narrowing:** Although this technique dates back to 1993 when Liu et al [38] reported sub-5nm silicon nanowire fabrication using self-limited oxidation-assisted narrowing, however it was not used to study the luminescence of SiNWs until recently. In [66]  $\text{TiSi}_2$ -catalyzed SiNW arrays grown on n-type  $\langle 100 \rangle$  silicon wafer are thermally oxidized to shrink to a diameter of  $3.3 \pm 1.6\text{nm}$ . The PL spectrum of these nanowires is

centered at  $\lambda=800\text{nm}$  and it is attributed to confinement. The PL decay time ( $\tau_d$ ) at input power excitation of  $I_{\text{ex}} < 0.1\text{W/cm}^2$  is  $50\mu\text{sec}$ . By increasing the input excitation intensity, the PL decay time decreases and this is the signature of Auger recombination which will be discussed in the next sub section.

Effect of radial strain on the PL spectrum was verified both experimentally and theoretically by Walavalkar et al [37] followed by a recent work from Demichel et al [67]. The importance of these two recent works is threefold. Firstly they show the feasibility of fabricating narrow ( $d \leq 3\text{nm}$ ) Si nanowires in which the pure quantum confinement is observable. Secondly they show that strain can be a potential degree of freedom in modulating the optical properties of Si nanowires although in these works strain is an unwanted artifact of nanowire oxidation. Thirdly the authors demonstrated that their experimental results are reproducible using TB method [68] which is a strength point for tight binding method. In [37] the visible and near-infrared (IR) PL spectrum of sub 10nm top-down fabricated SiNWs thinned by self-limited oxidation spans 600–800 nm wavelength range (1.5–1.9 eV). It is observed that after cooling of SiNW array in forming gas (5%  $\text{H}_2$ , 95%  $\text{N}_2$ ), the 1.9 eV peak disappears. This proves that the peak was due to hole trapping of isolated oxygen atoms. Hence the observed blue shift by decreasing the diameter is the evidence of quantum confinement, direct bandgap in narrow (2–4nm) SiNWs as well as radial strain due to oxide cladding which changes the band structure. Figure 1.8a shows an array of 50nm SiNWs etched into a single crystal silicon. The TEM image shows that the diameter of nanowire has shrunk to 4nm after thermal oxidation. As shown in Figure 1.8b the reduction of diameter increases the energy of the PL peak and this was reproduced by TB method including the radial strain [37].

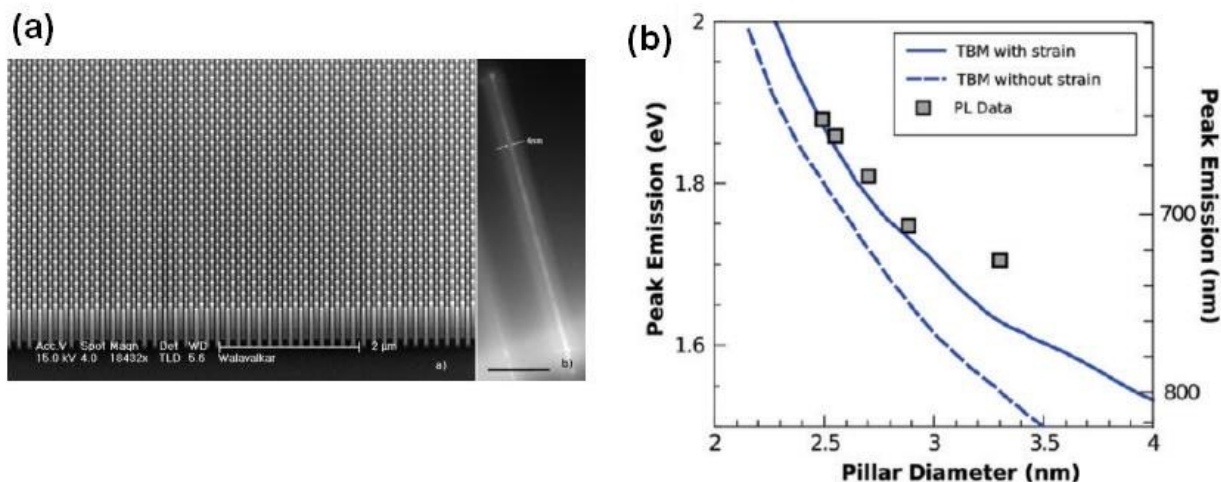


Figure 1.8 (a) An array of 50nm SiNWs. Inset shows the TEM image of a 4nm thick SiNW narrowed by thermal oxide. (b) Diameter dependence of the PL peak is compared with TB method with (solid line) and without (dashed line) radial strain. Reprinted with permission from [37]. Copyright 2010 American Chemical Society.

In [67] a multi-step strain-induced self-limited oxidation is used to decrease the diameter of SiNWs to 5nm. Initially the nanowires are 100nm-200nm thick and their PL spectrum is centered on the bulk bandgap of 1.08eV. The peak corresponds to a phonon-assisted electron-hole liquid (EHL) radiative recombination process in bulk silicon. The low temperature ( $T=10K$ ) ensures that carriers in the nanowires are in EHL many-body phase. The blue shift of the bandgap due to the diameter is successfully reproducible using TB method and the role of strain and confinement has been dissociated according to the model presented in Figure 1.9a. In this model the initial drop of quantum shift ( $\sigma$ ) is due to radial strain after which the quantum confinement upshift of bandgap ( $E_{QC}$ ) becomes more dominant and the bandgap increases (Figure 1.9b). Table 1.1 summarizes the results of the most recent PL experiments in which the role of quantum confinement was proven to be dominant over other mechanisms.

Reference	Growth/Fabrication method	Nanowire diameter (d)/direction	PL peak wavelength ( $\lambda_{max}$ )	PL decay time ( $\tau_d$ )
[10]	Electroless etching	Pore diameters from 2nm to 20nm/ NA	680nm	NA
[61]	Metal assisted etching	$d > 5nm$ /n-type (100) silicon wafer	650nm	NA
[13]	Wet etching	Pore diameters from 2.5nm to 3.5nm/n-type and p-type (111) silicon wafer	850nm	NA
[65], [64]	Porous template	$d =$ from 7.3nm to 2.2nm / $\langle 100 \rangle$	$\lambda_{max} =$ from 497nm to 620nm	20 nsec (bulk silicon = 4msec at $T=23^\circ C$ ).
[66]	Oxide assisted narrowing	$d = 3.3 \pm 1.6nm$ / on $\langle 100 \rangle$ silicon wafer	800nm	50 $\mu sec$
[37]	Oxide assisted narrowing	$2.5nm < d < 8nm$ / on $\langle 100 \rangle$ silicon wafer	$600nm < \lambda_{max} < 800nm$	$200nsec < \tau_d < 250nsec$
[67]	Oxide assisted narrowing	$d > 5nm$ / on (100) silicon wafer	$\lambda_{max} > 1160 nm$	NA

Table 1.1 Summary of the most recent PL experiments on SiNWs in which the role of quantum confinement is better dissociated from the other effects i.e. models (b) to (f) in Figure 1.7.

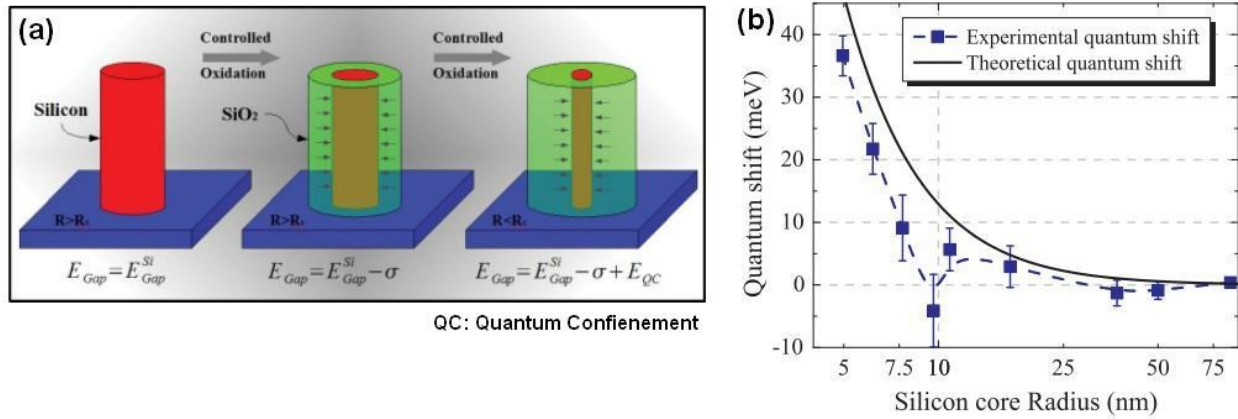


Figure 1.9 (a) A model for oxidation-assisted narrowing of SiNW. The bandgap energy initially decreases due to radial strain and then the role of QC gets stronger in narrower diameters. (b) Comparison of TB calculations with the measured values of the PL peak shift. Reprinted with permission from [67]. Copyright 2011 American Physical Society

### 1.2.1.3 Auger Recombination (AR)

Auger recombination is one of the non-radiative recombination processes in semiconductors which deteriorates the efficiency of LEDs, impedes the population inversion and decreases the gain in semiconductor lasers. This happens when the excess energy of electron-hole recombination (direct or phonon-assisted) is transferred to another carrier (electron or hole) rather than generating a photon. Figure 1.10 compares direct radiative recombination with electron-electron-hole (*eeh*) and hole-hole-electron (*hhe*) AR processes. Intuitively it is expected that higher density of free carriers (due to doping, high temperature or high power laser excitation) can increase the rate of AR process. Transfer of energy to the third carrier can also take place via absorption /emission of a phonon. In this case the AR process is of Phonon-Assisted (PA) type as shown in Figure 1.10d.

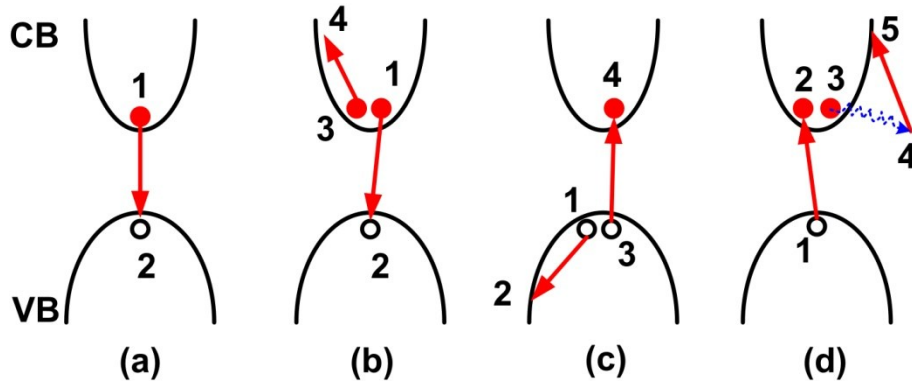


Figure 1.10 (a) Direct radiative recombination. Direct AR of (b) eeh type and (c) hhe type. (d) Indirect phonon assisted AR process. CB and VB stand for conduction band and valence band, respectively.

The Auger recombination time is related to the density of carriers via the following equations:

$$\frac{1}{\tau_{eeh}} = C_n(n_0)^2 \quad \text{and} \quad \frac{1}{\tau_{hhe}} = C_p(p_0)^2 \quad (1.2)$$

where  $n_0$  and  $p_0$  are electron and hole densities, respectively.  $C_n$  ( $C_p$ ) is the Auger coefficient for n-type (p-type) semiconductor, respectively. Since the initial laser excitation in the PL experiments generates high density of carriers, the initial recombination of electron-holes is dominated by AR process according to equation (1.2). Therefore AR manifests itself as a fast drop of PL peak as time goes by. This can be modeled as a double exponential decay curve as shown in Figure 1.11a [57].

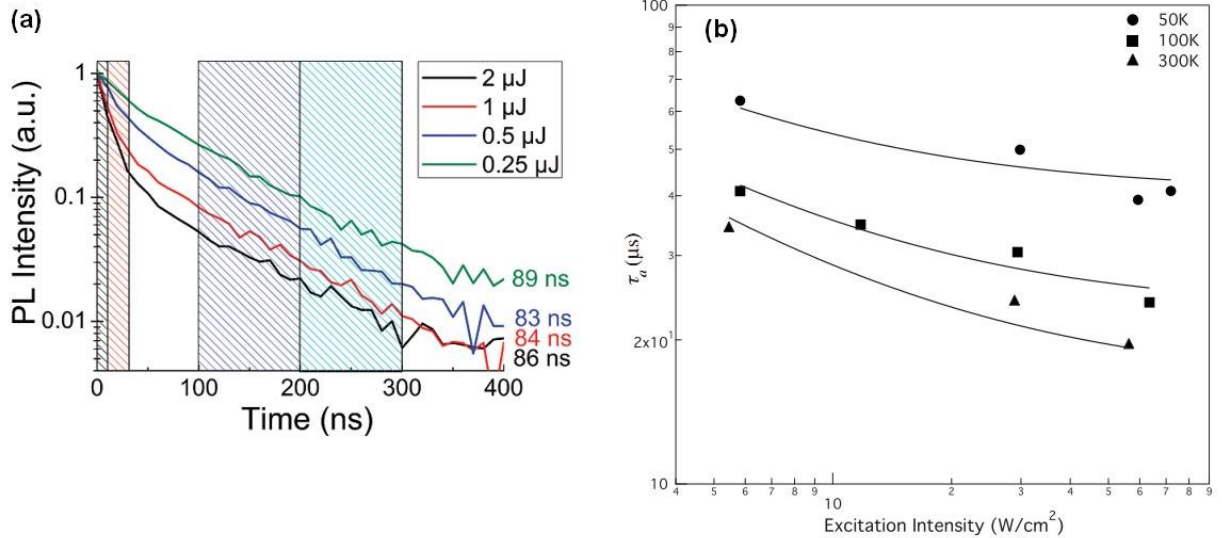


Figure 1.11 (a) PL decay curves versus optical pump intensity at T=10K for Au-catalyzed SiNWs. Reprinted with permission from [57]. Copyright 2009 American Chemical Society. (b) AR lifetime ( $\tau_a$ ) versus excitation intensity at three different temperatures for TiSi<sub>2</sub>-catalyzed SiNWs. Reprinted with permission from [66]. Copyright 2008 American Physical Society.

Also as it is evident in Figure 1.11a that the initial decay of PL peak (right after excitation is turned off) is intensity dependent. The TRPL is performed at T=10K with a 50nsec long laser pulse of different energies ranging from 0.25μJ to 2μJ. After the laser pulse ends, slope of the decay is independent of laser intensity and the time constant is 85nsec. The nanowires of this study are large (d~100nm) and have the same PL signature of bulk Si at 1.08eV. Since at the



beginning of laser pulse ignition an electron-hole plasma (EHP) is formed in the nanowire the initial AR process is significant. Guichard et al [66] have used the same TRPL study for narrow SiNWs ( $d \sim 3\text{nm}$ ) which are thinned by oxide-assisted narrowing. It is stated in this work that the best fit to experimental data is possible if Auger recombination is modeled as two-level exciton-exciton recombination (rather than three particle models i.e.  $hhe$  or  $eeh$ ). Therefore even in highest input laser pulse power of  $60\text{W/cm}^2$ , the AR recombination time in  $3\text{nm}$  SiNW can be  $20\mu\text{sec}$  at room temperature. This is because in excitons-exciton model the Auger lifetime is linearly dependent on the carrier density i.e.  $1/\tau_a = C_a n_0$ . Figure 1.11b shows the calculated AR lifetime for different temperatures versus the intensity of excitation laser.

### 1.2.2 Studies of Optical Absorption

Experimental studies of photo-absorption in SiNWs are mostly pivoting around the applications of SiNW arrays in solar cells, wave guides [69], color filters [70] and photonic crystals. Measurements of absorption, reflection, transmission and wave guiding characteristics of these structures reveals the electromagnetic wave scattering properties of the nanowire layers and it does not have any intimate relevancy to the quantum confinement and many-body effects within each SiNW. Furthermore the diameter of these SiNWs lies between  $1\mu\text{m}$  to a few tens of nanometers which means that the direct bandgap of SiNW plays no role in these experiments. In this sub section a few of these experiments are reviewed.

**Spectrum Widening:** What makes the SiNW array more attractive is its effectiveness in increasing the absorption in a wider spectrum. The optical properties of SiNWs arrays have been studied both experimentally and theoretically [71][72] in the context of solar cell application. Two types of SiNW arrays have been studied in [71]. The first type of array (type-A) is fabricated by galvanized wet etching of silicon on glass film. The thickness of SiNWs is in the range of  $20\text{--}100\text{nm}$  due to bundling to each other. The second type (type-B) is grown by a Au catalyst layer on the substrate using CVD process wherein a thicker Au layer increases the number of SiNWs per unit area. For type-A array, even though the incident light energies are below the bandgap energy of  $1.1\text{eV}$ , the sub-bandgap absorption is still higher due to IR trapping in the surface states. This was demonstrated by annealing the film in forming gas at  $T=400^\circ\text{C}$  which reduces the surface states, leading to a decrease in sub-bandgap absorption. Type-B SiNW array shows a significant enhancement in optical absorption (below  $800\text{nm}$ ) compared to solid Si film. This is due to the fact that increasing the Au layer thickness increases the array density and enhances the optical absorption. To enhance the light absorption in a broader spectrum ( $400\text{--}800\text{nm}$ ), Zhu et al [73] have grown arrays of hydrogenated amorphous SiNWs (a-Si:H) with  $300\text{nm}$  in diameter. Low reflectivity of a-Si:H nanowire and nano-cone (NC) array is attributed to the smooth change of refractive index in the boundary of air and a-Si:H layer, i.e. impedance matching. To

improve this boundary condition, an array of nano-cones has been grown (tip to base: 20 nm to 300 nm) which has higher absorbance because of the smoother change of refractive index in contrast to SiNW array.

Further evidence of light trapping and enhanced absorption can be witnessed in the experiment reported by Adachi et al [74]. It is shown that 15–40nm Sn-catalyzed VLS grown crystalline/amorphous core/shell SiNWs can have 95% absorption at  $\lambda < 550$  nm. This is larger than 50% absorption of a-Si thin film layer. It is observed that by increasing the diameter to 150–180 nm, the absorption tail can grow for  $\lambda > 750$  nm which is due to light trapping and confirms the previously reported observation in [71].

**Collimation and lensing:** A photonic crystal composed of 125 nm thick and 700 nm long SiNWs grown on 3  $\mu$ m thick SiO<sub>2</sub> layer with 437 nm pitch has been demonstrated by Shih et al [75]. Here the nanowire periodic structure acts as a lens which collimates IR ( $\lambda=1500$  nm) wavelengths to increase the absorption. Zhang et al [76] have reported fabrication of planar and vertical SiNW arrays showing high sensitivity to detect UV light at 390 nm. Strong wave guiding effect in 200 nm thick and 2.7  $\mu$ m long vertical SiNWs produces large optical gain of 35,000.

There are examples of using a single large diameter SiNW as photodiode, solar cell and photo transistor. A detailed review of these experiments and the performance of devices can be found in [28].

### 1.3 Organization of the Thesis

In the previous review we came across a few experiments in which the unwanted strain due to lattice mismatch of SiNW core with the surrounding material e.g. SiO<sub>2</sub> changed the PL spectrum. Motivated by the aforementioned studies and aiming at finding an application for SiNWs in lasers and LEDs, the scope of this thesis is to find the answer for the following questions:

- (a) *What is the amount of change of bandgap in SiNWs in response to intentionally applied axial strain?*
- (b) *How much the strain and the resultant change of band structure will cause change of effective mass, density of states; quantities which can modulate the mobility and/or conductance)?*
- (c) *How the strain-induced change depends on the crystallography of nanowire, and diameter?*
- (d) *Does the strain-induced change of band structure occur in other material systems like germanium nanowire?*
- (e) *Does the axial strain alter the light emission properties e.g. spontaneous emission time in SiNWs? If the answer is yes;*
- (f) *What are the mechanisms of change and how big are they?*

- (g) *What are the implications of these changes in terms of realization of a useful SiNW-based device?*
- (h) *How does temperature, diameter of nanowire, electric field, electron-phonon scattering affect on the strain induced changes of light emission?*
- (i) *How much is the effect of strain on the photo-absorption of a SiNW?*

Questions (a) to (c) are addressed in Chapter 2 using TB method. Chapter 3 is devoted to question (d) in which it is shown that effects of strain on germanium band structure follows the same physics of strain effect on the band structure of SiNW. Chapter 4 gives the details of the computational methods i.e. energy minimization with DFT, band structure calculation, momentum matrix element calculation in TB frame work using Slater orbitals. It also presents the mathematical derivation behind the spontaneous emission times in both direct and indirect bandgap nanowires. Method of generating matrices of electron-phonon scattering rates for Monte Carlo study of carrier evolution in indirect sub-bands is presented with the relevant algorithms. Questions (e) till (h) are addressed in Chapter 5. The results presented in this chapter are promising the possibility of population inversion in SiNWs. There is at least one order of magnitude change in spontaneous emission time in response to strain. This is further verified by Ensemble Monte Carlo (EMC) simulation by including multi-phonon scattering events under various temperatures and electric field along the nanowire length. Role of Longitudinal Acoustic (LA) and Optical (LO) phonons are investigated as well.

Chapter 6 deals with the calculation of light absorption spectrum and dielectric function of SiNWs using TB method. Here the question (i) is answered by showing that there is indeed a few orders of magnitude change in the band edge photo-absorption in response to strain. In addition the optical anisotropy in the band edge absorption and the role of diameter is presented. Chapter 7 enlists the shortcomings of the study and future outlook. Here I have presented the detailed algorithmic steps with which the problem of strain effects on the physics of SiNW can be pushed to the next level of accommodating many-body effects, nonlinearity, surface effects, etc.

## 1.4 Sources of Strain in SiNWs

Since strain is promising as a degree of freedom to tailor the electronic and optical properties of SiNWs, it is instructive to review some of the methods of applying strain to a SiNW or generally a nanostructure e.g. Carbon Nano Tube (CNT). Our aim is to show the feasibility of the implementing the ideas or proposed experiments in this thesis. Strain can be generated via *intrinsic* or *extrinsic* sources. Examples of experiments which use either intrinsic or extrinsic sources of strain are tabulated in Table 1.2 at the end of this section.

### 1.4.1 Intrinsic sources of strain

Effects of strain on the electronic properties of bulk materials (Si, Ge etc) have been extensively studied. The residual stress due to lattice mismatch between silicon and germanium can enhance the carrier mobility in Metal-Oxide-Semiconductor (MOS) transistors due to significant change of effective mass. Additionally it has been demonstrated that growing a germanium layer on silicon substrate can decrease the sub band splitting between indirect and direct bandgap in germanium [77][78]. This effect has shown to increase the light emission efficiency of optically [79] and electrically pumped [80] Ge-on-Si light source. Using TB method in Chapter 2 we will show that +2% strain can change the bandgap of bulk Ge from indirect to direct. This value of strain closely reproduces the +1.8% strain predicted in [78] as well as +2% value which is mentioned in the Ge-on-Si LED fabricated by Sun et al [79][80]. However these methods do not provide any option of changing the strain value or its direction because the strain is controlled by the alloy composition [81][82].

Generating strain in SiNWs is possible using internal sources like the lattice mismatch induced by the shell material e.g. germanium [83], SiO<sub>2</sub> [33][84][85][86][67], silica [65], metallization [2] or silicon nitride [87][88]. In the following subsection a few experiments are reviewed in which metallization, oxide and nitride are causes of residual strain.

#### 1.4.1.1 Strain induced from metallization

As mentioned before a SiNW-base GAA-FET has been implemented using SiO<sub>2</sub> or HfO<sub>2</sub> as gate dielectric and Polysilicon or TaN as gate contact [2]. The residual tensile strain due to TaN coverage is as high as 3% which corresponds to a stress value of 4GPa. It has been observed that the amount of residual strain is controllable by the TaN sputtering power and its thickness and interestingly there is no randomness in the final bending of floating nanowires (Figure 1.12) within an array.

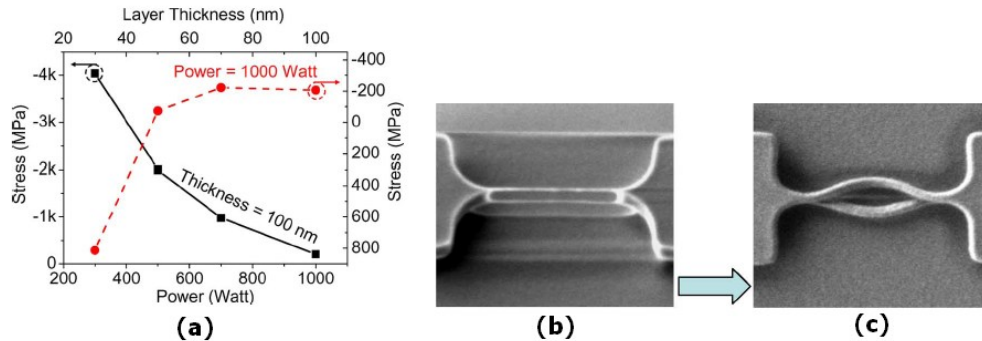


Figure 1.12 (a) Residual strain vs. TaN film thickness and sputtering power. Two parallel floating HfO<sub>2</sub>/TaN covered SiNW (b) before and (c) after TaN deposition. Reprinted with permission from [2]. Copyright 2007 IEEE.

#### 1.4.1.2 Strain induced from SiO<sub>2</sub>

Also it has been reported that in floating SiNWs, oxide-induced residual tensile strain can be as high as +1% which corresponds to 200MPa to 2GPa depending on the nanowire diameters. This will increase the mobility of the SiNW-based FETs by 100% compared to the non-bended SiNWs. Interestingly this improvement has been verified using Raman spectroscopy of strained and relaxed SiNWs in this work. The residual 1% strain corresponds to  $5.09\text{cm}^{-1}$  shift in Raman peak which is due to phonon deformation potential change [33].

Trans-conductance enhancement (by a factor of 1.5-3) due to strain is also reported by Seike et al [85] in which a 70nm thick [110] nanowire is under tensile stress arising from surrounding SiO<sub>2</sub> layer. It was further verified from Raman studies that the oxide cladding layer induces a strain of 350MPa on the SiNW core [84]. Attaining large values of strain has been reported in [86] which shows that in a 5nm thick SiNW, strain can reach up to +8% due to the self-limited oxidation layer which covers the floating SiNW.

#### 1.4.1.3 Strain induced from Silicon Nitride

In [87] and [88] the authors have shown that strain induced from the silicon nitride cladding of nanowire wave guide can generate a large second order nonlinear susceptibility because the residual transversal strain breaks the centro-symmetric nature of the crystal.

### 1.4.2 Extrinsic sources of strain

An alternative way of attaining large values of strain is using external means. Fortunately there are many reported methods of straining a CNT which could be reused or adapted for the purpose of straining a SiNW. A few extrinsic methods of generating strain in nanostructures are introduced in the following subsections.

#### 1.4.2.1 Atomic Force Microscopy (AFM)

Strain induced bandgap conversion was first predicted theoretically by [89]. Later on the experimental measurements were performed by applying strain to a CNT using an AFM probe [90][91][92]. Similarly the first measurement of Young's modulus of SiNWs was done by pushing an AFM probe on a cantilever SiNW [93]. It was shown that the Young's modulus ( $E$ ) of single clamped (cantilever beam) and double clamped (bridge) SiNWs are about 207GPa.

#### 1.4.2.2 Piezoelectric Actuators

Strain can also be applied to a CNT using a piezo-electrically controlled table as shown in [94]. Another example is a CNT-based FET which is mounted on an expandable piezoelectric stack. With this device up to 1.2% strain can be applied to the CNT [95].

#### 1.4.2.3 Deformable substrates

Embedding a biased CNT on a deflectable Alumina diaphragm can work as a pressure sensor [96]. The first evidence of piezo-resistivity in SiNWs was observed by R. He and P. Yang by fabricating a biased 50nm SiNW bridge embedded on a deformable steel plate [8]. They showed that application of both tensile and compressive strain to the SiNW is possible and this causes the change of resistivity; a proposal for a stress or pressure sensor. Ryu et al [97] showed that it is possible to fabricate long buckled SiNWs by embedding them in an already stretched elastomeric substrate. Releasing the substrate then makes the nanowires to buckle. In this way the bending of the substrate can apply  $\pm 3\%$  strain on SiNWs. In [98] a vertical SiNW-based FET is fabricated which can lend itself to easier application of compressive strain. The possibility of fabricating an array of silicon nanowires on plastic deformable substrate is demonstrated in [6].

Using a four point bending apparatus Jeong et al applied 90-110MPa strain to a 200nm long [110] silicon nanowire with variable diameter between 1nm - 20nm which is biased as a FET. It was proven that transversal as well as longitudinal strain can modulate the threshold voltage of a single electron transistor based on these SiNWs [99]. A simplified diagram of the apparatus and the amount of strain which can be attained as a function of the geometric parameters is shown in Figure 1.13.

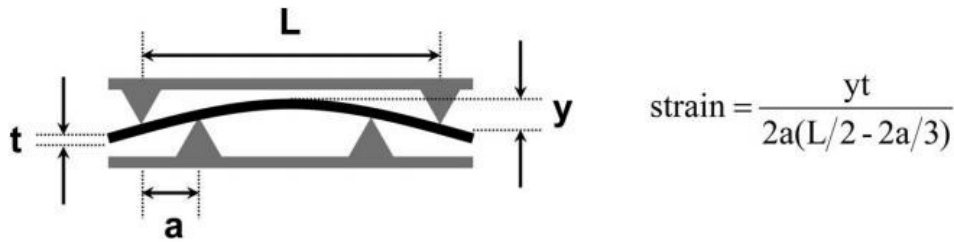


Figure 1.13 A four point bending apparatus to bend the wafer containing the SiNW-based FET. Reprinted with permission from [99]. Copyright 2009 American Institute of Physics.

#### 1.4.2.4 Miscellaneous Methods

Additionally we are also witnessing sophisticated methods of attaining strain in nano-structured materials. For example in [100] the effect of torsional strain on a free standing CNT was studied by attaching an imbalanced proof mass to the middle of it. Injecting electric charge to a bundle of CNTs can also induce contraction or expansion [101]. In [102] a device is made by patterning two piezoelectric nano-actuators on a 20nm thick silicon epilayer. The strain field generated by the actuators is able to change the exchange interaction between the nuclear and electronic spins of dopant phosphorous atoms. In [103] the authors report a method of generating strain wave using an intense heat created by a laser pulse. The strain

has shown to change the electronic states of a quantum dot embedded in a Fabry-Perot resonator.

#### **1.4.3 Strain Measurement**

Raman study of SiNWs can reveal useful information about the intrinsic sources of strain in SiNWs. Fukata et al [84] have investigated the phonon confinement and self-limiting oxidation in SiNWs grown by laser ablation method. Using Raman spectroscopy they have shown that the self-limitation of oxidation is due to compressive stress which builds up at Si/SiO<sub>2</sub> interface. Narrowing down the diameter of SiNWs from 20nm to 3nm reveals an asymmetric broadening feature in Raman spectrum which is due to phonon confinement effect. This asymmetric broadening is also observed in [104]. Before assigning any broadening effect to phonon confinement, the laser-induced heating problem should be resolved since it obscures the Raman response and causes more broadening. This is more pronounced for SiNWs due to their small cross section and low thermal conductivity as opposed to large area SOI and 2D structures [105]. The heating problem can be resolved using either metallic substrate [104] or soaking the nanowires under study into water [106]. There are other methods of measuring/visualizing strain in nano-scale devices. For example Moiré technique, off-axis electron holography and combination of both are introduced in [107]. However there is no report of using any of these methods in measuring the strain distribution in SiNW-based devices. This may be due to the planar nature of the method and requirements e.g. TEM sample preparation.

In *summary* it can be said that with the advent of new technologies applying strain to SiNWs or other nanostructured-materials is within reach. Looking at the time evolution of the previously introduced methods proves that using strain as a degree of freedom in nano-scaled electro-optical devices is getting closer to the realm of reality.

Category	method	Nanostructure type/size	strain/stress amount	Reference
<b>Extrinsic</b>	Elastomeric (PDMS) substrate	Bottom-up [111] SiNW (d=20-85nm)	$\pm 3\%$	[97]
	Deformable steel substrate	Bottom-up <111> SiNW (d=50-70nm)	$\pm 8 \times 10^7 \text{ Pa} = \pm 0.08\%$ *	[8]
	Four point contact deflection	Top-down [100] SiNW (d=1-20nm)	90 MPa -110 Mpa	[99]
	Piezoelectric Table	CNT	Max= +0.3%	[94]
	Piezoelectric Table	CNT	Min=+0.3% Max=+1.2%	[95]
	Alumina** membrane	CNT	Max = 0.1%	[96]
	Flexible PE*** substrate	CNT	Min/Max =NA, Strain detection resolution= 0.004%,	[108]
	Pushing by AFM tip	CNT	0% to +3%	[92]
	Pushing by AFM tip	CNT	From 0 to +0.8%	[91]
	Piezoelectric Actuator	20nm Si epilayer	From 0 to 0.15%	[102]
	In-situ stretching by SPM# tip during growth	Bottom-up <100> SiNW (d~5nm)	Tensile 0.3%	[109]
<b>Intrinsic</b>	Ge/Si lattice mismatch	Core/Shell Ge/SiNW bottom-up ( 19nm < d <sub>core</sub> < 26nm)	-1.03% < strain < -.87%	[83]
	Oxide induced	Top-down SiNW (d~ 5nm)	From 0 to +8%	[86]
	TaN metallization	Top-down SiNW (5nm < d < 7nm)	From 3 to +4% stress> 4GPa	[2]
	Nitride induced	Top-down SiNW (d~100-200nm)	Transversal, Min=-0.01%, Max=+0.03%	[87] [88]

Table 1.2 Summary of the methods with which strain can be generated in a 1D nanostructure e.g. SiNW or CNT. (\*) The Young modulus of bulk silicon (150GPa) is used here [119]. (\*\*) Alumina= Al<sub>2</sub>O<sub>3</sub>. (\*\*\*) PE= Poly Ester. (#) SPM= Scanning Probe Microscopy.



# Chapter 2

## Strain Effects on the Electronic Properties of Silicon Nanowires

In this chapter we investigated the effect of uniaxial strain on the band structure of SiNWs. Vital to realizing SiNW-based optoelectronic devices, we observed that the bandgap of nanowires can change from indirect to direct or vice versa in response to strain. By increasing the diameter of nanowires the value of the compressive strain which is required for this bandgap conversion becomes smaller. Also the change of bandgap in tensile strain regime appears to be indifferent to the diameter and is only dependent on the crystallographic direction of the nanowire. Direct to indirect bandgap conversion leads to the change of effective mass and density of states. The physical mechanism of change can be attributed to the crystallographic direction of nanowires and the nature of orbitals composing the valence and conduction bands. Furthermore we studied the strain effect on the bulk silicon crystal. Methods of tight binding calculation of band structure (nanowire and bulk silicon), strain application, structural relaxation of nanowire and calculation of density of states are all explained in detail in this chapter. The main results of this chapter were published in *Shiri, D., Kong, Y., Buin, A. K., and Anantram, M. P. Strain induced change of bandgap and effective mass in silicon nanowires. Appl. Phys. Lett. 93, 073114, (2008).*

### 2.1 Tight Binding (TB) Calculation of the Band Structure

The semi-empirical 10 orbital  $sp^3d^5s^*$  TB method which is well characterized for silicon is used with Jancu's parameters [110] to construct the Hamiltonian of the nanowire. In addition to being less computationally intensive, the TB scheme gives comparable results with experimental bandgap measurements and DFT based calculations which take the diameter sensitive GW-correction into account [111][112][68].

The nanowires which are cut from bulk 3D crystal of silicon are assumed to be periodic in  $z$  direction with  $xy$  plane regarded as the cross sectional plane. Figure 2.1 shows an example nanowire which has three unit cells in longitudinal direction ([110]) and one hexagonal cell in cross sectional plane. The Bloch equation is used to find the total Hamiltonian of the nanowire at each given  $k_z$ :

$$H = H_{22} + H_{21}e^{-ik_z\bar{d}} + H_{23}e^{+ik_z\bar{d}} \quad (2.1)$$

where  $H_{22}$  is TB Hamiltonian of the central unit cell,  $H_{21}$  is the interaction TB Hamiltonian between the 2<sup>nd</sup> and the 1<sup>st</sup> unit cell and  $H_{23}$  is the TB interaction Hamiltonian between the 2<sup>nd</sup> and the 3<sup>rd</sup> unit cell as shown in Figure 2.1b. The translation vector  $d$  is defined as  $[0 \ 0 \ a]$ . The unit cell length in periodic direction (z) is  $a=5.43\text{\AA}$  for  $[100]$  and  $a = 5.43/\sqrt{2}=3.83959\text{\AA}$  for  $[110]$  nanowires, respectively. It is evident that the matrices are Hermitian i.e.  $H_{21} = H_{23}^\dagger$ . The size of the total Hamiltonian is  $N_{orbit} \times N_{orbit}$  in which  $N_{orbit} = N_{Si} \times 10 + N_H$ .  $N_{Si}$  and  $N_H$  represent the number of Si and H atoms, respectively. Please note that the number of atomic orbitals assigned to Si and H atoms are 10 and 1, respectively. As an example the unit cell of the nanowire in Figure 2.1 has 6 Si atoms and 8 H atoms, hence the Hamiltonian size is a  $68 \times 68$  matrix.

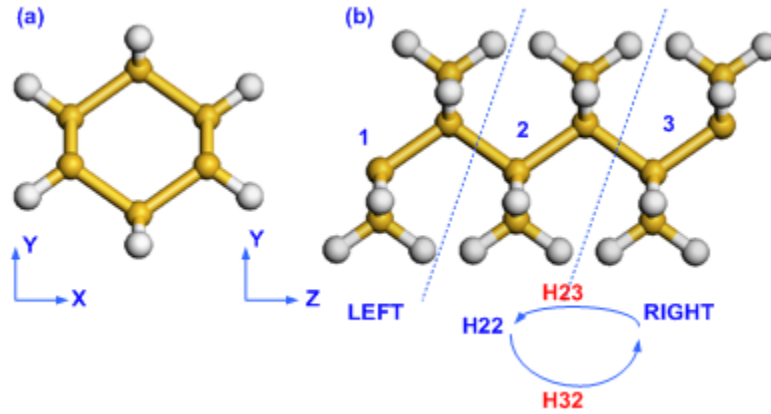


Figure 2.1 (a) Cross section of a  $[110]$  SiNW in  $xy$  plane with 6 Si atoms and 8 H atoms. (b) Three unit cells of  $[110]$  SiNW along  $z$  direction [Sideview of (a)]. The unit cell length is  $3.83959 \text{ \AA}$ .

To find the band structure, at each  $k_z$  value in the  $\left[-\frac{\pi}{a}, \frac{\pi}{a}\right]$  interval, the total Hamiltonian is filled according to equation 2.1 and then the MATLAB Eigen-solver is used to solve this equation:

$$H|n, \mathbf{k}\rangle = E|n, \mathbf{k}\rangle \quad (2.2)$$

The wave function or Eigen state of the nanowire i.e.  $|n, \mathbf{k}\rangle$  is a  $N_{orbit} \times 1$  column vector which can be expanded in terms of 10 orbital basis as:

$$|n, \mathbf{k}\rangle = \sum_{\alpha} C_{n\alpha}(\mathbf{k})|\alpha, \mathbf{k}\rangle \quad (2.3)$$

The index  $\alpha$  spans an s orbital, three p, five d and one extra  $s^*$  orbital for higher excitation. In another language in the Eigen state vector there are 10 numbers corresponding to each Si atom and 1 number for each H atom in the unit cell. Equation 2.2 is solved  $N_k$  times where  $N_k$  is the total number of grid points in 1D Brillouin Zone (BZ) of the nanowire.  $\mathbf{k}$  is the

electron wave vector and it is a continuous parameter. For a nanowire i.e. a 1D nanostructure, it is  $\mathbf{k} = k_z \hat{z}$ , where  $\hat{z}$  is the unit vector along the axis of the nanowire. The index  $n$  is the Eigen state index or quantum number and can change from 1 to  $N_{\text{orbit}}$ . For larger diameter nanowires ( $d > 3\text{nm}$ ) filling the Hamiltonian in equation 2.1 as sparse matrix significantly reduces the time required to solve equation 2.2. Recent calculations have shown that spin-orbit interaction does not change the general shape of the band structure and effective masses of [110] and [111] SiNWs [113]. Since the [110] is the main focus of this work (due its thermodynamic stability over other directions [31][26][27]) we have not included spin-orbit interaction in the calculations of this work. Including spin-orbit interaction within TB scheme is explained in [113]. Including excitonic effects (electron-hole coulomb interaction) increases the number of required TB coefficients for each Si atom from 10 to 100. This is because the basis for Hamiltonian needs to include all combinations of electron-hole orbitals. In this work excitonic effects are not included.

Finding the contribution of each orbital in a given Eigen state is possible by adding the squared value of the coefficients of the specific orbital for all atoms within a unit cell. For example to find out if conduction band is composed of p orbitals, we calculate the following value:

$$P = \sum_{i=1,2,3} \sum_{j=1}^{j=N_{\text{atom}}} |C_{i,j}|^2 \quad (2.4)$$

Where index  $i$  counts  $p_x$ ,  $p_y$  and  $p_z$  orbitals and  $j$  spans all atoms within a unit cell.

## 2.2 Strain Effects on the Band Structure of [110] and [100] SiNWs

Before application of uniaxial strain the nanowires are structurally relaxed using classical many body inter-atomic potential proposed in [114]. This potential which is implemented in GULP<sup>®</sup> [115] has successfully predicted the bulk silicon properties like Young modulus and stress tensors [114] and gives comparable results with DFT for energy of nanowire [116]. Dangling bonds on nanowires are terminated with hydrogen atoms to avoid any surface states in the band structure calculations. The unstrained unit cell of nanowire first optimized using constant pressure criteria in GULP. The energy minimization uses Conjugate Gradient (CG) algorithm to minimize the energy and stops when the maximum inter-atomic force in the unit cell reaches to a value below the given threshold (in this case 0.05 eV/ Å). The Si-Si and Si-H bond lengths are 2.35 Å and 1.44 Å, respectively, before optimization. After this step, a uniform axial strain followed by energy minimization under constant unit-cell volume constraint is applied. In this setting atoms within the unit cell are free to move but the unit cell length is kept fixed at the new strained value. The unit cell length ( $a$ ) is now modified by the desired amount of strain ( $\epsilon$ ) i.e.  $a = a_0(1+\epsilon)$ . The cross sections and side views of a 1.7nm [110] and 2.2 nm [100] SiNW are shown in Figure 2.2a and b, respectively.

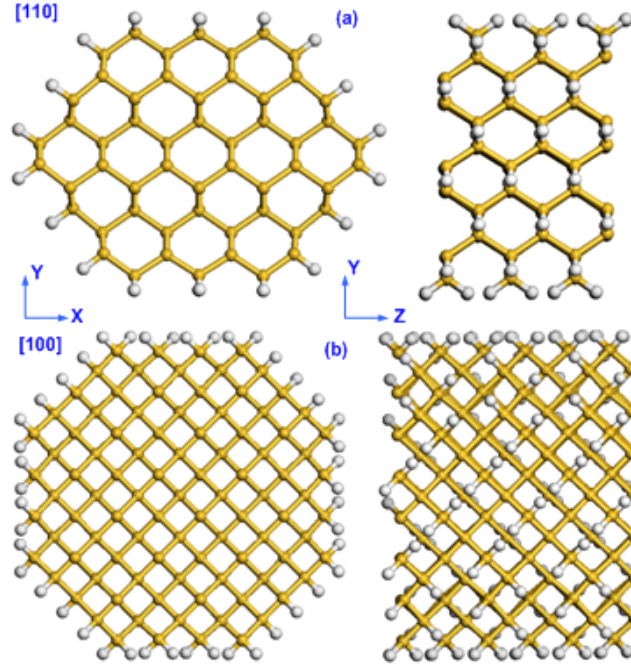


Figure 2.2 Cross sections (left) and side views (right) of three unit cells of (a) 1.7nm [110] and (b) 2.2nm [100] SiNW terminated with hydrogen atoms. For [110] SiNW, the diameter is defined as the average value of large and small diameters.

Figure 2.3a shows the bandgap ( $E_g$ ) versus strain for 1.7nm [110] SiNW. The following linear relationship is fitted to the bandgap value in the tensile region where the slope is approximately 100 meV/percent:

$$E_g = -0.1\alpha + 1.725 \text{ (eV)} \quad (2.5)$$

More importantly, for a compressive strain larger than -4%, the nanowire bandgap becomes indirect i.e. a direct-to-indirect bandgap transition occurs at -4% compressive strain. The band structure is plotted at strain values of +1% and -5% in Figure 2.3b. Although the bandgap values at these strains are comparable, it is clearly seen that the conduction band labeled **L** (light or low effective mass band) determines the bandgap at +1% strain while the conduction band labeled **H** (heavy or high effective mass band) determines the bandgap at -5%. In the chapter 5 and 6 we investigate the consequence of this direct-to-indirect bandgap transition in optical properties of silicon nanowires. We will see that by increasing the diameter, the -4% transition point shifts to values which are closer to 0% strain and this makes the application of compressive strain more easier and practical. The universality of the bandgap vs. strain features is ensured by showing that the direct-to-indirect transition also exists in a 2.2nm [100] SiNW [Figure 2.4]. In this nanowire the direct-to-indirect transition

occurs at a relatively small compressive strain of -1%. The bandgap versus strain in this case is fitted to the following equation in the tensile region:

$$E_g = -0.06\alpha + 1.85 \text{ (eV)} \quad (2.6)$$

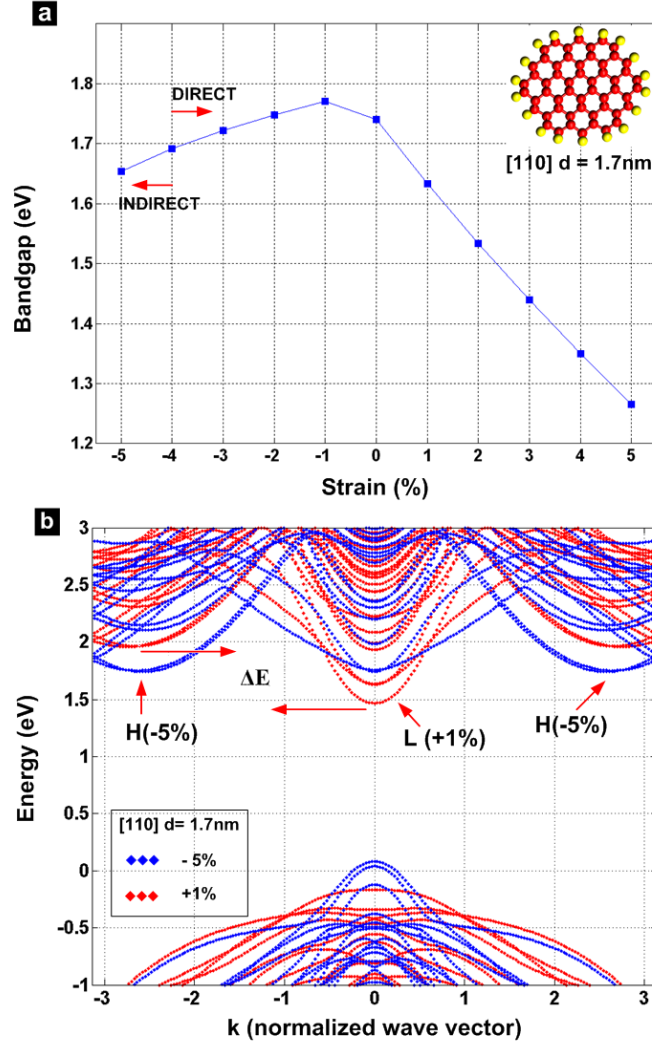


Figure 2.3 (a) Bandgap vs. strain for 1.7nm [110] SiNW and (b) the band structure at +1% and -5% strains. Blue (dark) curves show that the band structure is indirect at -5% and heavy bands (H) determine the bandgap and effective mass of electrons. Red (light) curves show that at +1% strain, the band structure becomes direct and light band (L) determines the effective mass. Reprinted with permission from [117]. Copyright 2008 American Institute of Physics.

While the bandgap change with strain ( $\approx 60$  meV) is smaller than that of [110], the direct-to-indirect transition and linearity of bandgap change are preserved. The smaller rate of bandgap

decrease with strain is attributed to the geometry of the bonds and orbital composition of conduction band minimum (CBM) and valence band maximum (VBM) states. Interestingly it can be seen in Figure 2.4 that by increasing the diameter the slope of bandgap change with strain in tensile regime remains the same. This shows that the change of bandgap depends only on the crystallographic direction of nanowire. However increasing diameter reduces the amount of compressive strain which is needed to observe the bandgap conversion.

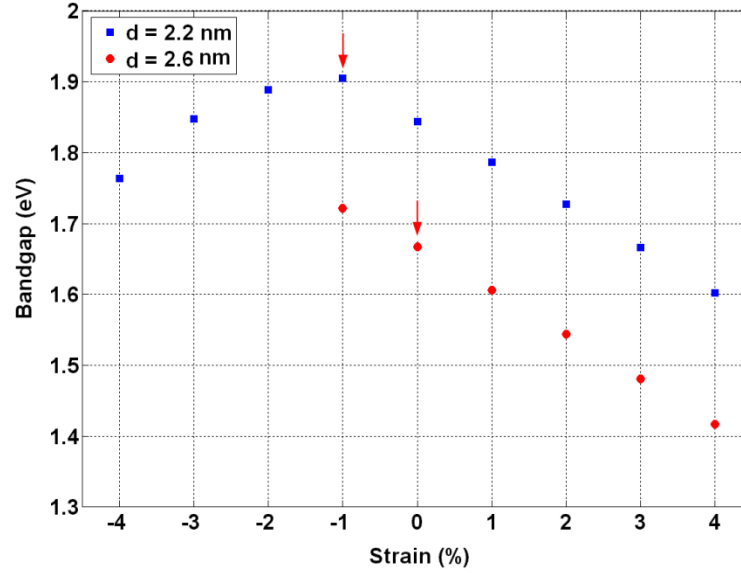


Figure 2.4 Bandgap versus strain for 2.2nm [100] SiNW (square ■). Direct-to-indirect transition occurs at -1% strain. Circles (●) show the same data for the 2.6 nm [100] SiNW with bandgap transition point now at 0% strain. Reprinted with permission from [117]. Copyright 2008 American Institute of Physics.

The generality of these features is further established by comparing the bandgap vs. strain curves for 1.7, 2.3 and 3.1nm diameter [110] SiNWs as plotted in Figure 2.5. Consistent with quantum confinement scheme and prior Scanning Tunneling Spectroscopy (STS) [31] and Photoluminescence (PL) [59] measurements, the bandgap value increases by narrowing the diameter. The physical reason for the right shift of direct-to-indirect bandgap transition point is that the energy difference between the **L** and **H** bands decreases by increasing the diameter of nanowire. Quantitatively, this energy difference [ $\Delta E$  of Figure 2.3a] is 419 meV, 231 meV and 146 meV for [110] nanowire with diameters of 1.7, 2.3 and 3.1 nm, respectively. The conduction band minimum is determined by the **L** and **H** band when the bandgap is direct and indirect, respectively. More compressive strain means less energy difference between the minimum of the **L** and **H** bands. This difference becomes zero at direct-to-indirect transition

point and becomes negative afterwards. Hence for larger nanowires (less  $\Delta E$ ), less compressive strain is required to achieve this transition.

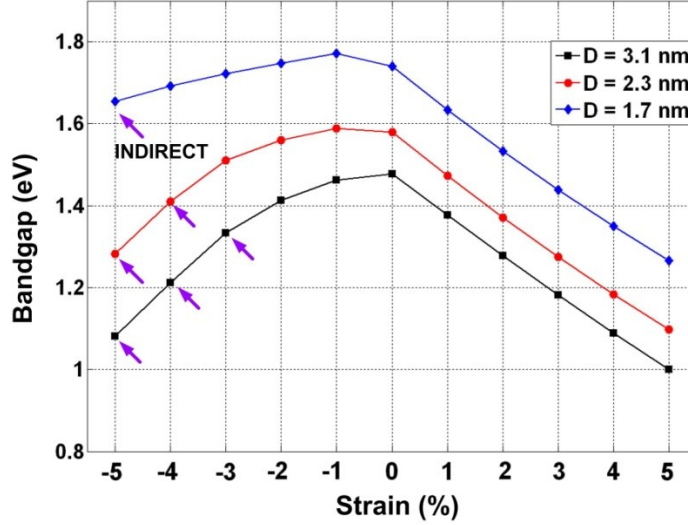


Figure 2.5 The square (■), circle (●) and diamond (◆) show bandgap versus strain for 1.7, 2.3 and 3.1 nm [110] SiNWs, respectively. Arrows indicate the strain value at which the bandgap becomes indirect. Reprinted with permission from [117]. Copyright 2008 American Institute of Physics.

In [110] SiNWs, the minimum of **L** (CBM1) and **H** (CBM2) bands are made of folded unprimed states in  $\Gamma$  ( $\Delta_4$ ) and bonding 3d orbitals in X ( $\Delta_2$ ), respectively [118]. Figure 2.6a shows the energies of CBM1, CBM2 and VBM1 versus strain in 1.7nm [110] SiNW. Since the CBM2 is a bonding state, its energy is decreased by applying the compressive strain [Figure 2.6b]. On the other hand the nanowire expands in the radial direction due to non-zero Poisson ratio. Therefore energy of the CBM1 increases since it is also a bonding state. As a result a conduction band flip occurs at compressive strain regime close to -5%.

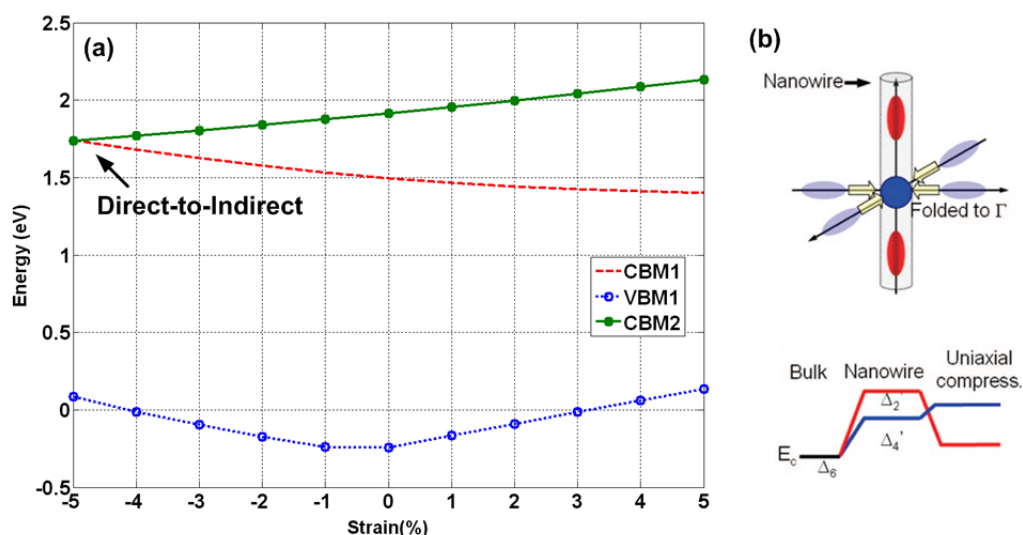


Figure 2.6 (a) Energy of heavy (CBM2) and light (CBM1) conduction band minima and valence band maximum (VBM1) versus strain in a 1.7nm [110] SiNW. (b)  $\Delta_2$  and  $\Delta_4$  correspond to the bonding states of CBM2 and CBM1, respectively. Panel b was adapted with permission from [118]. Copyright 2008 American Chemical Society.

Looking at CBM1, CBM2 and VBM1,2 energies versus strain reveals a different physics for [100] nanowires [Figure 2.7a]. In contrast to [110] nanowires, for [100] direction, the bandgap transition is due to valence band flip which occurs before the CBM1, CBM2 flip e.g. -1% for 2.2nm [100] SiNW. The VBM2 and VBM1 of Figure 2.7b are made of anti-bonding p and  $sp^3$  orbitals as shown in Figure 2.7c and 7d, respectively [118]. Since the VBM2 orbitals has a nodal plane in the axial direction, applying compressive strain increases the VBM2 energy [Figure 2.7c]. On the other hand, VBM1 energy decreases by compressive strain because its negative and positive lobes are orthogonal to the axial direction [Figure 2.7d]. Therefore axial compression causes radial expansion which means energy reduction as can be seen in VBM1 of Figure 2.7a. This explains the less compressive transition points for [100] nanowires compared to [110] nanowires of the same size.



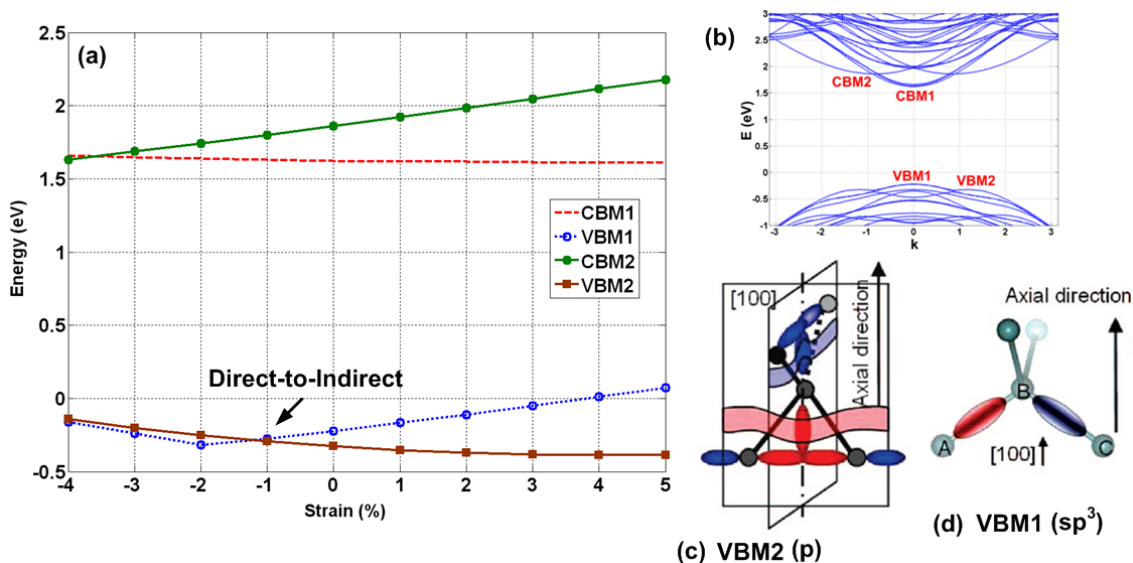


Figure 2.7 (a) Energy of heavy (CBM2) and light (CBM1) conduction band minima and direct (VBM1) and indirect (VBM2) valence band maxima vs. strain in a 2.2nm [100] SiNW. (b) Band structure of the unstrained nanowire as (a). (c) Anti-bonding p orbitals corresponding to VBM2. (d) Anti-bonding  $sp^3$  orbitals corresponding to VBM1. Panels (c) and (d) were adapted with permission from [118]. Copyright 2008 American Chemical Society.

### 2.2.1 Effective mass and Density of States

The movement of the **L** and **H** bands with strain causes an abrupt change in the effective mass of electrons within conduction band [Figure 2.8a] which occurs at the direct-to-indirect bandgap transition. The reason for the abrupt change is the larger initial mass of the **H** band, which determines the lowest lying conduction band once the nanowire becomes indirect. The change in the mass of the **L** and **H** bands with strain is small compared to this abrupt change [Figure 2.8a]. Interestingly, by increasing the diameter, the transition point in effective mass shifts toward the less compressive strain points. This change can be verified experimentally by measuring the change of density of states with STS [31] and electron mobility measurements [25][1].

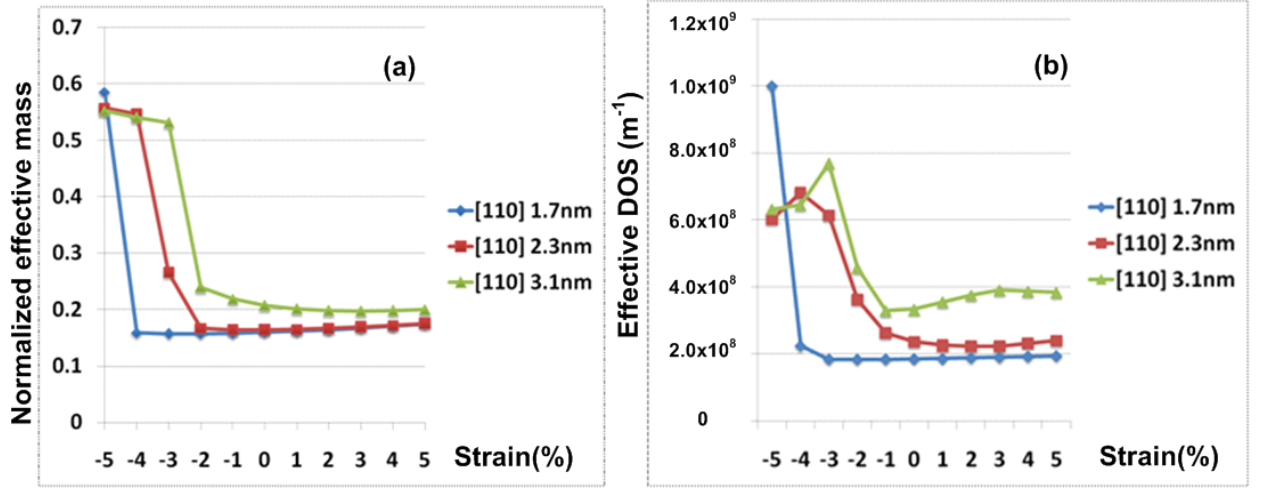


Figure 2.8 (a) The normalized effective mass ( $m^*/m_0$ ) vs. strain ( $m_0$  is the free mass of electron) for 1.7, 2.3 and 3.1nm [110] SiNW. (b) Effective density of states ( $N_c$ ) in versus strain. Reprinted with permission from [117]. Copyright 2008 American Institute of Physics.

To computationally investigate the strain effects on the density of states (DOS), two methods have been tried, first of which is the calculation of DOS using the surface Green Function. The iterative algorithm which finds the surface Green function is explained in Appendix A. Due to computationally intensive nature of the Green Function method for larger nanowires, a simpler and intuitive way is used based on the effective density of states ( $N_c$ ).  $N_c$  is expressed as the number of carriers per unit length ( $m^{-1}$ ) of the nanowire. In the derivation of the  $N_c$  we assume that the conduction bands which are not higher than  $3kT$  from  $E_{cmin}$ , have parabolic shape. Starting from the 1D density of state,  $g(E) = \sqrt{\frac{2m_i^*}{\pi^2 \hbar^2}} \frac{1}{\sqrt{E-E_i}}$ , the total carrier density in the sub-band  $i$  is found using  $n_i = \int_0^\infty f_{FD}(E)g(E) dE$ . Therefore:

$$n_i = \int_0^\infty f_{FD}(E)g(E) dE = \sqrt{\frac{2m_i^*}{\pi^2 \hbar^2}} \int_{E_i}^\infty \frac{1}{\sqrt{E-E_i}} \frac{dE}{1+e^{(E-E_f)/kT}} \quad (2.7)$$

Assuming  $E - E_f \gg kT$  and  $E'_i = E - E_i$  we have:

$$n_i = \sqrt{\frac{2m_i^*}{\pi^2 \hbar^2}} e^{(E_f-E_i)/kT} \int_0^\infty \frac{dE'}{\sqrt{E'_i}} e^{-E'/kT} = \sqrt{\frac{2m_i^* kT}{\pi^2 \hbar^2}} e^{(E_f-E_i)/kT} \int_0^\infty \frac{du}{\sqrt{u}} e^{-u} \quad (2.8)$$

Using  $\int_0^\infty \frac{du}{\sqrt{u}} e^{-u} = \sqrt{\pi}$ , the  $n_i$  reduces to:

$$n_i = \sqrt{\frac{2m_i^*kT}{\pi\hbar^2}} e^{E_f - E_i/kT} \quad (2.9)$$

Since the total density of carriers is  $n = \sum_{i=1}^N n_i$ , we may write:

$$n = e^{E_f/kT} \sqrt{\frac{2kT}{\pi\hbar^2}} \sum_{i=1}^N e^{-E_i/kT} \sqrt{m_i^*} \quad (2.10)$$

Skipping the rest of the manipulation and using  $E_{cmin} = E_1$  results in  $n = e^{E_f - E_1/kT} * N_c$  where  $N_c$  is:

$$N_c = \sqrt{\frac{2kT}{\pi\hbar^2}} \sum_{i=1}^N e^{E_1 - E_i/kT} \sqrt{m_i^*} \quad (2.11)$$

$m_i^*$  is the effective mass of sub band  $i$ .  $E_i$  and  $E_{cmin}$  are energies at the bottom of sub band  $i$  and the bottom of the lowest conduction sub band, respectively.  $kT$  and  $N$  are thermal energy ( $kT=26\text{meV}$  at  $T=300\text{K}$ ) and the number of subbands, respectively, in the  $3kT$  window starting from  $E_{cmin}$ . Figure 2.8b shows the strain dependent effective density of states ( $N_c$ ) for [110] SiNWs based on equation 2.11. The main physics behind the changes in Figure 2.8b are:

- 1) *Tensile strain*: In tensile strain region, the light conduction bands (at  $k_z = 0$ ) primarily contribute to  $N_c$ . Hence the value of  $N_c$  is smaller in the tensile strain region (Figure 2.9a).
- 2) *Diameter dependence*: The number of Eigen states in the  $3kT$  energy window from  $E_{cmin}$  increases with increasing the nanowire diameter because the energy level separation associated with quantum confinement decreases. As a result, the magnitude of  $N_c$  increases with increase in diameter.
- 3) The direct-to-indirect bandgap transition corresponds to a peak in  $N_c$ . There is a peak in  $N_c$  here because both the heavy (at  $k_z = 0$ , direct) and light (away from  $k_z=0$ , indirect) conduction bands contribute to  $N_c$  in the  $3kT$  window starting from  $E_{cmin}$  (Figure 2.9b).
- 4) At larger compressive strains,  $N_c$  shows a dip. The physics of this follows by noting that at compressive strains beyond the direct-to-indirect transition, the heavy

conduction bands (indirect bands) determine  $N_c$ . The light conduction bands have a much higher energy. Hence their contribution to  $N_c$  is less pronounced (Figure 2.9c).

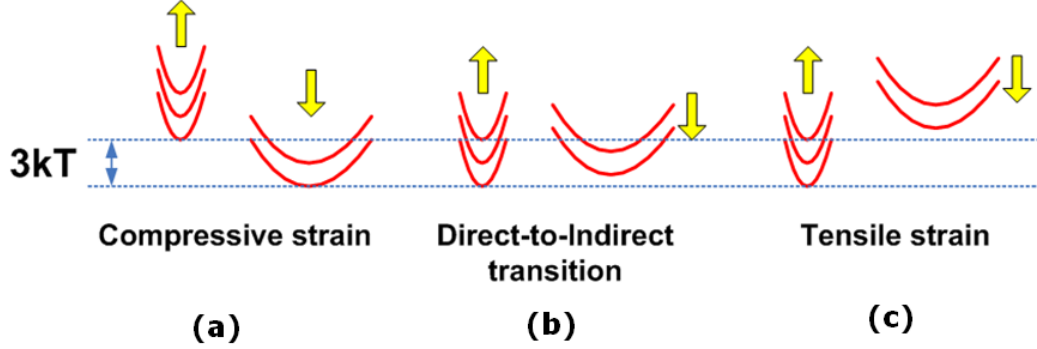


Figure 2.9 (a), (b) and (c) shows the strain induced band structure change in tensile strain regime, bandgap transition point and compressive strain regime, respectively.

Whether the aforementioned strain effects on the effective mass and density of state have a direct application in improving the mobility of a nanowire based transistor will depend on the details of its impact on electron-phonon scattering rates.

### 2.2.2 Strain Effects on the Bulk Silicon

To understand the difference between electromechanical responses of SiNWs and 3D bulk silicon crystal, we study the strain effect on the band structure of bulk silicon in this section. The band structure of bulk silicon (and similarly bulk germanium) is calculated with the same TB scheme used for nanowires. More details are explained in Appendix B. Calculation of bulk silicon band structure serves another purpose which is the calculation of photo absorption in bulk silicon. This proves useful in understanding the differences between photo-absorption spectra obtained with TB and DFT methods. Figure 2.10a shows 20 Eigenvalues calculated at each  $(k_x, k_y, k_z)$  point along  $[111]$  and  $[100]$  directions in 3D BZ of bulk silicon.

The constant energy surface corresponding to conduction band minimum is shown in Figure 2.10b which consists of 6 valleys. Using these valleys and finding out the way that they fold into the BZ center, we can predict which type of nanowire i.e. growth direction has direct or indirect bandgap. For example in  $[100]$  nanowire, the four unprimed (low effective mass) valleys fold into the BZ center ( $\Gamma$ ) and two other primed valleys (with higher effective mass along the transport direction i.e.  $k_z$ ) morph into two indirect sub bands. Therefore the SiNW in  $[100]$  direction shows a direct bandgap. In contrast to  $[100]$ , cutting a nanowire in  $[111]$  direction does not cause any folding into BZ center and results in an indirect bandgap.

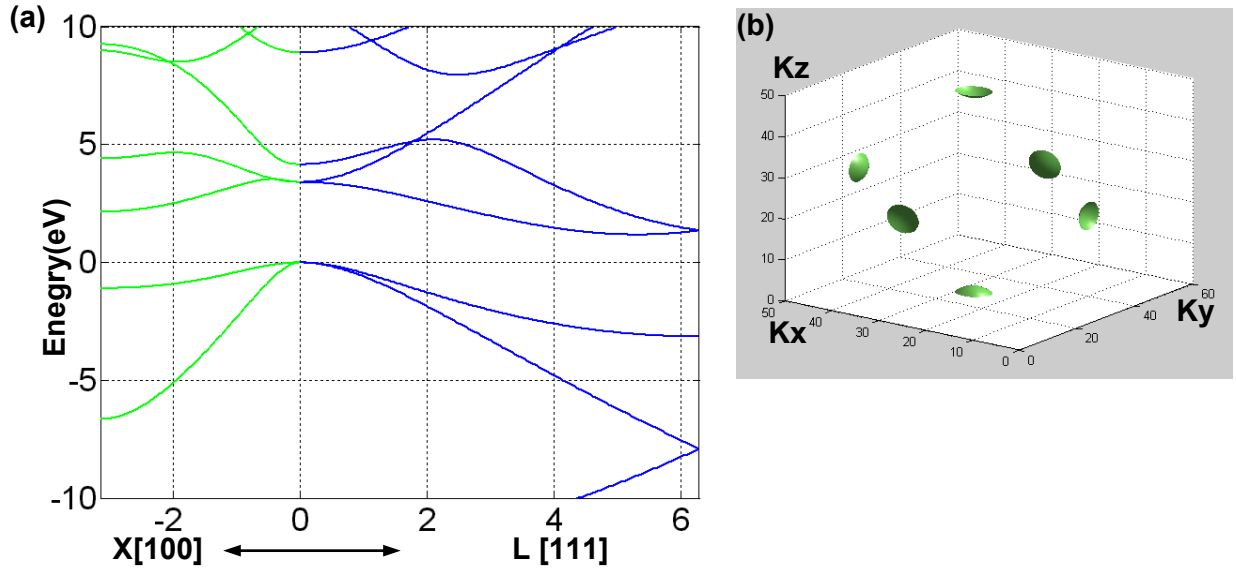


Figure 2.10 (a) Band structure of bulk silicon showing indirect bandgap (1.17eV) at off- $\Gamma$  point  $0.85\pi/a$ .  $\Gamma$  corresponds to  $k=[000]$  i.e. BZ center. (b) Constant energy surface corresponding to 6 conduction valleys.

We have simulated the application of biaxial  $[110]$  and uniaxial  $[100]$  strain on bulk silicon by: (1) changing the crystal size (unit cell length) along the direction of applied strain, (2) Using Poisson ratios of the material [119] to update the crystal geometry in directions which are perpendicular to strain direction and (3) updating the displacement vectors i.e.  $d_{13}$ ,  $d_{14}$ ,  $d_{15}$  which are defined in Bloch equation (equation B1 of Appendix B). Figure 2.11 shows the strain effects on the energy of the three points ( $\Gamma$ , X and L) within BZ of bulk silicon. As can be seen the energy of conduction band minimum which sits at  $\Gamma$  (highest curve in Figure 2.11), never gets smaller than the energies of X and L conduction sub bands. This means that indirect to direct bandgap is not achievable in bulk silicon under any amount of strain within the given range. On the other hand we have seen how strain causes indirect to direct bandgap conversion in 1D system like SiNW. This is of immense importance in implementing light sources using direct bandgap SiNWs.

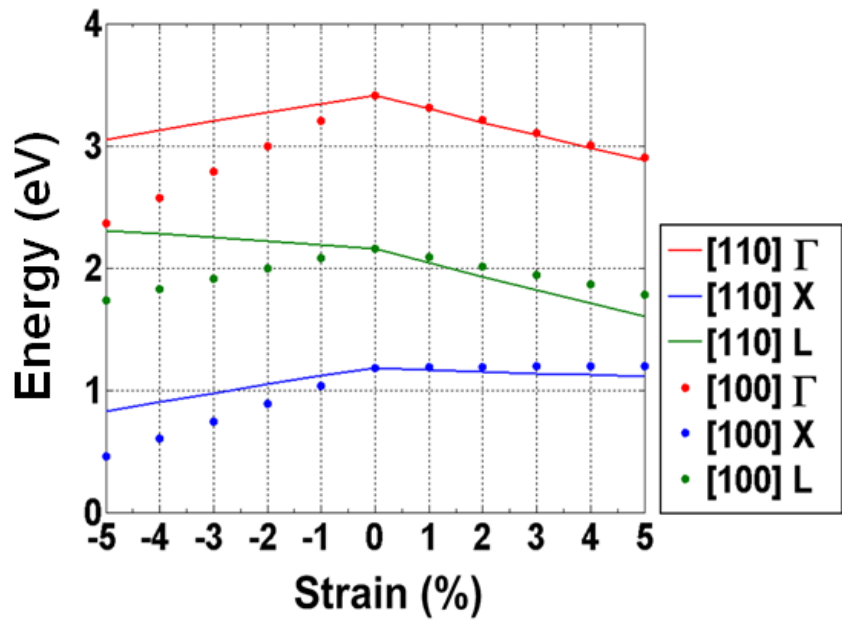


Figure 2.11 Biaxial  $[110]$  (lines) and uniaxial  $[100]$  (dots) strain effects on the energy of conduction sub bands at three different points in the BZ of the bulk silicon.

# Chapter 3

## Strain Effects on the Electronic Properties of Germanium Nanowires

Germanium nanowires (GeNW) have gained interest because of better mobility, smaller bandgap and a larger exciton Bohr radius which makes the quantum confinement effects more pronounced [122]. Using materials which are compatible with front-end CMOS fabrication i.e. In and Sb, it is now possible to catalyze the growth of narrow 10-20nm thick GeNWs [122][123]. There are recent examples of core/shell Ge/Si nanowires to implement high performance FET [1] and quantum bit (qubit) based on hole spin [5]. There is a recent theoretical work which proposes a genetic algorithm based adjustment of Ge content in core/shell Si/Ge nanowire to achieve direct bandgap [124]. Additionally germanium because of its small bandgap can potentially emit the wavelengths which are suitable for optical fiber communication.

In this chapter we report the effects of strain on the band structure and effective mass of narrow GeNWs using ab-initio DFT based methods. Similar to the case of SiNWs the indirect to direct bandgap conversion occurs in GeNWs which is also due to the nature of orbitals which compose the sub bands. Main results of this chapter were published in Y. Kong, D. Shiri, A. Buin, *First-principle investigation of strain effects on the electronic properties of germanium nanowires*, *Physica Status Solidi: RRL*, 3, No. 9, 281– 283 (2009).

### 3.1 Energy Minimization in DFT

Since the classical force field available in GULP does not provide the inter-atomic potential for germanium atoms and their compounds like Ge-H, both energy minimization and band structure calculations were obtained with DFT method in CASTEP<sup>®</sup> [125]. Exchange correlation of General Gradient Approximation (GGA) type with Perdew-Wang's functional (PW91) [126] is used to minimize the structural energy of hydrogen terminated [110] and [100] GeNWs. Energy cut-off and self-consistent field (SCF) tolerance are 180eV and  $1 \times 10^{-6}$ , respectively. The maximum residual force between atoms is set to 0.05eV/Å and maximum displacement is chosen to be 0.002Å. The BFGS algorithm [127] is chosen to reduce the energy on each atom below  $2 \times 10^{-5}$ eV/atom under a constant pressure constraint. Application of strain and further energy minimization steps are similar to those steps which were explained in previous chapter for SiNWs. Figure 3.1a and b show the *xy* cross section and side view of 1.97nm [110] GeNWs, respectively. As can be seen in Figure 3.1b, energy minimization causes the symmetric dihydride groups (GeH<sub>2</sub>) on the (100) plane of the [110]

nanowire cant from the plane parallel to the nanowire cross section. Canting  $\text{GeH}_2$  groups toward  $z$  direction or rearrangement of surface atoms for narrow Ge and Si nanowires results in lower energies for directions such as  $[110]$  over the  $[100]$  direction. This would suggest higher stability of  $[110]$  nanowire compared to  $[100]$  [27].

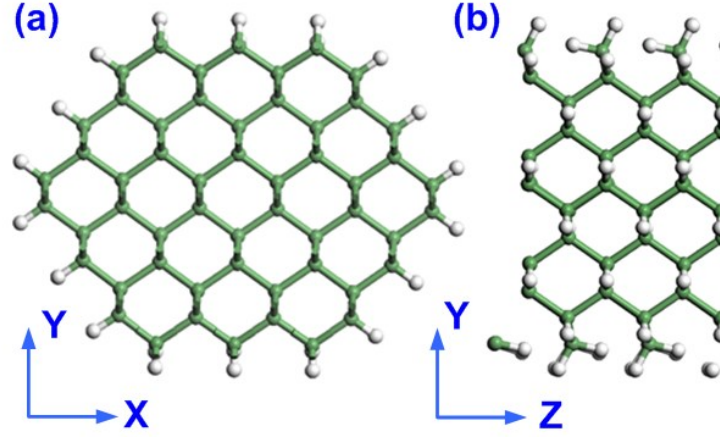


Figure 3.1 (a) Cross section of a 1.9nm  $[110]$  GeNW and (b) its side view showing three unit cells with canted  $\text{GeH}_2$  groups.

### 3.2 Band Structure of $[110]$ and $[100]$ GeNWs

The band structure of a relaxed and unstrained 1.97nm  $[110]$  nanowire is shown in Figure 3.2 which has a direct bandgap of  $E_g = 0.979\text{eV}$ . In contrast to bulk germanium with indirect bandgap ( $E_g = 0.664\text{eV}$ ), this direct bandgap of  $[110]$  nanowire is due to folding of four unprimed valleys of  $[100]$  and  $[111]$  directions into the  $\Gamma$  point as shown in Figure 3.3a. This results in a direct bandgap structure for  $[110]$  GeNW which has low electron effective mass of  $m^* = 0.1065$  in transport direction ( $z$ ). On the other hand cutting the bulk crystal in  $[111]$  and  $[100]$  direction results in indirect bandgap with high effective mass, because the primed valleys determine the conduction band minimum (CBM) which sits out of  $\Gamma$  point ( $k_z = \pm 0.57\pi/a$ ). Indirect bandgap of  $[100]$  and  $[111]$  GeNW confirms this explanation [128][129]. The detailed procedure of band structure calculation for bulk silicon based on the  $sp^3d^5s^*$  scheme is discussed in Appendix B and can be applied for bulk germanium as well.



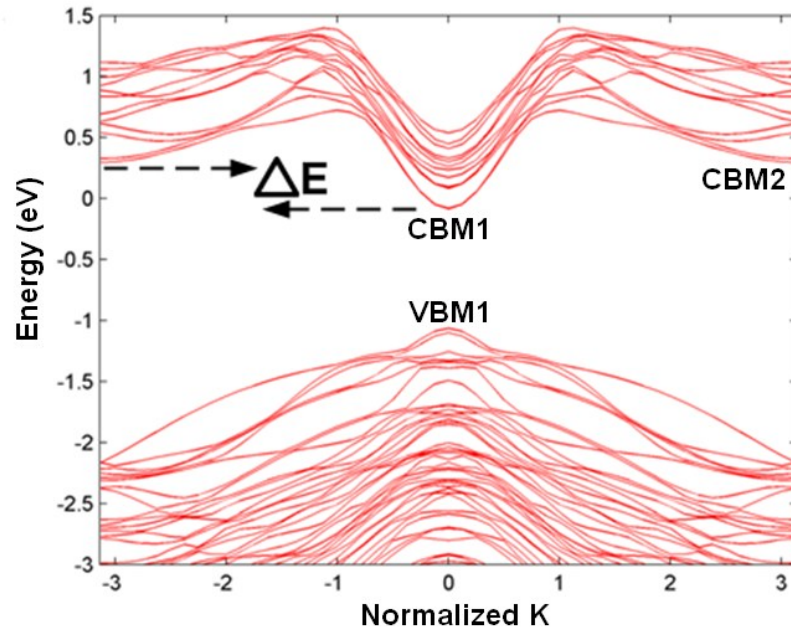


Figure 3.2 Band structure of a 1.97nm [110] GeNW shows direct bandgap. Reprinted with permission from [130]. Copyright 2009 Wiley-VCH.

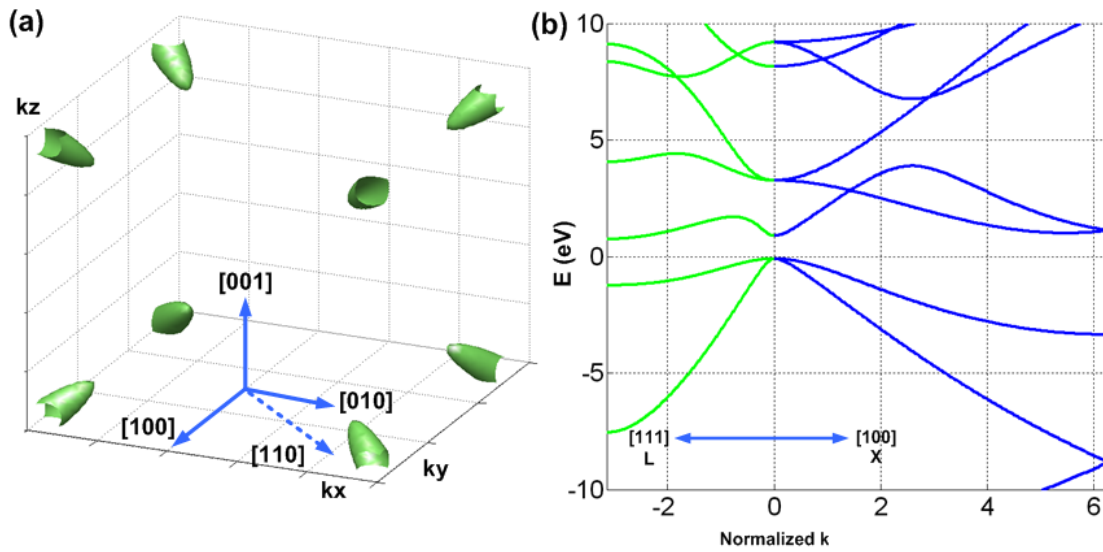


Figure 3.3 (a) Constant energy surface corresponding to conduction band minimum of bulk germanium at L point in BZ. (b) Band structure of bulk germanium showing indirect (0.66 eV) and direct (0.8 eV) bandgap values at L and  $\Gamma$  (BZ center) respectively

Figure 3.4 shows the band structure of an unstrained 2.5nm [100] GeNW with indirect bandgap of  $E_g = 1.15$  eV. As it is evident in Figure 3.3a, cutting the bulk crystal in the [100] direction results in an indirect bandgap with a high effective mass. Folding six L valleys into a point which sits out of  $\Gamma$  point ( $k_z = \pm 0.57\pi/a$ ), yields indirect bandgap (see CBM2 in Figure 3.4). Surface reconstruction effect is observed more significantly on the corners of narrow [100] GeNW (Inset of Figure 3.4).

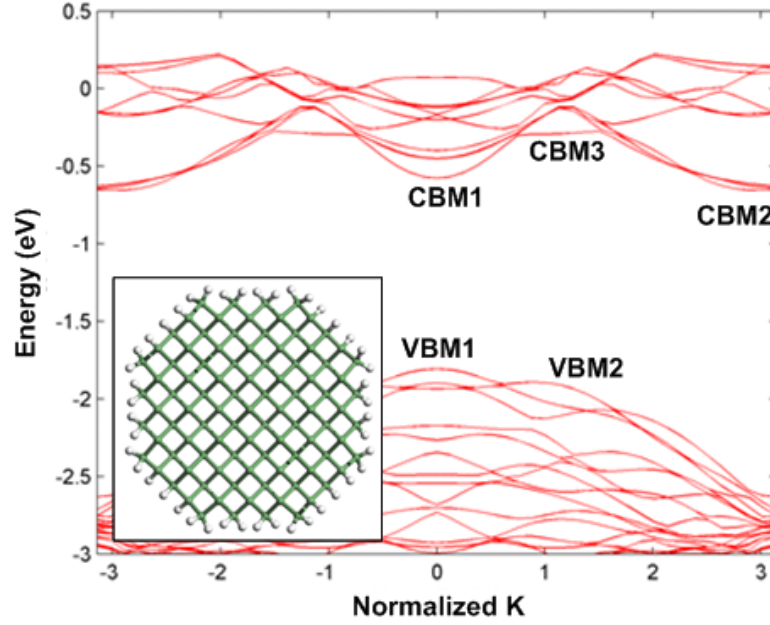


Figure 3.4 Band structure of a 2.5nm unstrained [100] GeNW with indirect bandgap. Inset: Cross section of the nanowire in  $xy$  plane. Reprinted with permission from [130]. Copyright 2009 Wiley-VCH.

### 3.3 Strain Effects

Effect of strain on the value of bandgap is shown in Figure 3.5a for a 1.97 nm [110] GeNW. The value of bandgap change at 3% compressive and tensile strain is +17.6meV/% and 42.8meV/%, respectively. Once the tensile strain reaches to +3%, the bandgap becomes indirect. This direct-to-indirect transition happens at -3% too. Looking at the band structure in 3 different strain points of +5%, 0% and -5% elucidates the physics behind this transition (Figure 3.5b).

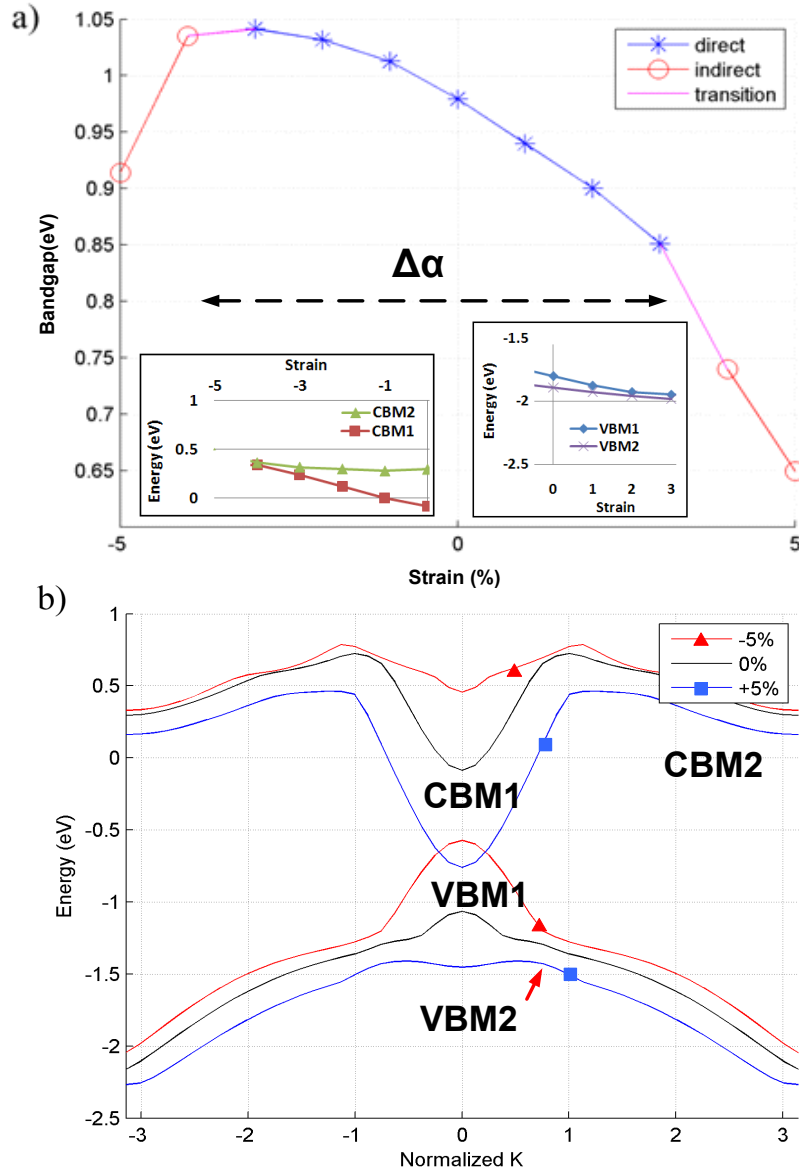


Figure 3.5 Bandgap values vs. strain for a 1.97nm [110] GeNW. Symbols  $\circ$  and  $*$  denote indirect and direct bandgap. (b) Symbols ( $\blacksquare$ ), ( $-$ ) and ( $\blacktriangle$ ) represent the band structure at +5%, 0 and -5% strains, respectively. Reprinted with permission from [130]. Copyright 2009 Wiley-VCH.

Within the compressive strain regime, the direct to indirect transition happens due to interchange of CBM1 and CBM2 (Inset of Figure 3.5a left). Also the VBM1 and VBM2 flipping causes direct to indirect transition at +3%. In another word the valence band maximum (VBM), which was previously at  $k_z=0$ , now shifts to the off-center point of  $k_z = 4\pi/25$ . Since the conduction band minimum (CBM) decreases, the whole effect is a reduction

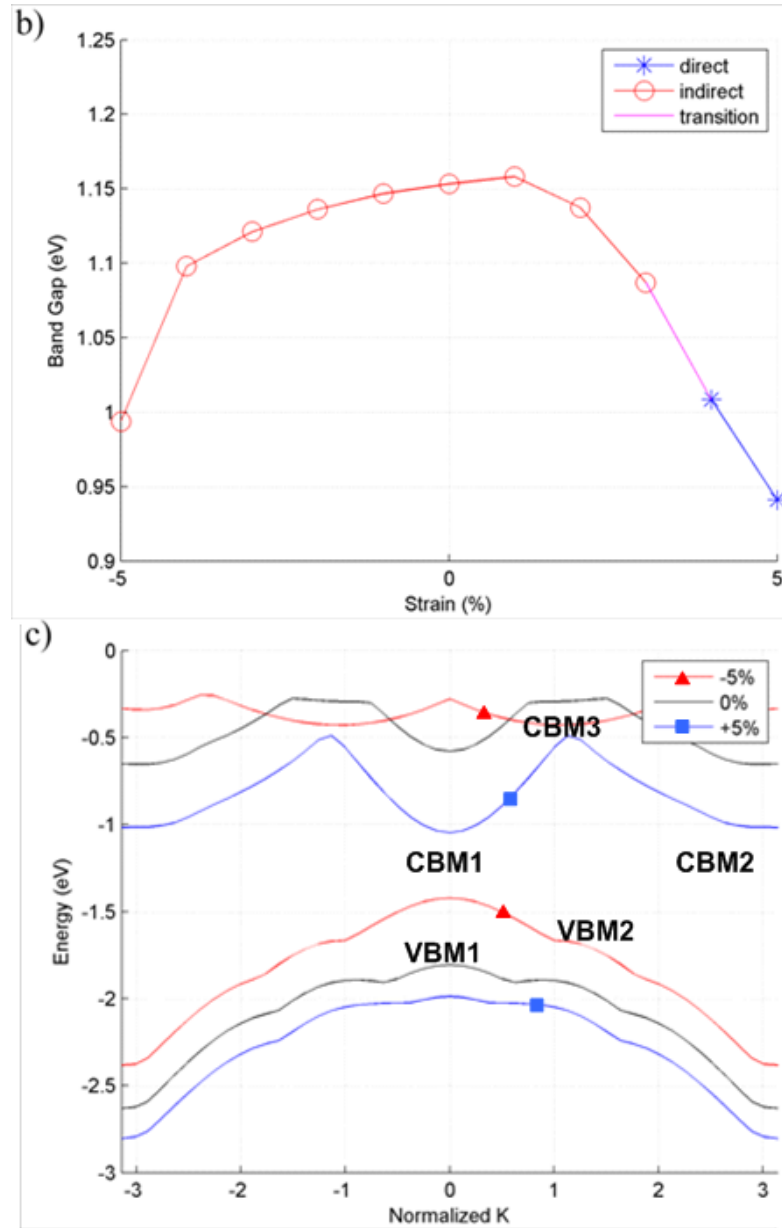


Figure 3.6 (a) Bandgap vs. strain for a 2.5nm [100] GeNW. Symbols of (■), (—), (▲) correspond to band structure at +5%, 0 and -5% strain values, respectively. Symbols ○ and \* denote indirect and direct bandgap. Reprinted with permission from [130]. Copyright 2009 Wiley-VCH.

of indirect bandgap in the tensile region. Increasing the diameter of the GeNW results in a decrease in the conduction (valence) band minimum (maximum) offset ( $\Delta E$  in Figure 3.2). This effect reduces the compressive (tensile) strain which is required for bandgap transition. Therefore the direct bandgap window of the nanowire shrinks ( $\Delta\alpha$  of Figure 3.5a) which suggest applications of large diameter GeNWs in optoelectronic devices based on strain.

Figure 3.6a depicts the bandgap of a 2.5nm [100] GeNW in response to strain. Within compressive strain, VBM1, CBM1 and CBM2 rise in energy. The CBM1 and CBM2 have different rates of change when subjected to compressive strain. Therefore, at a certain point (here -4%), both CBM1 and CBM2 have higher energy than the heavy band (CBM3) at  $k = 8\pi/25$  (Figure 3.6b). In the case of tensile strain, there is another indirect to direct bandgap conversion at +4%. In response to strain, CBM1 begins to decrease and eventually gaining a lower energy than that of the unstrained CBM2 at  $k = 23\pi/25$ . (see Figure 3.6b).

### 3.3.1 Effective Mass

For a 1.97nm [110] GeNW, effective masses for electrons and holes are 0.1065 and 0.1623, respectively. Figure 3.7 shows that corresponding to each direct-to-indirect transition, there are two jumps (3~4 times increase) in the effective mass of electrons and holes. For electrons, this change is attributed to CBM1 (light band) and CBM2 (heavy band) interchange. Under tensile strain, the hole mass increases and reaches to 0.66 during the direct to indirect transition. This is because the VBM shifts from light hole (LH) band at  $k = 0$  to a heavy hole (HH) band at  $k = 4\pi/25$ . On the other hand for 2.5nm [100] GeNW, VBM1 determines the valence band. Since the curvature of the VBM1 does not change with strain, the hole effective mass remains unchanged. Under highly compressive strain (-5%), the electron effective mass is much higher than its bulk value of 0.9525. Once the bandgap becomes direct in the highly tensile regime, the electron effective masses drops to  $m_e^* = 0.1602$ .

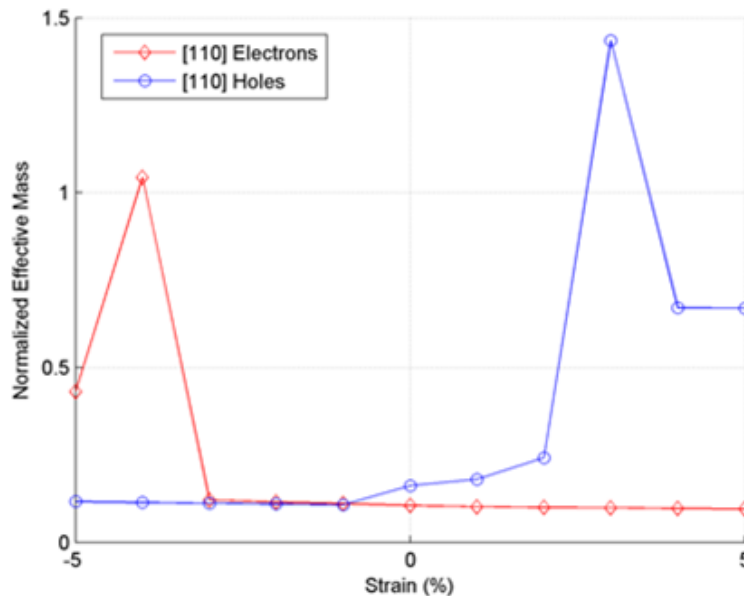


Figure 3.7 Effective mass of electrons and holes vs. strain in a 1.97nm [110] GeNW. Values are normalized to the rest mass of the electron ( $m_0$ ). Reprinted with permission from [130]. Copyright 2009 Wiley-VCH.

### 3.3.2 DFT and the Value of Bandgap

It is well known that standard DFT methodology with Local Density Approximation (LDA) underestimates the value of the band gap. The issue is crudely solved by adding a shift (which is called scissor operator) to the conduction bands relative to the valence band. The value of scissor operator for Ge is calculated to be 0.5eV [131], with which the value of bulk germanium bandgap in LDA (0.3eV) can be adjusted to be close to experimental value of 0.79eV [132]. The value of bandgap can be modified using GGA exchange correlation with PW91 functional. In contrast to LDA, GGA causes the valence orbitals of the atom (e.g. 3s and 3p for Si) to be substantially pushed away from the nucleus [132]. This causes weaker interaction between the valence charge ( $n_v$ ) and pseudo-core charge ( $n_c$ ) (which is a combination of ion and core electrons). The weaker interaction between the core and valence charge causes a softer solid, i.e. the larger equilibrium lattice constant after relaxation. This in turn will affect the exchange potential and therefore the bandgap of the material. Table 3.1 summarizes the values of bandgap and lattice constant calculated for bulk silicon and germanium which is adapted from [132].

	Si		Ge	
Bulk parameters	$a_0$ (Å)	$E_g$ (eV)	$a_0$ (Å)	$E_g$ (eV)
LDA	5.38 (-0.9%)	0.49	5.57 (-1.9%)	0.30
PW91+Pseudopotential	5.59 (+2.9%)	0.65	5.92 (+4.7%)	0.43
PW91+ core correction	5.45 (+0.4%)		5.73 (+1.2%)	
PW91+LAPW	5.50 (+1.3%)		5.75 (+1.6%)	
(experimental)	5.43	0.65 vs. 1.17	5.66	0.69 vs. 0.79

Table 3.1 Summary of bandgap calculations for bulk Si and Ge. Reprinted with permission from Table I & II of [132]. Copyright 1995 American Physical Society.

This lattice expansion effect on the bandgap can be understood by looking at the nonlinear term which exists in the GGA functional [133]:

$$S = \frac{|\nabla n(\mathbf{r})|^2}{n(\mathbf{r})^{4/3}} \quad (3.1)$$

In contrast to the charge density, which can be separated as  $n=n_c+n_v$ , the exchange potential cannot be separated due to the nonlinear term  $S$ . Therefore in the regions where the core and valence charge densities have large overlap, the amount of nonlinearity is more pronounced than the ends of the density distributions. We believe since Ge has  $4s$  and  $4p$  orbitals in its valence band, the greater spread of valence electrons (in contrast to  $3s$  and  $3p$  orbitals of Si) will explain the larger amount of lattice expansion and bandgap change compared to that of

Si (see Table 3.1). Although in Table 3.1 a bandgap change of 0.26eV (32.9% over experimental) is reported for a 1.2% change in lattice constants, we shall note that in our calculations the bandgap change with strain can nearly be of an order lower (20% change over  $\pm 5\%$  of strain range). This suggests that for our calculations, such large sensitivities in bandgap to lattice constants are reduced compared to that of bulk, thus decreasing imprecision arising from the variations in DFT method. This means GGA is a somewhat smoother approximation when applied to these nanowires rather than bulk crystals.

We should emphasize that although the quantitative values of strains and bandgap may depend on the methods or functional types, the qualitative feature of bandgap conversion and bandgap versus strain curve (which has always a maximum around zero percent strain) always remains independent of methods. The main physics of bandgap conversion lies in the nature of the orbitals along the bonds and their corresponding response to strain. Theoretical studies in [117][111][118][134] shows that regardless of the methods used in calculations, at some amount of strain direct to indirect bandgap conversion occurs.

### **3.4 Effect of strain on the band structure of bulk germanium**

The standard CMOS technology is benefitting from germanium as a stressor material with which the mobility of electrons in transistors can be improved. As a quest for direct bandgap, different epitaxial layers of SiGe, SiSnGe have been demonstrated in which the bandgap of Ge can change from indirect to direct under tensile strain which arises from lattice mismatch [82][81][78]. Using tight binding method as explained in Chapter 2 we applied biaxial [110] and uniaxial [100] strain on bulk germanium crystal. As can be seen in Figure 3.A1 at +2% uniaxial strain, the conduction band minimum in BZ center ( $\Gamma$  point) crosses the L band energy. Therefore in contrast to bulk silicon, a bandgap conversion occurs for germanium at +2%. In [78] the value of tensile strain of bandgap conversion is calculated to be +1.8% in germanium. It is noteworthy that bandgap conversion due to +2% strain which is induced from lattice mismatch is also observed experimentally in Ge-on-Si LEDs [79][80]. This is also a strength point for TB method which shows the capability of reproducing as well as predicting experimental results.

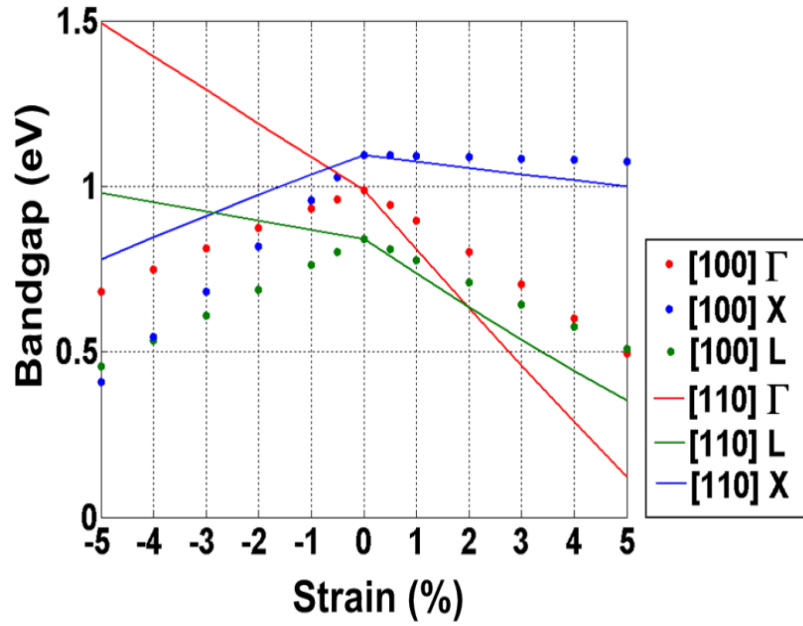


Figure 3.8 Biaxial [110] (line) and uniaxial [100] (dots) strain effects on the energy of conduction sub bands at three different points in BZ of bulk germanium.

A recent theoretical study using genetic algorithm also shows that alloying bulk silicon with germanium generates a direct bandgap with large optical dipole matrix element associated with that [135]. However in the epitaxial and alloy based systems the nature of bandgap conversion is not reversible since the value of strain is fixed after the fabrication. On the other hand GeNWs or alloyed SiGe nanowires provide the possibility of reversible change of bandgap using extrinsic strain application methods presented in Chapter 1.



# Chapter 4

## Spontaneous Emission Time in Silicon Nanowires: *Computational Methods*

As observed in the previous chapters the application of uniaxial strain to SiNWs led to the change of bandgap nature i.e. direct to indirect conversion depending on the amount and direction of applied the strain. Investigating the possibility of modulating the spontaneous light emission in SiNWs in response to uniaxial strain mandates the calculation of photon emission rates for both direct and indirect bandgap nanowires. Before moving to main results in chapter 5, this chapter focuses on the computational methods, mathematical derivations and the logic of the numerical codes used to calculate the spontaneous emission rates within tight binding scheme. Energy minimization, calculation of electron-photon interaction Hamiltonian matrix elements, first order emission rates and first order electron-phonon scattering rates are among the topics covered in this chapter. Thereafter the calculation of spontaneous emission rate in the indirect bandgap nanowires is discussed. The role of both Longitudinal Acoustic (LA) and Optical (LO) phonons are included using the second order perturbation theory. The evolution of carrier population in indirect bandgap nanowires is further studied under the influence of electric field and different temperatures by Ensemble Monte Carlo (EMC) simulation. Discussing the details of generating initial electron-phonon scattering rate matrices for this simulation concludes this chapter.

### 4.1 Energy Minimization

Energy minimization of nanowires is performed by Density Functional Theory (DFT) method within SIESTA<sup>®</sup> [136] (version 3.1) using Local Density Approximation (LDA) functional with Perdew-Wang (PW91) exchange correlation potential [126]. Spin polarized Kohn-Sham orbitals of double-zeta type with polarization (DZP) have been used. The Brillion Zone (BZ) has been sampled by a set of  $1 \times 1 \times 40$  k points along the axis of the nanowire (z axis). The minimum center to center distance of SiNWs is assumed to be at least 2nm to avoid any interaction between nanowires. Energy cut-off, split norm, maximum force tolerance and maximum stress tolerance are 680 eV (50 Ry), 0.15, and 0.01eV/Å and 1GPa, respectively. The relaxation stops if the maximum absolute value of inter-atomic forces is smaller than force tolerance and the maximum stress component is smaller than the stress tolerance. The energy of unstrained unit cell of nanowire is minimized using Conjugate

Gradient (CG) algorithm during which the *variable* unit cell option is selected. This means that the unit cell length of nanowire can relax to a new value according to the given force tolerance as above. Afterwards, for each percent of strain ( $\epsilon$ ) the unit cell is relaxed using the constant volume chosen by *fixed* unit cell option. With this option atoms are only free to move within the fixed unit cell volume. The result of each minimization step is fed to the next step of minimization. The unit cell length ( $U_c$ ) is then updated according to the value of applied strain ( $\epsilon$ ) i.e.  $U_{c\text{-new}} = U_{c\text{-old}}(1+\epsilon)$ . Following the aforementioned procedure the band structure of nanowire is calculated with tight binding method as already explained in Chapter 2.

## 4.2 Position and Momentum Matrix Element

As will be seen in the next section the calculation of electron-photon interaction Hamiltonian entails momentum or position operator matrix element calculation. In this section the method of finding the position matrix element within  $sp^3d^5s^*$  TB scheme is explained assuming the atomic orbitals to be of Slater type. Calculation of matrix element in  $sp^3s^*$  TB with Vogl's parameters was done for bulk and super-lattices of group III-V semiconductors [137][138]. Also the same calculation in  $sp^3d^2$  basis has been reported for surface effect study in GaAs [139] and dielectric response of molecules [140]. We start with an electronic Eigen-state given at a point along 1D BZ of SiNW which is expanded using 10 orbital basis.

$$|n, \mathbf{k}\rangle = \sum_{\alpha} C_{n\alpha}(\mathbf{k}) |\alpha, \mathbf{k}\rangle \quad (4.1)$$

The index  $\alpha$  spans 10 orbitals i.e. one  $s$ , three  $p$ , five  $d$  and one excited  $s^*$  orbital.  $|n, \mathbf{k}\rangle$  is the Hamiltonian eigenstate which satisfies  $H|n, \mathbf{k}\rangle = E_{n,\mathbf{k}}|n, \mathbf{k}\rangle$ . The wave vector of electron is  $\mathbf{k} = k_z \hat{z}$ , where  $\hat{z}$  is the unit vector along the axis of the nanowire. The index  $n$  is the Eigen state index and can change from 1 to  $N_{\text{orbit}}$  in which  $N_{\text{orbit}}$  is the total number of orbitals for one unit cell of nanowire i.e.  $N_{\text{orbit}} = N_{\text{Si}} \times 10 + N_H$ . The state  $|\alpha, \mathbf{k}\rangle$  is written in terms of planar waves weighted by local shape of each orbital:

$$|\alpha, \mathbf{k}\rangle = \frac{1}{\sqrt{N}} \sum_{\mathbf{R}} e^{i\mathbf{k} \cdot \mathbf{R}} |\alpha, \mathbf{R}\rangle \quad (4.2)$$

$|\alpha, \mathbf{R}\rangle$  is the orbital belonging to the atom which sits at position of  $\mathbf{R}$  i.e.  $|\alpha, \mathbf{R}\rangle = \alpha(\mathbf{r} - \mathbf{R})$  and as mentioned before it spans 10 different kind of orbitals.  $N$  is the number of unit cells per unit volume. The ortho-normality of states shown in equation 4.2 can be easily checked using two states with different orbitals ( $\alpha$  and  $\beta$ ) at two different points inside BZ (e.g.  $\mathbf{k}$  and  $\mathbf{k}'$ ):

$$\langle \beta, \mathbf{k}' | \alpha, \mathbf{k} \rangle = \frac{1}{\sqrt{N}} \sum_{\mathbf{R}} e^{-i\mathbf{k}' \cdot \mathbf{R}} \langle \beta, \mathbf{R} | \frac{1}{\sqrt{N}} \sum_{\mathbf{R}} e^{i\mathbf{k} \cdot \mathbf{R}} | \alpha, \mathbf{R} \rangle = \frac{1}{N} \sum_{\mathbf{R}} e^{i(\mathbf{k}-\mathbf{k}') \cdot \mathbf{R}} \langle \beta, \mathbf{R} | \alpha, \mathbf{R} \rangle \quad (4.3)$$

Applying the ortho-normality property of orbitals on each atom i.e.  $\langle \beta, \mathbf{R} | \alpha, \mathbf{R} \rangle = \delta_{\alpha, \beta}$  and the identity,  $\sum_{\mathbf{R}} e^{i(\mathbf{k}-\mathbf{k}') \cdot \mathbf{R}} = N \cdot \delta_{\mathbf{k}, \mathbf{k}'}$  the equation 4.3 results in  $\langle \beta, \mathbf{k}' | \alpha, \mathbf{k} \rangle = \delta_{\mathbf{k}, \mathbf{k}'} \cdot \delta_{\alpha, \beta}$  where all  $\delta$ s are of Krönecker type. Now the momentum matrix element between a conduction band state at  $\mathbf{k}$  and a valence band at  $\mathbf{k}'$  within BZ can be written as  $\langle n, \mathbf{k} | \mathbf{P} | m, \mathbf{k}' \rangle$ .

Using the identity of  $\frac{\partial}{\partial t} \mathbf{r} = \frac{i}{\hbar} [H, \mathbf{r}]$  [141], the momentum matrix element can be written in terms of position operator as follows. The Hamiltonian operator acts on each state according to  $H|n, \mathbf{k}\rangle = E_{n, \mathbf{k}}|n, \mathbf{k}\rangle$  therefore:

$$\begin{aligned} \langle n, \mathbf{k} | \mathbf{P} | m, \mathbf{k}' \rangle &= \left\langle n, \mathbf{k} \left| m_0 \frac{\partial}{\partial t} \mathbf{r} \right| m, \mathbf{k}' \right\rangle = \frac{im_0}{\hbar} \langle n, \mathbf{k} | H\mathbf{r} - \mathbf{r}H | m, \mathbf{k}' \rangle = \\ \frac{im_0}{\hbar} \langle n, \mathbf{k} | E_{n, \mathbf{k}}\mathbf{r} - \mathbf{r}E_{m, \mathbf{k}'} | m, \mathbf{k}' \rangle &= \frac{im_0}{\hbar} (E_{n, \mathbf{k}} - E_{m, \mathbf{k}'}) \langle n, \mathbf{k} | \mathbf{r} | m, \mathbf{k}' \rangle \quad (4.4) \end{aligned}$$

The position matrix element is then found by using the expansions given in equation 4.2 for  $|n, \mathbf{k}\rangle$  and  $|m, \mathbf{k}'\rangle$ :

$$\begin{aligned} \langle n, \mathbf{k} | \mathbf{r} | m, \mathbf{k}' \rangle &= \sum_{\alpha} C_{n\alpha}^*(\mathbf{k}) \sum_{\beta} C_{m\beta}(\mathbf{k}') \langle \alpha, \mathbf{k} | \mathbf{r} | \beta, \mathbf{k}' \rangle = \\ \sum_{\alpha\beta} C_{n\alpha}^*(\mathbf{k}) C_{m\beta}(\mathbf{k}') \langle \alpha, \mathbf{k} | \mathbf{r} | \beta, \mathbf{k}' \rangle &= \sum_{\alpha\beta} C_{n\alpha}^*(\mathbf{k}) C_{m\beta}(\mathbf{k}') \frac{1}{N} \sum_{\mathbf{R}} e^{i(\mathbf{k}-\mathbf{k}') \cdot \mathbf{R}} \langle \alpha, \mathbf{R} | \mathbf{r} | \beta, \mathbf{R} \rangle \quad (4.5) \end{aligned}$$

which results in:

$$\langle n, \mathbf{k} | \mathbf{r} | m, \mathbf{k}' \rangle = \sum_{\alpha\beta} C_{n\alpha}^*(\mathbf{k}) C_{m\beta}(\mathbf{k}') \langle \alpha(\mathbf{r} - \mathbf{R}) | \mathbf{r} | \beta(\mathbf{r} - \mathbf{R}) \rangle \cdot \delta_{\mathbf{k}, \mathbf{k}'} \quad (4.6)$$

The Krönecker delta ensures the momentum conservation i.e. a direct transition of electron from conduction to valence state or vice versa. By changing the variables as  $\mathbf{r} - \mathbf{R} = \mathbf{u}$ , the right hand side of equation 4.6 is further simplified:

$$\begin{aligned} \langle n, \mathbf{k} | \mathbf{r} | m, \mathbf{k}' \rangle &= \sum_{\alpha\beta} C_{n\alpha}^*(\mathbf{k}) C_{m\beta}(\mathbf{k}') \langle \alpha(\mathbf{u}) | \mathbf{u} + \mathbf{R} | \beta(\mathbf{u}) \rangle \cdot \delta_{\mathbf{k}, \mathbf{k}'} = \\ \sum_{\alpha\beta} C_{n\alpha}^*(\mathbf{k}) C_{m\beta}(\mathbf{k}') \delta_{\mathbf{k}, \mathbf{k}'} \{ \langle \alpha(\mathbf{u}) | \mathbf{u} | \beta(\mathbf{u}) \rangle + \mathbf{R} \langle \alpha(\mathbf{u}) | \beta(\mathbf{u}) \rangle \} \quad (4.7) \end{aligned}$$

Using ortho-normality of atomic orbitals, the second term can be reduced to a summation running over orbitals:

$$\sum_{\alpha\beta} C_{n\alpha}^*(\mathbf{k}) C_{m\beta}(\mathbf{k}') \delta_{\mathbf{k},\mathbf{k}'} \{ \langle \alpha(\mathbf{u}) | \mathbf{u} | \beta(\mathbf{u}) \rangle + \mathbf{R} \delta_{\alpha\beta} \} = \sum_{\alpha\beta} C_{n\alpha}^*(\mathbf{k}) C_{m\beta}(\mathbf{k}') \delta_{\mathbf{k},\mathbf{k}'} \langle \alpha(\mathbf{u}) | \mathbf{u} | \beta(\mathbf{u}) \rangle + \sum_{\alpha} C_{n\alpha}^*(\mathbf{k}) C_{m\alpha}(\mathbf{k}') \delta_{\mathbf{k},\mathbf{k}'} \cdot \mathbf{R} \quad (4.8)$$

The second term in the right hand side of equation 4.8 is element by element multiplication of valence and conduction eigenvectors which are weighted by coordinate of the atoms within one unit cell. The first term in the right hand side contains the overlapping integral between different orbitals of the same atom i.e.  $\langle \alpha(\mathbf{u}) | \mathbf{u} | \beta(\mathbf{u}) \rangle$  and it is called intra-atomic contribution. Since many of the overlapping integrals vanish due to symmetry, there is no need to calculate all 100 combinations and only 15 non-zero terms will remain. Here we explain in detail how to arrange the coefficients corresponding to each of these fifteen non-zero overlapping integrals.

Table 4.1 shows 10 coefficients (as defined in equation 4.1) corresponding to an Eigen state of a silicon atom within a unit cell. The second and the third columns correspond to valence and conduction states at a given  $\mathbf{k}$  in the BZ. Before introducing 15 nonzero terms for equation 4.8, it is instructive to look at a simple example of computing the first and the second terms of equation 4.8. We assume that there is only one silicon atom in a unit cell which has two orbitals only (e.g. s and  $p_z$ ). The valence and conduction eigenvector are written as  $[\alpha_1 \alpha_4]$  and  $[\beta_1 \beta_4]$ , respectively. Here the index 4 means that  $p_z$  orbital is the fourth orbital among 10 orbitals. The summations over  $\beta$  and  $\alpha$  are expanded consecutively:

$$\begin{aligned} \sum_{\alpha\beta} C_{n\alpha}^*(\mathbf{k}) C_{m\beta}(\mathbf{k}') \delta_{\mathbf{k},\mathbf{k}'} \langle s(\mathbf{u}) | \mathbf{u} | p_z(\mathbf{u}) \rangle &= \sum_{\alpha} C_{n\alpha}^*(\mathbf{k}) \{ C_{m\beta_1} \langle \alpha | z | s \rangle + C_{m\beta_4} \langle \alpha | z | p_z \rangle \} = \\ &= C_{n\alpha_1}^*(\mathbf{k}) \{ C_{m\beta_1} \langle s | z | s \rangle + C_{m\beta_4} \langle s | z | p_z \rangle \} + C_{n\alpha_4}^*(\mathbf{k}) \{ C_{m\beta_1} \langle p_z | z | s \rangle + C_{m\beta_4} \langle p_z | z | p_z \rangle \} \end{aligned} \quad (4.9)$$

For clarity purpose the coefficients  $C_{m\beta_i}$  and  $C_{n\alpha_i}$  are called  $\beta_i$  and  $\alpha_i$ , respectively in which  $i$  spans 1 to 10. Due to even symmetry of s and odd symmetry of  $p_z$  orbital, the first and the last terms in equation 4.9 vanish i.e.  $\langle s | z | s \rangle$  and  $\langle p_z | z | p_z \rangle$  are zero.

Therefore the first term in equation 4.9 is reduced to two terms which depend on overlapping between s and  $p_z$  orbitals:

$$\begin{aligned} \sum_{\alpha\beta} C_{n\alpha}^*(\mathbf{k}) C_{m\beta}(\mathbf{k}') \delta_{\mathbf{k},\mathbf{k}'} \langle s(\mathbf{u}) | \mathbf{u} | p_z(\mathbf{u}) \rangle &= \alpha_1^* \beta_4 \langle s | z | p_z \rangle + \alpha_4^* \beta_1 \langle p_z | z | s \rangle \\ &= (\alpha_1^* \beta_4 + \alpha_4^* \beta_1) \langle s | z | p_z \rangle \end{aligned} \quad (4.10)$$

For the second term of equation 4.8, the corresponding coefficients of the same orbital type but with different state indices (n and m) must be multiplied by the coordinate of the atom. This is equivalent to the dot product of eigenvectors of states n and m. Rewriting coordinate

vector of the atom as  $\mathbf{R} = \begin{pmatrix} z \\ z \end{pmatrix}$  and using the following multiplication generates the second term in the right hand side of equation 4.8:

$$[\alpha_1^* \quad \alpha_4^*] \cdot \begin{bmatrix} z \cdot \beta_1 \\ z \cdot \beta_4 \end{bmatrix} = \alpha_1^* \cdot z \cdot \beta_1 + \alpha_4^* \cdot z \cdot \beta_4 \quad (4.11)$$

With the same token as mentioned in the previous example, all 15 non-zero (symmetry allowed) overlapping terms and their corresponding coefficients can be written down as given in Table 4.2. These are the terms with which the first part in the right hand side of equation 4.8 can be generated. The left column shows the non-zero overlapping terms and the right column contains the corresponding coefficient of each term.

	$C_{na}(\mathbf{k})$	$C_{m\beta}(\mathbf{k}')$	Orbital type
<b><i>s</i></b>	$\alpha_1$	$\beta_1$	<i>s</i>
<b><i>p</i></b>	$\alpha_2$	$\beta_2$	<i>x</i>
	$\alpha_3$	$\beta_3$	<i>y</i>
	$\alpha_4$	$\beta_4$	<i>z</i>
<b><i>d</i></b>	$\alpha_5$	$\beta_5$	<i>xy</i>
	$\alpha_6$	$\beta_6$	<i>yz</i>
	$\alpha_7$	$\beta_7$	<i>zx</i>
	$\alpha_8$	$\beta_8$	$x^2-y^2$
	$\alpha_9$	$\beta_9$	$3z^2-r^2$
<b><i>s*</i></b>	$\alpha_{10}$	$\beta_{10}$	<i>s*</i>

Table 4.1 Components of eigenvectors (basis coefficients) for conduction and valence states of a Si atom within a unit cell.

Overlapping integrals	Weights
$\langle s z p_z \rangle$	$(\alpha_1^* \beta_4 + \alpha_4^* \beta_1)$
$\langle s^* z p_z \rangle$	$(\alpha_{10}^* \beta_4 + \alpha_4^* \beta_{10})$
$\langle p_z z d_{3z^2-r^2} \rangle$	$(\alpha_4^* \beta_9 + \alpha_9^* \beta_4)$
$\langle p_x z d_{zx} \rangle$	$(\alpha_2^* \beta_7 + \alpha_7^* \beta_2)$
$\langle p_y z d_{yz} \rangle$	$(\alpha_3^* \beta_6 + \alpha_6^* \beta_3)$
$\langle s x p_x \rangle$	$(\alpha_1^* \beta_2 + \alpha_2^* \beta_1)$
$\langle s^* x p_x \rangle$	$(\alpha_{10}^* \beta_2 + \alpha_2^* \beta_{10})$
$\langle p_x x d_{x^2-y^2} \rangle$	$(\alpha_2^* \beta_8 + \alpha_8^* \beta_2)$
$\langle p_y x d_{xy} \rangle$	$(\alpha_3^* \beta_5 + \alpha_5^* \beta_3)$
$\langle p_z x d_{zx} \rangle$	$(\alpha_4^* \beta_7 + \alpha_7^* \beta_4)$
$\langle s y p_y \rangle$	$(\alpha_1^* \beta_3 + \alpha_3^* \beta_1)$
$\langle s^* y p_y \rangle$	$(\alpha_{10}^* \beta_3 + \alpha_3^* \beta_{10})$
$\langle p_y y d_{x^2-y^2} \rangle$	$(\alpha_3^* \beta_8 + \alpha_8^* \beta_3)$
$\langle p_x y d_{xy} \rangle$	$(\alpha_2^* \beta_5 + \alpha_5^* \beta_2)$
$\langle p_y z d_{yz} \rangle$	$(\alpha_4^* \beta_6 + \alpha_6^* \beta_4)$

Table 4.2 Nonzero overlapping integrals and their corresponding weights in terms of eigenvector entries i.e.  $[\alpha_1 \dots \alpha_{10}]$  and  $[\beta_1 \dots \beta_{10}]$ . These are used to build the first term in the right hand side of equation 4.8.

#### 4.2.1 Slater Orbitals

So far no assumption was made about the type of the atomic orbitals in calculating the overlapping integrals. In this work we have calculated these integrals using Slater type orbitals [142]. In Slater method the radial part of a single electron wave function can be defined similar to a Hydrogen-like wave function:

$$\varphi(r) = N r^{n^*-1} e^{-\frac{Z-s}{n^*}r} \quad (4.12)$$

Where  $Z$  is the actual charge of the nucleus,  $s$  is a screening constant and  $n^*$  is effective quantum number.  $N$  is the normalization factor which is calculated by normalizing the whole orbital (angular and radial parts). Following Slater rules,  $s$  and  $p$  orbitals for Si have been calculated and they match with the orbitals reported in [143] for  $sp^3s^*$  TB method. Here we include  $3d$  and  $4s^*$  orbitals following the procedure in [144] wherein the authors have used  $d^*$  for III-V semiconductors. Table 4.3 lists the values of  $n^*$ ,  $Z-s$ , radial and angular parts of orbitals calculated for a silicon atom.

Orbital index	Orbital type	n*	Z-s	Radial and angular part
1	s	3	4.15	$0.37032 r^2 e^{-1.383r}$
2	p <sub>x</sub>	3	4.15	$0.37032 r^2 e^{-1.383r} \sin\theta \cos\phi$
3	p <sub>y</sub>	3	4.15	$0.37032 r^2 e^{-1.383r} \sin\theta \sin\phi$
4	p <sub>z</sub>	3	4.15	$0.37032 r^2 e^{-1.383r} \cos\theta$
5	d <sub>xy</sub>	3	1	$0.0049 r^2 e^{-0.3333r} \sin^2\theta \sin 2\phi$
6	d <sub>yz</sub>	3	1	$0.0098 r^2 e^{-0.3333r} \sin\theta \cos\theta \sin\phi$
7	d <sub>zx</sub>	3	1	$0.0098 r^2 e^{-0.3333r} \sin\theta \cos\theta \cos\phi$
8	d <sub>x<sup>2</sup>-y<sup>2</sup></sub>	3	1	$0.0049 r^2 e^{-0.3333r} \sin^2\theta \cos 2\phi$
9	d <sub>3z<sup>2</sup>-r<sup>2</sup></sub>	3	1	$0.0028 r^2 e^{-0.3333r} (3\cos^2\theta - 1)$
10	s*	3.7	1.45	$0.49 \times 10^{-4} r^{2.7} e^{-0.3919r}$

Table 4.3 Slater type orbitals of Si atom.

Values of non-zero overlapping integrals for Si are given in Table 4.4. Integration over radial part is found by numerical integration. For the angular part exact integration of spherical harmonics is found analytically using Wolfram Mathematica<sup>®</sup> online integrator in <http://integrals.wolfram.com/index.jsp>. The angular part of the orbitals or Y<sub>lm</sub> can be found in literature for example [145].

Non-zero overlapping integrals	value (Å)
$\langle s z p_z \rangle = \langle s x p_x \rangle = \langle s y p_y \rangle$	1.4636
$\langle s^* z p_z \rangle = \langle s^* x p_x \rangle = \langle s^* y p_y \rangle$	0.3697
$\langle p_z z d_{3z^2-r^2} \rangle$	0.4029
$\langle p_x z d_{zx} \rangle = \langle p_y z d_{yz} \rangle$	0.3525
$\langle p_x x d_{x^2-y^2} \rangle = \langle p_y x d_{xy} \rangle = \langle p_z x d_{zx} \rangle$	0.3525
$\langle p_y y d_{x^2-y^2} \rangle = \langle p_x y d_{xy} \rangle = \langle p_z y d_{yz} \rangle$	0.3525

Table 4.4 Non-zero overlapping integrals for Slater type orbitals in Si.

#### 4.2.2 Visualization of Wave functions and Matrix Elements

To visualize a the wave function corresponding to a given quantum number and  $k$  point in BZ, the eigenvector of that specific state is required. But in the next chapter we are mostly interested in conduction/valence band minimum/maximum states at BZ center ( $\Gamma$  point). Each given state is a  $N_{\text{orbit}} \times 1$  vector in which  $N_{\text{orbit}}$  is the total number of orbitals within a unit

cell of nanowire. The contents of the Eigen vector (state) are coefficients corresponding to each orbital of atoms in the unit cell. What is more needed is the spatial distribution of atomic orbitals which are already assumed to be of Salter type as found in previous section. Generally it is possible to plot every slice of probability density  $|\Psi(x,y,z)|^2$ . But mainly the variation of this quantity on  $xy$  plane (cross section) of the nanowire at a constant value of  $z$  i.e.  $z = z_p$  (As shown in Figure 4.1) is of interest. The  $z=z_p$  plane is converted to a  $N_{\text{grid}} = N_x \times N_y$  grid. The value of  $\Psi(x,y,z)$  is then evaluated at each grid point (e.g. P) by adding the contributions of all atomic orbitals within the given unit cell.

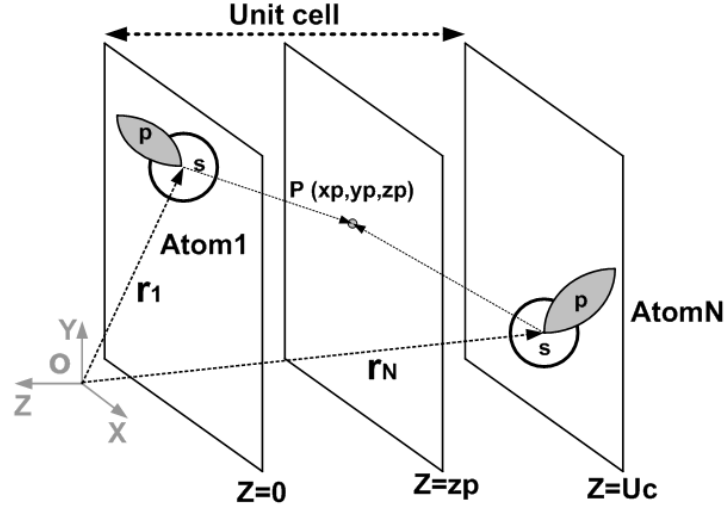


Figure 4.1 The contributions of atomic orbitals in the value of  $\Psi(x,y,z)$  are added at point P which is inside the cross sectional plane of ( $z=z_p$ ).

For simplicity it is assumed that each atom has two orbitals ( $s$  and  $p$ ) only. Hence the Eigen vector corresponding to the state of interest in Figure 4.1 is given as:

$$\psi = [\alpha_1 \beta_1 \alpha_2 \beta_2 \dots \alpha_N \beta_N]^T \quad (4.13)$$

Now at the given point P, the total value of probability amplitude,  $\Psi(x,y,z)$ , can be written as:

$$\begin{aligned} \psi(x_p, y_p, z_p) = & \alpha_1 \varphi_{sA1}(x_p - x_{A1}, y_p - y_{A1}, z_p - z_{A1}) + \beta_1 \varphi_{pA1}(x_p - x_{A1}, y_p - y_{A1}, z_p - z_{A1}) + \\ & \alpha_2 \varphi_{sA2}(x_p - x_{A2}, y_p - y_{A2}, z_p - z_{A2}) + \beta_2 \varphi_{pA2}(x_p - x_{A2}, y_p - y_{A2}, z_p - z_{A2}) + \dots + \\ & \alpha_N \varphi_{sAN}(x_p - x_{AN}, y_p - y_{AN}, z_p - z_{AN}) + \beta_N \varphi_{pAN}(x_p - x_{AN}, y_p - y_{AN}, z_p - z_{AN}) \end{aligned} \quad (4.14)$$



Where  $A_1$ ,  $A_2$  and  $A_N$  stand for the first, second and  $N$ 'th atom in the unit cell. Writing equation 4.14 in a more closed form gives:

$$\psi(x_p, y_p, z_p) = \sum_{n=1,2}^{j=1,2,\dots,N} C_{n,j} \phi_{n,A_j}(x_p - x_{A_j}, y_p - y_{A_j}, z_p - z_{A_j}) \quad (4.15)$$

The above summation is calculated in the innermost loop of a code and it is repeated  $N_{\text{grid}} \times N_{\text{atom}} \times N_{\text{orbital}}$  times in which  $N_{\text{orbital}}$  can be 10 or 1 depending on if the selected atom is a Si or H. Recall that the total number of orbitals in each unit cell is  $N_{\text{orbit}} = N_{\text{Si}} \times 10 + N_{\text{H}} \times 1$ . The complex conjugate of equation 4.15 is calculated to find out the value of  $|\Psi(x_p, y_p, z_p)|^2$  at grid point P. The aforementioned procedure is repeated  $N_{\text{grid}}$  times to fill an  $N_x \times N_y$  vector which stores the values of  $|\Psi(x, y, z_p)|^2$  on  $z = z_p$  plane. After normalization of this vector and converting it to a matrix in MATLAB<sup>®</sup> the visualization becomes straightforward. Please note that merely adding the squared absolute values of coefficients in equation 4.15 wipes out all quantum mechanical interference effects and results in a wrong plot. The same procedure as shown in Figure 4.1 can be modified to other cross sectional planes i.e.  $xz$  and  $zy$ . To find out which orbital has the most contribution in each state, the corresponding coefficients of other orbitals can be set to zero before the main  $\Psi(x, y, z)$  evaluation loop starts. In the following example it is shown how visualizing the wave functions will help to determine the symmetry allowed optical transitions in a SiNW. Figure 4.2 shows the cross section of a 2.2nm [100] SiNW in  $xy$  plane. The energy of the nanowire is minimized using SIESTA.

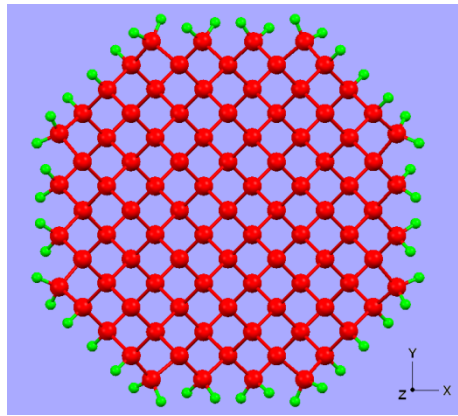


Figure 4.2 An energy minimized 2.2nm [100] SiNW.

The wave function corresponding to valence/conduction band minimum/maximum (at BZ center) is plotted in  $xy$  cross sectional plane of the nanowire in Figure 4.3. As can be seen the conduction and valence bands have even and odd symmetry with respect to the center of

rotation, respectively. Looking at the definition of position operator matrix element i.e.  $\langle \psi_c | \mathbf{r} | \psi_v \rangle = \int \psi_c^*(\mathbf{r}) \cdot \mathbf{r} \cdot \psi_v(\mathbf{r}) d\mathbf{r}$ , reveals that the integrand must have an even parity in order to obtain nonzero matrix element. Since  $x$  and  $y$  have odd parity they both make the integrand to be of even symmetry and as a result  $x$  and  $y$  polarized matrix elements are nonzero as opposed to  $z$ -polarized matrix element.

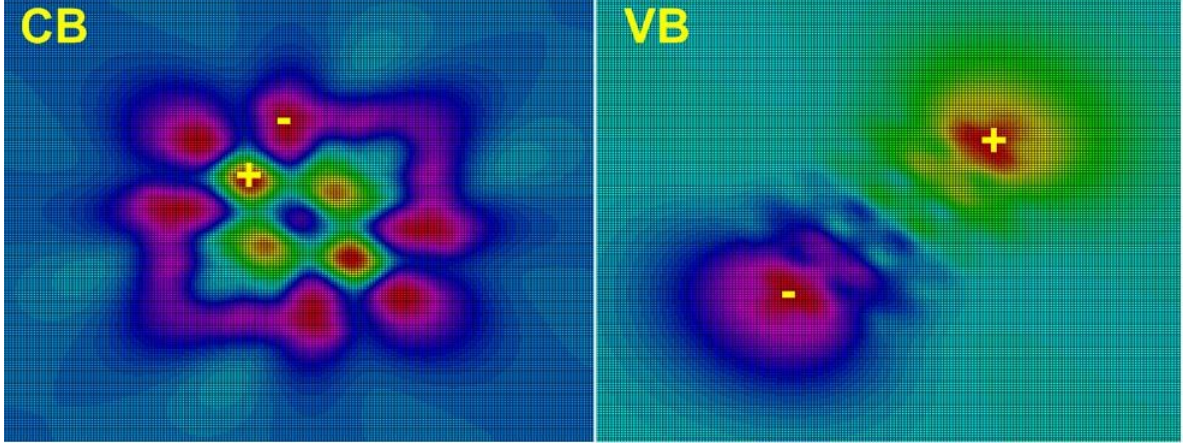


Figure 4.3 (a) Conduction band (CB) and (b) valence band (VB) states at BZ center. CB and VB have even and odd symmetry, respectively.

Figure 4.4 shows the normalized momentum matrix element along BZ of the nanowire in which  $x$  and  $y$  components are more dominant than  $z$ -polarized case and they are very close in value (ideally equal).

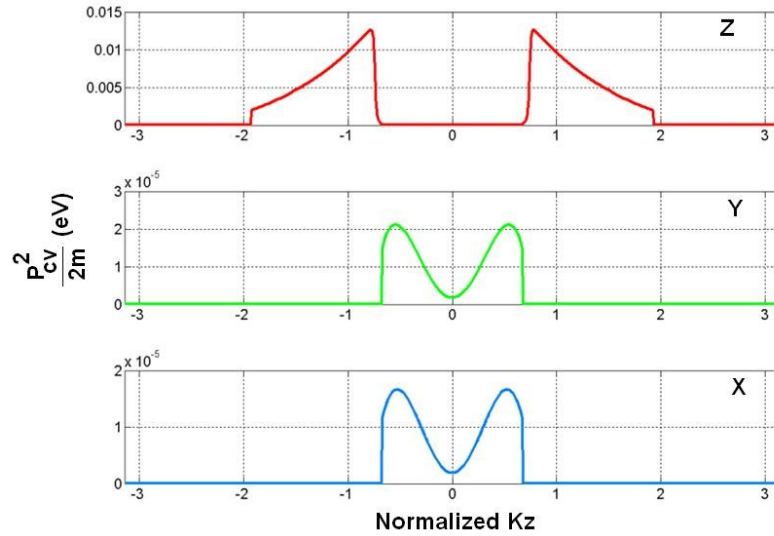


Figure 4.4 Normalized momentum matrix element ( $P^2_{cv}/2m$  in terms of eV) along the BZ  $[-\pi, \pi]$  of a 2.2nm [110] SiNW for  $z$ ,  $y$  and  $x$  polarizations, respectively

### 4.3 First Order Spontaneous Emission Process

The life time of an electron which is excited from a state in the valence band to its corresponding state in the conduction band is determined using the first order perturbation theory [141][146]. The conduction and valence states are at the same value of  $k$  (crystal momentum) along 1D BZ of SiNW and are called initial ( $i$ ) and final ( $f$ ) states, respectively. Then the radiative decay rate ( $1/\tau_{if}$ ) is written according to Fermi's golden rule as:

$$\left(\frac{1}{\tau}\right)_{i \rightarrow f} = \frac{2\pi}{\hbar} \sum_{k,\sigma} |\langle f | H_{eR} | i \rangle|^2 \delta(E_f - E_i) \quad (4.16)$$

where the summation runs over photon wave vectors ( $k$ ) and polarizations ( $\sigma$ ).  $E_f$  and  $E_i$  are energy of the final and initial mixed (electron and photon) states. The electron-photon (radiation) interaction Hamiltonian,  $H_{eR}$ , is written as follows which is based on decomposing of the field operator,  $\mathbf{A}$ , as a linear combination of planar modes  $A_{k,\sigma}$  in a space of volume  $V=L^3$

$$H_{eR} = -\frac{e}{m} \sum_{k',\sigma'} \sqrt{\frac{\hbar}{2V\epsilon\omega_{k'}}} \hat{\mathbf{p}} \cdot \hat{\mathbf{e}}_{k',\sigma'} (\hat{a}_{k',\sigma'} e^{ik'.r} + \hat{a}_{k',\sigma'}^\dagger e^{-ik'.r}) \quad (4.17)$$

$e$  is the value of electronic charge ( $1.602 \times 10^{-19}$  C),  $m$  is the free mass of electron ( $9.109 \times 10^{-31}$  Kg).  $\sigma'$ ,  $k'$  and  $\omega_{k'}$  are photon wave vector, polarization and angular frequency of the photon field, respectively.  $\hat{\mathbf{p}}$  is the momentum operator,  $\hat{\mathbf{e}}_{k',\sigma'}$  is the unit vector along polarization direction ( $\sigma'$ ).  $\hat{a}_{k',\sigma'}$  and  $\hat{a}_{k',\sigma'}^\dagger$  are photon annihilation and creation operators, respectively. The quantity  $\epsilon$  represents the dielectric constant of the medium. To find the matrix element of electron-photon Hamiltonian, the initial and final states are written as a mixed electronic (fermions) and photonic (bosons) state. Therefore  $|a_i, n_{k\sigma}\rangle$  shows the conduction band state including  $n_{k\sigma}$  photons. The final state has  $n_{k\sigma} + 1$  photons after electron transits from the conduction to the valence band i.e.  $|a_f, n_{k\sigma} + 1\rangle$ . The matrix element is then found by applying creation and annihilation operators on photon number states as follows:

$$\begin{aligned} \langle f | H_{eR} | i \rangle = & -\frac{e}{m} \left\langle a_f, n_{k\sigma} + 1 \left| \sum_{k',\sigma'} \sqrt{\frac{\hbar}{2V\epsilon\omega_{k'}}} \hat{\mathbf{p}} \cdot \hat{\mathbf{e}}_{k',\sigma'} (\hat{a}_{k',\sigma'} e^{ik'.r} + \hat{a}_{k',\sigma'}^\dagger e^{-ik'.r}) \right| a_i, n_{k\sigma} \right\rangle = \\ & -\frac{e}{m} \sqrt{\frac{\hbar}{2V\epsilon\omega_k}} \{ \sqrt{n_{k\sigma}} \langle a_f, n_{k\sigma} + 1 | \hat{\mathbf{p}} \cdot \hat{\mathbf{e}}_{k,\sigma} e^{ik.r} | a_i, n_{k\sigma} - 1 \rangle + \\ & \sqrt{n_{k\sigma} + 1} \langle a_f, n_{k\sigma} + 1 | \hat{\mathbf{p}} \cdot \hat{\mathbf{e}}_{k,\sigma} e^{-ik.r} | a_i, n_{k\sigma} + 1 \rangle \} \quad (4.18) \end{aligned}$$

Using ortho-normality of photon number states, equation 4.18 is reduced to:

$$\langle f|H_{eR}|i\rangle = -\frac{e}{m} \sqrt{\frac{\hbar}{2V\epsilon\omega_k}} \sqrt{n_{k\sigma} + 1} \langle a_f|\hat{\mathbf{p}} \cdot \hat{\mathbf{e}}_{k,\sigma} e^{-ik \cdot \mathbf{r}}|a_i\rangle \quad (4.19)$$

Since initial to final state transition results in an extra photon in the final state, the energy conserving term in Dirac's delta function is modified as:

$$E_f - E_i = E_{a_f} + \hbar\omega_k - E_{a_i} = E_{a_f} - E_{a_i} + \hbar\omega_k = 0 \quad (4.20)$$

where  $E_{ai}$  and  $E_{af}$  are initial and final energy of electronic states, respectively. Then according to equation 4.16, the total photon emission rate is given as:

$$\left(\frac{1}{\tau}\right)_{i \rightarrow f} = \frac{2\pi}{\hbar} \left(\frac{e}{m}\right)^2 \left(\frac{\hbar}{2V\epsilon}\right) \sum_{k,\sigma} \frac{n_{k\sigma} + 1}{\omega_k} |\langle a_f|\hat{\mathbf{p}} \cdot \hat{\mathbf{e}}_{k,\sigma} e^{-ik \cdot \mathbf{r}}|a_i\rangle|^2 \times \delta(E_{a_f} - E_{a_i} + \hbar\omega_k) \quad (4.21)$$

As can be seen the total emission rate is composed of a spontaneous term (where  $n_{k\sigma}=0$ ) and the stimulated emission which is proportional to  $n_{k\sigma}$ . Stimulated emission term is used in calculation of optical gain or loss (absorption) which is the topic of Chapter 6. Here we continue with  $n_{k\sigma}=0$  to find the spontaneous emission rate (time) in SiNWs. When the dimensions of the system under study are much smaller than the wavelength of the light e.g. molecules and quantum dots, the factor of  $e^{-ik \cdot \mathbf{r}}$  in equation 4.21 can be simplified using dipole approximation:

$$e^{-ik \cdot \mathbf{r}} = 1 - k \cdot \mathbf{r} - \frac{1}{2}(k \cdot \mathbf{r})^2 + \dots \approx 1, \text{ if } k \cdot \mathbf{r} = \frac{2\pi r}{\lambda} \ll 1 \quad (4.22)$$

However if the size of the system is comparable with the photon wavelength (e.g. for the case of bulk Si crystal or when the propagation of light is along the axis of the nanowire), then the approximation used in equation 4.22 is not valid anymore. In this case the procedure of Appendix C is used to calculate the matrix element. Summation over photon wave vectors ( $k$ ) can be converted to integration using:

$$\sum_k \dots \rightarrow \frac{V}{(2\pi)^3} \int \dots d^3k \quad (4.23)$$

Summation over photon polarization ( $\sigma$ ) can be calculated using Figure 4.5 in which two polarization vectors are chosen to be normal to the photon wave vector ( $k$ ) [141].

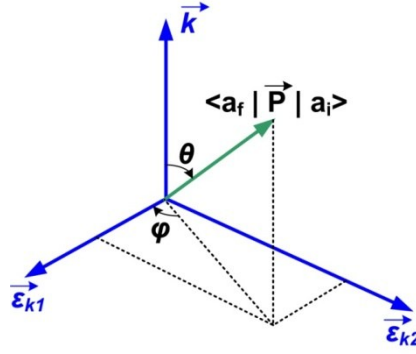


Figure 4.5 Photon polarization vectors are in a plane which is normal to the photon wave vector ( $k$ ). Without loss of generality the momentum of electron is assumed to have an angle ( $\theta$ ) with the photon propagation direction ( $k$ ). The sum over polarizations is then reduced to two terms:

$$\sum_{\sigma=1,2} |\langle u_f | \hat{\mathbf{p}} \cdot \hat{\mathbf{e}}_{k,\sigma} | u_i \rangle|^2 = \hat{\mathbf{e}}_{k1} \cdot |\langle u_f | \hat{\mathbf{p}} | u_i \rangle|^2 + \hat{\mathbf{e}}_{k2} \cdot |\langle u_f | \hat{\mathbf{p}} | u_i \rangle|^2 =$$

$$|\langle u_f | \hat{\mathbf{p}} | u_i \rangle|^2 \sin^2 \theta \cos^2 \varphi + |\langle u_f | \hat{\mathbf{p}} | u_i \rangle|^2 \sin^2 \theta \sin^2 \varphi = |\langle u_f | \hat{\mathbf{p}} | u_i \rangle|^2 \sin^2 \theta \quad (4.24)$$

where  $u_i$  and  $u_f$  are Bloch parts of the total electronic states ( $a_i$  and  $a_f$ ) and they are discussed in Appendix C. Writing the volume element as  $d^3k = k^2 dk \sin \theta d\theta d\varphi$ , the summation in equation 4.20 is reduced to:

$$\left(\frac{1}{\tau}\right)_{i \rightarrow f} = \frac{2\pi}{\hbar} \left(\frac{e}{m}\right)^2 \left(\frac{\hbar}{2V\epsilon}\right) \left(\frac{V}{8\pi^3}\right) \int \frac{k^2}{\omega_k} |\langle u_f | \hat{\mathbf{p}} | u_i \rangle|^2 \delta(E_{a_f} - E_{a_i} + \hbar\omega_k) dk \int_0^\pi \sin^3 \theta d\theta \int_0^{2\pi} d\varphi \quad (4.25)$$

The velocity of light in the material is  $v=c/n_r$ , where  $n_r$  is the low frequency refractive index of bulk Silicon. Writing  $\omega_k=vk$ , and using the sifting property of Dirac's delta function, the integration of equation 4.25 is continued as follows:

$$\int \frac{k^2}{\omega_k} |\langle u_f | \hat{\mathbf{p}} | u_i \rangle|^2 \delta(E_{a_f} - E_{a_i} + \hbar\omega_k) dk = \int \frac{k^2}{vk} |\langle u_f | \hat{\mathbf{p}} | u_i \rangle|^2 \delta\left(\hbar v \left(\frac{E_{a_f} - E_{a_i}}{\hbar v} + k\right)\right) dk =$$

$$\int \frac{k^2}{vk} |\langle u_f | \hat{\mathbf{p}} | u_i \rangle|^2 \frac{1}{\hbar v} \delta\left(\frac{E_{a_f} - E_{a_i}}{\hbar v} + k\right) dk = \frac{1}{\hbar v^2} |\langle u_f | \hat{\mathbf{p}} | u_i \rangle|^2 \frac{E_{a_i} - E_{a_f}}{\hbar v} \quad (4.26)$$

In which we have used  $\int_0^\pi \sin^3 \theta d\theta \int_0^{2\pi} d\varphi = 8\pi/3$ . Finally the spontaneous emission rate in equation 4.21 is given as:

$$\begin{aligned}
\left(\frac{1}{\tau}\right)_{i \rightarrow f} &= \frac{2\pi}{\hbar} \left(\frac{e}{m}\right)^2 \left(\frac{\hbar}{2V\epsilon}\right) \left(\frac{V}{8\pi^3}\right) \frac{1}{\hbar v^2} |\langle u_f | \hat{\mathbf{p}} | u_i \rangle|^2 \frac{E_{a_i} - E_{a_f}}{\hbar v} \frac{8\pi}{3} \\
&= \frac{e^2}{3\pi m^2 \epsilon v^3 \hbar} \frac{E_{a_i} - E_{a_f}}{\hbar} |\langle u_f | \hat{\mathbf{p}} | u_i \rangle|^2 \quad (4.27)
\end{aligned}$$

The momentum ( $\mathbf{p}$ ) matrix element can be transferred to position ( $\mathbf{r}$ ) representation using:

$$|\langle a_f | \hat{\mathbf{p}} | a_i \rangle|^2 = m^2 \omega_{if}^2 |\langle u_f | \hat{\mathbf{r}} | u_i \rangle|^2 \quad (4.28)$$

in which  $\omega_{if}$  is  $E_{a_i} - E_{a_f}/\hbar$ . Further simplification can be made if we write  $\epsilon = \epsilon_r \epsilon_0 = n_r^2 \epsilon_0$  and  $v = c/n_r$ :

$$\left(\frac{1}{\tau}\right)_{i \rightarrow f} = \frac{n_r e^2}{3\pi \epsilon_0 c^3 \hbar} \omega_{if}^3 |\langle u_f | \hat{\mathbf{r}} | u_i \rangle|^2 \quad (4.29)$$

The position matrix element is found using the procedure explained in the previous section. This equation gives three values corresponding to three different photon polarization i.e.  $x$ ,  $y$  or  $z$ .

#### 4.4 Second Order Spontaneous Emission Process

To find the spontaneous emission life time of an excited electron in the indirect conduction band minimum first we need to observe the energy difference between the conduction band states i.e.  $\Delta\Omega$  as shown in Figure 4.6. When  $\Delta\Omega$  is less than the Debye energy of LA phonons ( $E_{\text{Debye}} = 54$  meV) many secondary states in direct conduction sub band are available to which an electron can scatter from indirect sub band by absorbing a LA phonon. Alternatively, when  $\Delta\Omega$  is less than the maximum energy of LO phonons,  $E_{\text{LO}} = 63$  meV, a few secondary states in direct conduction sub band can be found to which an electron can scatter from indirect sub band by absorbing a LO phonon. This implies that if the secondary state within the direct conduction sub band is not at the BZ center, the only possible first order transition is due to LA phonon absorption. Otherwise both LA and LO phonon absorption processes will contribute in the first order inter-sub band scattering event. The process of finding secondary states can be understood by recalling that LO and LA phonons are modeled as dispersion-less and a linear dispersion around BZ center, respectively [147]. On the other hand if the energy difference between conduction band minima is larger than the maximum available energy of phonons i.e.  $\Delta\Omega > E_{\text{debye}}$ , the transition is possible only through virtual momentum states and this mandates using second order perturbation theory. Qualitatively we might expect that indirect bandgap hinders light emission from a SiNW because the emission

of a photon is now a slow second order phonon-mediated process. In this section we formulate the spontaneous emission time using the second order perturbation theory by including Longitudinal Acoustic (LA) and Longitudinal Optical (LO) phonons, respectively.

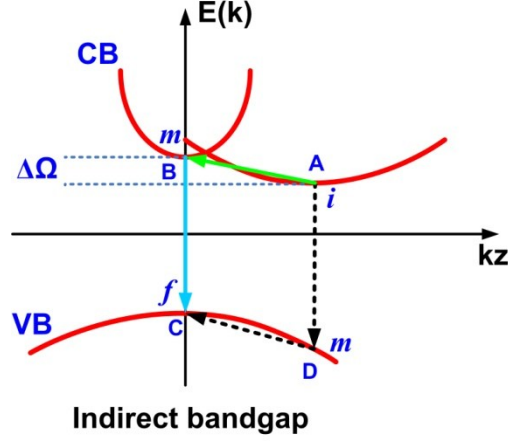


Figure 4.6 Schematic of an indirect bandgap SiNW band structure. Difference between direct and indirect conduction sub band minima is shown as  $\Delta\Omega$ . This quantity determines the order of light emission process in an indirect bandgap nanowire. There are two possible transitions from indirect conduction minimum ( $i$ ) to the valence band maximum ( $f$ ): (1) via intermediate states ( $m$ ) within the valence band (ADC) or (2) via intermediate states ( $m$ ) within the conduction band (ABC).

#### 4.4.1 LA Phonons

The spontaneous emission lifetime of an electron in indirect conduction sub band (state  $i$ ) is determined by the following equation. The recombination of this electron with a hole residing at BZ center is possible through virtual transitions to intermediate states (states  $m$ ) in the first conduction band (via phonon emission and absorption) or the last valence band. The transition rate or  $1/\tau_{if}$  is written as:

$$\tau_{if}^{-1} = \frac{2\pi}{\hbar} \sum_{k', \sigma'} \sum_{\bar{q}, l} \left| \langle f | \tilde{H} | i \rangle + \sum_{k_m} \frac{\langle f | \tilde{H} | m \rangle \langle m | \tilde{H} | i \rangle}{E_i - E_m} \right|^2 \delta(E_f - E_i) \quad (4.30)$$

where  $k', \sigma'$  are photon wave vector and polarization, respectively.  $\bar{q}$  and  $l$  are the phonon wave vector and branch index, respectively. The perturbation Hamiltonian,  $\tilde{H}$ , is expressed as  $\tilde{H} = H_{eP} + H_{eR}$  in which  $H_{eP}$  and  $H_{eR}$  are electron-phonon and electron-radiation (photon) interaction Hamiltonians, respectively. Summation over  $k_m$  stands for summation over all intermediate (virtual) states within the first conduction band or the last valence band.  $\Delta E_{im} = E_i - E_m$  is the energy difference between the initial ( $E_{cmin}$ ) and intermediate state(s). The first order term in equation 4.30 can be written as  $\langle f | \tilde{H} | i \rangle = \langle f | H_{eP} | i \rangle + \langle f | H_{eR} | i \rangle = 0$  due to the following reasons. Firstly the initial and final states have different momentum

therefore  $\langle f|H_{eR}|i\rangle = 0$ . Secondly the energy difference of initial and final states are much larger than the phonon energy, therefore the energy cannot be conserved i.e.  $\langle f|H_{eP}|i\rangle = 0$ . The second order term can be expanded as:

$$\langle f|\tilde{H}|m\rangle\langle m|\tilde{H}|i\rangle = \langle f|H_{eP}|m\rangle\langle m|H_{eP}|i\rangle + \langle f|H_{eP}|m\rangle\langle m|H_{eR}|i\rangle + \langle f|H_{eR}|m\rangle\langle m|H_{eP}|i\rangle + \langle f|H_{eR}|m\rangle\langle m|H_{eR}|i\rangle \quad (4.31)$$

The first and the fourth term on the right hand side of equation 4.31 are zero with the same logic which was explained for the first order perturbation terms. Therefore:

$$\langle f|\tilde{H}|m\rangle\langle m|\tilde{H}|i\rangle = \langle f|H_{eP}|m\rangle\langle m|H_{eR}|i\rangle + \langle f|H_{eR}|m\rangle\langle m|H_{eP}|i\rangle \quad (4.32)$$

The first term in the right hand side of equation 4.32 corresponds to a direct optical transition from initial state ( $i$ ) to an intermediate state ( $m$ ) in the valence band (AD in Figure 4.6) followed by an indirect phonon assisted transition from ( $m$ ) to the final state in valence band ( $f$ ) (DC in Figure 4.6). Similarly the second term in the right hand side of equation 4.32 represents an indirect transition to an intermediate state ( $m$ ) in the conduction band (AB in Figure 4.6) followed by a direct optical transition from ( $m$ ) to the same final state in valence band (BC in Figure 4.6).

Since there is a large number of intermediate states, the interference effects in the summation over  $k_m$  can be neglected and the summation is performed over the squared values of individual terms in equation 4.30 i.e.  $|\sum_m \beta_m|^2 \cong \sum_m |\beta_m|^2$  and  $\beta$  stands for an  $m$ -dependent term. Thus:

$$\left| \sum_{k_m} \frac{\langle f|\tilde{H}|m\rangle\langle m|\tilde{H}|i\rangle}{E_i - E_m} \right|^2 = \sum_{k_m} \left\{ \frac{|\langle f|H_{eP}|m\rangle|^2 |\langle m|H_{eR}|i\rangle|^2}{(E_{i:A} - E_{m:D})^2} + \frac{|\langle f|H_{eR}|m\rangle|^2 |\langle m|H_{eP}|i\rangle|^2}{(E_{i:A} - E_{m:B})^2} \right\} \quad (4.33)$$

$E_{i:A}$ ,  $E_{m:D}$  and  $E_{m:B}$  correspond to total energies of initial states, intermediate state on valence band (D in Figure 4.6) and intermediate state on conduction band (B in Figure 4.6), respectively. Since the energy difference between conduction and valence band is at least one order of magnitude larger than the energy difference within the conduction band i.e.  $E_{i:A} - E_{m:D} \gg E_{i:A} - E_{m:B}$ , the first term in equation 4.33 can be neglected. To find the average lifetime of an electron residing in the indirect  $E_{\text{cmin}}$ , all possible transitions from this state to all states in the valence band must be considered, provided that they are weighted by the Fermi factor or availability of empty states in the valence band throughout the BZ of SiNW. Hence spontaneous emission life time of an electron in the indirect conduction band minimum  $1/\tau_i$  is defined as:



$$\tau_i^{-1} = \sum_{k_f} \frac{2\pi}{\hbar} \sum_{k',\sigma'} \sum_{\bar{q},l} \sum_{k_m} \frac{|P|^2 |O|^2}{(\Delta E_{im})^2} \delta(E_f - E_i) F(k_f) \quad (4.34)$$

$F(k_f)$  is the Fermi factor at each valence state ( $k_f$ ).  $|O|^2$  and  $|P|^2$  represent  $|\langle m|H_{ep}|i\rangle|^2$  and  $|\langle f|H_{eR}|m\rangle|^2$ , respectively.  $E_i$ ,  $E_m$  and  $E_f$  correspond to the energy of the mixed (Fermions and Bosons) initial ( $i$ ), intermediate ( $m$ ) and final ( $f$ ) states, respectively. They are found by assuming that there is already  $n_{k,\sigma}$  photons and  $n_{q,l}$  phonons in the system. For the initial and intermediate states in the conduction band, the energies can be written as:

$$E_i = E_{ci} + n_{k,\sigma} \hbar \omega_{k,\sigma} + n_q \hbar \omega_q, \quad E_m = E_{cm} + n_{k,\sigma} \hbar \omega_{k,\sigma} + (n_q \pm_a^e 1) \hbar \omega_q \quad (4.35)$$

Where  $e(a)$  represents emission (absorption) of a phonon. Similarly the final energy in the valence band (after emission of a photon) can be written as:

$$E_f = E_{vf} + (n_{k,\sigma} + 1) \hbar \omega_{k,\sigma} + (n_q \pm_a^e 1) \hbar \omega_q \quad (4.36)$$

Hence  $\Delta E_{im}$  is:

$$\Delta E_{im} = E_m - E_i = E_{cm} - E_{ci} \pm_a^e \hbar \omega_q \quad (4.37)$$

And the argument of Dirac's delta function may be written as:

$$\delta(E_f - E_i) = \delta(E_i - E_f) = \delta(E_{ci} - E_{vf} - \hbar \omega_{k,\sigma} \mp_a^e \hbar \omega_q) \quad (4.39)$$

The electron-LA phonon Hamiltonian matrix element,  $|P|^2$ , is found using the procedure which is shown in equations (10-12) of [148]. The electron-photon interaction Hamiltonian matrix element is found using the same method which was discussed in section 4.3. Here  $|O|^2$  is rewritten as:

$$|O|^2 = \left(\frac{e}{m}\right)^2 \frac{\hbar (n_{k',\sigma'} + 1)}{2V\epsilon\omega_{k',\sigma'}} \left| \langle a_f | \hat{P} \cdot \hat{\epsilon}_{k',\sigma'} e^{-i\mathbf{k}' \cdot \mathbf{r}} | a_m \rangle \right|^2 \quad (4.40)$$

To keep the spontaneous emission term we choose  $n_{k',\sigma'} = 0$ . Inserting these matrix elements into equation 4.34 yields:

$$\tau_i^{-1} = \frac{2\pi}{\hbar} \left(\frac{e}{m}\right)^2 \frac{\hbar}{2V\epsilon} \frac{D^2 \hbar}{2\rho V} \sum_{k_f} \sum_{k',\sigma'} \sum_{\bar{q},l} \frac{1}{\omega_{k',\sigma'}} |\langle u_f | \hat{P} \cdot \hat{\epsilon}_{k',\sigma'} | u_m \rangle|^2 \frac{|\bar{q}|^2}{\omega_q} \frac{|S(|\bar{q}|)|^2 B_{\pm}(|\bar{q}|)}{(E_{cm} - E_{ci} \pm \frac{e}{a} \hbar \omega_q)^2} \delta(E_{ci} - E_{vf} - \hbar \omega_{k',\sigma'} \mp \frac{e}{a} \hbar \omega_q) \cdot F(k_f) \quad (4.41)$$

Where  $S(|\bar{q}|)$  is the overlap factor or matrix element of  $e^{iq \cdot r}$  terms which is defined in equation (13) of [148]. The summation over photon (radiation) wave vectors and polarizations follows the same procedure as discussed in section 4.3. Assuming a linear dispersion for LA phonons means that  $\omega_q = v_s |\bar{q}|$ , in which  $v_s$  is the velocity of sound in Silicon ( $v_s = 9.01 \times 10^5$  cm/sec) and  $\omega$  is the angular frequency of phonon.  $D$  and  $\rho$  represent electron deformation potential ( $D = 9.5$  eV) and mass density ( $\rho = 2329$  Kg/m<sup>3</sup>). Now we have:

$$\tau_i^{-1} = \frac{2\pi}{\hbar} \left(\frac{e}{m}\right)^2 \frac{\hbar}{2V\epsilon} \frac{D^2 \hbar}{2\rho V} \frac{1}{3\pi^2 v v_s} \sum_{k_f} \sum_{\bar{q},l} |\langle u_f | \hat{P} | u_m \rangle|^2 |\bar{q}| \frac{|S(|\bar{q}|)|^2 B_{\pm}(|\bar{q}|)}{(E_{cm} - E_{ci} \pm \frac{e}{a} \hbar \omega_q)^2} \cdot F(k_f) \int k' dk' \delta(E_{ci} - E_{vf} - \hbar \omega_{k'} \mp \frac{e}{a} \hbar \omega_q) \quad (4.42)$$

Using sifting properties of Dirac's delta function,  $\omega_{k'} = vk'$  ( $v$  is velocity of light in silicon and it is  $v = c/n_r$ ) and converting the momentum matrix element to position representation yields:

$$\tau_i^{-1} = \frac{2\pi}{\hbar} \frac{\hbar}{2V\epsilon} \frac{e^2 D^2 \hbar}{2\rho} \frac{1}{3\pi^2 \hbar^2 c^3 v_s} \sum_{k_f} \omega_{fm}^2 |\langle u_f | \hat{r} | u_m \rangle|^2 F(k_f) \sum_{\bar{q}} |\bar{q}| |S(|\bar{q}|)|^2 B_{\pm}(|\bar{q}|) \frac{E_c(k_i) - E_v(k_f) \mp \frac{e}{a} \hbar \omega_q}{(E_c(k_m) - E_c(k_i) \pm \frac{e}{a} \hbar \omega_q)^2} \quad (4.43)$$

$E_{cm}$ ,  $E_{ci}$  and  $E_{vf}$  have been replaced by  $E_c(k_m)$ ,  $E_c(k_i)$  and  $E_v(k_f)$ , respectively to recall that they are conduction and minimum state energies at the corresponding  $k$  values. To perform summation over all phonon wave vectors, we use the linearity of phonon dispersion i.e.  $\omega_q = v_s |\bar{q}| = v_s \sqrt{q_t^2 + q_z^2}$ . At each final state ( $k_f$ ), the longitudinal component of phonon momentum is given by  $q_z = k_m - k_i = k_f - k_i$ , because  $m$  and  $f$  indices are moving together (due to momentum conservation imposed by direct transitions between  $|m\rangle$  and  $|f\rangle$ ). Corresponding to this  $q_z$ , the maximum allowable transversal component of phonon momentum,  $\tilde{q}_{t,max}$ , is found by:

$$\tilde{q}_{t,max} = \sqrt{\left| \frac{E_{debye}}{\hbar v_s} \right|^2 - q_z^2} \quad (4.44)$$

Therefore there are many phonon wave vectors which have a common longitudinal component ( $q_z$ ) and their transversal (radial) component starts from  $\tilde{q}_{t,min} = 0$  to  $\tilde{q}_{t,max}$  as

shown in Figure 4.7. If  $\left| \frac{E_{debye}}{\hbar v_s} \right| > q_z$ , then a phonon is available otherwise its contribution to equation 4.43 is zero.

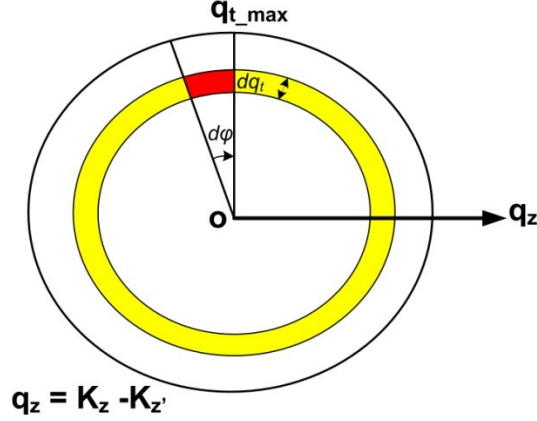


Figure 4.7 Available LA phonons with a common  $q_z$  and transversal vectors which span  $\tilde{q}_{t\_min} = 0$  to  $\tilde{q}_{t\_max}$ .

Therefore the summation over phonon wave vectors reduces to integration over area of the circle shown in Figure 4.7. Since the element of area is  $\tilde{q}_t d\tilde{q}_t d\phi$  then:

$$\sum_{\tilde{q}}[...] = \frac{A}{4\pi^2} \int [...] \cdot \Delta q_{Area\ element} = \frac{A}{4\pi^2} \int_0^{2\pi} [...] \cdot d\phi \int_0^{\tilde{q}_{t\_max}} \dots \tilde{q}_t d\tilde{q}_t \quad (4.45)$$

$S(|\tilde{q}|)$  is the only term which depends on  $\phi$ , therefore:

$$\begin{aligned} \tau_i^{-1} = & \frac{2\pi}{\hbar} \frac{\hbar}{2V\epsilon} \frac{e^2 D^2 \hbar}{2\rho} \frac{1}{3\pi^2} \frac{n_r^3}{\hbar^2 c^3 v_s} \sum_{k_f} \omega_{fm}^2 |\langle u_f | \hat{r} | u_m \rangle|^2 F(k_f) \times \\ & \frac{A}{4\pi^2} \int_0^{\tilde{q}_{t\_max}} \sqrt{\tilde{q}_t^2 + q_z^2} \frac{E_c(k_i) - E_v(k_f) \mp \frac{e}{\hbar} \hbar v_s \sqrt{\tilde{q}_t^2 + q_z^2}}{\left( E_c(k_m=k_f) - E_c(k_i) \pm \frac{e}{\hbar} \hbar v_s \sqrt{\tilde{q}_t^2 + q_z^2} \right)^2} B_{\pm}(|\tilde{q}|) \left[ \int_0^{2\pi} |S(|\tilde{q}|)|^2 d\phi \right] \tilde{q}_t d\tilde{q}_t \quad (4.46) \end{aligned}$$

where  $\Phi(\tilde{q}_t, q_z) = \int_0^{2\pi} |S(|\tilde{q}|)|^2 d\phi$  is a dimensionless form factor.  $B_{\pm}(|\tilde{q}|)$  is the Bose-Einstein factor of phonons and it is  $1/(e^{\frac{\hbar\omega_q}{K_B T}} - 1)$  for absorption and  $1 + \frac{1}{e^{\frac{\hbar\omega_q}{K_B T}} - 1}$  for

emission of a phonon. The result of integration over  $\tilde{q}_t$  cannot be simplified analytically and for the rest of the derivation it is shown by  $\text{Ph}_{LA}(k_f, k_i)$  which depends on  $k_m = k_i$ . Further simplification of equation 4.46 results in:

$$\tau_i^{-1} = \frac{2\pi}{\hbar} e^2 \frac{\hbar}{2V\epsilon} \frac{D^2 \hbar}{2\rho} \frac{1}{3\pi^2} \frac{n_r^3}{\hbar^2 c^3 v_s} \sum_{k_f} \omega_{fm}^2 |\langle u_f | \hat{\mathbf{r}} | u_m \rangle|^2 F(k_f) \cdot \frac{A}{4\pi^2} Ph_{LA}(k_f, k_i) \quad (4.47)$$

Converting the summation over  $k_f$  into integration yields:

$$\tau_i^{-1} = \frac{2\pi}{\hbar} e^2 \frac{\hbar}{2V\epsilon} \frac{D^2 \hbar}{2\rho} \frac{1}{3\pi^2} \frac{n_r^3}{\hbar^2 c^3 v_s} \frac{A}{4\pi^2} \frac{L}{2\pi} \int dk_f \omega_{fm}^2 |\langle u_f | \hat{\mathbf{r}} | u_m \rangle|^2 F(k_f) \cdot Ph_{LA}(k_f, k_i) \quad (4.48)$$

After factoring out all physical constants and using  $\epsilon = \epsilon_r \epsilon_0 = n_r^2 \epsilon_0$ , the life time of electron in indirect conduction band minimum is given by the following equations which is implemented numerically.

$$\tau_i^{-1} = \frac{e^2 D^2 n_r}{\epsilon_0 \rho c^3 v_s \hbar} \frac{1}{48\pi^4} \sum \omega_{fm}^2 |\langle u_f | \hat{\mathbf{r}} | u_m \rangle|^2 F(k_f) \cdot Ph_{LA}(k_f, k_i) \Delta k_f \quad (4.49)$$

As it is discussed in Chapter 5, by making a few simplifying assumptions, the numerical equation 4.49 is reduced to a much simpler semi-analytic equation.

#### 4.4.2 LO Phonons

For LO-phonon mediated light emission, the second order perturbation is used if  $\Delta\Omega > E_{LO}=63\text{meV}$ . Otherwise two cases should be considered separately. If  $\Delta\Omega = E_{LO}$  then there exists an intermediate state at  $k_z=0$  to which the electron can scatter in via a first order process. If  $\Delta\Omega < E_{LO}$  then there will be no optical phonon for the first order scattering between indirect and direct conduction band minima. In return electron can scatter to somewhere within the direct sub band and after that it can scatter to the direct sub band bottom through a series of electron-LA phonon scattering events. However the stronger role of LO phonons may return the electron back to its original position within the indirect sub band bottom. Calculation of the first order electron-phonon scattering events is discussed in the next section.

Derivation of indirect spontaneous emission life time including optical phonons proceeds with the same logic as discussed in the previous section, but extra modifications are needed due to the different nature of optical phonons. Firstly the electron-phonon interaction Hamiltonian matrix element,  $|P|^2$ , should be replaced with:

$$|\langle i | H_{op} | f \rangle|^2 = \frac{|D_{op}|^2 \hbar}{2\rho V \omega_0} |S(|\tilde{\mathbf{q}}|)|^2 (N(\hbar\omega_0) + \frac{1}{2} \pm \frac{e}{a} \frac{1}{2}) \delta_{k'_z, k_z \pm q_z} \quad (4.50)$$

Where it is assumed that LO phonon is dispersion-less i.e. all phonons have constant energy of  $E_p = \hbar\omega_0 = 63$  meV regardless of their momentum (wave vector).  $D_{op}$  is the electron deformation potential for LO phonon ( $D_{op}=11 \times 10^8$  eV/cm). Krönecker delta imposes momentum conservation i.e.  $k'_z = k_z \pm q_z$ . Secondly  $\Delta E_{im}$  in equation 4.34 and Dirac's delta function in equation 4.39 are modified accordingly i.e.

$$\Delta E_{im} = E_{cm} - E_{ci} \pm \hbar\omega_0, \quad \delta(E_f - E_i) = \delta(E_{ci} - E_{vf} - \hbar\omega_{k,\sigma} \pm \hbar\omega_0) \quad (4.51)$$

Including the aforementioned changes and using the electron-photon interaction Hamiltonian matrix element,  $|O|^2$ , as given in equation 4.40, the life time calculation starts from equation 4.34 to give:

$$\tau_i^{-1} = \frac{2\pi}{\hbar} \left(\frac{e}{m}\right)^2 \frac{\hbar}{2V\epsilon} \frac{|D_{op}|^2 \hbar}{2\rho V \omega_0} \sum_{k_f} \sum_{k',\sigma'} \sum_{\tilde{q},l} \frac{1}{\omega_{k',\sigma'}} |\langle f | \hat{p} \cdot \hat{\epsilon}_{k',\sigma'} | m \rangle|^2 \frac{|S(|\tilde{q}|)|^2 B_{\pm}(\hbar\omega_0)}{(E_{cm} - E_{ci} \pm \hbar\omega_0)^2} \delta(E_{ci} - E_{vf} - \hbar\omega_{k',\sigma} \pm \hbar\omega_0) \cdot F(k_f) \quad (4.52)$$

The summation over photon wave vectors and polarizations can be performed similar to the case of LA phonons (section 4.4.1). With the help of Dirac's delta function equation 4.52 is reduced to:

$$\tau_i^{-1} = \frac{2\pi}{\hbar} \frac{\hbar}{2V\epsilon} \frac{e^2 |D_{op}|^2 \hbar}{2\rho V \omega_0} \frac{V}{3\pi^2} \frac{n_i^3}{\hbar^2 c^3} \sum_{k_f} \omega_{fm}^2 |\langle u_f | \hat{r} | u_m \rangle|^2 F(k_f) \sum_{\tilde{q}} |S(|\tilde{q}|)|^2 B_{\pm}(\hbar\omega_0) \frac{E_c(k_i) - E_v(k_f) \pm \hbar\omega_0}{(E_c(k_m) - E_c(k_i) \pm \hbar\omega_0)^2} \quad (4.53)$$

Summations over  $k_f$  and  $\tilde{q}$  can be converted to integrations. Recalling that  $k_f$  and  $k_m$  step together i.e.  $k_m = k_f$  and  $B_{\pm}$  is independent of  $\tilde{q}$ , further simplifications result in:

$$\tau_i^{-1} = \frac{e^2 |D_{op}|^2 n_i^3}{\epsilon \rho c^3 \hbar \omega_0} \cdot \frac{1}{48\pi^4} \cdot B_{\pm}(\hbar\omega_0) \int_{k_f} \omega_{fm}^2 |\langle u_f | \hat{r} | u_m \rangle|^2 \left\{ \int_{q_t=0}^{q_{cm}^{max}} q_t \int_0^{2\pi} |S(q_t, q_z, \varphi)|^2 d\varphi dq_t \right\} \times \frac{E_c(k_i) - E_v(k_f) \pm \hbar\omega_0}{(E_c(k_f) - E_c(k_i) \pm \hbar\omega_0)^2} F(k_f) dk_f \quad (4.54)$$

where  $\{\dots\}$  returns a quantity which depends on  $k_f$  since  $q_z = k_f - k_i$ . This quantity and Bose-Einstein factor,  $B_{\pm}$ , are merged together and called  $\text{Ph}_{LO}(k_f)$  for the sake of brevity. The spontaneous emission life time is then given as:

$$\tau_i^{-1} = \frac{e^2 |D_{op}|^2 n_r^3}{\epsilon_0 \rho c^3 \hbar \omega_0} \cdot \frac{1}{48\pi^4} \int_{k_f} dk_f \omega_{fm}^2 |\langle u_f | \hat{r} | u_m \rangle|^2 Ph_{LO}(k_f) \frac{E_c(k_i) - E_v(k_f) \pm \hbar \omega_0}{(E_c(k_f) - E_c(k_i) \pm \hbar \omega_0)^2} F(k_f) \quad (4.55)$$

For the sake of one to one correspondence with equation 4.49 which gives the same quantity by including LA phonons, the integration over  $k_f$  is converted to a numerical summation as shown below. Also using  $\epsilon = \epsilon_r \epsilon_0 = n_r^2 \epsilon_0$  simplifies the pre-factors.

$$\tau_i^{-1} = \frac{e^2 |D_{op}|^2 n_r}{\epsilon_0 \rho c^3 \hbar \omega_0} \cdot \frac{1}{48\pi^4} \sum \omega_{fm}^2 |\langle u_f | \hat{r} | u_m \rangle|^2 F(k_f) \frac{E_c(k_i) - E_v(k_f) \pm \hbar \omega_0}{(E_c(k_f) - E_c(k_i) \pm \hbar \omega_0)^2} Ph_{LO}(k_f) \Delta k_f \quad (4.56)$$

In the next chapter we discuss how further assumptions can reduce this numerical equation into a semi-analytic equation. Comparing the roles of LA and LO phonons in the spontaneous emission time and scattering rates will be discussed in the next chapter as well.

## 4.5 First Order Electron-Phonon Scattering Rates

Calculation of the first order electron-phonon scattering rate serves two purposes. As it was mentioned in section 4.4 when  $\Delta\Omega < E_{LO/LA}$ , the light emission process can be modelled as two consecutive first order processes, the first of which is electron-phonon scattering. In the model the emission rate is determined by the slowest process. As will be seen in the next chapter, the electron-phonon scattering events are faster than direct photon emission processes which are in the range of (10µsec - 0.1µsec).

Also to study the carrier population statistics of indirect sub bands under the influence of electric field, temperature and multi electron-phonon scattering events, we use standard Ensemble Monte Carlo (EMC) methodology. In order to use the EMC simulator, calculation of electron-phonon scattering rates is necessary. EMC simulations were done by Professor Amit Verma [149]. The author calculated all scattering rates as a part of his thesis work. For each initial state starting from indirect conduction sub band minimum (in an indirect bandgap nanowire), all possible final states within the same subband and higher sub bands with corresponding scattering rates for both phonon types (LA/LO) should be utilized. Both inter- and intra-sub band electron-phonon scattering events are calculated and special matrices are filled in a specific order which is required for EMC code.

### 4.5.1 Electron-LA phonon scattering

Figure 4.8 shows how an electron at the bottom of the indirect conduction band can scatter into many available secondary states within  $E_{Debye}$  window. If the rate of each scattering event is called  $W(k_z, k'_z, \tilde{q})$ , then the total scattering rate of the electron at  $k_z$  is found by summation over all available secondary states ( $k'_z$ ) and phonon wave vectors ( $\tilde{q}$ ) i.e.:

$$W_{k_z} = \sum_{k'_z, \tilde{q}} W(k_z, k'_z, \tilde{q}) = \sum_{k'_z} \sum_{\tilde{q}} W(k_z, k'_z, \tilde{q}) = \sum_{k'_z} W(k_z, k'_z) \quad (4.57)$$

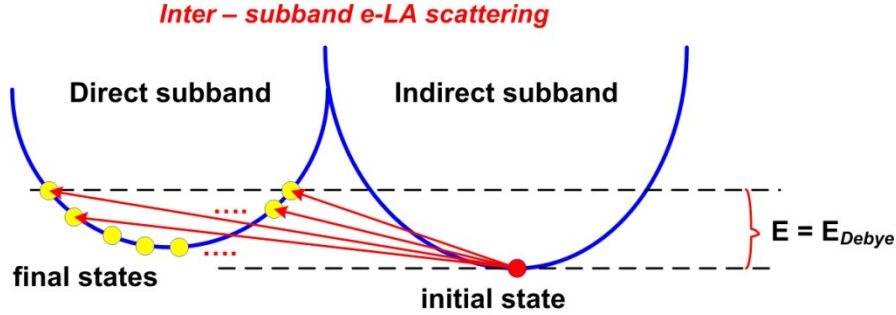


Figure 4.8 Inter-sub band electron-LA phonon scattering events starting from  $k_z$ .

Total momentum relaxation rate is found by the same equation in which individual rates,  $W$ , are weighted by a factor of  $(1 - k_z/k'_z)$ . Derivations of momentum relaxation rates have been explained in detail in [147][148]. Here we explain how the total scattering rate ( $W_{k_z}$ ) as well as each individual scattering rate [ $W(k_z, k'_z)$ ] can be saved for the purpose of spontaneous emission calculation and EMC simulation. Using Fermi's golden rule, the rate of a single scattering event can be written as follows where both momentum and energy are conserved and  $\psi$  corresponds to the mixed (electron and phonon) states.

$$W(k_z, k'_z, \tilde{q}) = \frac{2\pi}{\hbar} |\langle \psi_{k_z} | H_{eP} | \psi_{k'_z} \rangle|^2 \delta(E(k'_z) - E(k_z) \pm \hbar\omega(\tilde{q})) \cdot \delta_{q_z, k'_z - k_z} \quad (4.58)$$

The electron-phonon interaction Hamiltonian for phonons of LA type is given as:

$$H_{eP} = D \sum_{\tilde{q}} i|\tilde{q}| \sqrt{\frac{\hbar}{2\rho V\omega(\tilde{q})}} (a_{\tilde{q}} e^{i\tilde{q} \cdot r} + a_{\tilde{q}}^\dagger e^{-i\tilde{q} \cdot r}) \quad (4.59)$$

where  $a_{\tilde{q}}$  and  $a_{\tilde{q}}^\dagger$  are annihilation and creation operators. Since the  $z$  component of the phonon wave vector ( $q_z$ ) is determined by conservation of momentum i.e.  $q_z = k'_z - k_z$ , the summation over phonon wave vectors spans all transversal components of phonon wave vectors. It is converted to integration according to:

$$\sum_{k'_z} \dots \rightarrow \frac{L_z}{2\pi} \int \dots dk_z = \frac{L_z}{2\pi} \int \dots dq_z \quad \text{and} \quad \sum_{\tilde{q}} \dots = \sum_{q_x, q_y} \dots = \frac{A}{4\pi^2} \iint \dots dq_x dq_y \quad (4.60)$$

where A denotes area of the nanowire. The area element for integration in equation 4.60 can be written in terms of radial (transversal) components of phonon momentum by converting the Cartesian coordinate to the polar one:

$$dq_x dq_y = q_t dq_t d\phi \quad (4.61)$$

The angle,  $\phi$ , changes from 0 to  $2\pi$ . Using the same procedure as discussed in [148] the electron-LA phonon interaction Hamiltonian matrix element is reduced to equation 4.62 in which U stands for Bloch part of the electronic states.

$$|\langle U_{k_z} | H_{eP} | U_{k'_z} \rangle|^2 = \frac{D^2 \hbar |\tilde{q}|^2}{2\rho V \omega_q} |S(|\tilde{q}|)|^2 B_{\pm}(|\tilde{q}|) \quad (4.62)$$

$B_{\pm}(|\tilde{q}|)$  is the Bose-Einstein factor of phonons and it is  $1/(e^{\frac{\hbar\omega_q}{k_B T}} - 1)$  for absorption and  $1 + \frac{1}{e^{\frac{\hbar\omega_q}{k_B T}} - 1}$  for emission of a phonon. With transversal (radial) and longitudinal components

of phonon wave vectors ( $q_t$  and  $q_z$ ), the absolute value of phonon wave vector can be written as  $|\tilde{q}| = \sqrt{q_t^2 + q_z^2}$ . The structure factor  $S(|\tilde{q}|)$  is defined as follows where  $m$  and  $m'$  are index of atoms in one unit cell.  $k_1$  and  $k_2$  denote the electron wave vector (momentum) of two different states and  $\mathbf{r}_m$  is the coordinate of  $m$ 'th atom.

$$S(|\tilde{q}|) = \sum_m |C_{1m}(k_1)|^2 |C_{2m}(k_2)|^2 + \sum_{m,m', m \neq m'} C_{1m}(k_1) C_{2m}^*(k_2) C_{2m'}^*(k_2) C_{1m'}(k_1) e^{-i\tilde{q} \cdot (\mathbf{r}_{m'} - \mathbf{r}_m)} \quad (4.63)$$

It is assumed that there is no overlap between the atomic orbitals of two neighboring unit cells i.e. the orbitals which belong to the same atom can have nonzero overlapping (interaction). The coefficients,  $C_{1m}$ , are the elements of the nanowire Eigen state ( $N_{\text{orbit}} \times 1$  vector) at  $k_1$  and as explained before they contain 10 numbers corresponding to orbitals of Si atom with index ( $m$ ). In this work a different method is used to implement  $S(|\tilde{q}|)$  which is simpler than equation 4.61 (which is used in [148]). In Appendix D it is shown that both methods return the same value regardless of apparent differences.

Inserting equation 4.63 in equation 4.62 and using the result in equation 4.57 yields:

$$W_{k_z} = \frac{V}{(2\pi)^3} \cdot \frac{2\pi}{\hbar} \iiint |\tilde{q}|^2 \frac{D^2 \hbar}{2\rho V \omega(\tilde{q})} B_{\pm}(|\tilde{q}|) \cdot |S(|\tilde{q}|)|^2 \times \delta(E(k'_z) - E(k_z) \pm \hbar\omega(\tilde{q})) \cdot \delta_{k_z, k'_z \pm q_z} \cdot q_t dq_t d\phi dq_z \quad (4.64)$$



Using the linear dispersion of LA phonon we may write:

$$W_{k_z} = \frac{D^2}{8\pi^2 \rho} \iiint \frac{q_t^2 + q_z^2}{v_s \sqrt{q_t^2 + q_z^2}} B_{\pm}(|\tilde{\mathbf{q}}|) \cdot |S(|\tilde{\mathbf{q}}|)|^2 \cdot \delta(E(k'_z) - E(k_z) \pm \hbar\omega(\tilde{\mathbf{q}})) \cdot \delta_{k_z, k'_z \pm q_z} \cdot q_t dq_t d\varphi dq_z \quad (4.65)$$

Further simplification of equation 4.65 results:

$$W_{k_z} = \frac{D^2}{8\pi^2 \rho v_s} \iiint q_t \sqrt{q_t^2 + q_z^2} B_{\pm}(|\tilde{\mathbf{q}}|) \cdot |S(q_t, q_z, \varphi)|^2 \times \delta(E(k'_z) - E(k_z) \pm \hbar\omega(\tilde{\mathbf{q}})) \cdot \delta_{k_z, k'_z \pm q_z} \cdot dq_t d\varphi dq_z \quad (4.66)$$

Since  $|S(q_t, q_z, \varphi)|^2$  is the only term which depends on  $\varphi$ , therefore the integration over  $\varphi$  can be replaced by  $\Phi(q_t, q_z)$  which is  $\Phi(q_t, q_z) = \int_0^{2\pi} |S(q_t, q_z, \varphi)|^2 d\varphi$ .

$$W_{k_z} = \frac{D^2}{8\pi^2 \rho v_s} \iint q_t \sqrt{q_t^2 + q_z^2} B_{\pm}(|\tilde{\mathbf{q}}|) \cdot \Phi(q_t, q_z) \times \delta(E(k'_z) - E(k_z) \pm \hbar\omega(\tilde{\mathbf{q}})) \cdot \delta_{k_z, k'_z \pm q_z} \cdot dq_t dq_z \quad (4.67)$$

The precise calculation of scattering rate mandates large number of points in  $[0, 2\pi]$  interval ( $N_{k_z} > 1000$ ). Now the Dirac delta function can be manipulated as:

$$\begin{aligned} \delta(E(k'_z) - E(k_z) \pm \hbar\omega(\tilde{\mathbf{q}})) &= \delta(E(k'_z) - E(k_z) \pm \hbar v_s |\tilde{\mathbf{q}}|) \\ &= \delta\left(\hbar v_s \left(\frac{E(k'_z) - E(k_z)}{\hbar v_s} \pm |\tilde{\mathbf{q}}|\right)\right) = \frac{1}{\hbar v_s} \delta\left(\frac{E(k'_z) - E(k_z)}{\hbar v_s} \pm |\tilde{\mathbf{q}}|\right) \end{aligned} \quad (4.68)$$

where we have used  $\delta(ax) = \delta(x)/a$ . Replacing  $|\tilde{\mathbf{q}}|$  with  $\sqrt{q_t^2 + q_z^2}$  and using Krönecker's delta which imposes  $q_z = k'_z - k_z$  i.e.,

$$E(k'_z) - E(k_z) = E(k_z \pm q_z) - E(k_z) = \Delta E_{kk'} \quad (4.69)$$

we get,

$$W_{k_z} = \frac{D^2}{8\pi^2 \rho v_s} \frac{1}{\hbar v_s} \iint q_t \sqrt{q_t^2 + q_z^2} \cdot B_{\pm}(|\tilde{\mathbf{q}}|) \cdot \Phi(q_t, q_z) \cdot \delta\left(\frac{\Delta E_{uv}}{\hbar v_s} \pm \sqrt{q_t^2 + q_z^2}\right) dq_t dq_z \quad (4.70)$$

The integration over  $q_t$  can be simplified more using  $\delta(f(x)) = \frac{1}{|f'(x_0)|} \delta(x_0)$ , where  $x_0$  is the single root of the function  $f(x)$  found by  $f(x)=0$ .

$$|\tilde{q}| = \sqrt{q_t^2 + q_z^2} = \pm \frac{\Delta E_{kk'}}{\hbar v_s} \rightarrow q_t = + \sqrt{\left(\frac{\Delta E_{kk'}}{\hbar v_s}\right)^2 - q_z^2} \quad (\text{Since } q_t > 0) \quad (4.71)$$

Equation 4.70 can be simplified further:

$$W_{k_z} = \frac{D^2}{8\pi^2 \rho \hbar v_s^2} \iint q_t |\tilde{q}| B_{\pm}(|\tilde{q}|) \cdot \Phi(q_t, q_z) \cdot \delta\left(\frac{\Delta E_{kk'}}{\hbar v_s} \pm |\tilde{q}|\right) dq_t dq_z \quad (4.72)$$

Recalling that  $B_{\pm}(|\tilde{q}|)$  is only a function of  $|\tilde{q}|$ . Using equation 4.71 a relation between  $dq_t$  and  $d|\tilde{q}|$  can be found as follows:

$$|\tilde{q}| = \sqrt{q_t^2 + q_z^2} \rightarrow d|\tilde{q}| = 2q_t \cdot \frac{dq_t}{2\sqrt{q_t^2 + q_z^2}} = \frac{q_t dq_t}{|\tilde{q}|} \rightarrow q_t dq_t = |\tilde{q}| d|\tilde{q}| \quad (4.73)$$

Replacing  $q_t dq_t$  according to equation 4.74 and using the sifting property of Dirac's delta function, equation 4.72 can be reduced to:

$$W_{k_z} = \frac{D^2}{8\pi^2 \rho \hbar v_s^2} \int \left(\pm \frac{\Delta E_{kk'}}{\hbar v_s}\right)^2 \left(B_{\pm}\left(\left|\pm \frac{\Delta E_{kk'}}{\hbar v_s}\right|\right)\right) \Phi\left(q_t = \sqrt{\left(\frac{\Delta E_{kk'}}{\hbar v_s}\right)^2 - q_z^2}, q_z\right) dq_z =$$

$$\frac{D^2}{8\pi^2 \rho \hbar^3 v_s^4} \int \Delta E_{kk'}^2 \left(B_{\pm}\left(\left|\pm \frac{\Delta E_{kk'}}{\hbar v_s}\right|\right)\right) \Phi\left(q_t = \sqrt{\left(\frac{\Delta E_{kk'}}{\hbar v_s}\right)^2 - q_z^2}, q_z\right) dq_z \quad (4.74)$$

If we write the integration as a discrete summation over grid points along the 1D BZ, then rewriting equation 4.74 reveals how it is possible to single out individual rate ( $W(k_z, k'_z)$ ) between a pair of given states. Recalling that  $\Delta q_z = \Delta k'_z$  we can write:

$$W_{k_z} = \sum_{k'_z} W(k_z, k'_z) =$$

$$\sum_{k'_z} \frac{D^2}{8\pi^2 \rho \hbar^3 v_s^4} \Delta E_{kk'}^2 B_{\pm}\left(\left|\pm \frac{\Delta E_{kk'}}{\hbar v_s}\right|\right) \Phi\left(q_t = \sqrt{\left(\frac{\Delta E_{kk'}}{\hbar v_s}\right)^2 - q_z^2}, q_z\right) \Delta k'_z \quad (4.75)$$

#### 4.5.2 Electron-LO phonon scattering

Similar to equation 4.57, the total electron-LO phonon scattering rate can be written as:

$$W_{k_z} = \sum_{k'_z, \tilde{\mathbf{q}}} W(k_z, k'_z, \tilde{\mathbf{q}}) \quad (4.76)$$

The only difference is that individual scattering rate between  $k_z$  (at indirect conduction sub-band) and  $k'_z$  (at direct conduction sub-band), includes LO phonon with wave vector  $\tilde{\mathbf{q}}$  and it is given by Fermi's golden rule similar to equation 4.58:

$$W(k_z, k'_z, \tilde{\mathbf{q}}) = \frac{2\pi}{\hbar} \left| \langle U_{k_z} | H_{op} | U_{k'_z} \rangle \right|^2 \delta(E(k'_z) - E(k_z) \pm_a^e \hbar \omega_0) \quad (4.77)$$

The electron-LO optical phonon interaction Hamiltonian matrix element is given as:

$$\left| \langle i | H_{op} | f \rangle \right|^2 = \frac{|D_{op}|^2 \hbar}{2\rho V \omega_0} |S(\tilde{\mathbf{q}})|^2 B_{\pm} (N(\hbar \omega_0) + \frac{1}{2} \pm_a^e \frac{1}{2}) \delta_{k'_z, k_z \pm q_z} \quad (4.78)$$

Similar to the case of LA phonons,  $S(\tilde{\mathbf{q}})$ ,  $B_{\pm}$  and  $\omega_0$  are structure factor, Bose-Einstein factor and frequency of dispersion-less LO phonon, respectively. Following the same procedure given for acoustic phonons, the summations in equation 4.76 can be simplified as follows:

$$W_{k_z} = \frac{|D_{op}|^2}{8\pi^2 \rho \omega_0} \int_{q_z} \left( \int_0^{q_c} q_t \left[ \int_0^{2\pi} |S(q_z, q_t, \phi)|^2 d\phi \right] dq_t \right) \cdot B_{\pm} \left( N(\hbar \omega_0) + \frac{1}{2} \pm_a^e \frac{1}{2} \right) \cdot \delta(F(k'_z)) dq_z \text{ (or } dk'_z) \quad (4.79)$$

The maximum allowable value of phonon transversal component within the BZ of bulk silicon which is  $q_c$  is equal to  $1.9\pi/a$  [148]. For each value of  $q_z$  which is determined by the momentum difference of two consecutive states (i.e.  $q_z = k'_z - k_z$ ), there are infinite allowed values for transversal component of  $\mathbf{q}$  within  $[0, q_c]$  interval.  $F(k'_z)$  is the energy difference of initial and final states which is expressed as a function of  $k'_z$  i.e.  $F(k'_z) = E(k'_z) - E(k_z) \pm_a^e \hbar \omega_0$ . To further simplify the integration over  $q_z$  in equation 4.79 the following property of Dirac's delta function is used:

$$\delta(F(k'_z)) = \sum_{q_p} \frac{\delta(k'_z - q_p)}{\left| \frac{\partial F(k'_z)}{\partial q_z} \right|_{q_z=q_p}} = \sum_{q_p} \frac{\delta(k'_z - q_p)}{\left| \frac{\partial E(k'_z)}{\partial q_z} \right|_{q_z=q_p}} \quad (4.80)$$

where  $\frac{\partial F(k'_z)}{\partial k'_z} = \frac{\partial E(k'_z)}{\partial k'_z} = \frac{\partial E(k'_z)}{\partial q_z}$  and  $q_p$  are solutions of  $F(k'_z) = 0$  or in another word those final states ( $k'_z$ ) which satisfy the energy conservation of  $E(q_p) = E(k_z) \mp_a^e \hbar\omega_0$ . Inserting right hand side of equation 4.80 into equation 4.79 yields:

$$W_{k_z} = \frac{|D_{op}|^2}{8\pi^2\rho\omega_0} \int_{q_z} \int_0^{q_c} \Phi(q_t, q_z) dq_t \cdot B_{\pm} \left( N(\hbar\omega_0) + \frac{1}{2} \pm_a^e \frac{1}{2} \right) \cdot \sum_{q_p} \frac{\delta(k'_z - q_p)}{\left| \frac{\partial E(k'_z)}{\partial q_z} \right|_{q_z=q_p}} \cdot dq_z \quad (4.81)$$

where  $\Phi(q_t, q_z) = \int_0^{2\pi} |S(q_z, q_t, \phi)|^2 d\phi$ . To single out the individual scattering rate i.e.  $W(k_z, k'_z)$ , the integration over  $q_z$  is written in its discrete form and noting that  $\Delta q_z = \Delta k'_z$  we have:

$$W_{k_z} = \sum_{k'_z} W(k_z, k'_z) = \sum_{k'_z} \frac{|D_{op}|^2}{8\pi^2\rho\omega_0} \int_0^{q_c} \Phi(q_t, q_z) dq_t B_{\pm} \left( N(\hbar\omega_0) + \frac{1}{2} \pm_a^e \frac{1}{2} \right) \cdot \sum_{q_p} \frac{\delta(k'_z - q_p)}{\left| \frac{\partial E(k'_z)}{\partial q_z} \right|_{q_z=q_p}} \Delta k'_z \quad (4.82)$$

By interchanging summation over  $k'_z$  and  $q_p$  we have:

$$\begin{aligned} W_{k_z} &= \sum_{k'_z} W(k_z, k'_z) \\ &= \sum_{k_p} \frac{|D_{op}|^2}{8\pi^2\rho\omega_0} \int_0^{q_c} \Phi(q_t, q_z) dq_t B_{\pm} \left( N(\hbar\omega_0) + \frac{1}{2} \pm_a^e \frac{1}{2} \right) \frac{1}{\left| \frac{\partial E(k'_z)}{\partial q_z} \right|_{k'_z=k_p}} \\ &= \sum_{k_p} W(k_z, k_p) \quad (4.83) \end{aligned}$$

$k_p$  are those values of secondary state wave vectors ( $k'_z$ ) which satisfy the  $F(k'_z) = 0$ . Hence corresponding to each  $k_z$  (initial state) there are a few secondary states ( $k_p$ ) to which electron can scatter by absorbing or emitting a LO phonon. And the total rate is simply found by adding each individual term according to equation 4.83. Albeit the derivative of  $E(k'_z)$  can be calculated numerically, two methods are introduced in Appendix E may result in semi-analytic simpler versions of equation 4.83 in case the effective mass approximation is applicable.

### 4.5.3 Post processing of scattering data for EMC simulation

The electron-LA phonon and LO phonon scattering rates (both inter- and intra-sub band) are implemented in MATLAB according to equation 4.75 and equation 4.83, respectively.

For the purpose of EMC study of carrier population's within indirect sub band, we consider a few conduction sub bands starting from the first one. The number of required sub bands is determined by the energy distance between them. For example if the N'th conduction sub band is more than  $3kT$  (78 meV at  $T=300K$ ) above the previous N closely packed sub bands, it can be discarded and the calculation is focused on the first N sub bands. The same procedure is applied to valence sub bands as well when hole-phonon scattering events are of interest. Figure 4.9 shows the algorithm or pseudo code of saving individual electron-LA phonon scattering rates for initial states within the first sub band (*band1*). The same method can be applied to the case when initial states are in second sub band (*band2*).

```

FOR i=1:Nkz    % (Nkz : number of grid points along BZ)
    find available states within  $E_i - E_{debye} \leq E_i \leq E_i + E_{debye}$ 
    2nd-k-indices(i,:)=k'z indices
END
FOR i=1:Nkz
    read Ei,b1,  $\psi_{i,b1}$ , ki,b1
    FOR j=1:length_of(2nd_k_indices(i,:))
        read kz_idx=2nd-k-indices(i,j)
        IF kz_idx(j) ∈ band1
            save  $\psi_{j,b1}$  and Ej,b1 and kj,b1
        ELSE
            save  $\psi_{j,b2}$  and Ej,b2 and kj,b2
        END
        Calculate W(ki,b1,kj,bx)  $x \in \{b1,b2\}$  (EQ.75)
        IF Ei,b1 > Ej,bx (LA emission)
            Indiv_emit(i,j)= W
        ELSE (LA absorption)
            Indiv_absorb(i,j)= W
        END
    END
END
Grouped_abs_emit ← CALL indiv-absorb-emit-sorter
Total_scatt_rate=sum_of_columns(Grouped_abs_emit) (full EQ.75)
Plot(kzi, Total_scatt_rate)

```

Figure 4.9 Flowchart of saving individual rates for e-LA phonon scattering events.

The function “*indiv\_absorb\_emit\_sorter*” is grouping the individual emission/absorption rates and adds them together. Decision is made based on the number of  $k_j$  (secondary state indices) which determines if the secondary state belongs to *band1*(intra-sub band) or *band2* (inter sub band). Figure 4.10 shows the concept of the grouping of individual absorption and emission rates and sorting them according to inter- or intra-sub band scattering. The algorithm behind “*indiv\_absorb\_emit\_sorter*” is shown in Figure 4.11. The same algorithm of Figure 4.9 is applicable to the case of electron-LO phonon scattering (using equation 4.83) but special care is required when secondary states are saved in the first loop of Figure 4.9.

In contrast to LA phonons which have a continuum of energies from 0 to  $E_{\text{Debye}}$ , the LO phonons have all a constant energy of  $E_{\text{LO}}=63$  meV. Thus if the criteria to choose the secondary state is set to be  $E_i - 63\text{meV} \leq E_i \leq E_i + 63\text{meV}$ , there may be cases with no phonon due to coarse grid of  $k_z$  axis. On the other hand by choosing these criteria of  $E_i - 63\text{meV} \pm \text{Tol} \leq E_i \leq E_i + 63\text{meV} \pm \text{Tol}$ , it is possible to find many secondary states close to each other within the tolerance window. The function “*single k-selector*” takes care of this problem by selecting a unique index among many closely spaced indices. For example if the indices of available secondary states which are sorted in a vector are something like  $K_{\text{index}} = [17\ 18\ 19\ 25\ 33\ 34\ 35\ 90\ 171\ 172\ 173\ 174\ 175\ 233]$ , then the output must be  $K_{\text{select}} = [18\ 25\ 34\ 173\ 233]$ .

In differentiating the energy band with respect to  $k_z$  extra care is necessary to avoid the asymmetry problem since numerical differentiation of a  $N \times 1$  vector is a  $(N-1) \times 1$  vector. The scattering data were calculated at both room temperature and  $T=77\text{K}$  for an indirect bandgap nanowire. Results of EMC simulation and effects of temperature on the population of carriers will be discussed in the next chapter.

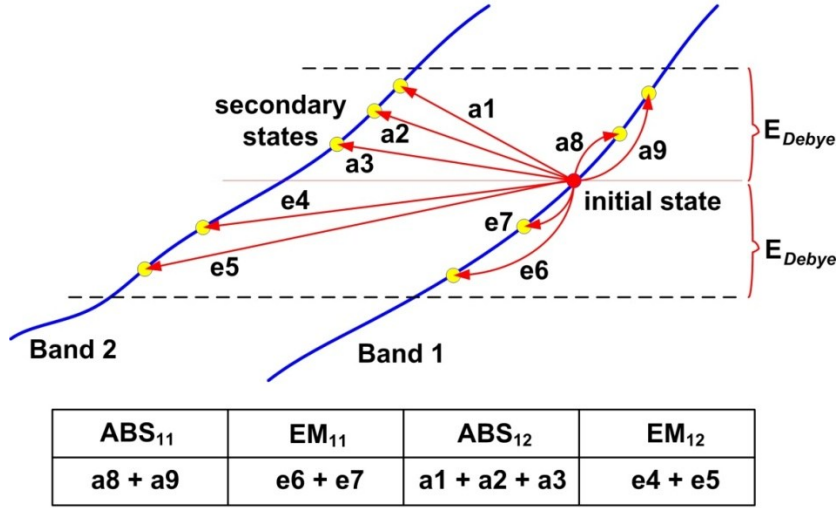


Figure 4.10 Grouping and sorting individual LA phonon absorption (a) and emission (e) rates according to intra- or inter-sub band nature of the event. ABS and EM represent absorption and emission of phonons, respectively. A subscript like 12 means scattering from band1 to band2.

```

FOR i=1:Nkz (each initial state in band1)
  AB=indiv_abs(i,:); EM=indiv_emit(i,:);
  2nd_k_index=2nd_k_indices(i,:);
END
FOR each pair of (AB,EM) vectors DO
  Make AB and EM to be the same size
  FOR m=1:size(2nd_k_index)
    IF 2nd_k_index ∈ band1
      Z(m)=1
    ELSE
      Z(m)=2
    END
  END
  ABS11=ABS12=0; EM11=EM12=0; % initializing
  FOR m=1:size(AB)
    IF Z(m)=1
      ABS11=ABS11+AB(m);
    ELSE
      ABS12=ABS12+AB(m);
    END
  END
  REPEAT the previous loop for EM
END
Grouped_abs_emit=[ ABS11, EM11, ABS12, EM12]
GO to line#1 and REPEAT the same for (each initial state in band2)

```

Figure 4.11 Algorithm of grouping and sorting individual LA/LO phonon absorption and emission rates.

# Chapter 5

## Spontaneous Emission Time in Silicon Nanowires: *Results*

In Chapter 4 the computational methods and algorithms for investigating the strain effects on the spontaneous emission in SiNWs were presented. The main results were published in Scientific Reports as “*Shiri, D., Verma, A., Selvakumar, C.R. & Anantram, M.P. Reversible Modulation of Spontaneous Emission by Strain in Silicon Nanowires. Sci. Rep. 2, 461; DOI:10.1038/srep00461 (2012)*”. In this chapter the main results are reprinted with permission from the aforementioned article followed by more discussions regarding the role of Local Field Effects (LFE) on spontaneous emission time, strain induced sub band exchange, semi-analytic approximation of 2<sup>nd</sup> order spontaneous emission time, justification of using TB in the band structure calculation and many-body (exciton) effects.

### 5.1 Outline

*Our main finding is that a one to two orders of magnitude change in spontaneous emission time occurs due to two distinct mechanisms: (A) Change in wave function symmetry, where within the direct bandgap regime, strain changes the symmetry of wave functions, which in turn leads to a large change of optical dipole matrix element. (B) Direct to indirect bandgap transition which makes the spontaneous photon emission to be of a slow second order process mediated by phonons. This feature uniquely occurs in silicon nanowires while in bulk silicon there is no change of optical properties under any reasonable amount of strain. These results promise new applications of silicon nanowires as optoelectronic devices e.g. strain-modulated light emitters or absorbers. Our results are verifiable using existing experimental techniques of applying strain to nanowires.*

### 5.2 Introduction

Potential advantages of silicon nanowires (SiNWs), such as quantum confinement, large surface-to-volume ratio, adjustable bandgap, sensitivity of electronic properties to surface ligands and mechanical excitation and compatibility with mainstream silicon technology have resulted in a flurry of experimental and theoretical investigations of these nanostructures. Over the years SiNWs have been explored for use in transistors [1][2], logic circuits [3] and memory [4], quantum computing [5], chemical [6] and biological [7] sensors, piezo-resistive sensor [8], nano mechanical resonator [9] and thermoelectric converters [10][11]. We are also witnessing the utilization of SiNWs in optoelectronic applications, such as in solar cells [12][13], photodetectors [15][14], and avalanche



photodiodes [16][17]. The basic properties and applications of Si nanowires are discussed further in references [23][24]. Efficient light emission in SiNWs requires direct bandgap and symmetry allowed optical transition between conduction and valence states. In other word to have a nonzero optical transition matrix element which is defined as

$$\langle \psi_c | \mathbf{r} | \psi_v \rangle = \int \psi_c^*(\mathbf{r}) \cdot \mathbf{r} \cdot \psi_v(\mathbf{r}) d\mathbf{r} \quad (5.1)$$

the integrand should have an even symmetry.  $\Psi_c$ ,  $\Psi_v$  and  $\mathbf{r}$  represent conduction band state (wave function), valence band state and position operator, respectively. In bulk silicon and large diameter SiNWs the conduction band minimum and valence band maximum have different values of momentum within the Brillouin Zone (BZ) of the crystal. Spontaneous emission of a photon which arises from electron-hole recombination is a momentum conserving process. As photons cannot provide the momentum difference in these materials, a phonon absorption/emission is necessary, making it a weaker second order process. Vital to realizing SiNW-based light emitting devices, narrow diameter [110] and [100] SiNWs are direct bandgap. This arises from folding of four degenerate indirect X conduction valleys of bulk silicon into the BZ center ( $\Gamma$  point) due to confinement in transverse directions [150]. In addition to direct bandgap, the possibility of adjusting the bandgap with mechanical strain provides a new degree of freedom for SiNWs. Computational studies using both tight binding [151][117][152] and Density Functional Theory (DFT) [153][118][111][134] have shown that axial strain changes the bandgap of narrow SiNWs. Additionally it causes direct to indirect bandgap conversion.

On the experimental side, recent research points to promising directions for applications involving strain in nano-structures. For example, strain that is generated by an acoustic wave can modulate the energy levels of an artificial atom (quantum dot) and initiate lasing inside a Fabry-Perot device [103]. Similarly, the energy levels of a phosphorous atom embedded in a SiGe super lattice can be modulated by acoustic waves travelling back and forth in the super lattice [154]. There is evidence of modulation of threshold voltage in a transistor by transverse as well as longitudinal strains applied to the SiNW-based channel [99]. Carrier mobility enhancement due to residual tensile strain from the oxide layer in Gate-All-Around (GAA) 5nm thick SiNWs have been reported [2]. He and Yang [8] have reported a large diameter ( $d$ ) SiNW ( $d > 50\text{nm}$ ) bridge in which the piezo-resistivity is varied by deformation of the substrate. Deforming an elastomeric substrate can apply  $\pm 3\%$  strain to the buckled SiNWs grown on the substrate [97]. Strain induced by the cladding of SiNWs causes a blue shift in the UV Photoluminescence (PL) spectrum [59]. Similarly the observed red shift in the PL spectrum of 2-9nm thick SiNWs is also attributed to the radial strain induced by oxide cladding [37]. *[More examples were presented in the first chapter of the thesis].*

Motivated by the aforementioned experiments, the scope of our work is to address this question: Is it possible to modulate the spontaneous emission time of electrons in SiNWs using axial strain? We demonstrate for the first time that applying strain can change the

spontaneous emission time by more than one order of magnitude. The underlying reasons are a change in the symmetry of electronic wave functions and a change in the nature of the bandgap (direct or indirect), with strain. Qualitatively we might expect that converting direct bandgap to indirect bandgap hinders light emission from a SiNW because the emission of a photon is now a slow second order phonon-mediated process. We use DFT and TB methods to quantify the change of spontaneous emission time (see **Methods** section or Chapter 4 of the thesis).

### 5.3 Results

The cross section and electronic structure of an unstrained 1.7nm [110] SiNW are shown in Figure 5.1a-b. All SiNWs in this work have direct bandgap at 0% strain (Figure 5.1b), where the bandgap is observed to be inversely proportional to the SiNW diameter ( $d$ ). For example the bandgap of 1.26nm, 1.7nm, 2.3nm and 3.1nm diameter SiNWs are 2.24eV, 1.74eV, 1.58eV and 1.477eV, respectively. The bandgap values are calculated using the tight binding framework after the atomic structure of the nanowires is relaxed by DFT. This effect of SiNW diameter on the bandgap agrees with experimental results using scanning tunneling spectroscopy (STS) [31] and the observed blue shift in PL spectrum of small SiNWs [59]. It is also observed that by increasing the diameter of SiNWs the difference between direct and indirect conduction band minima (band offset or  $\Delta E_{\text{cmin}}$  in Figure 5.1b) decreases. This aspect is important for this work, since it implies a corresponding decrease in the value of compressive strain (threshold strain) required to change the bandgap from direct to indirect [151][117]. The values of the threshold strain for 1.7nm, 2.3nm and 3.1nm [110] SiNWs are -5%, -4% and -3%, respectively.

#### 5.3.1 Direct bandgap regime

If the conduction and valence states in the center of the 1<sup>st</sup> BZ are called initial ( $i$ ) and final ( $f$ ) states, respectively, the spontaneous emission rate or  $1/\tau_{\text{spon}}$  can be written as

$$\frac{1}{\tau_{\text{spon}}} = \frac{2e^2 n_r}{3m^2 \epsilon_0 c^3 \hbar} \omega_{if} |\langle \psi_i | \hat{\mathbf{e}} \cdot \mathbf{P} | \psi_f \rangle|^2 \quad (5.2)$$

where  $m$ ,  $e$ ,  $\epsilon_0$ ,  $c$ ,  $\hbar$  are free mass of electron, magnitude of electronic charge, free space dielectric permittivity, speed of light in vacuum, and Planck's constant, respectively.  $n_r$  is the refractive index of SiNW, which is assumed to have the same value as of bulk silicon ( $n_r=3.44$ ) within the optical spectrum of interest. For all nanowires in this work, the bandgap lies in the 1-2eV range, and the maximum change of bandgap due to strain can be as large as 500 meV (in a strain window of  $\pm 5\%$ ). Therefore assuming a constant value for the refractive index causes up to a 14% change in our calculated results (which is a small effect as we are discussing more than an order of magnitude change in  $\tau_{\text{spon}}$ ). The quantity of  $\omega_{if}$  is the frequency of the emitted photon, which is defined as  $\Delta E_{if}/\hbar$ . Here  $\Delta E_{if}$  is the energy

difference between initial ( $i$ ) and final ( $f$ ) states at the BZ center, which is the bandgap  $E_g$ .  $P_{if}^2 = |\langle \Psi_i | \hat{\mathbf{e}} \cdot \mathbf{P} | \Psi_f \rangle|^2$  is the matrix element of the momentum operator  $\mathbf{P}$ , between initial (conduction) and final (valence) states.  $\Psi_i$  and  $\Psi_f$  are the wave functions of the initial (conduction) and final (valence) states.  $\hat{\mathbf{e}}$  is the direction of polarization. The value of momentum matrix element normalized to electronic mass,  $P_{cv}^2/2m$ , between conduction ( $\Psi_i$ ) and valence ( $\Psi_f$ ) bands along the BZ is plotted for an unstrained 1.7nm diameter [110] SiNW (Figure 5.1c).

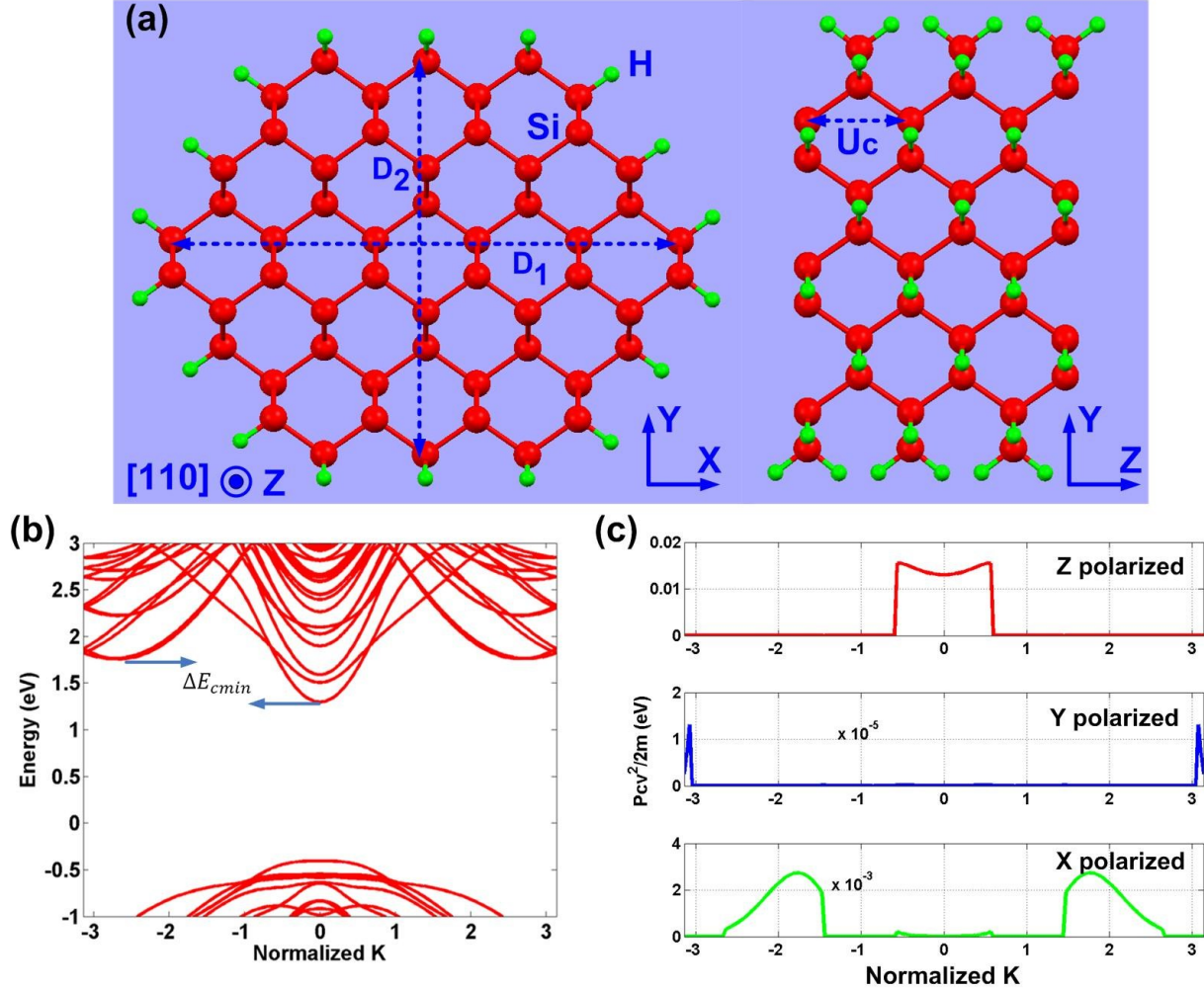


Figure 5.1 (a: left) Cross section of a [110] SiNW with the diameter ( $d$ ) of 1.7nm in xy plane. Diameter ( $d$ ) is defined as average of large ( $D1$ ) and small ( $D2$ ) diameters. Right panel shows the side view of two unit cells along the length of nanowire ( $z$ ) with unit cell length of  $U_c$ . Dark and bright atoms represent Si and H atoms, respectively. (b) Electronic structure of the 1.7nm diameter [110] SiNW, which shows direct bandgap i.e. conduction/valence band minimum/maximum reside on the BZ center ( $K=0$ ). Band offset,  $\Delta E_{cmin}$ , is smaller for larger diameter nanowires. (c) Normalized momentum matrix element,  $P_{cv}^2/2m$  (in eV) between conduction and valence band along BZ. Red, Blue and green correspond to Z, Y and X polarizations of emitted photon.

Corresponding to each direction of photon polarization (x, y and z), there are 3 different values for  $P_{cv}^2$ , which in turn leads to three different values for  $\tau_{\text{spont}}$  according to equation (5.2). As Figure 5.1c suggests, the momentum matrix element corresponding to z-polarized photons is significantly larger than the corresponding amounts for x- and y- polarized cases at BZ center. This difference manifests itself as a large spontaneous emission rate for z-polarized photons. This implies that the emitted light from the SiNW is mostly polarized along the length of the nanowire. In other words, if the average rate of spontaneous emission is defined as  $\tau_{\text{avg}}^{-1} = \tau_x^{-1} + \tau_y^{-1} + \tau_z^{-1}$ , then the degree of anisotropy or  $\tau_{\text{avg}}/\tau_z$  has a value close to unity. Our approach of neglecting dielectric mismatch is justified because local field effects do not cause a significant change in the dielectric function of nanowire for z-polarized light [155][156]. *This issue is further discussed in sub section 5.6.1.* The squared momentum matrix element in equation (5.2) is inversely proportional to the area of the nanowire or  $d^2$ , which can be explained using the particle in a box model [45][46]. Combination of this effect and the bandgap change with diameter results in the direct proportionality of spontaneous emission time to the cross sectional area. For 1.7nm, 2.3nm and 3.1nm diameter [110] SiNWs, the value of  $\tau_{\text{avg}}$  is calculated to be  $1.47 \times 10^{-7}\text{s}$ ,  $2.3 \times 10^{-7}\text{s}$ , and  $4 \times 10^{-7}\text{s}$ , respectively. For the SiNWs investigated in this work, the bandgap remains direct for most of the strain values in the  $\pm 5\%$  range. For 1.7nm, 2.3nm and 3.1nm [110] SiNWs the bandgap becomes indirect once the compressive strain reaches -5%, -4% and -3%, respectively [151][117].

As long as the bandgap is direct, photon emission is a first order process and its rate is governed by equation (5.2). The average spontaneous emission times for [110] axially aligned SiNWs in this study are tabulated in Table 5.1. As can be seen in Table 5.1, compressive strain leads to an increase of spontaneous emission time by one to two orders of magnitude. This is due to the movement of sub bands in the compressive strain regime. As pictured in the graphics of Figure 5.2a, the rise of the second valence sub band (V2) due to its anti-bonding nature is more dominant than the rate with which the first valence sub band (V1) rises or the conduction sub band (C1) falls. As a result, V2 determines the new highest valence band. The aforementioned mechanism can be further understood by looking at Figure 5.2b that shows the normalized probability density ( $|\Psi|^2$ ) of conduction and valence states at BZ center. Comparing the valence/conduction bands (VB/CB) at 0% and -2% strain values shows that the dominant change is due to the valence band symmetry change induced by compressive strain (e.g. -2% ). Left panel of Figure 5.2b shows that the newly raised valence sub band (V2) has different wave function symmetry as opposed to the centrosymmetric nature of valence band V1 at 0% and +2% strains. Therefore the matrix element,  $\langle \Psi_c | \mathbf{r} | \Psi_v \rangle$ , changes accordingly and modulates the spontaneous emission time (rate) through equation (2). Comparing wave function symmetries of valence and conduction bands at strain values of 0% and +2%, as in Figure 5.2b (center and right panel), further illustrates why the spontaneous emission time is almost unchanged within this tensile strain regime. Further

evidence of strain effect on the wave function symmetry (and momentum matrix element) is shown in sub section 5.6.2 where it is explained how the sub band exchange will alter the value of matrix element and hence the spontaneous emission time through equation (5.2).

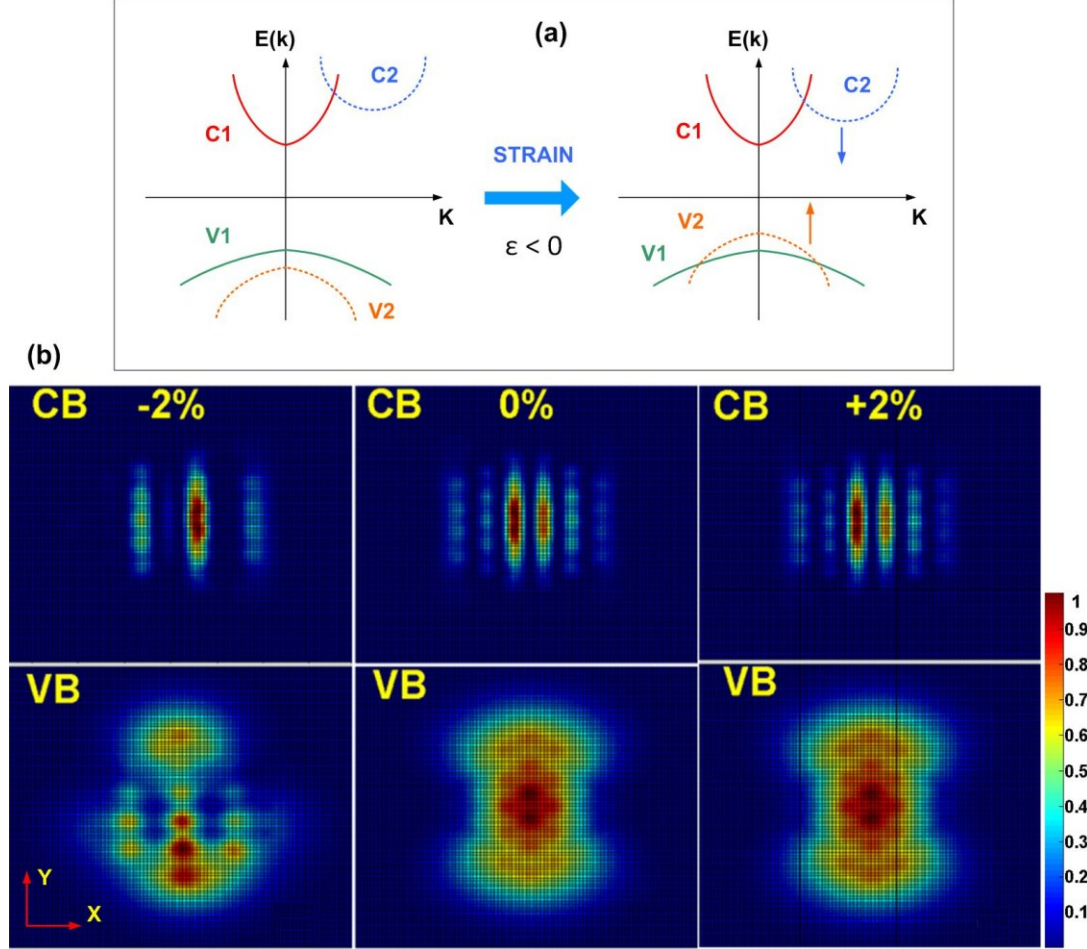


Figure 5.2 (a) Effect of compressive strain on second valence sub band (V2) which results in the change of wave function symmetry. From left to right, it can be seen that compressive strain raises the energy of V2 faster than it lowers the energy of C2. (b) Normal ized squared value of wave function ( $|\Psi|^2$ ) in the cross sectional plane of a 1.7nm [110] SiNW. From left to right strain values are -2%, 0% and +2%, respectively. Valence and conduction band states (VB and CB) are at BZ center. As can be seen in the left panel (for -2% strain) the change of symmetry is more pronounced for valence sub band.

Average spontaneous emission time, $\tau_{\text{avg}}$ (s)			
Strain (%)	1.7 nm	2.3 nm	3.1 nm
+2%	$1.49 \times 10^{-7}$ s	$2.50 \times 10^{-7}$ s	$3.77 \times 10^{-7}$ s
0%	$1.47 \times 10^{-7}$ s	$2.30 \times 10^{-7}$ s	$4.00 \times 10^{-7}$ s
-2%	$2.32 \times 10^{-6}$ s	$3.12 \times 10^{-6}$ s	$6.32 \times 10^{-5}$ s

Table 5.1 Average spontaneous emission time,  $\tau_{\text{avg}}$  (s) vs. diameter (nm) of [110] SiNWs. Although all nanowires in these strain values have direct bandgap, the change of  $\tau_{\text{avg}}$  with compressive strain is mainly due to valence sub band exchange.

### 5.3.2 Direct to indirect bandgap conversion

The second kind of strain induced change of spontaneous emission arises from a direct to an indirect bandgap conversion. Figure 5.3a elucidates this mechanism, in which, a compressive strain lowers the indirect conduction sub band C2, resulting in an indirect bandgap. Figure 5.3b-c shows the band structure of a 3.1nm SiNW at 0% and -5% strains, respectively. As can be seen in Figure 5.3c the heavy (H) or high effective mass sub-band (C2) has a lower energy than the light (L) or low effective mass direct conduction sub band (C1). The energy difference between two conduction band minima or band offset ( $\Delta\Omega$ ) [Figure 5.3a (right panel)] matters in determining the order of phonon-mediated spontaneous emission process. As mentioned before,  $\Delta E_{\text{cmin}}$  (Figure 5.1b) is inversely proportional to the nanowire diameter. As a result, a large diameter SiNW has a larger value of  $\Delta\Omega$ . For 1.7nm, 2.3nm and 3.1nm diameter [110] SiNWs,  $\Delta\Omega$  is 21meV, 56meV and 80meV, respectively at -5% strain. When  $\Delta\Omega$  is less than the Debye energy of LA phonons ( $E_{\text{Debye}} = 54$  meV) many secondary states in direct conduction sub band are available to which an electron can scatter from indirect sub band by absorbing a LA phonon. Alternatively, when  $\Delta\Omega$  is less than the maximum energy of LO phonons,  $E_{\text{LO}} = 63$  meV, a few secondary states in direct conduction sub band can be found to which an electron can scatter from indirect sub band by absorbing a LO phonon. This implies that if the secondary state within the direct conduction sub band C1 is not at the BZ center, the only possible 1<sup>st</sup> order transition is due to LA phonon absorption. Otherwise both LA and LO phonon absorption processes will contribute in the 1<sup>st</sup> order inter-sub band scattering event. The process of finding secondary states can be understood by recalling that LO and LA phonons are modelled as dispersion-less and a linear dispersion around BZ center, respectively [147].



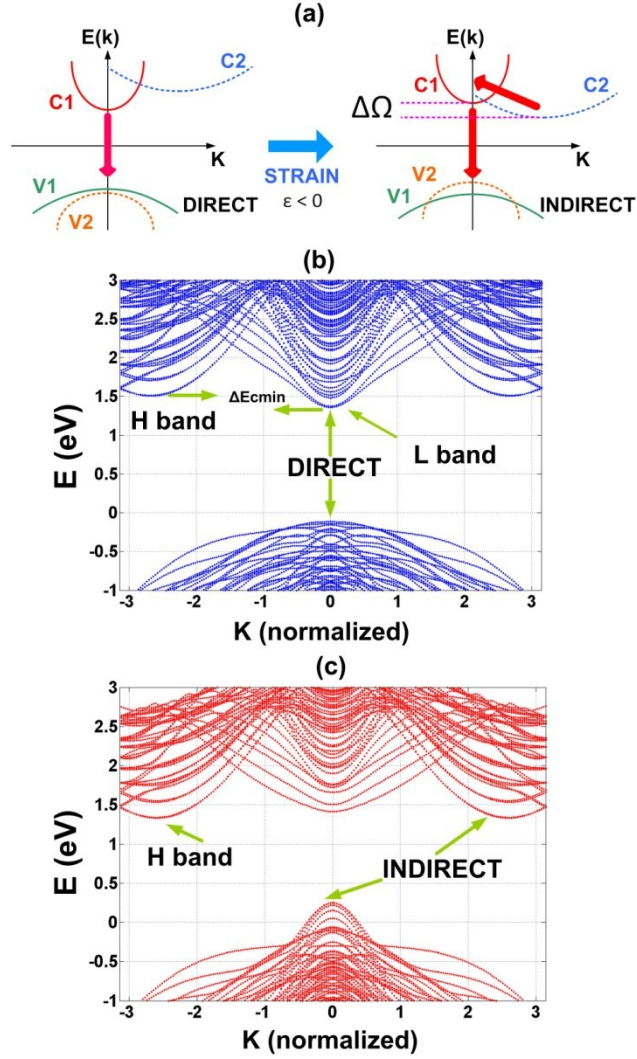


Figure 5.3 (a) Mechanism of bandgap conversion in response to compressive strain is due to lowering of C2 sub band. Electronic structure of (b) unstrained and (c) -5% strained 3.1nm [110] SiNW. The indirect conduction band minimum of strained case (c) is lower than the direct conduction band minimum by  $\Delta\Omega=80$  meV. This quantity determines the order of phonon mediated process for light emission.

#### 5.3.2.1 First order transition

Within the regime of small  $\Delta\Omega$ , the spontaneous emission is modeled as two consecutive 1<sup>st</sup> order processes as shown in Figure 5.4a (top panel), the first of which is an electron-phonon scattering event from indirect sub band minimum to the direct sub band minimum (via emission or absorption of a phonon), while the second is a direct transition from conduction

band to valence sub band maximum via emission of a photon. With this model, the total spontaneous emission rate is limited by the slower of the two processes, which is the optical transition. Figure 5.4b shows the inter-sub band electron-phonon scattering rates for electrons making transition between the indirect sub band minimum at  $K_z = 0.8\pi/U_c$  to the direct sub band minimum at  $K_z = 0$ , where  $U_c$  is the nanowire unit cell length. One can observe that the scattering rate due to LO phonons is 2 orders of magnitude higher than the scattering due to LA phonons. Therefore when the nanowire bandgap is indirect with  $\Delta\Omega < E_{\text{Debye}} = 54 \text{ meV}$  or  $\Delta\Omega < E_{\text{LO}} = 63 \text{ meV}$ ,  $\tau_{\text{spon}}$  is determined by the slower (optical transition) process. Recalling Figure 5.4a (top panel) and the rates given in Figure 5.4b,  $\tau_{\text{spon}}$  is calculated by equation (5.2). This results in spontaneous emission times that are comparable with that of direct bandgap nanowires i.e. in the  $10^{-5}$ - $10^{-7}$  second range, depending on the value of  $P_{\text{cv}}^2$ .

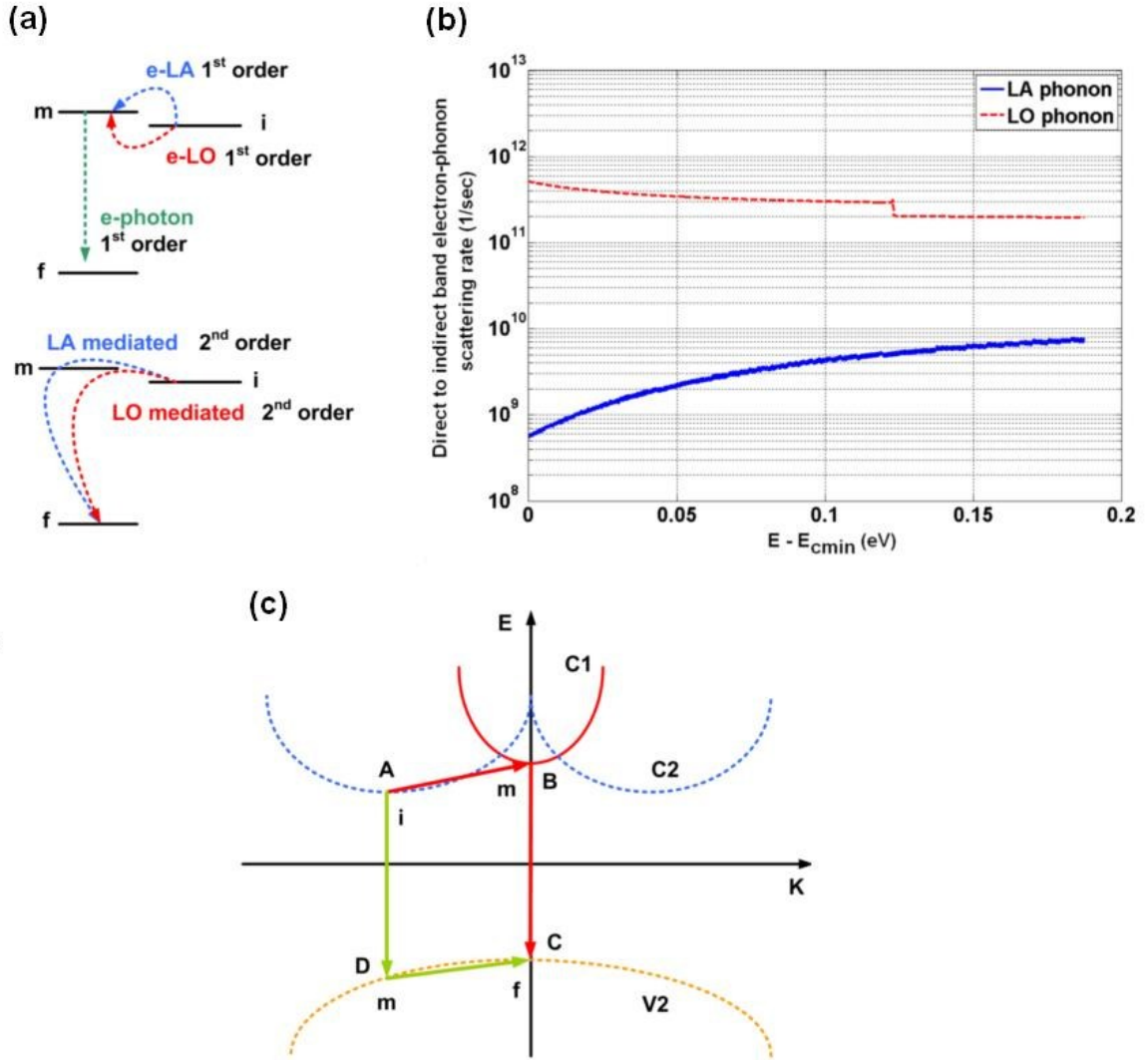




Figure 5.4 (a) Top: Two serial 1st order processes which model the light emission calculation in indirect bandgap nanowires with  $\Delta\Omega < E_{LO/LA}$ . Bottom: A model based on a 2nd order process presented for calculation of light emission in indirect nanowires with  $\Delta\Omega > E_{LO/LA}$ . (b) Inter-sub band (direct to indirect) electron-phonon scattering rate ( $s^{-1}$ ) versus the energy starting from the bottom of direct conduction band ( $E-E_{cmin}$ ). As can be seen scattering times for electron-LO phonon and electron-LA phonon scattering events are in the order of 1ps and 100ps, respectively. (c) Possible second order transitions from indirect conduction sub band to the valence band maximum. As it is discussed in the **Results** section the  $A \rightarrow D \rightarrow C$  event is less probable than  $A \rightarrow B \rightarrow C$ . Initial, intermediate and final states are represented by  $i$ ,  $m$  and  $f$ , respectively.

### 5.3.2.2 Second order transition

For indirect bandgap SiNWs in which  $\Delta\Omega > E_{Debye}/E_{LO}$  (e.g. 3.1nm diameter [110] SiNW at -5% strain), the spontaneous emission is possible through two second order processes that correspond to LA and LO phonons [Figure 5.4a (bottom panel)]. The rate of both processes is given by second order perturbation theory. Equation (5.3) shows the spontaneous emission lifetime of an electron in indirect conduction sub band. The recombination of this electron with a hole residing at BZ center is possible through virtual transitions to intermediate states  $\Psi_m$  in the first conduction band (via phonon emission and absorption)

$$\frac{1}{\tau_{spon}} = \frac{2\pi}{\hbar} \sum_{K_f} \sum_{\mathbf{k}', \sigma} \sum_{\mathbf{q}, \lambda} \left| \sum_{K_m} \frac{\langle \psi_f | H_{e-R} | \psi_m \rangle \langle \psi_m | H_{e-P} | \psi_i \rangle}{E_i - E_m} \right|^2 \delta(E_i - E_f) \delta_{\mathbf{k}_i - \mathbf{k}_m, \pm \mathbf{q}} F(E_f) \quad (5.3)$$

Here,  $H_{e-R}$  and  $H_{e-P}$  are electron-photon (radiation) and electron-phonon interaction Hamiltonians, respectively. The innermost summation is over all intermediate states. Indices  $i$ ,  $m$  and  $f$  correspond to initial (indirect conduction band minimum), intermediate (within the 1<sup>st</sup> conduction band) and final (within the last valence band) states.  $\Psi_i$ ,  $\Psi_m$  and  $\Psi_f$  are Bloch states of initial ( $i$ ), intermediate ( $m$ ) and final ( $f$ ) states, respectively. As shown in Figure 5.4c, this transition is possible through two processes of  $A \rightarrow B \rightarrow C$  and  $A \rightarrow D \rightarrow C$ . The process of  $A \rightarrow D \rightarrow C$  is not included in equation (3) since for  $D \rightarrow C$  transition, the denominator of the inner most terms i.e.  $E_i - E_m$  is large ( $> 3\text{eV}$ ). Hence the contribution of  $A \rightarrow D \rightarrow C$  processes is negligible. Two outer summations are performed over phonon wave vector and branches ( $\mathbf{q}$ ,  $\lambda$ ) and photon wave-vector and polarizations ( $\mathbf{k}'$ ,  $\sigma$ ), respectively. The outermost summation is over all final states within the valence band, which are weighted by Fermi-Dirac occupancy written as  $F(E_f)$ . Dirac and Kröneckner delta functions impose energy and momentum conservation, respectively. After converting summations to integration and calculating the interaction Hamiltonian matrix elements [148][157], the following equation results for spontaneous emission time including LA phonon

$$\frac{1}{\tau_{spont}} = \frac{e^2 D^2 n_r}{\epsilon_0 \rho c^3 v_s \hbar} \frac{1}{48\pi^4} \sum \omega_{fm}^2 |\langle \psi_f | \hat{r} | \psi_m \rangle|^2 F(k_f) \cdot Ph_{LA}(k_f, k_i) \Delta k_f \quad (5.4)$$

$D$ ,  $\rho$  and  $v_s$  represent electron deformation potential ( $D= 9.5$  eV), mass density ( $\rho= 2329$  Kg/m<sup>3</sup>) and velocity of sound in silicon ( $9.01 \times 10^5$  cm/sec), respectively [148][157].  $\omega_{fm} = \Delta E_{fm}/\hbar$ , where  $\Delta E_{fm}$  is energy difference between final and intermediate state.  $Ph_{LA}(k_f, k_i)$  contains integration over all possible transverse phonon wave vectors ( $q_t$ ), Bose-Einstein occupancy factors and matrix element of terms like  $e^{iq \cdot r}$  i.e.  $\langle \Psi_m | e^{iq \cdot r} | \Psi_i \rangle$  [see equation 4.49 in section 4.4 of Chapter 4 for more information]. The electron wave vectors at initial (final) states are represented by  $k_i$  ( $k_f$ ).  $\Delta k_f$  is  $k_z$ -space grid element (resolution) along the BZ of the nanowire. This equation is evaluated numerically. The corresponding equation for spontaneous emission time by including LO phonon is given by

$$\frac{1}{\tau_{spont}} = \frac{e^2 |D_{op}|^2 n_r}{\epsilon_0 \rho c^3 \hbar \omega_0} \cdot \frac{1}{48\pi^4} \sum \omega_{fm}^2 |\langle \psi_f | \hat{r} | \psi_m \rangle|^2 F(k_f) \frac{E_c(k_i) - E_v(k_f) \pm \hbar \omega_0}{(E_c(k_f) - E_c(k_i) \pm \hbar \omega_0)^2} Ph_{LO}(k_f) \Delta k_f \quad (5.5)$$

where a dispersion-less optical phonon energy of  $\hbar \omega_0 = 63$  meV has been assumed.  $Ph_{LO}(k_f)$  contains integration over all possible LO phonon wave vectors ( $q_t$ ), Bose-Einstein occupancy factors and matrix element of terms like  $e^{iq \cdot r}$  i.e.  $\langle \Psi_m | e^{iq \cdot r} | \Psi_i \rangle$  [see Chapter 4, section 4.4 and equation 4.56 for more information].  $D_{op}$  is the electron deformation potential for LO phonon ( $D_{op} = 11 \times 10^8$  eV/cm) [148][157].  $E_c$  and  $E_v$  represent the energy of conduction and valence states at a given wave vector ( $k_i$  or  $k_f$ ), respectively.

Equations (5.4) and (5.5) can further be reduced to semi-analytic equations by making a few simplifying assumptions. First the momentum matrix element between conduction and valence bands can be assumed to be constant around the BZ center (Figure 5.1c). Even if this value varies around BZ center, a corresponding drop of off center values of Fermi-Dirac factor,  $F(E_f)$ , makes this approximation plausible. More simplifications are also possible if the energy of phonon (e.g.  $\hbar \omega_0$  in equation (5.5)) is neglected in comparison with  $E_c(k_i) - E_v(k_f) = E_{gindir}$  and  $E_c(k_f) - E_c(k_i) = \Delta \Omega$ . As a result, equations (5.4) and (5.5) can be reduced to a semi-analytic equation as follows

$$\frac{1}{\tau_{spont}} = \beta_{LO/LA} E_{gdir}^2 R_{cv}^2 E_{gindir} \int_{k_f = -\pi/U_c}^{k_f = +\pi/U_c} F(k_f) \cdot S_{q_t}^{LO/LA}(k_f) \cdot dk_f \quad (5.6)$$

where the constant value,  $R_{cv}$ , is the position matrix element between conduction and valence state at BZ center.  $E_{gdir}$  and  $E_{gindir}$  represent the direct and indirect bandgap values, respectively.  $\beta_{LO/LA}$  is a proportionality factor that contains all relevant constants as given in equations (5.4) and (5.5). The term  $S^{LA/LO}$  represents  $Ph_{LA}$  in equation (5.4) or  $Ph_{LO}$  of equation (5.5) which is multiplied by simplified energy quotient [see equations 4.49 and 4.56 in Chapter 4, section 4.4]. The results of the semi-analytic method are less than 30% off from the numerical method. Details of finding the semi-analytic approximation (equation 5.6) are presented in sub section 5.6.3.

At room temperature ( $T = 300$  K) and  $E_{\text{Fermi}} = E_{\text{vmax}}$ , the average spontaneous emission time due to LA phonons is  $\tau_{\text{avg}} = 3.4 \times 10^3$  s. Including LO phonons results in  $\tau_{\text{avg}} = 16$  s, which reveals the strong role of LO phonons in the second order light emission process as well. It is noteworthy that increasing the Fermi level or decreasing the temperature will lead to less available empty states in the valence band; hence larger spontaneous emission time than above is expected. Table 5.2 lists the spontaneous emission time for an indirect bandgap 3.1nm [110] SiNW at -5% strain for both LA and LO mediated cases. The stronger LO mediated scattering governs the indirect light emission process according to Figure 5.4a (bottom panel). Furthermore, the strong optical anisotropy along z direction is evident in Table 5.2.

Spontaneous emission time (s) for indirect bandgap nanowire		
Polarization	LA phonons included	LO phonons* included
$\tau_x$	$7.5 \times 10^5$ s	$3.5 \times 10^3$ s
$\tau_y$	$5.4 \times 10^5$ s	$1.9 \times 10^3$ s
$\tau_z$	$3.4 \times 10^3$ s	16.1 s
$\tau_{\text{avg}}$	$3.5 \times 10^3$ s	16.1 s

Table 5.2 Spontaneous emission time (s) in a 3.1nm [110] SiNW (at -5% strain with indirect bandgap). (\*) Role of LO phonons is more significant than LA phonons (100 times more) in determining the emission times.

## 5.4 Discussions

Based on the aforementioned results we anticipate that preparing an inverted population of electrons in the indirect sub band and the subsequent application of strain may cause efficient light emission due to the indirect to direct bandgap conversion. To ensure that there are sufficient carriers in the indirect sub band under realistic conditions of multiple sequential electron-phonon scattering events and an applied electric field, we have calculated the relative occupancy of direct and indirect sub bands using Ensemble Monte Carlo (EMC) simulations [158] (*for details refer to **Methods** section or Chapter 4 of the thesis*). Figure 5.5a includes the contributions from the first two sub bands which are less than 4meV apart (C1 and C2 are taken together; see the Inset of Figure 5.5a). As can be seen, the occupancy shows only a relatively small variation across the electric field range considered. The occupancy of the indirect sub bands decreases from approximately 95% at low electric fields, to approximately 92% at 25kV/cm. The factor of ~10 difference between occupancies of indirect and direct sub bands (Figure 5.5a) suggests that periodically straining a biased SiNW can induce population inversion and lasing corresponding to indirect to direct bandgap

conversion cycle. The observed increase in the occupancy of electrons in the direct sub band at higher electric fields is attributed to the transition of electrons away from the negative  $\mathbf{k}_z$  sub bands within BZ as they respond to the electric field. This can be observed in Figure 5.5b, which depicts the time evolution of the electron distribution function under different electric fields. The lack of a significant change in the distribution with electric field is primarily attributed to the high electron-phonon scattering rate due to LO phonon emission, and is a feature consistent with other small diameter nanomaterials such as single-wall carbon nanotubes (CNT) [159], and unstrained SiNWs [160]. This can be understood by comparing Figure 5.5b with Figure 5.5c that depicts the total electron-phonon (LA and LO) scattering rates for conduction sub bands C1 and C2. Under an applied electric field, electrons initially near the bottom of the sub bands gain crystal momentum until they reach the peaks associated with the onset of LO phonon emission. This inelastic-scattering event prevents electrons from gaining further momentum, and induces the observed behavior in Figure 5.5b.

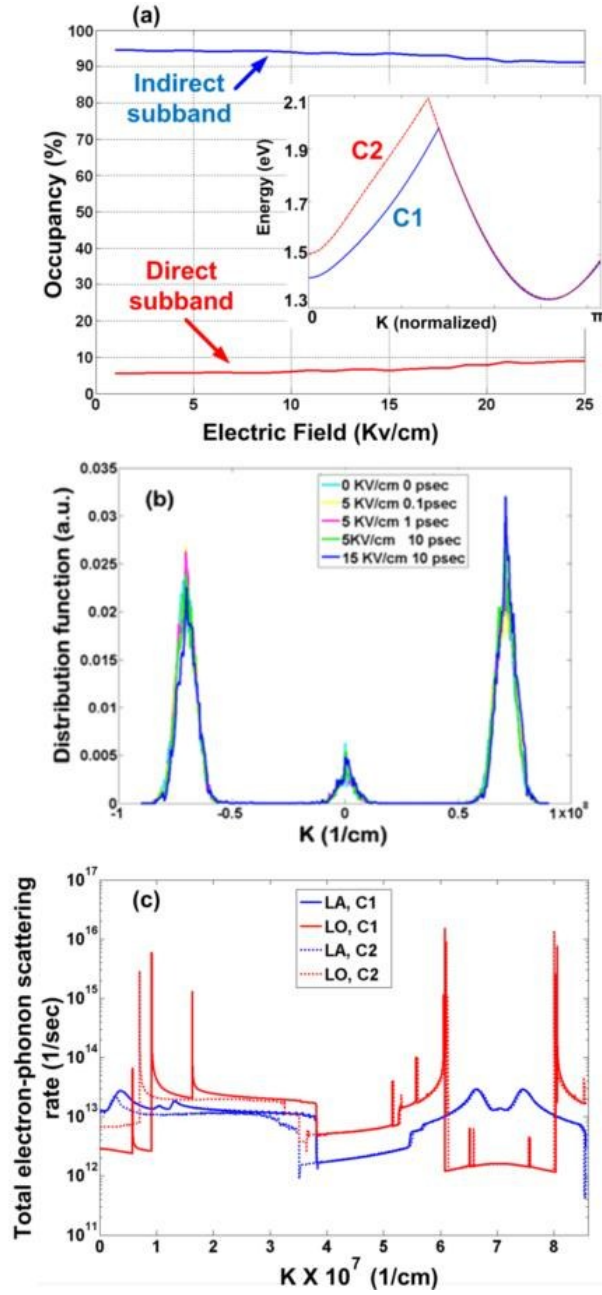


Figure 5.5 (a) Occupancy of indirect and direct sub bands vs. electric field for a 3.1nm [110] SiNW at -5% strain (indirect bandgap). Inset shows the positive half of the BZ (i.e.  $k$  spans  $[0, \pi]$ ) with two conduction sub bands used in the EMC simulation. (b) Time evolution of the electron distribution function under different electric fields. (c) The total LA and LO electron-phonon scattering rates. In the legend, C1 and C2 show the initial sub band from which the electron starts to be scattered by emission/absorption of LA and LO phonons.

To investigate the role of temperature in the aforementioned carrier population analysis we have also conducted simulations for occupancy of the sub bands at 77K. It is observed that the occupancy of the direct part of the sub bands (near BZ center) at 77K (as shown in Figure 5.6) is negligible compared to 300K (Figure 5.5b). The emission of LO phonons for inter and intra-sub band scattering events are indeed very strong, and are the dominant players. As soon as an electron gains 63 meV of energy, it emits a phonon and makes a transition to either the same indirect sub band bottom with a very high scattering rate, or the opposite indirect sub band bottom. Because of this very high scattering rate, electrons do not gain enough energy to make a transition to the direct sub band bottom.

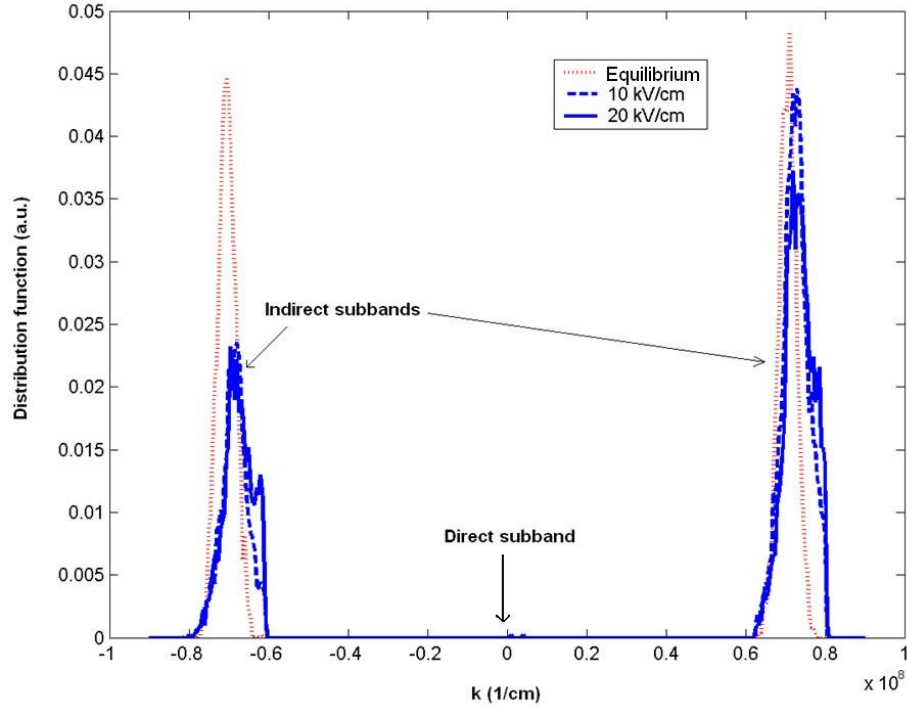


Figure 5.6 Time evolution of electron distribution function under different electric fields at low temperature ( $T=77\text{K}$ ). The distribution function is calculated by Professor Amit Verma [149] using the scattering data calculated by the author.

Also there is another mechanism at work which depletes the direct subband from carriers at  $T=77\text{K}$ . As it is shown in figure 5.7, the transition from direct subband to indirect occurs through two LO emission events (AB and AC in Figure 5.7). This is because the rate of electron-LO scattering is at least two orders of magnitude larger than electron-LA phonon scattering. At  $T=300\text{K}$ , the direct to indirect transition (AB and AC) or vice versa (BA and CA) are almost symmetric since the emission (direct to indirect sub band) and absorption (indirect to direct sub band) have almost the same transition time ( $10^{-11}\text{ s}$ ) according to Table 5.3. Although electrons at B and C can thermalize by LA emission and reach to the indirect

sub band bottom, however LO absorption processes are still stronger than e-LA emission event (at T=300K).

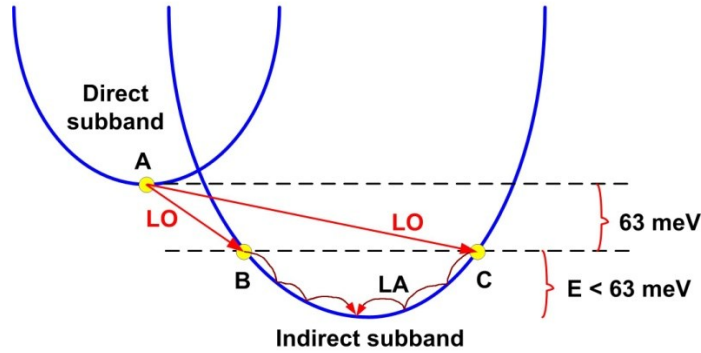


Figure 5.7 Direct to indirect transition through LO phonon emission (AB and AC transitions) followed by LA emission to reach to the indirect sub band bottom.

On the other hand at 77K the LO absorption rates drop by 3 orders of magnitude ( $1/\text{rate}=10^{-8}$  s) while emission rates have still the same order as 300K case i.e.  $1/\text{rate}=10^{-11}$  s. This asymmetry means that electrons have more chance to escape from direct sub band and reach indirect subband (through B and C and LA emission) rather than the reverse. The asymmetry between LO absorption (BC, BA) and LO emission (AB and AC) transition rates is evident in Table 5.3.

Another non-radiative effect which matters in studying the carrier population is the Auger recombination which can deplete the indirect sub bands. However photoluminescence study of SiNWs with a diameter of  $3.3\text{nm}\pm 1.6\text{nm}$ , as a function of temperature and optical pump intensity has shown [66] that the fastest Auger recombination time can be 19  $\mu\text{s}$ . Since this time is much more than the electron-phonon scattering times that we deal with, we have neglected the Auger recombination effect in our work.

Direct to indirect sub band transition rates				
Temperature	A $\rightarrow$ B	A $\rightarrow$ C	B $\rightarrow$ A	C $\rightarrow$ A
T=300 K	$9.7 \times 10^{10} \text{ sec}^{-1}$	$1.5 \times 10^{11} \text{ sec}^{-1}$	$6 \times 10^{10} \text{ sec}^{-1}$	$6 \times 10^{10} \text{ sec}^{-1}$
T= 77 K	$8.8 \times 10^{11} \text{ sec}^{-1}$	$1.4 \times 10^{11} \text{ sec}^{-1}$	$4.6 \times 10^8 \text{ sec}^{-1}$	$4.9 \times 10^8 \text{ sec}^{-1}$

Table 5.3 Electron-LO phonon scattering rates for direct to indirect sub band transitions at two different temperatures. A, B and C states are introduced in Figure 5.7. Note that the transitions through LO phonon emission (A  $\rightarrow$  B and A  $\rightarrow$  C) are almost unchanged at both temperatures.

Finally we speculate on how the idea of strain-modulated spontaneous emission time can be developed for SiNWs. There are many examples of recently implemented platforms and methods to apply strain to a single CNT. Piezoelectrically driven table [94], pressure driven deformable substrate [96] and applying force by an atomic force microscope probe [91] are among the methods of generating mechanical strain in CNTs. Additionally there are examples of using a deformable substrate to modulate the energy band diagram of piezoelectric zinc oxide nanowires via strain [161]. Embedding SiNWs on plastic [6], elastomeric [97] and metallic deformable substrates [8] all show that our results are verifiable using existing methods. It is also advantageous that the direct to indirect conversion and the resulting modulation of spontaneous emission time is a reversible process. However the strain value which results from embedding SiNWs in silicon dioxide or nitride shell is unchangeable. The observed population difference in Figure 5.5a and 5.6 leads us propose an experiment to observe population inversion and lasing in SiNWs (Figure 5.8). If we assume that an indirect bandgap SiNW (under compressive strain) is biased under a moderate electric field, there will be a larger population of electrons in indirect sub band (Figure 5.8a). After releasing the strain (or applying tensile strain) to make the nanowire direct bandgap (Figure 5.8b), the population which is still significant can scatter to the direct sub band (within picosecond time scales) and stimulated emission takes place, provided that suitable feedback and gain mechanisms have already been designed for such SiNW. It is noteworthy that although strain may cause changes in optical properties of silicon quantum dots, electrical injection and reversible application of strain are practical issues which render the usability of silicon quantum dots difficult.



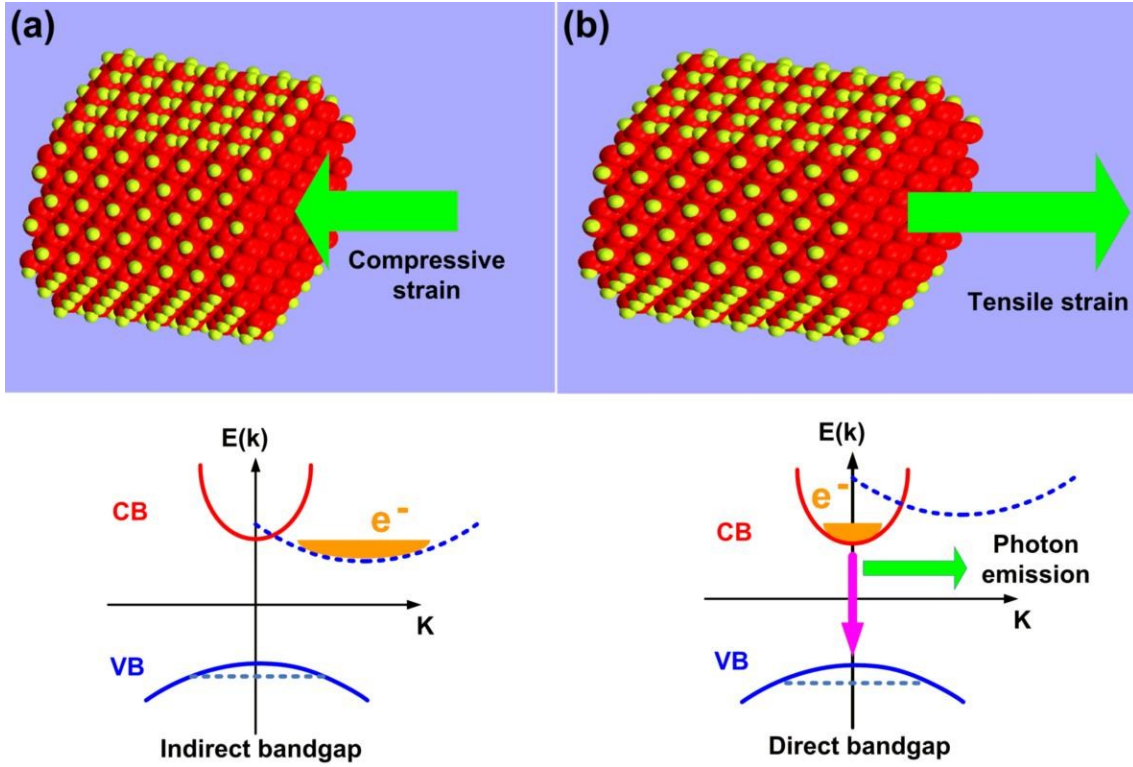


Figure 5.8 (a) Injecting current in a compressively strained nanowire (top) which has an indirect bandgap (bottom) can generate an initial population in SiNW. Although non-radiative processes may deplete this sub band of most of those injected carriers, there will still be a factor of 10 difference in the electron occupancy between the indirect and direct sub bands. (b) During strain release or when applying tensile strain (top), the initial population can scatter into the direct sub band via electron-phonon scattering processes within picosecond time scale. Thereafter (bottom) the inverted population can initiate lasing (coherent stimulated emission) if the nanowire is already embedded in a suitable mode enhancing cavity. In the case of incoherent (spontaneous) emission the light has a broader spectrum suitable for light emitting diode (LED) applications. Similar set up can be devised for light absorption (i.e. photocurrent) modulation using strain.

In summary, we found that *the spontaneous emission time can be modulated by more than one to two orders of magnitude due to strain via two distinct physical mechanisms, a feature that is not observable in bulk silicon crystal*. To more accurately take into account the excitation of carriers from the indirect to direct conduction bands via multiple phonon scattering, we have simulated the nanowire via Ensemble Monte Carlo simulations at room temperature. We found that non-radiative scattering events deplete the initial population of carriers from the indirect sub band. However under moderate electric fields there is still a factor of 10 difference between indirect and direct sub band occupancies. This is of significance when we consider a nanowire device in which lasing and population inversion can be inhibited or initiated by periodic application of axial strain. A similar scheme can also

be proposed to modulate the photo-absorption of narrow SiNWs, either due to wave function symmetry change or direct to indirect band gap conversion. Change of wave function symmetry can potentially induce large nonlinear optical effects in nanowires in response to strain [87][88] which merits a deeper study. While the calculations are performed for silicon nanowires, similar phenomena should exist in nanowires made out of other material systems.

## 5.5 Methods

*This section can be skipped if you have already studied Chapter 4.* The nanowires in this work are cut from bulk silicon crystal in [110] direction and dangling silicon bonds on the surface are terminated with hydrogen atoms (Figure 5.1a). The diameters of the nanowires range from 1.7nm to 3.1nm. The cross section of nanowires lies in the x-y plane, and z is the axial direction of each nanowire. The relative stability of [110] direction compared to [100], which is quantified as free energy of formation [27], is experimentally verified [31][26]. Energy minimization of nanowires is performed by Density Functional Theory (DFT) method within SIESTA<sup>®</sup> [136] (version 3.1) using Local Density Approximation (LDA) functional with Perdew-Wang (PW91) exchange correlation potential [126]. Spin polarized Kohn-Sham orbitals of double-zeta type with polarization (DZP) have been used. The Brillion Zone (BZ) has been sampled by a set of 1×1×40 k points along the axis of the nanowire (z axis). The minimum center to center distance of SiNWs is assumed to be at least 2nm to avoid any interaction between nanowires. Energy cut-off, split norm, maximum force tolerance and maximum stress tolerance are 680 eV (50 Ry), 0.15, and 0.01eV/Å and 1GPa, respectively. The relaxation stops if the maximum absolute value of inter-atomic forces is smaller than force tolerance and the maximum stress component is smaller than the stress tolerance. The energy of the unstrained unit cell of the nanowire is minimized using Conjugate Gradient (CG) algorithm during which *variable* unit cell option is selected. Afterwards, for each percent of strain ( $\epsilon$ ) the unit cell is relaxed using the constant volume chosen by *fixed* unit cell option. With this option atoms are only free to move within the fixed unit cell volume. The result of each minimization step is fed to the next step of minimization. The unit cell length ( $U_c$ ) as defined in Figure 5.1a (right) is updated according to the applied strain value  $\epsilon$ , i.e.  $U_{c\text{-new}} = U_{c\text{-old}}(1+\epsilon)$ . The electronic structure is calculated within 10 orbital semi-empirical  $sp^3d^5s^*$  tight binding scheme [110]. This is to avoid bandgap underestimation due to DFT and diameter sensitive many-body GW corrections. More discussions are made in sub section 5.6.4 regarding the justification of using TB instead of DFT in the calculation of band structure.

The orbitals of silicon atoms (i.e. s, p, d and  $s^*$ ) are assumed to be of Slater [142] type in which the radial part of each orbital is given by the following equation

$$R(r) = N r^{n^*-1} e^{-\frac{Z-s}{n^*}r} \quad (5.7)$$

where  $N$  is the normalization factor and  $Z$  is the atomic number. The shielding constant ( $s$ ) and effective quantum number ( $n^*$ ) are found using the rules given by Slater [142].

To calculate the spontaneous emission life times in direct bandgap nanowires [equation (5.2) in the main section], Fermi's golden rule with first order perturbation theory [146] is used. The matrix element of electron-photon interaction Hamiltonian ( $H_{e-R}$ ) can be simplified to momentum matrix element,  $\langle \Psi_i | \hat{\mathbf{e}} \cdot \mathbf{P} | \Psi_f \rangle$ . This is further reduced to its position representation and integrals of type  $\langle \alpha(\mathbf{r}-\mathbf{R}_o) | \mathbf{r} | \beta(\mathbf{r}-\mathbf{R}_o) \rangle$ . Here  $\mathbf{r}$  is the position operator,  $\alpha$  and  $\beta$  are atomic orbitals of which  $\Psi_i$  and  $\Psi_f$  are composed. These integrals have two parts i.e.  $\mathbf{R}_o \delta_{\alpha\beta} + \langle \alpha(u) | u | \beta(u) \rangle$  where  $\mathbf{R}_o$  is the position of the atom. The second part consists of radial and angular integration of Slater type orbitals which are both found analytically using Wolfram Mathematica<sup>®</sup> online integrator (<http://integrals.wolfram.com/index.jsp>). Among 100 combinations of 10 orbitals, 15 of them have symmetry-allowed nonzero value.

The first order electron-phonon scattering rates are also calculated using Fermi's golden rule within the first order perturbation scheme [146]. The electron-phonon interaction Hamiltonian ( $H_{ep}$ ) is of deformation potential type for bulk LA and LO phonons. As it is stated by M. Nawaz et al [162], taking confined LO phonons into account will reduce the scattering rate. Thus phonon confinement does not have an adverse effect on the spontaneous emission times calculated for indirect nanowires. Also it is shown that there is only a 10% difference in calculated mobility between the cases where bulk and confined phonons are used [163]. Details of calculating the electron-phonon interaction Hamiltonian matrix elements and scattering rate have been skipped and the interested reader can refer to [148][157]. For indirect bandgap nanowires with larger energy offset (i.e.  $\Delta\Omega > E_{LO}/E_{LA}$ ), second order perturbation method is used in which all interaction Hamiltonian matrix elements are calculated likewise. The expressions for spontaneous emission time are explained in the main section.

To further investigate the carrier population statistics of indirect sub bands under the influence of electric field and multi electron-phonon scattering events, we use standard Ensemble Monte Carlo (EMC) methodology [158]. In setting up our EMC simulation, we consider an infinitely long, defect free SiNW with a uniform temperature. The electric field is also uniform and directed along the axis of the SiNW. In performing the simulation, tabulated values of two lowest conduction sub bands of 3.1nm diameter [110] SiNW with indirect bandgap (due to -5% strain) (C1 and C2 in the Inset of Figure 5.5a) are used. For each initial state starting from indirect conduction sub band minimum, all possible final states within C1 and C2 with corresponding scattering rates for both phonon types (LA/LO) were utilized. Both inter- and intra-sub band electron-phonon scattering events have been calculated. The rest of the conduction sub bands are not included in the simulation since the third conduction sub band is at least 100meV above the first two sub bands (C1 and C2 in Figure 5.5a). Electron transport is confined to the first BZ, which is divided into 8001 k grid

points (4000 positive  $k$  and 4000 negative  $k$  values) and for which the tabulated energy values and electron-phonon scattering rates are computed and stored. Electrons are initially injected into the SiNW at the bottom of an indirect sub band and the simulation is initially executed for 500,000 scattering cycles at 0 kV/cm electric field so as to allow the electrons to approach as close to an equilibrium distribution as possible.

## 5.6 Addendum

### 5.6.1 Local Field Effects (LFE) on the spontaneous emission time

In the calculation of spontaneous emission time for [110] Si nanowires it was observed that there is a strong anisotropy which is induced from the symmetry of wave functions and matrix elements. In another language the transition matrix elements of x,y polarized light ( $\langle \Psi_c | x | \Psi_v \rangle$  and  $\langle \Psi_c | y | \Psi_v \rangle$ ) are negligible when they are compared to z-polarized case (i.e.  $\langle \Psi_c | z | \Psi_v \rangle$ ). This in turn means that optical transition is stronger when the electric field is polarized along the nanowire axis (z).

Another kind of optical anisotropy is induced from the Local Field Effect (LFE). This is due to the change of internal electric field in 1D nanostructure which arises from the form of polarization vector,  $P$ . As it is shown in Figure 5.9 when the external electric field ( $E_{ext}$ ) is parallel with the axis of the nanowire, depolarization field ( $E_{dep}$ ) is negligible since it is proportional to  $P/L^2$  where  $L$  is the length of the nanowire. In case of perpendicular electric field, the induced polarization reduces the local electric field via  $E_{dep} = -2\pi P$  since  $E = E_{ext} + E_{dep}$ . In both cases the polarization vector is proportional to the external electric field.

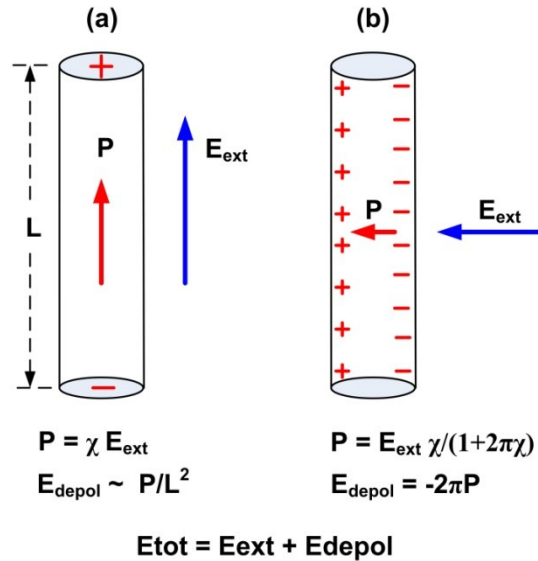


Figure 5.9 Effect of external field on the local (internal) electric field when it is parallel (a) and perpendicular (b) to the nanowire.

To see how LFE will effect on the spontaneous emission times reported in Table 5.1, we recall equation (5.1) which shows that the spontaneous emission rate is proportional to refractive index and momentum matrix element squared i.e.

$$\frac{1}{\tau} \propto n|P_{cv}|^2 \text{ or } \frac{1}{\tau} \propto \sqrt{\epsilon}|P_{cv}|^2 \quad (5.8)$$

When LFE is taken into account it causes strong anisotropy of dielectric function of nanowire which is different from the symmetry induced anisotropy (as mentioned above or as discussed in [164]). As it is reported in [155] and [156] dielectric function for parallel polarized electric field has no significant change after including LFE. On the other hand when the electric field is perpendicular to the nanowire, the absorption edge shifts to higher energies ( $> 4\text{eV}$ ) and dielectric permittivity drops significantly. This means that the anisotropy due to LFE is stronger than the symmetry induced one (our calculated anisotropy). As can be seen in Figure 5.10 since  $\epsilon_{\parallel}(\omega)$  is almost the same with and without LFE for a [110] Si nanowire, it can be said that including LFE for z polarized case does not change the spontaneous emission time.

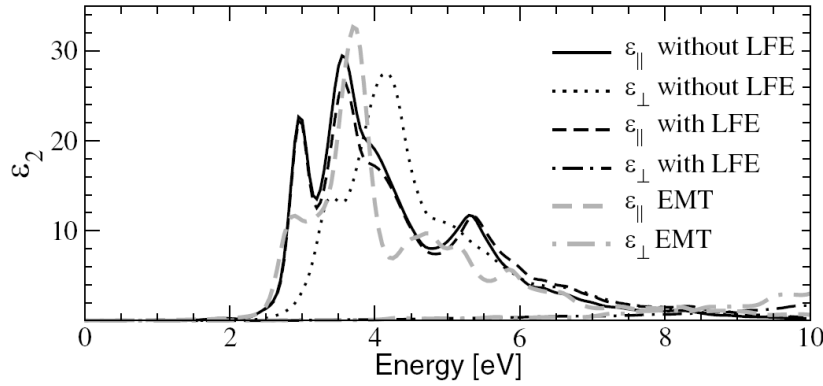


Figure 5.10 Imaginary part of dielectric function for a 2.2nm [110] SiNW. Reprinted with permission from [155]. Copyright 2005 American Physical Society.

On the other hand for perpendicular polarization (x and y), the significant decrease of  $\epsilon_{\perp}(\omega)$  after LFE inclusion, reduces the x,y-polarized spontaneous emission time. This in turn enhances the difference between z-polarized and xy-polarized spontaneous emission times only and does not affect the average spontaneous emission times in our results (e.g. Table 5.1). This is because the average spontaneous emission times in [110] SiNWs are mainly determined by the z-polarized term.

However in the case of [100] SiNWs the band structure (symmetry) induced anisotropy makes the x and y polarized component of the spontaneous emission more dominant. Therefore including LFE will enhance the z-polarized component (due to LFE induced anisotropy which favors parallel polarization). However the amount of enhancement depends on the value of  $\langle \Psi_c | z | \Psi_v \rangle$  too. On the other hand the x,y polarized components are reduced

by the LFE-induced reduction of  $\epsilon_2 \perp (\omega)$  as well as internal electric field modification according to equation 5.9 which is discussed in [165].

$$E_{int} = \frac{2\epsilon_0}{\epsilon + \epsilon_0} E_{ext} \quad (5.9)$$

### 5.6.2 Sub band exchange due to strain

As we observed in sub section 5.3.1, the symmetry of the wave function changes because different subbands within the valence band are shifted by different energies when strain is applied. We now provide further evidence of this by plotting the energy bands of a SiNW at two different strain values of -2% and -3%. Figure 5.11 shows the highest two valence subbands at -2% strain.

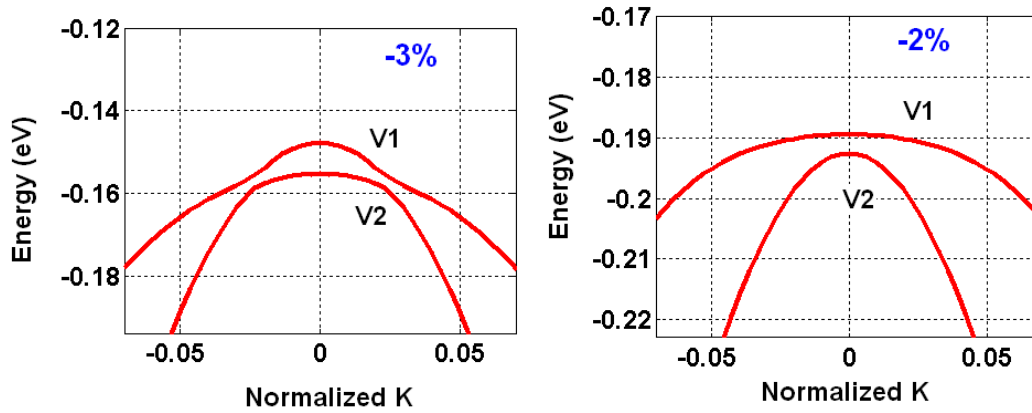


Figure 5.11 Valence subbands of a 1.7nm [110] SiNW at -2% (right) and -3% (left) strains.

When the strain is increased, these two subbands shift by different amounts. As a result at -3% they have flipped in order. As can be seen the energy of V2 sub band (for -2% strained nanowire) increases and it becomes a new sub band (V1 for -3% strained nanowire). For the case of -2% strain the values of momentum matrix element (for both C1-V1 and C1-V2 transitions) as well as normalized squared value of wave functions for both V1 and V2 are plotted in Figure 5.12. As can be seen in the right panel the C1-V1 transition has stronger matrix element hence smaller spontaneous emission time. On the other hand C1-V2 transition is a slower process (left panel of Figure 5.12).

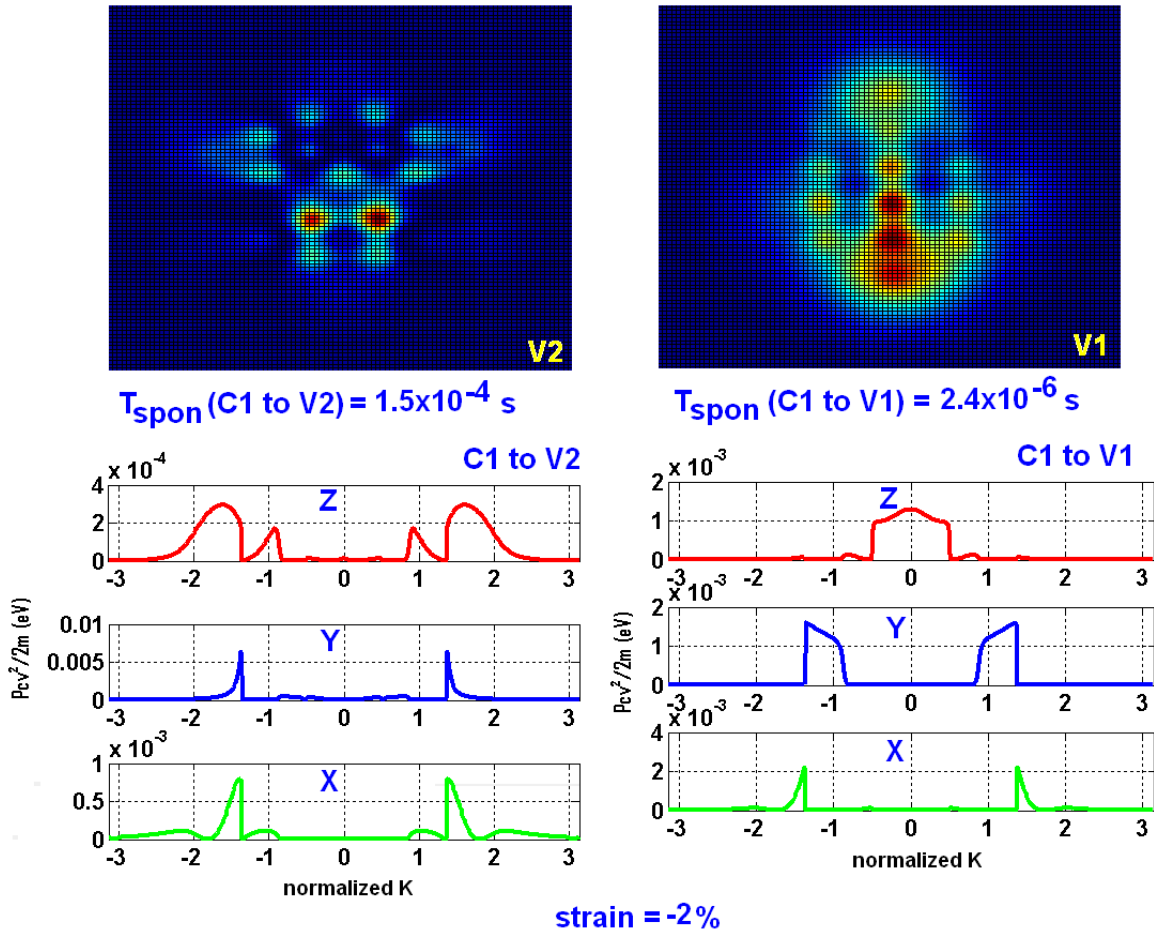


Figure 5.12 Right panel: Normalized probability density plot of (V1) and optical matrix element of C1-V1 transition for z, y and x polarizations. Left panel: Normalized probability density plot of (V2) and optical matrix element of C1-V2 transition.

Now we look at -3% strained nanowire in which a flip of V1 and V2 has taken place. As shown in Figure 5.13 the role of V1 and V2 has now interchanged i.e. the former V2 (for -2% strained nanowire) is now determining the strength of C1-V1 transition (after suffering from a little change and 180 degree rotation) because it is now working as V1 for -3% strained nanowire. Therefore the smaller value of  $\langle \Psi_c | \mathbf{r} | \Psi_v \rangle$  or optical dipole matrix element has resulted. This in turn leads to slower lifetime for C1-V1 in contrast to C1-V2 in which V2 is the former V1 (for -2% strained nanowire) which had larger value for z-polarized optical dipole matrix element. The difference in the matrix element for states V1 and V2 lead to the difference in spontaneous emission times. Note that the conduction band does not change in this range of strain values.

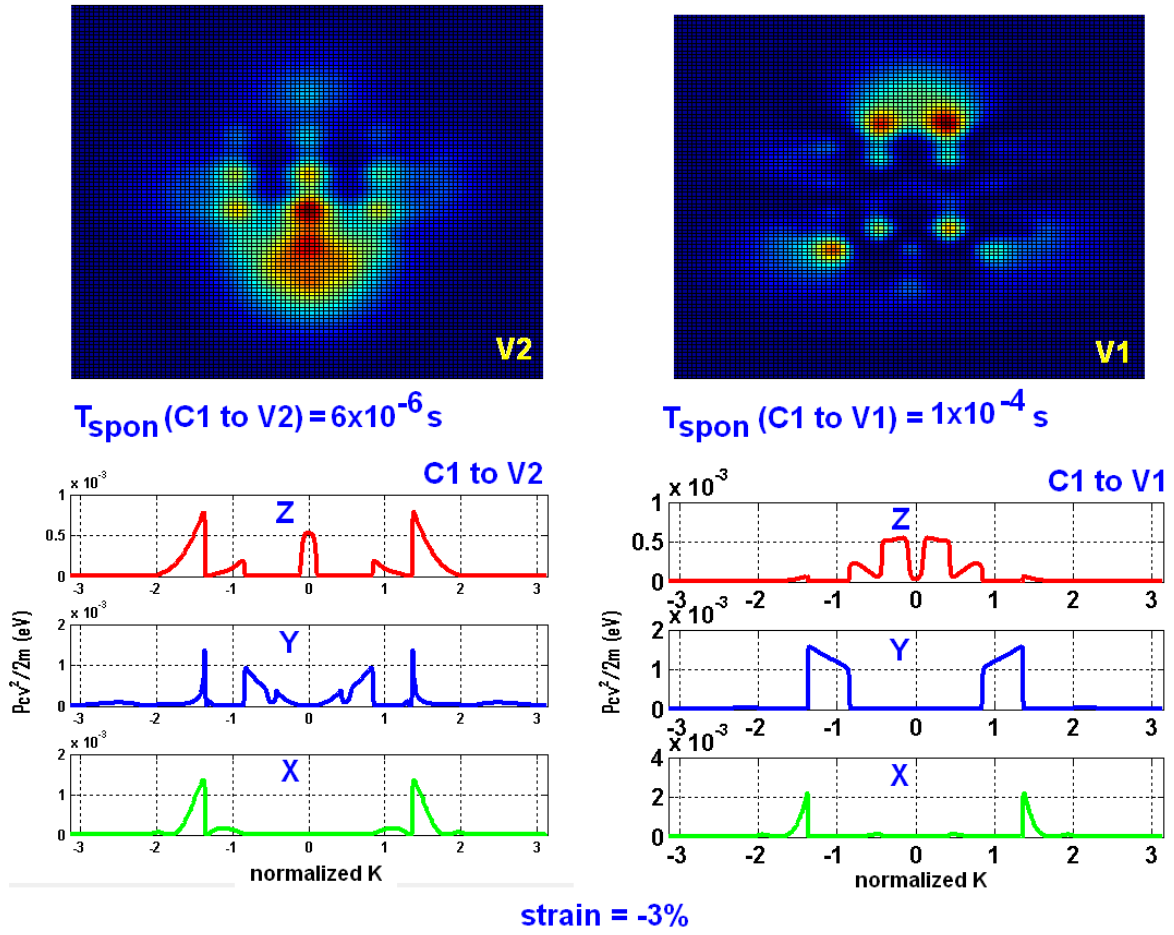


Figure 5.13 Right panel: Normalized probability density plot of (V1) and optical matrix element of C1-V1 transition for z, y and x polarizations. Left panel: Normalized probability density plot of (V2) and optical matrix element of C1-V2 transition.

### 5.6.3 Semi-analytic equation for 2nd order spontaneous emission

Performing the summation over all final states as required in equation (4.49) and (4.56) are the most time consuming parts of the spontaneous emission rate calculation. Therefore having a semi-analytic expression to reduce the time proves useful. Additionally being able to separate the terms corresponding to electron-photon and electron-phonon interaction is instructive because these two processes and their roles in the optical quantities of interest can be studied separately. It is shown here that how a few simplifying assumptions can yield a semi-analytic equation for spontaneous emission time.

Since the Fermi factor in valence band drops significantly at energies far from the valence band maximum ( $E_{vmax}$  at  $k_f = 0$ ). Therefore in equations 4.49 and 4.56, the frequency term,  $\omega_{mf}$ , can be approximated by its value at  $k_f=0$  which is  $E_{gdir}/\hbar$ . The reason of this



approximation is that the difference between  $\omega_{mf}$  and  $E_{gdir}/\hbar$  is already masked by very small value of Fermi factor far from the BZ center (i.e. at  $k_f > 0$  or  $k_f < 0$ ) thus  $\omega_{mf} \approx E_{gdir}/\hbar$ . For the same reason as above and by looking at the value of matrix element versus  $k_z$  (Figure 5.1c), it is possible to use a constant position matrix element for all  $k_f$  values around the BZ center. Therefore the position matrix element can be calculated at  $k_f = 0$  and its value through all BZ points can be assumed to be equal to this constant amount i.e.  $|\langle u_f | \hat{r} | u_m \rangle|^2 = R_{mf}^2$  which contains three constant numbers corresponding to  $x$ ,  $y$  and  $z$  polarizations. Albeit the electron-phonon structure factor,  $\Phi(\tilde{q}_t, q_z)$  is an oscillating function of  $q_t$ , its value remains in the same range for all values of  $k_f$  i.e.  $\int_0^{2\pi} |S(|\tilde{q}|)|^2 d\phi = \alpha^2$  where  $\alpha^2$  is the maximum of structure factor within the range of  $k_f$ . So this approximation will give the worst spontaneous rate i.e. higher rate than the exact numerical one given by equations 4.49 and 4.56. Additionally the energy of acoustic phonon,  $\hbar\omega_q$ , can be ignored as being compared with indirect bandgap i.e.  $E_c(k_i) - E_v(k_f) \mp_a^e \hbar\omega_q \approx E_{gindir}$  in which  $E_{gindir}$  is indirect bandgap of nanowire and it is  $E_{gindir} = E_{cmin\_indir} - E_{vmax}$ . The quantity in the denominator of equation 4.46,  $E_c(k_m = k_f) - E_c(k_i)$ , can be approximated as  $\Delta E_{cmin}$ . Here it can be assumed that the only contribution comes from the phonon which has the minimum transversal wave vector i.e.  $\hbar\omega_q = \hbar v_s q_z$  and  $q_{t\_min} = 0$ . Starting from equation 4.46, the simplification proceeds as follows:

$$\tau_i^{-1} = \beta_{LA} E_{gdir}^2 R_{mf}^2 E_{gindir} \int dK_f F(k_f) PH_{LA}(k_f, k_i) \quad (5.10)$$

Where  $PH_{LA}(k_f, k_i)$  is what remains after factoring out  $E_{gindir}\alpha^2$  from  $Ph_{LA}(k_f, k_i)$  in equation 4.46.  $\beta_{LA}$  contains the rest of the constant factors of equation 4.46 and it is:

$$\beta_{LA} = \frac{e^2 D^2 n_r^3}{48\pi^4 \rho \epsilon \hbar^3 c^3 v_s} \quad (5.11)$$

After expanding  $PH_{LA}(k_f, k_i)$  and  $F(k_f)$  we have a new equation for indirect spontaneous emission time due to LA phonons which is:

$$\tau_i^{-1} = \beta_{LA} E_{gdir}^2 R_{mf}^2 E_{gindir} \alpha^2 \int \frac{1}{e^{\frac{F-E_v(K_f)}{k_B T}} + 1} \int_{q_{t\_min}=0}^{q_{t\_max}=\sqrt{q_D^2 - q_z^2}} \frac{dq_t \cdot q_t \cdot |\tilde{q}| B_{\pm}(|\tilde{q}|)}{(\Delta E_{cmin} \pm \hbar v_s q_z)^2} dK_f \quad (5.12)$$

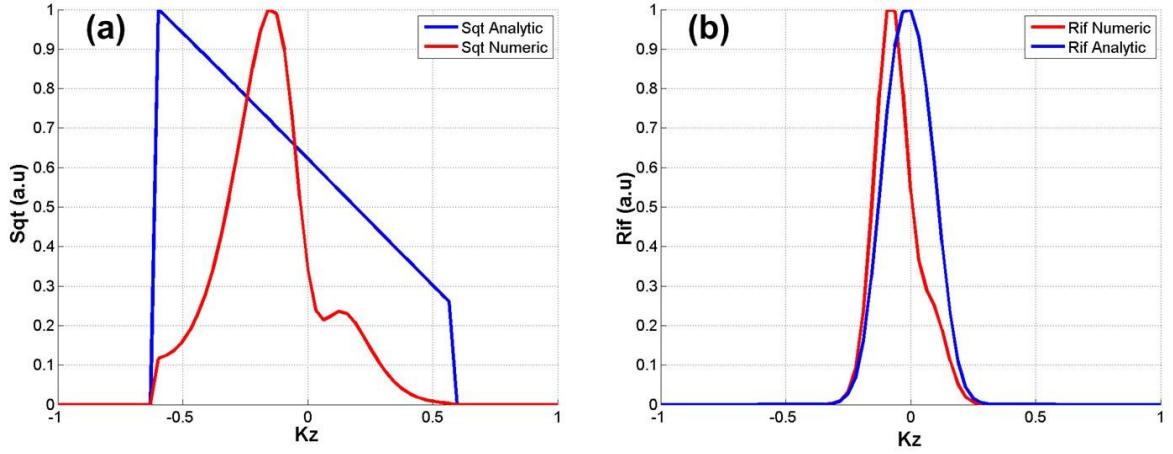


Figure 5.14 (a) Summation over transversal phonon wave vector,  $S_{qt}$ . Blue and red curves correspond to analytic and numerical calculation of form factor at each iteration of  $k_f$ . Summation is confined to  $[-0.5, 0.5]$  interval for the sake of visibility. (b) Multiplying by Fermi factor confines the previous summation in the region close to  $k_z = 0$ . This calculation is for a 3.1nm [110] SiNW in -5% strain.

Figure 5.14 shows the difference between  $PH_{LA}$  and  $Ph_{LA}$  around the BZ center. As can be seen in Figure 5.14b, the difference is reduced once  $PH_{LA}$  is shaped by the Fermi factor. Although the integration over transversal phonon wave vectors in equation 4.49 and 5.12 are different along the BZ ( $S_{qt}$  in Figure 5.14a), however the small Fermi factor for  $k_f > 0$  and  $k_f < 0$  clears the difference. Hence the main contribution comes from the values centered on  $k_f = 0$  which are very close in both methods. Further simplification of equation 5.12 is possible if it is assumed that phonon energy is negligible compared to  $\Delta E_{cmin}$ . This results the following equation which gives the same order of magnitude for spontaneous emission rate. However a factor of 3 or 4 difference is observed due to neglecting  $\hbar v_s q_z$  in denominator which was  $\Delta E_{cmin} \pm \hbar v_s q_z$ .

$$\tau_i^{-1} = \frac{\beta_{LA} E_{gdir}^2 R_{mf}^2 E_{gindir} \alpha^2}{\Delta E_{cmin}^2} \int \frac{1}{\frac{F - E_v(K_f)}{e^{\frac{\hbar v_s q_z}{k_B T}} + 1}} \int_{q_{t,min}=0}^{q_{t,max}=\sqrt{q_D^2 - q_z^2}} dq_t \cdot q_t \cdot |\bar{q}| B_{\pm}(|\bar{q}|) dK_f \quad (5.13)$$

For a 3.1nm [110] SiNW which has indirect bandgap in -5% strain,  $\Delta E_{cmin} = 80 \text{ meV}$  and  $\hbar v_s q_z = 39.8 \text{ meV}$ , therefore the factor of 3 difference can be expected due to neglecting the phonon energy. The indirect spontaneous emission rate including optical phonons can also be simplified with the same procedure as motioned above. Firstly the position operator matrix element and optical frequency can be approximated to be constant and equal to their value at BZ center ( $k_f = 0$ ) i.e.

$$\omega_{fm}^2 |\langle u_f | \hat{r} | u_m \rangle|^2 = \frac{E_{gdir}^2}{\hbar^2} R_{mf}^2 \quad (5.14)$$

Secondly the energy of LO/TO phonon can be ignored compared to the indirect bandgap value i.e.  $E_c(k_i) - E_v(k_f) \pm \hbar\omega_0 \cong E_c(k_i) - E_v(k_f) = E_{gindir}$ . As a result the nominator in equation 4.56 as well as matrix element and frequency can be factored out to yield:

$$\tau_i^{-1} = \beta_{LO} E_{gdir}^2 R_{mf}^2 E_{gindir} \sum F(k_f) \frac{Ph_{LO}(k_f) \Delta K_f}{(E_c(k_{m=f}) - E_c(k_i) \pm \hbar\omega_0)^2} \quad (5.15)$$

Where  $\beta_{LO}$  contains other constant factors in equation 4.56 which is

$$\beta_{LO} = \frac{e^2 D_{op}^2 n_r^3}{\epsilon \rho c^3 \hbar^3 \omega_0} \cdot \frac{1}{48\pi^4} \quad (5.16)$$

#### 5.6.4 DFT vs. TB (band structure calculation)

The change of bandgap value with diameter for [110] SiNWs is calculated using TB method (Figure 5.15a). As can be seen by increasing the diameter the value of bandgap decreases and shows the same trend as discussed in DFT-based calculations by [166][164]. More importantly it follows the same experimental observation using Scanning Tunneling Spectroscopy (STS) of [110] nanowires reported in [31].

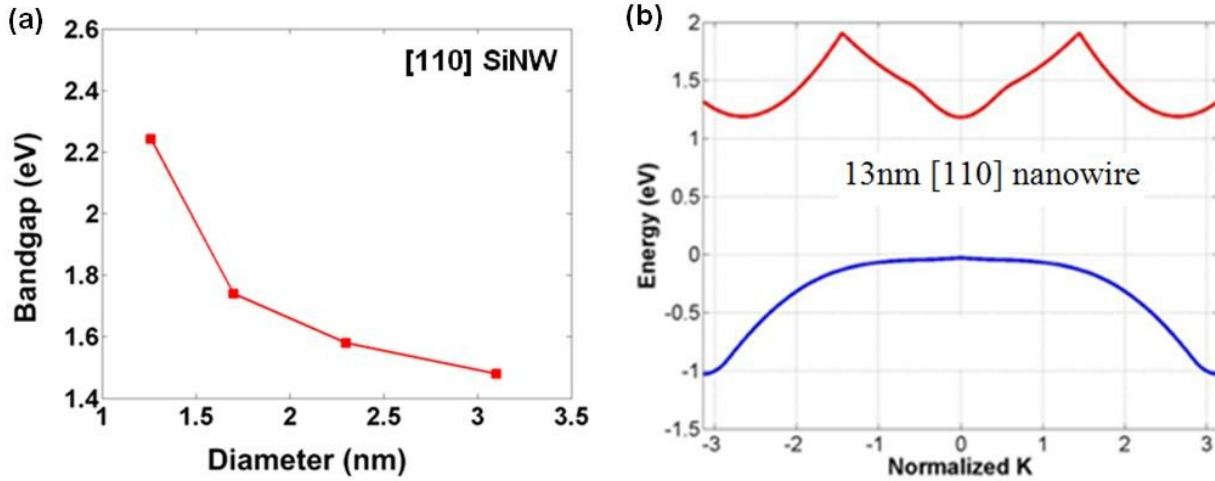


Figure 5.15 (a) Diameter dependence of bandgap value for [110] SiNWs. (b) Band structure of a 13nm [110] SiNW (first conduction band and the last valence band are shown only).

It is also expected that by increasing the diameter, the nanowire bandgap approaches to that of bulk silicon. This is verified this by calculating that bandgap of a large (13nm diameter) [110] SiNW using a sparse tight binding Hamiltonian matrix. Figure 5.15b shows that the value of bandgap is 1.17 eV which is very close to that of bulk Si. This further verifies that

TB method gives comparable bandgap values and trend as with other many-body calculations (except LDA-based method which suffers from the inherent bandgap underestimation). It must be added that many-body GW corrections which are used to shift the bandgap value are sensitive to the nanowire radius [164]. Due to these reasons we chose TB method to calculate the band structure. With this method we could concentrate on the physics of emission and the order of magnitude change that is being looked for due to direct to indirect bandgap conversion.

In addition the tight binding method has been successful in regenerating the bulk band structure as well as correctly simulating the boundary conditions i.e. surface passivation. Trends of bandgap change with diameter of Si nano-crystals is also agrees with DFT based calculations [167]. Justification of using TB in calculating the band structure was further made showing that it can successfully reproduce radial strain effect on the PL spectrum of SiNWs [37][67].

#### **5.6.5 Many-body (exciton) effects**

Within  $sp^3d^3s^*$  tight binding scheme and by including the excitons effects Sanders and Chang [45] have shown that the emission life time for direct bandgap ideal square cross section [100] nanowires changes from  $10^{-5}$  sec to  $10^{-4}$  sec (depending on diameter). Although we have not included the exciton effects in our calculations, for [100] Si nanowires with comparable diameter, our method yields lifetime values in the same ballpark of  $10^{-4}$ sec. It is shown in [168] that the excitons decay time for a  $D=3.3$ nm [110] Si nanowire is 20  $\mu$ sec. Our single particle tight binding calculations performed for a 3.1nm [110] Si nanowire (*without DFT-based energy minimization*) shows that the emission life time is in the order of 10 $\mu$ sec. Furthermore we have observed that there is a significant difference between the momentum matrix elements of an idealized nanowire and the one whose energy is minimized using DFT method. To find out how does including excitons affect spontaneous emission times we need to do comparison for the same set of structurally relaxed (energy minimized) nanowires. Works which address exciton effects e.g. [45][168] perform their calculation for idealized Si nanowires i.e. those without energy minimization. Therefore it cannot be said precisely if the observed difference in the results (e.g. radiative lifetimes) is due to excitons or energy minimization.

# Chapter 6

## Photo absorption in Silicon Nanowires

Effect of strain on the electronic band structure and light emission of SiNWs were discussed in the previous chapters. As mentioned before, the change of wave function symmetry and direct to indirect bandgap conversion are two main mechanisms which lead to the change of spontaneous emission time in response to strain. The possibility of achieving population inversion in silicon nanowires as discussed in Chapter 5 is promising the implementation of silicon nanowire-based lasers. Comparing with bulk (3D) and quantum well (2D) semiconductors, 1D nanostructures i.e. SiNWs are advantageous due to [169]:

- (a) Less threshold current
- (b) Less sensitivity of threshold current to the temperature
- (c) Less amount of wavelength (color) change with the injected current (lower chirp)
- (d) Narrower gain spectrum due to sharp 1D density of states (DOS)
- (e) Easier tuning of the wavelength by changing the diameter or applying strain

On the other hand interaction of electronic states in quantum dots with the surrounding environment poses different problems. For example the emitted photon from a quantum dot wanders randomly in frequency [170]. This causes spectral broadening as well as random on-off (blinking) of the emitted light in the time domain [171]. Motivated by the aforementioned studies, the main goal of this chapter is the computational study of photo absorption in SiNWs and its dependence on parameters like diameter, crystallography and strain. Due to the equivalence of the stimulated emission rate and absorption rate i.e. ( $R_{stim}=R_{abs}$ ), this study will automatically lead to the calculation of gain spectrum in SiNWs as well. It is noteworthy that the study of photo absorption in SiNWs is the first step to move to the next level of including nonlinearities (e.g. multi-photon absorption) and investigating the possibility of enhancing the nonlinear susceptibilities in SiNWs by strain (see future work in Chapter 7).

In this chapter we start from the quantum mechanical formulation of the dielectric function of semiconductors and reformulate it for a nanowire by including 1D Joint Density of States (JDOS) and using tight binding wave functions for conduction and valence states of SiNWs. The reasons of choosing TB method in our studies have been already discussed in sub section 5.6.4 of Chapter 5. It is noteworthy again that bandgap underestimation in DFT makes direct comparison of absorption of SiNWs with that of bulk silicon less straightforward. On the other hand TB has already shown success in reproducing the band structure of bulk silicon as well as the experimental shift of PL spectrum due to strain [37][67].

The absorption spectrum can then be found using both real and imaginary parts of the dielectric functions. The real part of the dielectric function is calculable from the imaginary part using Kramers-Krönig integrals. Also using the effective mass approximation (EMA) significantly increases the calculation speed in contrast to the fully numerical approach. After it is shown that both methods have agreeable results, the effect of diameter, photon polarization, crystallography, and axial strain on the photo absorption of SiNWs are investigated.

In this work we have not calculated the phonon-assisted absorption spectrum in indirect bandgap nanowires. Hence the effect of strain on the absorption arises due to the change of wave function symmetry only and not due to direct to indirect bandgap conversion. Calculating the absorption in indirect bandgap semiconductors has been already discussed in the literature for example in [146][172][173][174]. Also a recent DFT study reports the calculation of absorption spectrum (phonon assisted part) in bulk silicon using the second order perturbation theory [175]. In this chapter the DFT method implemented in SIESTA package is used to calculate the direct part of the absorption spectrum of bulk silicon. A comparison is then made with the TB result as well as experimental data. Next it is shown how to adapt the photo absorption formulations to calculate the optical gain in SiNWs. This proves useful in obtaining the first estimation of lasing parameters for a SiNW-based laser.

This chapter is organized by starting from the review of methods, reformulating the numerical and semi-analytic absorption for SiNWs and calculation of bulk silicon absorption. The second part contains the results and discussions. The third part is devoted to the formulation of optical gain for a 1D nanostructure. The fourth part introduces the experimental methods of measuring the absorption in nanowires.

## 6.1 Methods

Calculation of the absorption is closely related to the calculation of dielectric function of the material. In macroscopic point of view this quantity is generally a tensor which relates the displacement vector ( $D$ ) and the applied electric field ( $E$ ) through:

$$D_{\alpha}(\mathbf{q}, \omega) = \epsilon_{\alpha\beta}(\mathbf{q}, \omega)E_{\alpha}(\mathbf{q}, \omega) \quad (6.1)$$

For anisotropic solids (non-cubic crystals) the non-diagonal elements of  $\epsilon_{\alpha\beta}$  are nonzero.  $\omega$  and  $\mathbf{q}$  are frequency and wave vector of the AC electromagnetic field. In addition to the above constitutive equation, the electric field can induce a current density ( $J$ ) in the material through the following equation:

$$J_{\alpha}(\mathbf{q}, \omega) = -\frac{i\omega}{4\pi}[\epsilon_{\alpha\beta}(\mathbf{q}, \omega) - \delta_{\alpha\beta}]E_{\alpha}(\mathbf{q}, \omega) \quad (6.2)$$

$\delta_{\alpha\beta}$  represents a diagonal unit matrix (tensor). The above macroscopic equation is used in conjunction with the perturbation theory to find the dielectric function of the material microscopically. Therefore knowing the band structure of the material and all electronic states are necessary. Quantum mechanical treatment of dielectric function of solid was first demonstrated in [176][177] and [178]. Later this method was used for calculation of optical properties in bulk copper [179] and silicon nano crystals [180]. Here the procedure presented in [178] is introduced briefly because of its instructive value. In this method the single particle Hamiltonian of the periodic solid is perturbed by time dependent magnetic and electric potentials i.e.  $\mathbf{A}(\mathbf{r},t)$  and  $V(\mathbf{r},t)$ , respectively.

$$\mathcal{H} = \frac{1}{2m} [\mathbf{p} + \left( \frac{e\mathbf{A}(\mathbf{r},t)}{c} \right)]^2 + V(\mathbf{r},t) + U(\mathbf{r}) \quad (6.3)$$

The unperturbed periodic potential of the atoms in crystal is shown by  $U(\mathbf{r})$ . Since the typical laser powers used in the PL studies (see Chapter 1) is in the  $\text{kW}/\text{cm}^2$  range it is possible to ignore the nonlinear perturbation terms i.e.  $A^2$ , and retain the linear terms only. The response of the electrons in the solid to the perturbations manifests itself as the change of charge and current density i.e.  $\rho(\mathbf{r},t)$  and  $\mathbf{J}(\mathbf{r},t)$ , respectively. It is noteworthy that since the charge and current density are related through the continuity equation,  $\text{div}.\mathbf{J} + \partial\rho/\partial t = 0$ , calculation of both quantities is not necessary i.e. finding  $\rho(\mathbf{r},t)$  is sufficient.

The next step is using the Liouville equation which describes the time evolution of the single particle density matrix ( $\wp$ ) according to:

$$i\hbar \partial\wp/\partial t = [\mathcal{H}, \wp] \quad (6.4)$$

Density matrix formalism is explained in section 1.7 of [169]. In this formalism the expectation value of a given operator (observable),  $\mathbf{A}$ , can be calculated simply using  $\langle \mathbf{A} \rangle = \text{Trace}(\wp \mathbf{A})$ . Equation 6.4 can be linearized with respect to  $\mathbf{A}$  and  $V$  by writing the density matrix as  $\wp = \wp^0 + \wp^1$  where the first and the second term correspond to the unperturbed and perturbed density matrix, respectively. The unperturbed part is already known from the following equation:

$$\wp^0 |\mathbf{k}l\rangle = f_0(E_{kl}) |\mathbf{k}l\rangle \quad (6.5)$$

The Fermi-Dirac factor is shown as  $f_0$ .  $\mathbf{k}$  and  $l$  represent the electron wave vector and quantum number (band index) of the unperturbed electronic state i.e.  $|\mathbf{k}l\rangle$  which is given as:

$$|\mathbf{k}l\rangle = \frac{1}{\sqrt{V}} e^{i\mathbf{k} \cdot \mathbf{r}} u_{kl} \quad (6.6)$$

$V$  is the volume of the crystal and  $u_{kl}$  shows the cell-periodic part (Bloch part) of the electronic state. Having the first order perturbed part of density matrix ( $\rho^1$ ), the induced charge density can be found using:

$$\rho^{ind}(\mathbf{r}, t) = \text{Trace}(\rho^1) \rho_{op}^0(\mathbf{r}) \quad (6.7)$$

$\rho_{op}^0(\mathbf{r})$  is quantum mechanical charge density operator given as  $\rho_{op}^0(\mathbf{r}) = e\delta(\mathbf{r} - \mathbf{r}_e)$  where  $e$  and  $r_e$  represent charge of electron and its position in the crystal, respectively. Inserting  $\rho$  into equation (6.4) and multiplying it from right (left) by  $|\mathbf{k}\mathbf{l}\rangle$  ( $\langle\mathbf{k} + \mathbf{q} \mathbf{l}'|$ ) make it possible to find  $\rho^1$  and  $\rho^{ind}(\mathbf{r}, t)$ , subsequently. The quantum number of the new state is shown by  $l'$  and the wave vector change of electron is due to the photon which has the wave vector of  $\mathbf{q}$ . Using  $\rho^{ind}(\mathbf{r}, t)$  and continuity equation the value of  $J^{ind}(\mathbf{r}, t)$  is known at this stage. Finally  $\epsilon(\mathbf{q}, \omega)$  can be calculated using constitutive equation of (6.2) by knowing  $J^{ind}(\mathbf{r}, t)$ .

If it is assumed that the wavelength of the incoming light is larger than the unit cell length ( $U_c$ ) of the solid ( $\lambda \gg U_c$ ), then it can be said that  $q=2\pi/\lambda$  is zero and the dielectric tensor is given as:

$$\epsilon(0, \omega) = 1 - \frac{4\pi e^2 N}{mV\omega^2} + \frac{4\pi e^2}{m^2 V \omega^2} \sum_{ll'k} \frac{|\langle l k | P | l' k \rangle|^2 f_0(E_{l'k}) - f_0(E_{lk})}{\hbar\omega + E_{l'k} - E_{lk} + i\eta} \quad (6.8)$$

$N$  is the number of unit cells in the crystal and  $\eta$  is the broadening factor.

In the process of obtaining equation (6.8) the local field effect was ignored i.e. it was assumed that there is no distinction between macroscopic and microscopic potentials and electric fields. Otherwise a microscopic potential,  $V^{ind}(\mathbf{r}, t)$ , is induced from the macroscopic excitation which is  $V(\mathbf{r}, t)$ . Hence before starting the previous procedure (e.g. equation 6.7),  $V^{ind}(\mathbf{r}, t)$  must be first calculated from  $V(\mathbf{r}, t)$  using perturbation theory. Later on  $V^{ind}(\mathbf{r}, t)$  enters the main procedure as a new perturbation (as if LFE was not included). In addition to ignoring LFE and assuming a linear response, the following assumptions are made before we proceed to the next stage.

- (a) Nanowire is assumed to be an isotropic media i.e.  $\mathbf{D}$  is always parallel with  $\mathbf{E}$ . This is because for cubic crystals like silicon the dielectric tensor is isotropic.
- (b) Although equation (6.8) is general and it includes both intra and inter sub band transitions, however inter subband transitions are considered only for SiNWs. This is because the bandgap of SiNWs is large and at room temperature the conduction band is empty. Hence  $l$  and  $l'$  span valence and conduction sub bands, respectively. On the other hand for materials like Bismuth the bandgap of



nanowire is 123meV which means the conduction band has significant number of electrons and transitions like  $C_1$  to  $C_2$  and  $C_1$  to  $C_3$  etc. are possible.

- (c) Due to (b)  $f_0(E_{lk}) = 0$  and  $f_0(E_{l'k}) = 1$  which means that the conduction band is empty and the valence band is full. This is equivalent of assuming  $T=0$  K for SiNW too. The absorption which is calculated by this assumption is called *intrinsic* absorption.

Finding the imaginary part of  $\varepsilon(0, \omega)$  (equation 6.8) is straightforward. Converting CGS to SI unit (multiplying to  $1/4\pi\epsilon_0$ ) and using the Lorentzian approximation of Dirac's delta function (equation 6.9), results in equation (6.10) which is also used in [45][181].

$$\delta(\hbar\omega + E_{lk} - E_{l'k}) = \frac{1}{\pi} \frac{\eta}{(\hbar\omega + E_{l'k} - E_{lk})^2 + \eta^2} \quad (6.9)$$

$$\varepsilon_2(\omega) = \text{imag}(\varepsilon(0, \omega)) = \frac{\pi e^2}{\epsilon_0 m^2 V \omega^2} \sum_{ll'k} |\langle u_{lk} | \hat{\mathbf{e}} \cdot \mathbf{P} | u_{l'k} \rangle|^2 \delta(\hbar\omega + E_{l'k} - E_{lk}) \quad (6.10)$$

$\hat{\mathbf{e}}$  is a unit vector parallel with the photon polarization and  $\epsilon_0$  is dielectric permittivity of vacuum. As already discussed in Chapter 4, the momentum matrix element can be converted to its position representation.

### 6.1.1 Numerical Method

The one dimensional band structure of SiNW allows more simplification of the equation 6.10 for numerical calculation. In case of nanowire,  $\mathbf{k}$  is a 1D vector along the axis of the SiNWs (z axis) i.e.  $\mathbf{k} = k\hat{z}$  and summation over  $\mathbf{k}$  is reduced to:

$$\sum_{\mathbf{k}} \dots = 2 \times \frac{L_{nw}}{2\pi} \int_{1D \text{ BZ}} \dots dk \quad (6.11)$$

Where  $L_{nw}$  is the length of the nanowire and extra factor of 2 takes the spin degeneracy into account. Let  $E_{cv}(\mathbf{k}) = E_c(\mathbf{k}) - E_v(\mathbf{k})$  (note that  $l$  and  $l'$  are now replaced by  $v$  and  $c$ ). Now Dirac's delta function can be expanded using the roots of the following equation:

$$E_{cv}(\mathbf{k}) - \hbar\omega = 0 \quad (6.12)$$

As a result we have:

$$\delta(E_{cv}(k) - \hbar\omega) = \sum_{Kzp} \frac{\delta(k - Kzp)}{\left| \frac{\partial E_{cv}(k)}{\partial k} \right|} \quad (6.13)$$

Using equation 6.13, the dielectric function (equation 6.10) can be written as:

$$\epsilon_2(\omega) = \frac{e^2}{\epsilon_0 m_0^2 A_{nw} \omega^2} \sum_{c,v} \int_k |\langle u_c | \hat{e} \cdot \bar{\mathbf{P}} | u_v \rangle|^2 \sum_{Kzp} \frac{\delta(k-Kzp)}{\left| \frac{\partial E_{cv}(k)}{\partial k} \right|} dk \quad (6.14)$$

By interchanging the integration and the last summation and using the sifting property of Dirac's delta we may write:

$$\epsilon_2(\omega) = \frac{2e^2}{\epsilon_0 m_0^2 A_{nw} \omega^2} \sum_{c,v} \sum_{Kzp \geq 0} \frac{|\langle u_c | \hat{e} \cdot \bar{\mathbf{P}} | u_v \rangle|^2}{\left| \frac{\partial E_{cv}(k)}{\partial k} \right|_{@Kzp \geq 0}} \quad (6.15)$$

Where  $A_{nw}$  is the cross sectional area of the nanowire. Corresponding to each polarization direction ( $\hat{e} = x, y, z$ ) there are three values for dielectric function. After calculation of the band structure and Eigen states with  $sp^3d^5s^*$  tight binding method (see Chapters 2 and 4), all possible combinations of valence to conduction transitions (i.e.  $E_{cv}$  and corresponding matrix elements  $\langle u_c | \hat{e} \cdot \bar{\mathbf{P}} | u_v \rangle$ ) are found for all given  $k$  values along the BZ. The method of implementing equation 6.15 is depicted in Figure 6.1 for an example of a band structure having 2 and 3 valence and conduction bands, respectively. If the nanowire has 2 valence bands and 3 conduction bands with 100 points along the BZ ( $0$  to  $\pi$ ), then it is required to store 600 different values for  $E_{cv}$  and optical matrix element. Now at each value of frequency ( $\omega$ ) we search for the number of  $k$  points at which  $E_{cv}(k) = \hbar\omega$ . According to Figure 6.1 this is equivalent to finding how many times the modified band structure i.e.  $E_{cv}(k)$  crosses the horizontal  $\hbar\omega$  line.

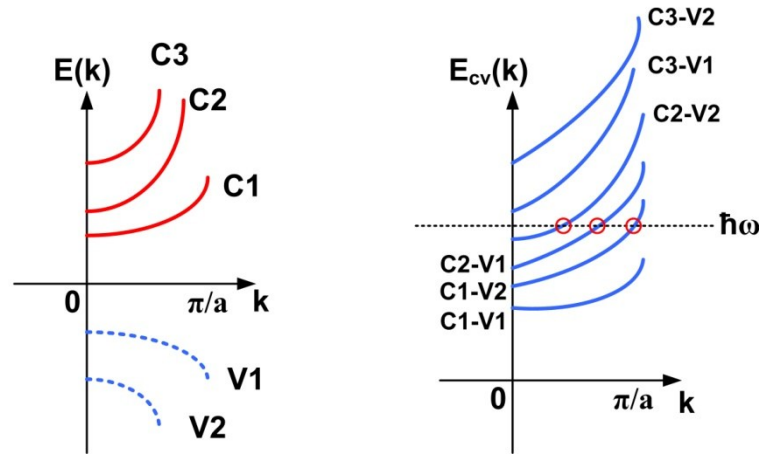


Figure 6.1 Method of finding the number of available transitions (c and v combinations) corresponding to each given photon energy  $\hbar\omega$ .

In order to calculate the absorption,  $\alpha(\omega)$ , firstly it is required to calculate the extinction ratio,  $\kappa(\omega)$ . The extinction ratio can be expressed in terms of real part and imaginary part of

dielectric function i.e.  $\epsilon_1(\omega)$  and  $\epsilon_2(\omega)$ , respectively. Since the imaginary part of dielectric function has been already calculated, it is possible to find the real part by applying the Kramers-Krönig theorem [169]. We first show how this results in a formulation for  $\epsilon_1(\omega)$  which is then evaluated numerically. To show this, equation 6.10 is directly inserted into the Kramers-Krönig integral as follows:

$$\begin{aligned}
\epsilon_1(\omega') &= 1 + \frac{2}{\pi} P \left( \int_0^\infty \frac{\epsilon_2(\omega) \omega d\omega}{\omega^2 - \omega'^2} \right) \\
&= 1 + \frac{2}{\pi} P \left( \int_0^\infty \frac{\pi e^2}{\epsilon_0 m_0^2 V \omega^2} \sum_{c,v} \sum_k |\langle u_c | \hat{e} \cdot \bar{\mathbf{P}} | u_v \rangle|^2 \delta(E_{cv}(\mathbf{k}) - \hbar\omega) \frac{\omega d\omega}{\omega^2 - \omega'^2} \right) \\
&= 1 + \frac{2e^2}{\epsilon_0 m_0^2 V} P \left( \int_0^\infty \sum_{c,v} \sum_k |\langle u_c | \hat{e} \cdot \bar{\mathbf{P}} | u_v \rangle|^2 \delta(E_{cv}(\mathbf{k}) - \hbar\omega) \frac{d\omega}{\omega(\omega^2 - \omega'^2)} \right) \\
&= 1 \\
&\quad + \frac{2e^2}{\epsilon_0 m_0^2 V} \sum_{c,v} \sum_k |\langle u_c | \hat{e} \cdot \bar{\mathbf{P}} | u_v \rangle|^2 \int_0^\infty \delta(E_{cv}(\mathbf{k}) - \hbar\omega) \frac{\hbar^2 d\hbar\omega}{\hbar\omega((\hbar\omega)^2 - (\hbar\omega')^2)}
\end{aligned}
\tag{6.16}$$

Further simplification is possible using sifting property of Dirac's delta and converting the summation over  $k$  vectors to an integration.

$$\epsilon_1(\omega') = 1 + \frac{4e^2 \hbar^2}{\pi \epsilon_0 m_0^2 A_{nw}} \sum_{c,v} \int_{k=0}^{k=\pi} |\langle u_c | \hat{e} \cdot \bar{\mathbf{P}} | u_v \rangle|^2 \frac{dk}{E_{cv}(\mathbf{k})((E_{cv}(\mathbf{k}))^2 - (\hbar\omega')^2)} \tag{6.17}$$

Evaluating equation 6.17 requires three summation loops. The first loop runs over the incoming light frequencies ( $\omega'$ ). The second loop runs over all combinations of valence to conduction band transitions ( $cv$ ) and the third loop runs over all discrete  $k$  points along the BZ (0 to  $\pi$ ). After this step both real and imaginary parts of the dielectric function are used to find the extinction ratio ( $\kappa$ ) and refractive index ( $n$ ) of SiNW according to:

$$\kappa = \sqrt{\frac{\epsilon_1^2 + \epsilon_2^2 - \epsilon_1}{2}} \quad \& \quad n = \sqrt{\frac{\epsilon_1^2 + \epsilon_2^2 + \epsilon_1}{2}} \tag{6.18}$$

The relation between the absorption coefficient and the extinction ration is given as follows [169]:

$$\alpha(\omega) = \frac{4\pi\kappa(\omega)}{\lambda_0} = \frac{4\pi\kappa(\omega)}{c/f} = \frac{2\omega\kappa(\omega)}{c} \quad (6.19)$$

### 6.1.2 Semi-analytic Method to Calculate Absorption

As discussed in the previous section implementing equations 6.15 and 6.17 requires storing all combinations of valence to conduction transitions (i.e. storing the corresponding energy differences and matrix elements) which renders the fully numerical method very slow. In this section a simpler semi-analytic formulation is presented with which a good approximation of absorption can be found in a shorter amount of time. The simplifying assumptions are as follows:

*Firstly* it is assumed that the band structure is of hyperbolic shape with an assigned effective mass for each band. Therefore energy of each band can be written in effective mass theory formalism as:

$$E_c(k) = E_{cmin} + \frac{\hbar^2 k^2}{2m_c^*}, E_v(k) = E_{vmax} - \frac{\hbar^2 k^2}{2m_v^*} \rightarrow E_{cv}(k) = E_g + \frac{\hbar^2 k^2}{2\mu_{cv}} \quad (6.20)$$

where  $\mu_{cv}$  is the reduced effective mass of conduction and valence band pair i.e.  $\mu_{cv} = \frac{m_c^* m_v^*}{m_c^* + m_v^*}$

*Secondly* it is assumed that the optical matrix element around BZ center is almost constant i.e. its value does not depend on the electron wave vector ( $k$ ). As a result for a given combination of bands (e.g.  $c_i$  and  $v_j$ ), matrix element of transitions at each  $k$  value is equal to the matrix element value given at  $k=0$  i.e.:

$$|\langle u_c | \hat{e} \cdot \bar{\mathbf{P}} | u_v \rangle|^2 = |\langle u_c | \hat{e} \cdot \bar{\mathbf{P}} | u_v \rangle|_{@kz=0}^2 = |\mathbf{P}_{cv}(kz=0)|^2 \quad (6.21)$$

With these assumptions, equation 6.15 is reduced to:

$$\epsilon_2(\omega) = \frac{2e^2}{\epsilon_0 m_0^2 A_{nw} \omega^2} \sum_{c,v} \frac{|\mathbf{P}_{cv}(kz=0)|^2}{\left| \frac{\hbar^2 k}{2\mu_{cv}} \right|} \quad (6.22)$$

The summation over  $k_{zp}$  is not required here since the horizontal line of  $\hbar\omega$  always intersects each  $E_{cv}(k)$  at one point. The next crossing due to the next  $E_{cv}(k)$  is already taken into account in the summation over  $cv$  in equation 6.22. This equation can be simplified by replacing  $k$  with the following value:

$$k = \frac{\sqrt{2\mu_{cv}}}{\hbar} \sqrt{E_{cv}(k) - E_{g,cv}} = \frac{\sqrt{2\mu_{cv}}}{\hbar} \sqrt{\hbar\omega - E_{g,cv}} \quad (6.23)$$

Where  $E_{g,cv}$  represents the minimum of  $E_{cv}(k)$  [i.e.  $E_{cv}(k_z=0)$ ] for the corresponding  $cv$  index. For example in Figure 6.1,  $E_{g,cv}$  spans six values hence equation 6.23 is reduced more to the following equation in which the summation adds the six terms sequentially.

$$\epsilon_2(\omega) = \frac{2e^2}{\epsilon_0 m_0^2 A_{nw} \omega^2} \sum_{c,v} \frac{|P_{cv}(kz=0)|^2 \sqrt{2\mu_{cv}}}{\hbar \sqrt{\hbar\omega - E_{g,cv}}} = \frac{2\sqrt{2}e^2}{\epsilon_0 m_0^2 A_{nw} \omega^2 \hbar} \sum_{c,v} \frac{|P_{cv}(kz=0)|^2 \sqrt{\mu_{cv}}}{\sqrt{\hbar\omega - E_{g,cv}}} \quad (6.24)$$

Implementation of the above equation requires two nested loops. The first runs over photon energy values,  $\hbar\omega$ , and the second runs over all different combinations of conduction and valence band ( $cv$ ) with their corresponding energy difference and optical matrix element given at  $k_z=0$  only. Therefore this method is more advantageous over the fully numerical method (equation 6.15) if we prove that both methods give reasonably similar results. To obviate the singularities at  $\hbar\omega = E_{g,cv}$ , we can use the following approximation by introducing a broadening factor of  $\eta$  [45]:

$$\frac{1}{\sqrt{x}} \cong \frac{1}{\sqrt{x+i\eta}} = \frac{\sqrt{x-i\eta}}{\sqrt{x^2+\eta^2}} \cong \text{real}\left(\frac{\sqrt{x-i\eta}}{\sqrt{x^2+\eta^2}}\right) \quad (6.25)$$

Similar to the method presented in section 6.1.1, the real part of the dielectric function is found by inserting equation 6.24 into Kramers-Krönig integral.

$$\epsilon_1(\omega) = 1 + \frac{4\sqrt{2}e^2}{\pi\epsilon_0 m_0^2 A_{nw} \omega^2 \hbar} \sum_{c,v} |P_{cv}(kz=0)|^2 \sqrt{\mu_{cv}} P\left(\int_0^\infty \frac{d\omega'}{\omega'(\omega'^2 - \omega^2) \sqrt{\omega' - \frac{E_{g,cv}}{\hbar}}}\right) \quad (6.26)$$

The right hand side of equation 6.26 can be simplified further using Wolfram Mathematica<sup>®</sup> online integrator available in (<http://integrals.wolfram.com/index.jsp>). However in this work we have used the code which is available from [182]. This code receives  $\epsilon_2(\omega)$  as an input vector and directly applies Kramers-Krönig integral to return  $\epsilon_1(\omega)$  as the output vector. Calculating extinction ratio and absorption are then completed using equations 6.18 and 6.19.

### 6.1.3 Direct Absorption in Bulk Silicon

Comparing the absorption spectra calculated by tight binding and DFT methods, reveals the differences between these methods and their degree of success in reproducing the experimental data. Although the absorption in the band edge of bulk silicon is of indirect nature, here we focus on generating the absorption for those portions of spectrum in which direct transition is possible. The indirect (phonon-assisted) part of the absorption spectrum in bulk silicon was already calculated by J. Noffsinger et al in [175].

Since the integration over the 3D BZ of bulk silicon is time consuming, the calculation of Eigen states and absorption can be confined to an irreducible wedge as shown in Figure 6.2. Since this wedge is 1/48'th of the whole BZ, the calculated quantities within this wedge must

be weighted correctly. The precision of calculation increases by increasing the number of points (samples) taken from the wedge.

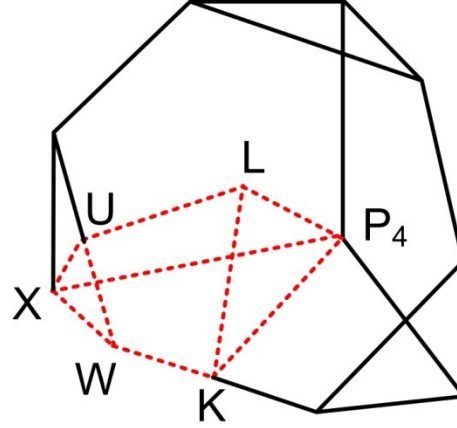


Figure 6.2 The first BZ of the reciprocal lattice with emphasis on the first octant (solid line) which carries: (b) the first irreducible wedge (dashed line).

Calculation of direct absorption in bulk silicon starts with the calculation of Eigen states and Eigen energies. In this step a discrete 3D  $k$ -space is built by dividing the 3D space of  $(0, 2\pi/a) \times (0, 2\pi/a) \times (0, 2\pi/a)$  into  $N_x \times N_y \times N_z$  points. The unit cell of bulk silicon is  $a = 5.43 \text{ \AA}$ . Then a search routine is used to find those  $(k_x, k_y, k_z)$  from this space which are surrounded by the five faces of the wedge given by the following equations [183]:

$$k_x + k_y + k_z = \frac{3}{2} \frac{2\pi}{a} \quad \& \quad k_x = k_z \quad \& \quad k_y = k_z \quad \& \quad k_z = \frac{2\pi}{a} \quad \text{and} \quad k_z = 0 \quad (6.27)$$

Then  $N_w$  triplets of  $(k_x, k_y, k_z)$  are found within the wedge which are saved for the next step of Eigen state/energy calculation. Forming the  $20 \times 20$  tight binding Hamiltonian matrix for bulk silicon was previously explained in Appendix B. Therefore for each triplet of  $(k_x, k_y, k_z)$  within the wedge, the total Hamiltonian (equation B1 of Appendix B) is filled and the Eigen problem of  $(H\psi = E\psi)$  is solved. It is noteworthy that corresponding to each triplet, 20 Eigen states and Eigen-energies are found and saved in the structures depicted in Figure 6.3. For bulk silicon, the first 4 Eigen-states and energies belong to the valance band and the rest (16 states) compose the conduction band. Hence there are 64 possible valance to conduction band transitions at each given 3D  $k$  point within the irreducible wedge.

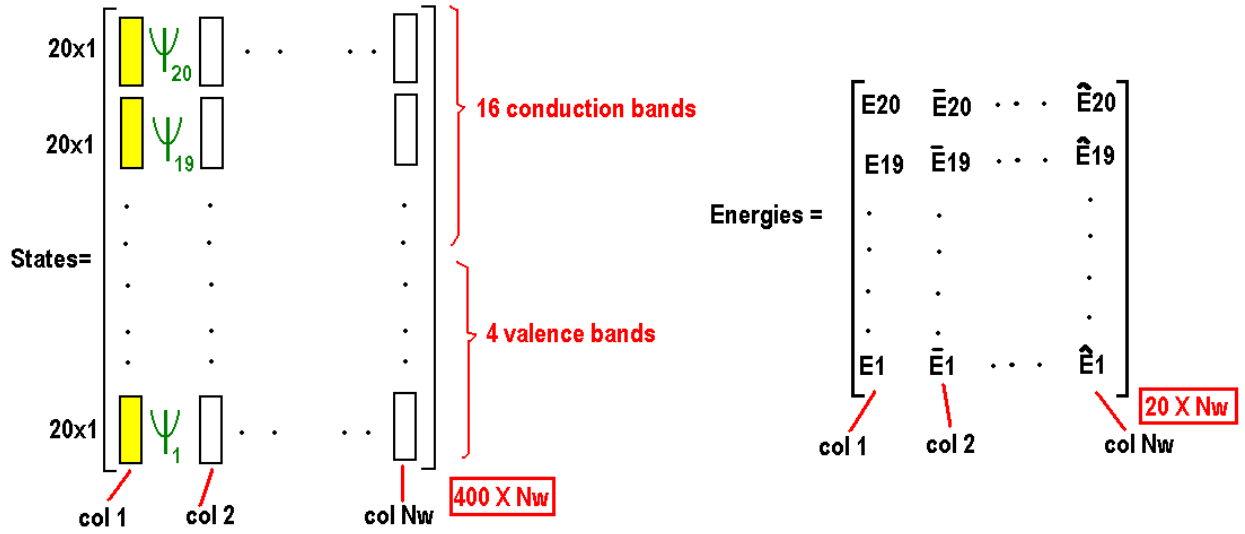


Figure 6.3 Format of saving the states and energies found for  $N_w$  triplets of  $(k_x, k_y, k_z)$  within the irreducible wedge.

Afterwards the equation 6.10 is used to find the imaginary part of dielectric function. After replacing the summation over  $\mathbf{k}$  with 3D integration and using the Lorentzian broadening function to approximate the Dirac delta function, we have:

$$\epsilon_2(\omega) = \frac{\pi e^2}{\epsilon_0 m_0^2 V \omega^2} \sum_{c,v} \frac{2 \times V \times 48}{8\pi^3} \int_{\bar{K}} |\langle u_c | \hat{e} \cdot \bar{\mathbf{P}} | u_v \rangle|^2 \frac{\gamma/\pi}{(E_{cv}(\mathbf{k}) - \hbar\omega)^2 + \gamma^2} d^3k \quad (6.28)$$

where  $\gamma$  is the broadening with the value of 10-20 meV and the element of volume is  $d^3k = dk_x dk_y dk_z$ .

$$\epsilon_2(\omega) = \frac{16e^2\gamma}{\pi^3 \epsilon_0 m_0^2 \omega^2} \sum_{c,v} \int_{\bar{K}} |\langle u_c | \hat{e} \cdot \bar{\mathbf{P}} | u_v \rangle|^2 \frac{d^3k}{(E_{cv}(\mathbf{k}) - \hbar\omega)^2 + \gamma^2} \quad (6.29)$$

Implementing equation 6.29 requires three loops corresponding to the photon energy ( $\omega$ ), 64 combinations of sub bands ( $cv$ ) and  $N_w$  values of  $\mathbf{k}$  triplets within the wedge. The Kramers-Krönig code given in [182] is used to find the real part of the dielectric function from equation (6.29). The total absorption is found by adding three values corresponding to three different polarizations (x, y, z). The calculation of  $\epsilon_2(\omega)$  with DFT method was implemented in SIESTA code. The result were post processed using available Fortran codes (*optical.f* and *output.f*) to find  $\epsilon_1(\omega)$  as well as  $\alpha(\omega)$ . Details of the methods to calculate the absorption spectrum can be found in SIESTA manual [136].

## 6.2 Results & Discussions

### 6.2.1 Absorption in bulk Silicon

Absorption spectrum of bulk silicon is calculated by TB and it is compared with experimental data [184] in Figure 6.4. Firstly it is observed that the TB-based absorption spectrum starts at 3.42 eV which is consistent with the value of direct bandgap in bulk silicon. However DFT-based spectrum starts at a lower value and this is due to the well-known problem of underestimating the bandgap due to the LDA functional used in this method. Secondly the close match between the experimental data and TB and DFT results supports the application of tight binding method for studying the light absorption in SiNWs.

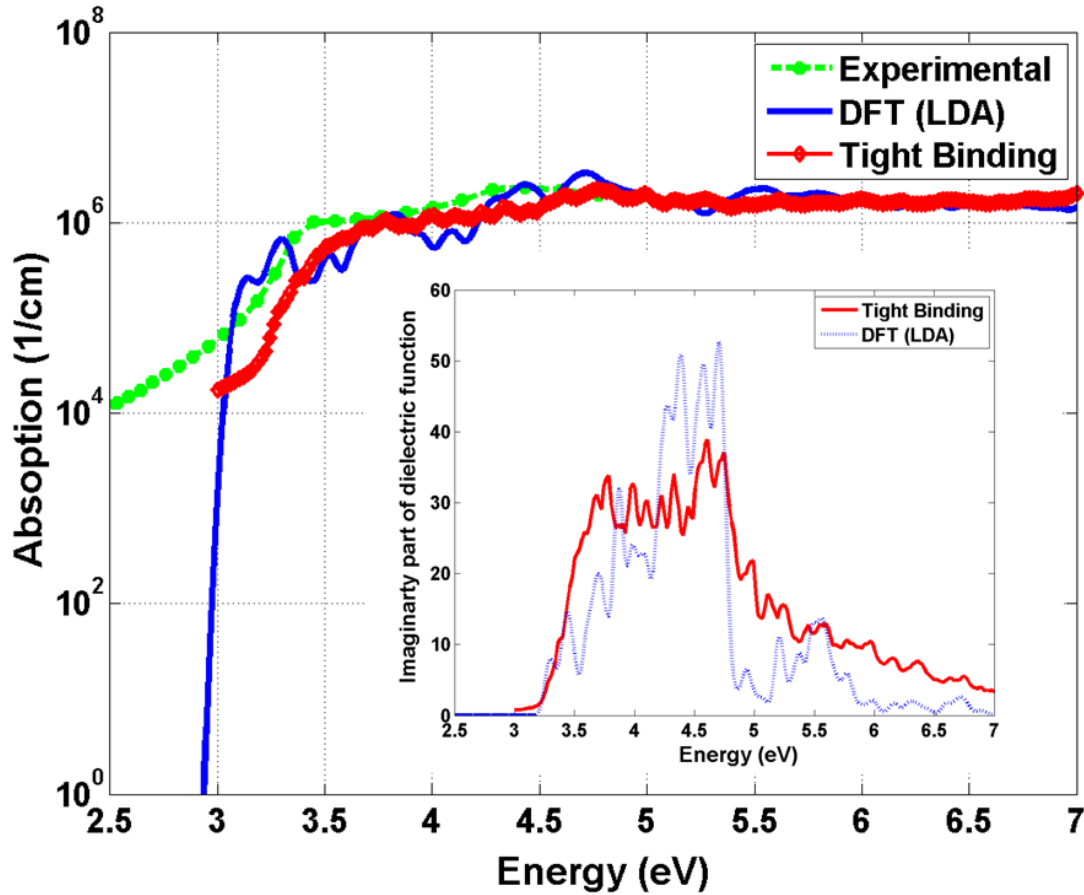


Figure 6.4 The absorption spectrum of bulk silicon was calculated by DFT and TB. A comparison was made with experimental data provided in [184]. Inset: Imaginary part of dielectric function of bulk silicon, ( $\epsilon_2(\omega)$ ), calculated by TB and DFT methods

The low energy tail ( $E < 3.24\text{eV}$ ) of the absorption spectrum which was calculated by TB method is the numerical artifact and it has no physical meaning. This arises because the low



energy skirts of many Lorentzian functions (last term of equation 6.29) were being added together and resulted in a non-zero value. Inset of Figure 6.4 shows the imaginary part of dielectric function,  $\epsilon_2(\omega)$ , calculated by TB and DFT methods. The results are in close agreement. The static dielectric constant for bulk silicon with TB is 10.1055 which is close to the experimental value of 11.9 at room temperature [185] and the values reported in [180] for different TB methods.

### 6.2.2 Comparison of Fully Numerical and Semi-analytic Methods

Figure 6.5 compares the absorption spectra calculated in the full numerical method (section 6.1.1) with those in the semi-analytic approach (section 6.1.2) for two different nanowires. Using the semi analytic method significantly reduces the calculation time. It is less than 1/10 of the time compared to the fully numerical method, which takes 1 hour and 8 hours to compute 0.5nm and 1.1nm [110] SiNWs, respectively. Since the values of sub-bandgap absorption is zero it cannot be shown in logarithmic plots. Also it is evident that smaller diameter nanowire ( $d=0.5\text{nm}$ ) has a larger bandgap value than the thicker one ( $d=1.1\text{ nm}$ ).

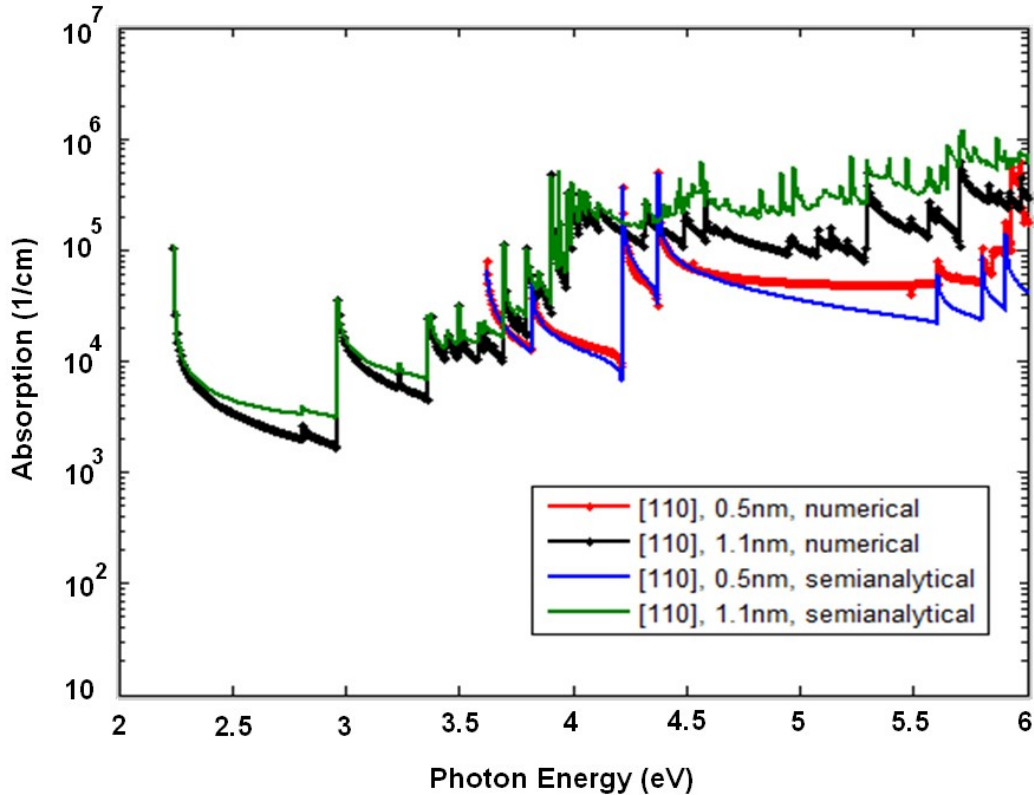


Figure 6.5 Comparison of the absorption spectra for 0.5nm and 1.1nm [110] SiNWs, calculated by fully numerical and semi-analytic methods.

In terms of accuracy it is apparent from Figure 6.5 that the semi-analytic approach can produce comparable results especially for energy values below 4.5eV. This is because the  $E_{cv}(k)$  fit to Effective Mass Approximation (EMA) for this energy range and beyond that the curves tend to have different or even negative curvature. However many of the peak positions still match even though the magnitudes do not. Overall, the semi-analytic method proves useful in quick calculation of absorption spectrum within energy ranges which are close to the band edge. Unless specified the absorptions calculated for SiNWs in this chapter (within tight binding scheme) are based on the semi-analytic method.

### 6.2.3 Anisotropy, Diameter and Strain

As it was observed in Chapter 5, [110] SiNWs have strong optical anisotropy. This means that the optical transition matrix element is stronger when the incident or emitted photon polarization is parallel with the nanowire axis. The same effect is observed in the band edge absorption spectrum of SiNWs. As Figure 6.6 shows the absorption for z polarized incoming photon is 6 orders of magnitude higher than the same quantity for x and y polarizations in a 1.7nm [110] SiNW. In photodetectors made from SiNWs this effect could make the induced photocurrent to be polarization dependent. This can have applications in the detection of polarized photons.

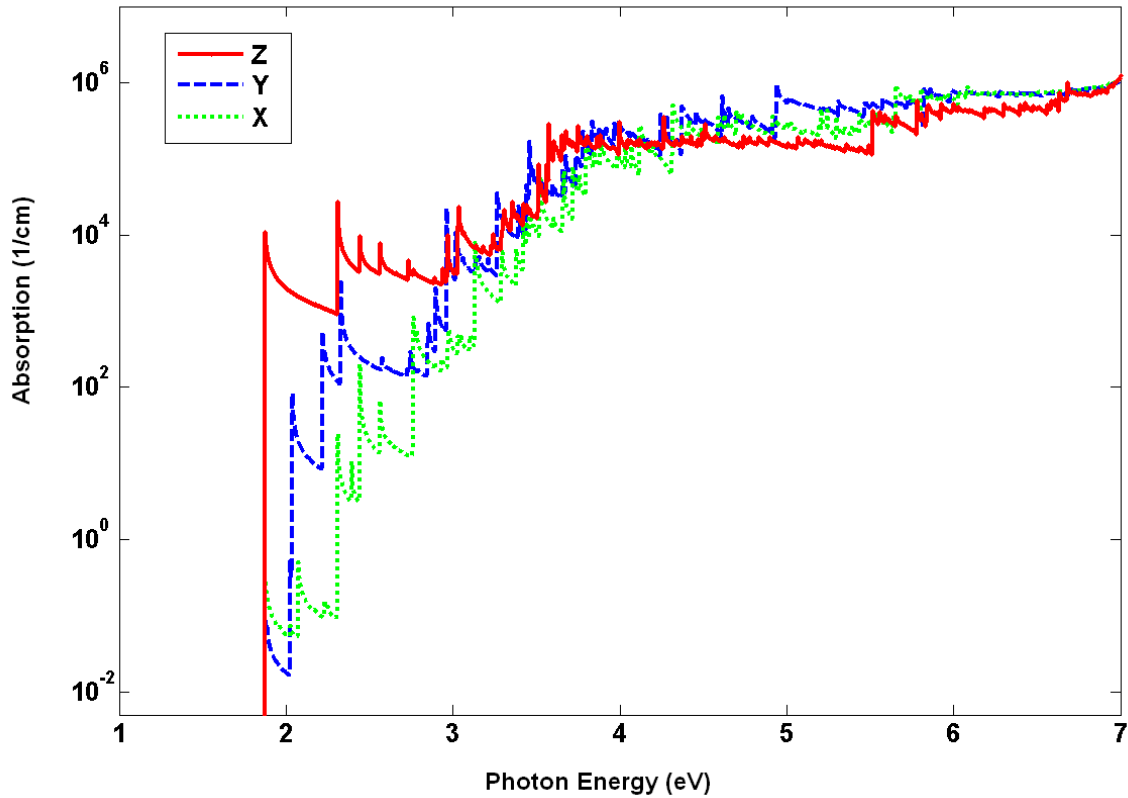


Figure 6.6 The absorption spectrum of a 1.7nm [110] SiNW for three different polarizations of the incoming photon.

As it was observed in Chapter 5 the z-polarized matrix elements had stronger role in determining the value of spontaneous emission time in 2.3nm and 3.1nm [110] SiNWs. This means that the value of absorption for z-polarized photon is also larger for these SiNWs. It is also noticed that the absorption is inversely proportional to the diameter of the nanowire, due to the decrease of optical dipole matrix element. Change of matrix element with diameter (confinement) has been explained using the particle in a box model and it was previously observed in the context of spontaneous emission time in Chapter 5. Figure 6.7 depict the absorption spectra of 1.7nm, 2.3nm and 3.1nm [110] SiNWs for z-polarized photon, showing that the band edge absorption is enhanced by narrowing down the diameter.

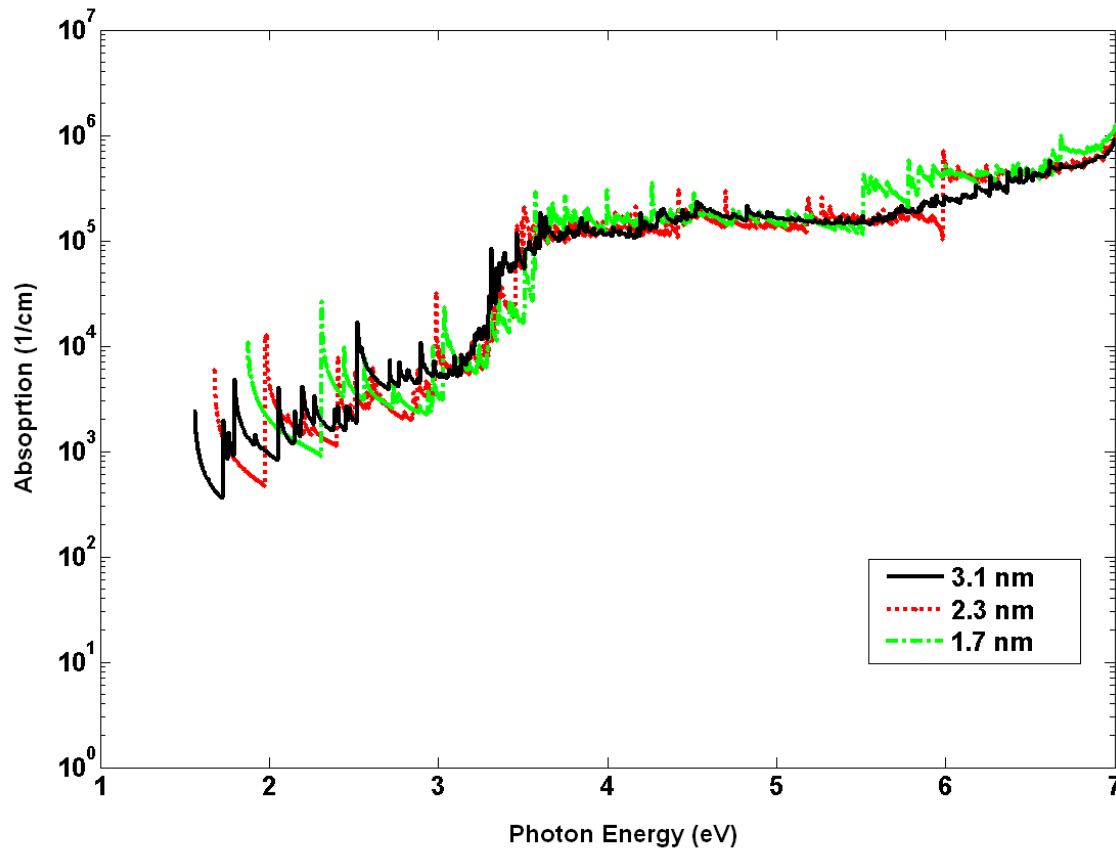


Figure 6.7 The absorption spectra of three SiNWs with different diameters (photon polarization is along the z axis).

For the sake of clarity the absorption spectrum in Figure 6.7 is magnified around the band edge in order to show the exact difference of 1.7nm, 2.3nm and 3.1nm [110] SiNWs absorption. As can be seen in Figure 6.8 the first absorption peak belongs to a 3.1nm [110]

SiNW. It has the smallest band edge absorption compared to the rest of the nanowires, because of its small matrix element value. Recall from Chapter 5 that one of the main strain effects on the spontaneous emission was through the change of optical transition matrix element which was in turn due to the change of wave function symmetry. As it was observed before, the symmetry of wave functions was almost intact in the tensile strain regime which resulted in very close values of spontaneous emission time for this regime. On the other hand by entering into compressive strain regime, the spontaneous emission time decreased a few orders of magnitude. This is due to the valance band flip which changed the wave function symmetry.

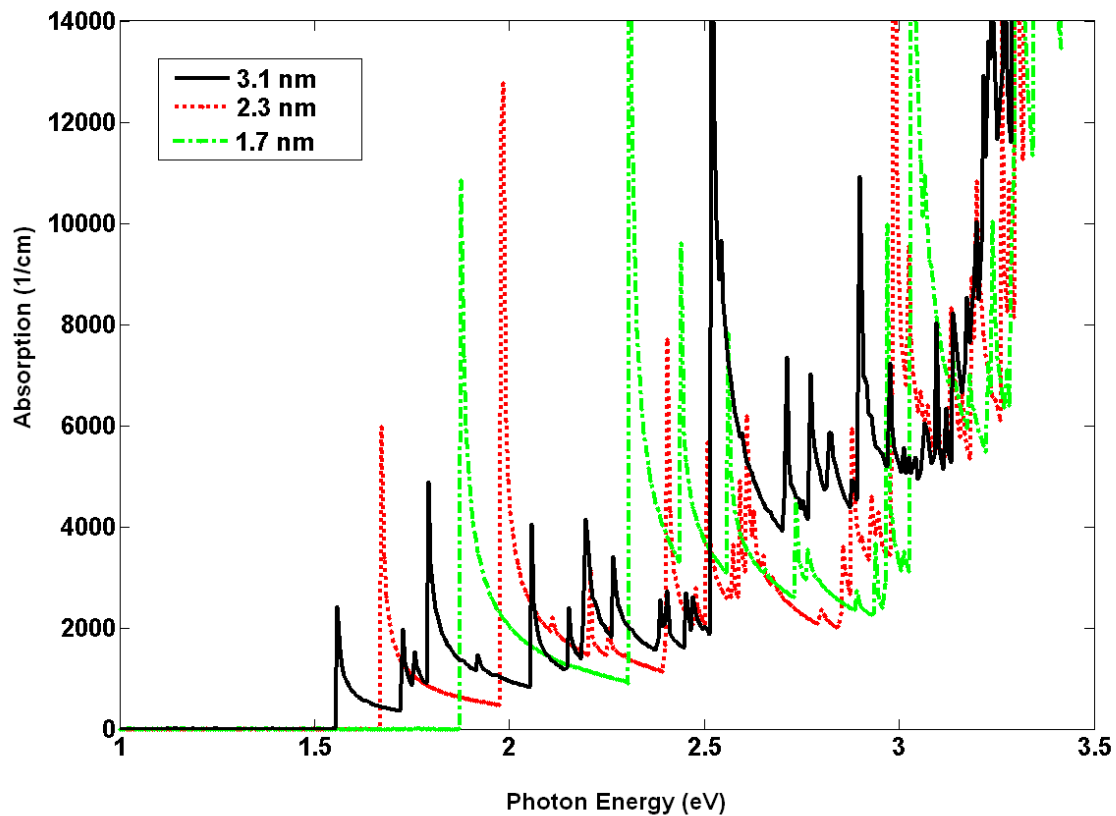


Figure 6.8 The magnified section of the absorption spectra around the bandgap energy which was shown in Figure 6.7. (Incoming photons are z polarized).

In the context of absorption we surmise that this mechanism can also cause a large amount of change in the absorption by entering into the compressive strain regime. Figure 6.9 shows the absorption spectrum of a 1.7nm [110] SiNW at -2%, 0% and +2% strain values. As it is evident the values of absorption for 0% and +2% strained nanowires are fairly close to each other, however for the compressively strained nanowire (-2%) we observe one order of

magnitude drop of absorption. This is due to the valence band interchange that was already discussed in Chapter 5. The normalized momentum matrix element value for 0% and +2% strained nanowires is 15meV while for -2% strained nanowire it is 1.5meV. This can explain one order of magnitude difference between absorption values at 0% and -2% strains.

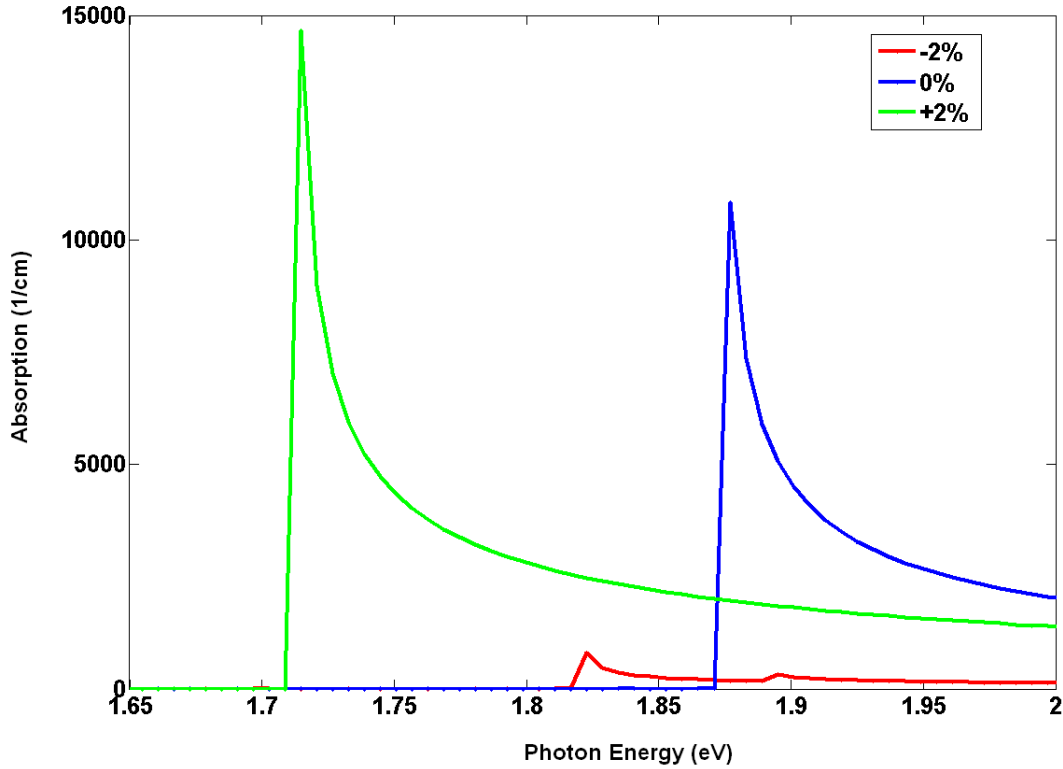


Figure 6.9 Absorption spectra for -2%, 0% and +2% strained 1.7nm [110] SiNW. (Incoming photons are z polarized).

#### 6.2.4 Bulk silicon vs. SiNW

Figure 6.10 compares the value of experimental absorption measured by [184] and the calculated value of absorption for a 2.3nm [110] SiNW under +5% strain. Since the unstrained bandgap of [110] nanowires in this work are more than that of bulk silicon, a strained nanowire is chosen for comparison purpose. The nanowire under study has a direct bandgap at 1.1eV hence it is expected to observe higher amount of absorption for this nanowire as opposed to bulk silicon which has an indirect bandgap at 1.1eV. For this nanowire it is assumed that the input light is polarized along the z axis. As it is expected in the energy range of 1-2 eV, the nanowire has greater amount of absorption than bulk silicon. Within this range the absorption process in bulk silicon is a second order and slow process mediated by phonons. Additionally by looking at Figure 6.8 it is evident that at for 1.7nm

SiNW at  $E_g=2\text{eV}$  the value of absorption is  $140000\text{ cm}^{-1}$  which is 3~4 times larger than that of bulk silicon at the same value energy.

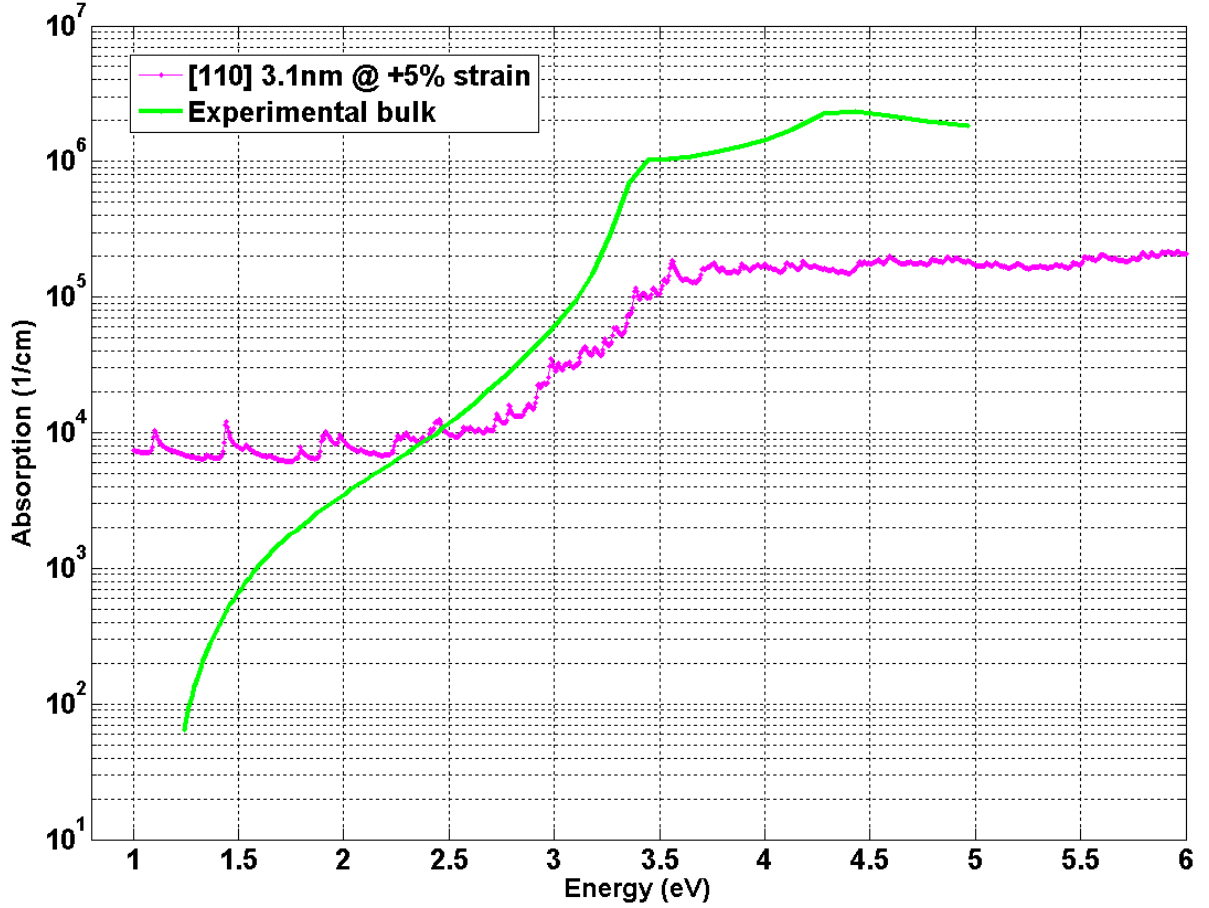


Figure 6.10 Comparison of the bulk silicon absorption spectrum (experimental) with that of a 2.3nm [110] SiNW at +5% strain (tight binding calculation)

### 6.2.5 [100] SiNW

Comparing the absorption spectrum of [110] and [100] SiNWs is also instructive since it reveals the role wave function symmetry has in determining the anisotropy. As it was discussed in subsection 4.2.2 of Chapter 4, due to the even parity of the integrand in position matrix element formulation, both x and y polarizations have equal values of matrix element in contrast to the z polarized case which has a zero value. This can be observed in the absorption spectrum of this nanowire near the band edge. Figure 6.11 shows the absorption spectrum of a 2.2nm [100] unstrained SiNW in a wide energy range including the magnified portion of band edge area (Inset). As it can be seen on the bandgap value the absorption is dominantly determined by x and y polarizations and for the z polarized case the matrix element (hence the absorption) value is zero.

The same kind of anisotropy was observed by DFT+LDA calculations performed for ( $d \sim 1\text{nm}$ ) narrow [100] SiNWs [49] although the bandgap values and diameters of nanowires are different. In contrast to the previously observed optical anisotropy for [100] SiNWs, another DFT study using GGA functional of PBE type has shown that for a 1.9nm [100] SiNW the band edge absorption for x and y polarizations are zero [181]. The nonzero band edge absorption for the z polarized light is attributed to the symmetry group of valence and conduction states which is of course different from the one presented in [49]. However the different anisotropy observed in Yoshioka's work could be due to inclusion of LFE in DFT. As it was discussed in Chapter 5, LFE obscures the anisotropy due to wave function for [100] SiNWs.

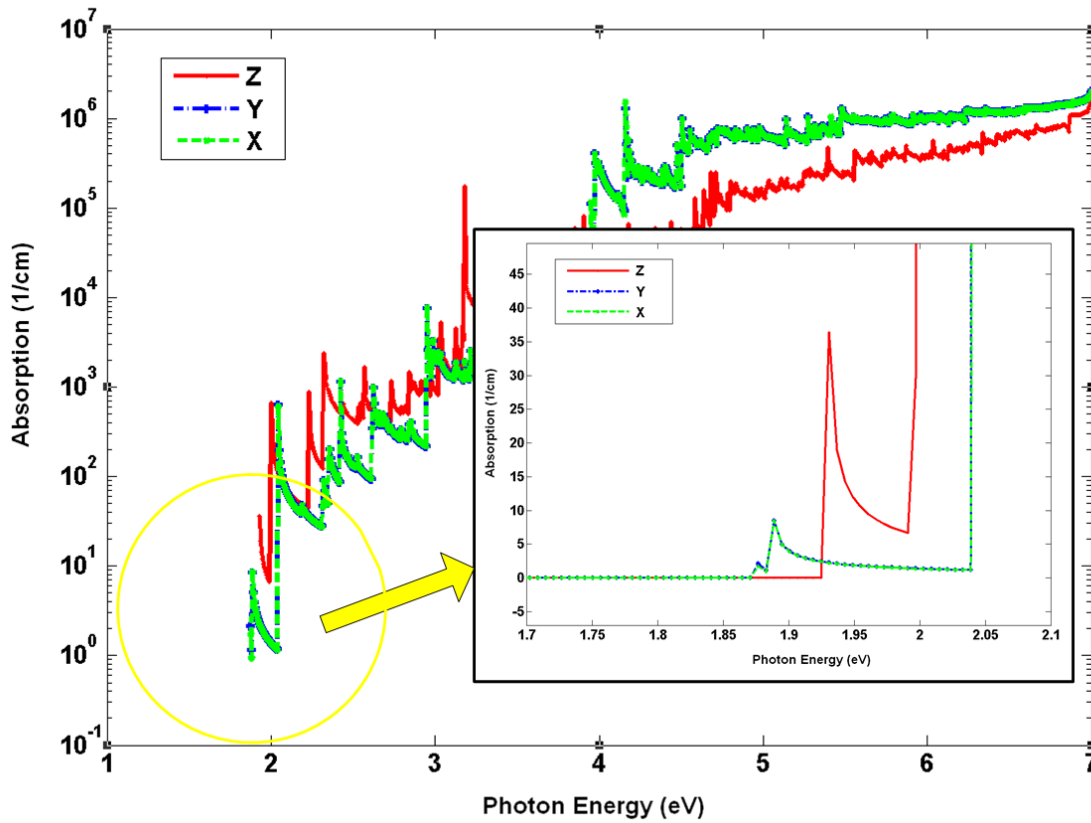


Figure 6.11 The absorption spectrum of a 2.2nm [100] SiNW. Inset shows that the band edge absorption is nonzero for x and y polarized photons while it is zero for z polarized photons.

### 6.3 Conditions for optical gain

So far the focus has been on the intrinsic absorption spectrum calculation in which the valence and conduction band are assumed to be full and empty, respectively. However, if the nanowire is doped then it is probable to find free electrons in the first conduction band and

empty states (holes) at the top of the valence band. The inclusion of the band occupancy in the absorption spectrum is possible by modifying equation 6.10 as discussed in [173][169]. Here we use the same assumptions that we made in the derivation of semi-analytic formula for absorption and continue as follows:

$$\alpha(\omega_k) = \frac{e^2}{\epsilon_0 n_r \omega_k c A_{nw}} \sum_{c,v} \omega_{c,v}^2 \int_{k_z} |\bar{\mathbf{r}}_{c,v}|^2 \delta(E_{c,v}(k_z) - \hbar\omega_k) (f_v(k_z) - f_c(k_z)) dk_z \quad (6.30)$$

where  $f_v(k_z)$  and  $f_c(k_z)$  are the values of Fermi-Dirac factors for valence band and conduction band evaluated at  $k_z$ :

$$f_c(k_z) = \frac{1}{1 + e^{\frac{E_c(k_z) - E_{Fc}}{kT}}} \quad \& \quad f_v(k_z) = \frac{1}{1 + e^{\frac{E_v(k_z) - E_{Fv}}{kT}}} \quad (6.31)$$

Where  $E_{fc}$  and  $E_{fv}$  are quasi-Fermi levels of  $n$  and  $p$  doped nanowires in the non-equilibrium state. This picture is suitable for a device in which nanowire is of core/shell  $n/p$  type or a tandem like  $np$  doped nanowire. Using equation 6.31 and rewriting  $E_c(k_z)$  and  $E_v(k_z)$ , we can write:

$$f_c(k_z) = \frac{1}{1 + e^{\frac{E_c(k_z) - E_{Fc}}{kT}}} = \frac{1}{1 + e^{\frac{E_{g,cv} + \frac{\mu_{cv}}{m_c^*} (E_{c,v}(k_z) - E_{g,cv}) - E_{Fc}}{kT}}} \quad (6.32)$$

$$f_v(k_z) = \frac{1}{1 + e^{\frac{E_v(k_z) - E_{Fv}}{kT}}} = \frac{1}{1 + e^{\frac{-\frac{\mu_{cv}}{m_v^*} (E_{c,v}(k_z) - E_{g,cv}) - E_{Fv}}{kT}}} \quad (6.33)$$

The frequency of incoming photon ( $\omega_{cv}$ ) is equal to  $E_{cv}/\hbar$ . The position matrix element in equation 6.30 is found from  $|\langle u_c | \hat{\mathbf{e}} \cdot \bar{\mathbf{P}} | u_v \rangle|^2$  as follows:

$$|\langle u_c | \hat{\mathbf{e}} \cdot \bar{\mathbf{P}} | u_v \rangle|^2 = m_0^2 \omega_{cv}^2 |\langle u_c | \hat{\mathbf{e}} \cdot \bar{\mathbf{r}} | u_v \rangle|^2 = m_0^2 \omega_{cv}^2 |\bar{\mathbf{r}}_{c,v}|^2 \cong m_0^2 \omega_{cv}^2 |\bar{\mathbf{r}}_{c,v}|_{@kz=0}^2 \quad (6.34)$$

By expanding the Dirac Delta function using its roots and noticing that the effective mass approximation yields only one root corresponding to each hyperbola (i.e.  $\omega_k = \omega_{cv}$ ), we may write:

$$\alpha(\omega_k) = \frac{e^2 \omega_k}{\epsilon_0 n_r c A_{nw}} \sum_{c,v} \frac{|\bar{\mathbf{r}}_{c,v}|_{@kz=0}^2}{\left| \frac{\hbar^2 k}{2\mu_{cv}} \right|} (f_v(@E_{cv} = \hbar\omega_k) - f_c(@E_{cv} = \hbar\omega_k)) \quad (6.35)$$

Using equation 6.23 we have:



$$\alpha(\omega_k) = \frac{e^2 \omega_k}{\epsilon_0 n_r c A_{nw}} \frac{\sqrt{2\mu_{cv}}}{\hbar} \sum_{c,v} \frac{|\bar{r}_{c,v}|^2_{@k_z=0}}{\sqrt{\hbar\omega_k - E_{g,cv}}} (f_v(@E_{cv} = \hbar\omega_k) - f_c(@E_{cv} = \hbar\omega_k)) \quad (6.36)$$

Where Fermi factors in equations 6.32 and 6.33 must be updated by replacing  $E_{c,v}(k_z)$  with  $\hbar\omega_k$ . The singularity at  $E_{c,v}(k_z) = \hbar\omega_k$  can be avoided in the same manner as explained in section 6.1.2. It is also evident that in equation 6.35, the summation over  $c,v$  contains all combinations of valence to conduction transitions at BZ centre ( $k_z=0$ ).

The importance of equation 6.36 is in the study of conditions where the optical gain can be achieved in SiNWs. As long as  $f_v(@E_{cv} = \hbar\omega_k) - f_c(@E_{cv} = \hbar\omega_k) > 0$  the absorption is positive i.e. the medium is still dissipative. In order to obtain optical gain (or negative absorption) in a medium we must have  $f_v(@E_{cv} = \hbar\omega_k) - f_c(@E_{cv} = \hbar\omega_k) < 0$ . This condition implies that  $E_{Fc} - E_{Fv} > E_c - E_v = \hbar\omega$ . The carrier density for transparency condition ( $n_{transp}$ ) is the minimum density at which the absorption vanishes i.e.  $\alpha(\hbar\omega) = 0$  (i.e.  $f_v=f_c$ ). After this point the absorption becomes negative (amplifying medium) and the maximum of the gain increases linearly with injected current density.

#### 6.4 Measurement of the Absorption

It is instructive to look at a few methods of measuring the photo-absorption in nanowires since they show how successfully the theoretical results match with experiments and secondly how they will enable us to extract more useful information about the nanowire properties i.e. bandgap value, its temperature dependence, phonon frequencies, plasma frequency and carrier densities.

In the calculation of absorption in this work it is assumed that nanowires have infinite length and each nanowire is ideally isolated from other nanowires. It is as if the nanowires are closely packed together like an array and there are infinite potential barriers between them which hinder the wave function overlapping i.e. tunneling. In reality however the nanowires are more separated and the space in between is filled by air, template material in which the nanowires are molded or even the oxide layer which have covered the nanowires. In this case since the wavelength of the incoming light is larger than the thickness of each individual nanowire, it is not possible to linearly subtract the absorption value of the air, oxide or template material from the total absorption. Black et al [186] have shown that using the inverse of Effective Medium Theory (EMT) makes it possible to extract the absorption of Bismuth nanowires molded in an alumina template. Interestingly the calculations based on effective mass approximation can reproduce the experimental data. Maxwell-Garnett (MG) EMT states that if the components of a composite system are smaller than the wavelength of electromagnetic wave, then the relationship between dielectric functions of guest (nanowire), host (template) and composite (nanowire array) can be written as:

$$\frac{\epsilon_{composite} - \epsilon_{host}}{\epsilon_{composite} + K\epsilon_{host}} = f \frac{\epsilon_{guest} - \epsilon_{host}}{\epsilon_{guest} + K\epsilon_{host}} \quad (6.37)$$

Volume fraction or fill factor (FF) is defined as  $f$  and  $K$  is the screening parameter. To find the absorption (or dielectric function) of guest material (nanowire), the absorption of the composite (nanowire array) as well as the host (empty template, bare substrate) are measured separately. This is performed by measuring the room temperature frequency dependent transmission (T) and reflectance (R) using the apparatus explained in [186]. The dielectric constant can be found by recalling that refractive index ( $n$ ) and extinction coefficient ( $\kappa$ ) are related to the measured R and T according to equation 6.18 and the following equations:

$$R = \frac{(n-1)^2 + \kappa^2}{(n+1)^2 + \kappa^2} \quad T = \frac{(n-1)^2 + \kappa^2}{(n+1)^2 + \kappa^2} \quad (6.38)$$

Having found  $\epsilon_{host}$  and  $\epsilon_{composite}$  and solving equation 6.37 for the unknown value of  $\epsilon_{guest}$  results in:

$$\epsilon_{guest} = \epsilon_{host} \frac{K\epsilon_{composite} - K\epsilon_{host} + f\epsilon_{composite} + f\epsilon_{host}}{-\epsilon_{composite} + \epsilon_{host} + fK\epsilon_{host} + f\epsilon_{composite}} \quad (6.39)$$

Thereafter the absorption spectrum of the guest material (nanowires) is found. If the transmission (T) is very small then the MG EMT method does not work properly. In this case the value of T should be extracted from the measured value of R using Kramers-Krönig integration. Using MG EMT method it is shown that the bandgap of 40nm thick bismuth nanowires is 123meV in contrast to its bulk value of 36meV.

UV-visible transmission as well as IR reflectance measurement of nanowires can also provide more information about the frequency of optical phonons, plasma frequency, free carrier density and temperature dependence of the bandgap value. Within the IR range the dielectric function can be written as the sum of contributions from optical phonons and free carriers [187]:

$$\epsilon = (n - i\kappa)^2 = \epsilon_{\infty} \left( 1 - \frac{\omega_p^2}{\omega^2 + i\omega\gamma} + \frac{\omega_L^2 - \omega_T^2}{\omega_T^2 - \omega^2 - i\omega\Gamma} \right) \quad (6.40)$$

Plasma frequency due to free carriers with density of  $n_f$  is given as  $\omega_p = (4\pi n_f e^2 / m^* \epsilon_{\infty})^{1/2}$  where  $m^*$  is the effective mass of electrons.  $\epsilon_{\infty}$  is the high frequency dielectric constant.  $\Gamma$  and  $\gamma$  are phonon and plasmonic broadening (damping) factors, respectively.

After measuring the reflectance spectrum and looking for maxima and its boundaries it is possible to find the longitudinal and transversal optical phonon frequencies i.e.  $\omega_L$  and  $\omega_T$ . The band at which the reflectance value is ideally 100% corresponds to Reststrahlen (German:

“residual radiation”) band and its boundaries are determined by the optical phonon frequencies.

The minimum of reflectivity (equation 6.39) occurs when  $\epsilon=1$ . Using equation (6.41) and measuring two minima of the reflectance data makes it possible to find  $\omega_p$  and then  $n_f$ . On the other hand  $n_f$  can be used to calculate the concentration of donors or if it is already known, it can return the value of donor ionization energy.

Figure 6.12 shows the reflectance spectrum measured for a layer of 10nm-50nm thick GaN nanowires grown on Si substrate [187]. Measuring the temperature dependence of the band edge in UV-visible transmission spectrum and comparing it with the corresponding data for bulk material reveals how weak or strong the temperature effect on the nanowire bandgap can be.

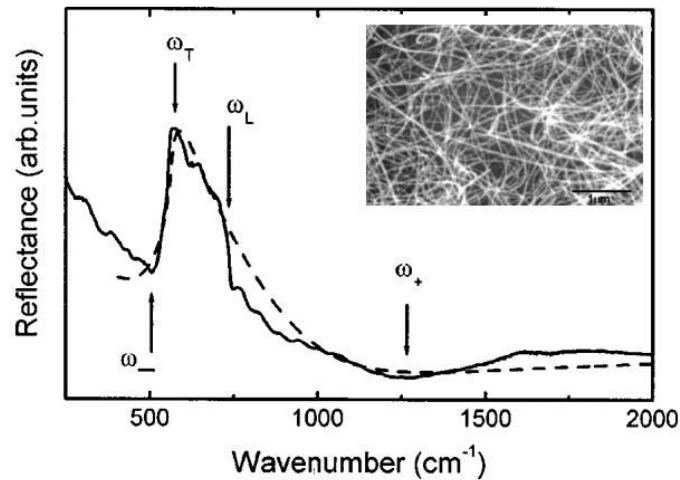


Figure 6.12 Measured reflectance of GaN nanowires (Inset). The boundaries of the maximum reflectance portion of the spectrum correspond to LO and TO phonon energies. The minima are used to extract the information regarding plasma frequency. Reprinted with permission from [187].

Copyright 2001 American Institute of Physics.

# Chapter 7

## Conclusions

### 7.1 Summary

In this thesis the electronic and optical properties of SiNWs were studied computationally.

In **Chapter 1** the experimental works related to the light emission from SiNWs were reviewed to sketch a bigger picture of the current research trends in this area. This was followed by enlisting the main questions of the thesis and the agenda. Then a summary of the experiments was presented in order to show the possibility of implementing a proof of concept strain modulated SiNW light emitter.

In **Chapter 2** it was shown that uniaxial strain can change the value and the nature of the bandgap in SiNWs. Using TB method it was observed that each 1% tensile strain can cause 100meV and 80meV change of bandgap value for [110] and [100] SiNWs, respectively. Evaluating this for SiNWs of different diameter showed that the value of the bandgap change solely depends on the crystallographic direction. This proves the advantage of silicon nanowires in contrast to carbon nanotubes (CNT) wherein the bandgap change rate is strongly dependent on the chirality and diameter.

The next observation was that strain can cause direct-to-indirect bandgap conversion by raising or lowering the valence and conduction sub bands. Corresponding to this conversion there is a 3-4 times change in effective mass of electrons and density of states. This effect can be exploited in pressure, force and stress sensors made of a single or an array of SiNWs on a deformable substrate. The amount of required strain for such bandgap conversion moves toward lower compressive strain values as the diameter increases. This is of practical value because for nanowires fabricated by either top-down or bottom-up methods, the diameter can be around 5nm or more. Hence it is easier to achieve the bandgap conversion without using higher amount of compressive strain which may cause buckling problem. The results of this chapter were published in [151] and later in [117]. Later DFT-based studies showed the same bandgap conversion for SiNWs [111][118][134]. The quantitative differences in the values of strains or bandgap changes with strain can be attributed to the inherent difference between TB and DFT methods, but regardless of this, the physics of strain-induced change of bandgap is qualitatively the same and method-independent.

In **Chapter 3** a DFT study was performed for germanium nanowires [130] showing that they can undergo direct-to-indirect bandgap conversion is achievable in this material as well. It is observed that there are two direct-to-indirect conversion points in [110] GeNWs; one in the tensile and the other at the compressive strain points. Similar to the trends observed in SiNWs, the window of strain values becomes narrower as the diameter increases. The

advantage of using GeNWs or alloy Si/Ge nanowires is the possibility of achieving lower bandgap values. These values correspond to longer wavelengths (IR) which are suitable for application in optical fiber communication systems.

In **Chapter 4** a detailed account of the computational methods, derivations and algorithms were presented. Firstly it was shown how to calculate the electron-photon interaction Hamiltonian matrix element in the TB framework. Using the first and second order perturbation theory, the formulation of spontaneous emission time in direct and indirect nanowires was derived, respectively. The method and algorithm to calculate and generate matrices containing all possible electron-phonon scattering rates were presented. This chapter forms the basis of investigating the strain effect on the spontaneous emission time of SiNWs which is the content of **Chapter 5**. The possibility of changing the spontaneous emission time with strain is questioned here based on the observed direct-to-indirect bandgap conversion in SiNWs. Since the photon emission in indirect bandgap nanowire is mediated by phonons, it is a second order and slow process. It is found that spontaneous emission time of direct bandgap Si nanowires (in the order of  $\mu\text{sec}$ ) can be increased by more than two orders of magnitude when the bandgap becomes indirect. The role of both LA and LO phonons was studied and it was observed that the role of the optical phonons is 100 times stronger than acoustic phonons.

Another mechanism which changes the spontaneous emission time even in the direct bandgap nanowires is change of the symmetry of valence and conduction state wave functions which in turn leads to the change of optical matrix element. In order to investigate the possibility of using the direct to indirect bandgap conversion in generating a population inversion, we performed an Ensemble Monte Carlo (EMC) simulation in collaboration with Professor Amit Verma from Texas A&M University-Kingsville [149]. As part of my thesis I calculated the electron-phonon scattering rates for intra- and inter-subband scattering events by including both acoustic and optical phonons. The EMC calculations were performed by Professor Verma. Here we investigated the evolution of electron population under an electric field and various temperatures. It is shown that there is a factor of 10 difference between the population of electrons in direct and indirect sub bands even though fast electron-phonon scattering events scatter the carriers out of the indirect band. The role of temperature in the population evolution was investigated as well. Interestingly the dominance of carrier population in indirect sub band for an indirect bandgap nanowire is valid at both  $T=300$  and  $T=77\text{K}$ . This proves that a population inversion can be generated in a nanowire under compressive strain. Releasing this strain (returning the bandgap to direct) can induce efficient direct emission of a photon. Finally an experiment is proposed to generate population inversion based upon the aforementioned idea and results [188]. Also a few device ideas to performing this experiment were filed as a patent application [189]. This study however is not limited to SiNWs. The codes, derivations and methodology which are developed in this

thesis can be generalized to other material systems e.g. core/shell nanowires made from Si and Ge as well as group III-V material nano systems.

In **Chapter 6** the absorption spectra of SiNWs were calculated using TB method. The effect of diameter, optical anisotropy (wave function symmetry), strain and crystallographic direction on the absorption of SiNWs was investigated. It was observed that strain can change the band edge absorption by at least one order of magnitude due to the change of symmetry of wave functions and optical matrix element. The optical anisotropy also manifests itself in the different values of band edge absorption corresponding to different polarizations of incoming photons. Vital for the application of SiNWs in solar cells we found that SiNW can have 100 times larger absorption compared to bulk Si in the same range of IR energy ( $E_g=1.1$  eV). This can be of practical importance if we think of matrix of SiNWs embedded on a deformable stretched substrate used as a solar panel.

It is believed that these contributions promise new applications of SiNWs in the realm of photonics. It also provides a basis for further theoretical investigation of strain effects on photocurrent, nonlinear optical properties, many-body interactions as well as non-radiative processes like Auger recombination in nanowires. Strain as a degree of freedom can tailor the band structure and Eigen states of a nanowire and provide new insight about the mechanisms with which the Auger recombination can be suppressed; the nonlinearity can be enhanced, among others. On the other hand it helps experimenters to devise new SiNW-based devices or enable them to explain the experimental observations using developed theoretical models involving strain effects on optical/electronic properties.

## **7.2 Future Work**

This thesis work naturally raises a few questions which merit further theoretical study. In the context of population inversion generated by compressive strain, the role of other scattering events like surface scattering and non-radiative recombination's i.e. Auger recombination should be evaluated. These effects, if not mitigated, can deplete the indirect sub band of electrons before reversing the strain could cause direct light emission. Since the main results of the thesis are pivoting around the spontaneous emission time and light absorption in SiNWs, I would like to speculate on how Auger Recombination (AR) and higher order (nonlinear) absorption e.g. Two Photon Absorption (TPA) can be quantified based on the methodology, codes and formulations presented in the thesis and comment on the potential hurdles that need to be overcome.

### **7.2.1 Auger Recombination**

Auger recombination is a non-radiative mechanism which limits the efficiency of nano-lasers and Light Emitting Diodes (LED). Hence understanding of the AR process in nanowires can help to come up with ideas of suppressing it and improving the performance of SiNWs-based

light emitters. Previous theoretical studies of Auger recombination were only devoted to bulk 3D semiconductors [190]. There are two recent works which calculate AR time in bulk semiconductors using DFT-based method. First Heinemann et al used DFT-LDA scheme to calculate the direct inter-band AR of electron-electron-hole (*eeh*) type in ZnMgO alloys [191]. In the second work Govoni et al addressed *eeh* and hole-hole-electron (*hhe*) AR processes in bulk silicon and GaAs [192]. Using DFT-LDA with quasi-particle (GW) corrections to the bandgap value they showed that direct Purely Collisional (PC) AR times in n-type silicon and p-type GaAs match with the experimental values. The large discrepancy of theory and experiment in the case of p-type silicon and n-type GaAs was attributed to other kinds of AR processes i.e. Phonon Assisted (PA) AR which was taken into account in their work. PAAR type of recombination was already investigated by Takeshima et al in III-V bulk semiconductors using effective mass approximation [193]. Before this, PAAR processes in bulk silicon, germanium and GaP were studied using pseudo-potential method [194].

The close agreement of experimental and theoretical values of AR times for bulk semiconductors proves the reliability of DFT-based calculations as well as the validity of recombination models assigned to the AR process i.e. *eeh* and *hhe*. Such theoretical studies have not yet been done for SiNWs. However there are two samples of experiments performed to measure the Auger recombination time in III-Nitride [195] and silicon nanowires [66]. The measurements are based on excitation-dependent Photoluminescence (PL) and time resolved PL spectroscopies. By extrapolation and fitting the experimental data to the rate equations, estimated value of Auger recombination coefficient ( $C_a$ ) was extracted. In the case of [195] with large diameter ( $20\text{ nm} < d < 50\text{ nm}$ ) nanowires, the fitting to bulk semiconductors rate equations works well and AR time scales with carrier density ( $N$ ) according to  $1/N^2$ . On the other hand for narrow diameter ( $d = 3.3 \pm 1.6\text{ nm}$ ) SiNWs of [66], it was shown that the best fit is possible only if a two level model is assumed for a nanowire in which two excitons recombine. Hence in contrast to *eeh* and *hhe* models, the AR time scales with  $1/N$ . Computational study of AR process including *eeh*, *hhe* and bimolecular (exciton-exciton) recombination models and comparison with existing experimental data reveals which model and under what condition (e.g. temperature, diameter, doping value) is dominant in nanowires.

Evaluating the effect of strain on AR time is also useful in simulating the realistic experimental conditions in which SiNWs are fabricated e.g. residual radial and axial strain due to cladding material, temperature gradients among others. This will also determine whether applying strain (by any of the aforementioned methods discussed in this thesis) can be used to inhibit or reduce the AR rate. Figure 7.1 summarizes the strategy of computationally investigating the Auger recombination process in SiNWs or any nanowire of different material within tight binding and DFT frameworks. Although every exploration

may face other unprecedented hurdles and challenges, here a few of the known challenges and questions which may arise during this computational study are listed as follows:

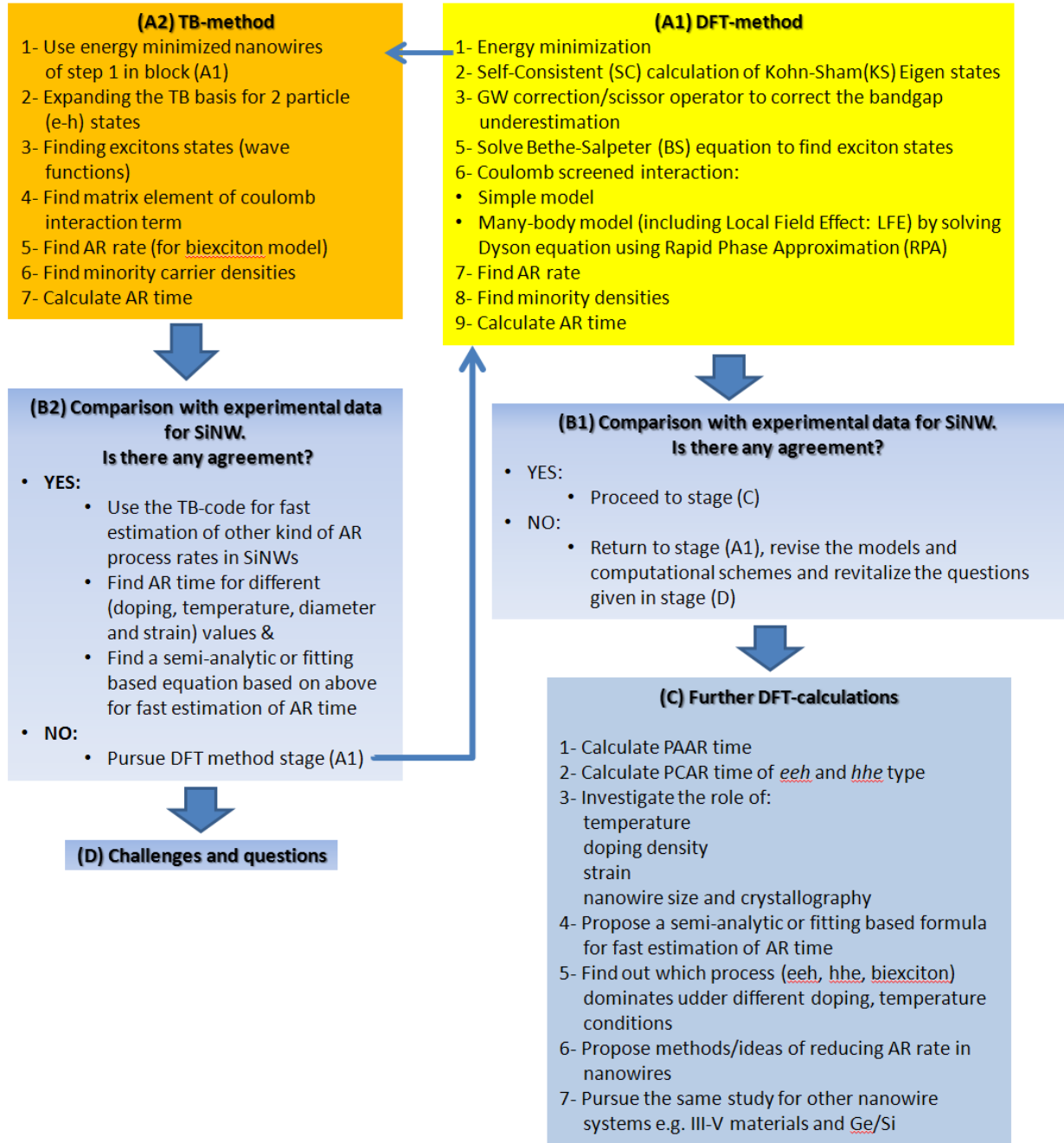


Figure 7.1 The flowchart of computational study of AR in SiNWs using tight binding and DFT methods.

1- What representation [position ( $\mathbf{r}$ ) or momentum ( $\mathbf{k}$ )] should be chosen to start with?



- 2- How to resolve the bandgap underestimation issue (selection between scissor operator and diameter sensitive many-body GW correction)?
- 3- How to perform 4D integrations in  $k$  space? (Parallel computing of nested summations over  $k$  or using a Monte Carlo based integration?)
- 4- How to include Local Field Effects (LFE) and how much are they important?
- 5- How much is the effect of Coulomb screening on the dielectric function of the material?
- 6- How much error using bulk phonons will induce in case if confined phonons are ignored to avoid complexity?
- 7- How much error is introduced if the Umklapp process is ignored?
- 8- How to include the effect of dopant atoms on the band structure?
- 9- How to include the enhanced coulomb interaction in low doping density regime?
- 10- What kind of phonon is dominant in the phonon assisted AR processes?

Block D of the flowchart (Figure 7.1) contains the aforementioned challenges and questions.

### 7.2.2 Two Photon Absorption

Two Photon Absorption (TPA) is a nonlinear second order process involving two photons which has already been studied in bulk semiconductors [196][197], SiGe super lattice [198] as well as quantum dots [199][200]. The motivation behind this study is twofold. Firstly it is known that Si-based Avalanche Photo Diodes (APD) provide higher efficiency (>70%) and lower dark current [201]. However the large bandgap in Si hinders using this material for photo detection in optical fiber communication systems which are based on long wavelength IR ( $\lambda = 1300-1600\text{nm}$ ). Therefore it is proposed that exploiting TPA process in silicon might be a solution to introduce Si-based photodetectors in optical fiber communication systems.

Secondly enhancing the TPA rate in silicon is useful for solar cell applications. Converting the long wavelength portion of the solar spectrum ( $\lambda > 1000\text{nm}$ ) to electron-hole pair is not efficient in crystalline silicon solar cells. The photon up converters are mixture of lanthanide ion couples ( $\text{Yb}^{3+}\text{-Er}^{3+}$ ) which are added to the solar cells in order to convert two low energy IR photons into a visible (e.g.  $530\text{nm}$ ) photon [202]. However the efficiency of up conversion process is still low (1%) and sophisticated techniques like light focusing (using lens or collimator), broadening the lanthanide absorption by sensitization (adding quantum dots) and plasmonic effects (using metallic nanostructures) are required which are not cost effective. If the TPA process in SiNW shows promising efficiencies it can provide a low cost solution for solar cell improvement rather than expensive Lanthanide materials. It can be surmised that in the context of two photon absorption, SiNW with its direct bandgap and optical anisotropy can show interesting physical effects depending on the polarization of two photons and the wave function symmetry.

The methods of calculating TPA coefficient can be divided into two main categories: (a) *Perturbation-based* methods and (b) *non-perturbative* methods.

### 7.2.2.1 Perturbation-based methods

In the first category the TPA can be calculated directly from the second order perturbation theory based upon the definition of TPA [197][199]. Here the tight binding method can be used to find the Eigen states of SiNW followed by calculation of optical matrix elements based on the methods presented in Chapter 4. The second approach in the category of (a) is based on the relationship between TPA and the third order nonlinear susceptibility,  $\chi^3$ , which is defined as follows [203]:

$$\beta_2(\omega) = \frac{\omega}{2n^2c^2\epsilon_0} \text{imag}(\chi^{(3)}(\omega; \omega, -\omega, \omega)) \quad (7.1)$$

where  $\beta_2$ ,  $\epsilon_0$ ,  $\omega$  and  $n$  are TPA coefficient, dielectric permittivity of the vacuum, frequency of the incoming photon and the refractive index of material in the given frequency, respectively. This method has been used to calculate TPA in SiGe super lattice [198], silicon cubic quantum dots [200] and bulk silicon and ZnSe [204]. With this method, the problem of finding TPA is reduced to the calculation of  $\chi_{imag}^{(3)}(\omega; \omega, -\omega, \omega)$  and  $\chi_{imag}^{(3)}(\omega_1; -\omega_2, \omega_2, \omega_1)$  for degenerate and non degenerate TPA, respectively. Here  $\omega_1$  and  $\omega_2$  are signal and pump frequency, respectively. Calculation of  $\chi^3$  can be performed based on (i) direct definition of  $\chi^3$  and (ii) using DFT method. In the former case (i) the tight binding method is used to calculate all matrix elements and summations over the intermediate virtual states, frequencies and  $k$  values within the BZ (similar to the methods presented in Chapter 4 and 6). However it should be noted that the third order nature of the formulation makes the calculations very time consuming and provision must be made to speed up the nested summation loops over intermediate states.

DFT-based methods are computationally more advantageous than the perturbation-based methods since there is no need to perform time consuming summations over all intermediate excited states. On the other hand it is well known that Time Independent DFT (TIDFT) method is reliable only at giving the correct ground state of a nano-system. This problem is circumvented however by using Time Dependent DFT (TDDFT) method [205]. Calculation of nonlinear susceptibilities with DFT is based on the calculation of polarization,  $\mathbf{P}$ , in response to the applied electric field,  $\mathbf{E}$ . In this method the dipole induced by electric field is added as a perturbation,  $H_{pert} = -\vec{E} \cdot \vec{r}$  to the unperturbed Hamiltonian of the system. Therefore this method is not applicable to periodic systems i.e. a nanowire which has at least one infinitely long dimension (e.g.  $z$ ). However if the electric field direction is parallel with the smallest non-periodic dimension of the nano-system, some elements of susceptibility

tensor can be extracted. For example for a nanowire which is periodic along  $z$  direction, the polarization,  $\mathbf{P}$ , can be calculated in response to electric field in  $x$  and  $y$  (cross section of the nanowire) directions [206].

In TDDFT method after calculation of the ground state at  $t=0$  using Kohn-Sham equations, the next sample of time-dependent electric field,  $\mathbf{E}(t)$ , is inserted into the perturbation Hamiltonian as  $H_{pert}(\Delta t) = -\vec{\mathbf{E}}(\Delta t) \cdot \vec{\mathbf{r}}$ . Thereafter the electron density is updated self-consistently at this time step (similar to the time-independent case) and the new  $\mathbf{P}(t)$  is found accordingly:

$$P(t) = \int d^3 \vec{r} \rho(\vec{r}, t) \vec{r} \quad (7.2)$$

Here the polarization,  $\mathbf{P}(t)$ , includes all orders of nonlinearity in response to  $\mathbf{E}(t)$ . Using Fourier transform, the susceptibilities can be extracted from  $\mathbf{P}(t)$  as it is explained in detail in [205] for two organic molecules. In TIDFT however the polarization is calculated in each DFT step as a function of static electric field. The final result is compared with the Taylor expansion of  $\mathbf{P}$  vs.  $\mathbf{E}$  to extract the tensor elements of  $\chi^{(2)}$  or  $\chi^{(3)}$  with appropriate assumptions about the values of  $x$ ,  $y$  and  $z$  component of the electric field. Therefore in the first DFT step the ground state of nano-system (i.e. an energy minimized nanowire) is calculated. In the next steps the structure is clamped to avoid ionic (nucleus) movement. It is also assumed that the frequency of interest and its second and third harmonics are smaller than the bandgap ( $E_g$ ) value, so there is no electronic excitation. On the other hand these frequencies must be higher than the ionic frequencies to avoid ionic oscillations and quench their contribution [207]. Therefore with this method, it is not possible to find the frequency dependent value of susceptibilities and what is obtained at the end is a constant number which may prove useful since it gives an approximation of the susceptibility value for the nanowire under study.

#### 7.2.2.2 Non-perturbative methods

This method is based on the Volkov's approach. In contrast to perturbation-based methods in which all electronic states are assumed to be of stationary type, in Volkov's method the electron and hole states are dressed by a time dependent electromagnetic potential,  $\mathbf{A}(\mathbf{r}, t)$ . This method was successfully applied to bulk III-V semiconductors [196][208][209] as well as indirect bulk silicon by including electron-phonon interaction Hamiltonian [201]. Using effective mass approximation makes this method faster than the perturbation-based methods and it can address the degenerate and non-degenerate TPA as well as Raman processes. After calculating the TPA coefficient it can also return the values of third order susceptibilities using the equation 7.1.

### 7.2.3 Surface Effects

Effect of the non-passivated surfaces e.g. oxide or nitride termination on the electronic and optical properties of SiNWs also matters in determining the performance of SiNW-based devices under more realistic conditions. The following methods can be starting steps for modeling such effects in SiNWs:

- (a) Generating a unit cell of the nanowire covered by oxide or nitride of a specific crystallography. The cladding material should completely terminate all dangling silicon bonds on the nanowire surface.
- (b) Performing a DFT-based energy minimization of the unit cell.
- (c) Repeating this relaxed unit cell periodically to generate a nanowire model with oxide or nitride surface termination.
- (d) Using tight binding method to calculate the band structure and Eigen states of the resultant core/shell nanowire.

The same methodology as above can be generalized to study the strain effects on the band structure of a core/shell Ge/Si nanowire. These nanowires have recently gained interest due to their potential application in quantum computing based on the hole-spin qubit [5] as well as bandgap tunability due to the added Ge content [124].

# Appendices

## Appendix A: Density of States (DOS) Calculation using Surface Green Function

To apply the surface Green function method to a nanowire, three unit cells of the nanowire are considered (Figure A1). The first and the third unit cells can be regarded as the left and right leads respectively.  $H_{21}$ ,  $H_{22}$  and  $H_{23}$  are the minimum sub-matrixes that are needed to solve the problem.  $H_{21}$  is the TB interaction Hamiltonian between 2nd unit cell and the left lead,  $H_{22}$  is the Hamiltonian of the 2nd unit cell,  $H_{23}$  is the interaction of 2nd unit cell and the right lead (Figure A1).

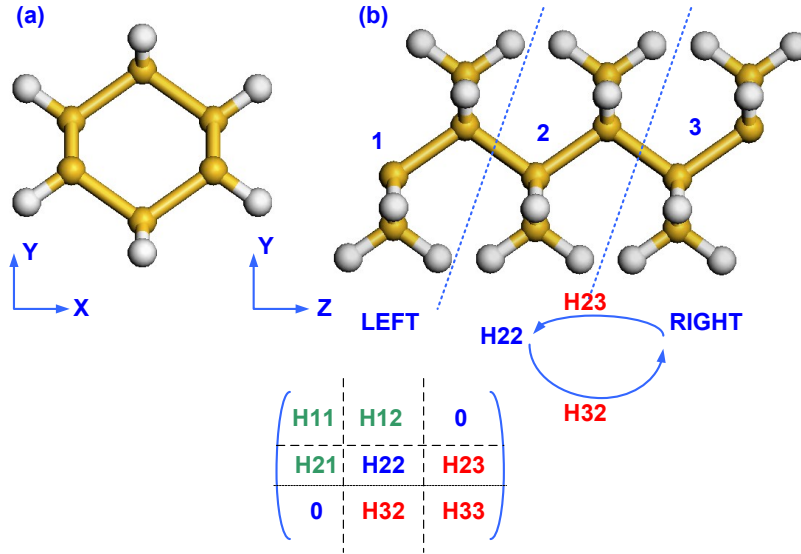


Figure A1 (a) Front view and (b) side view of a 0.6nm [110] SiNW terminated with hydrogen. The 1st and the 2nd unit cell are taken as the left and right leads, respectively.

Using the aforementioned TB interaction Hamiltonians, the total Green function can be constructed as shown in equation A1. Definitions and derivations of this equation can be found in great detail in [120]. To calculate the Green function, the surface Green functions  $g_{11}$  and  $g_{33}$  are found by iteratively solving equation A1.

$$G = [E + i\eta - H_{22} - H_{23}g_{33}H_{32} - H_{21}g_{11}H_{12}]^{-1} \quad (A1)$$

Then the density of states (DOS) is given using:

$$DOS(E) = \frac{1}{\pi} \text{Im}\{\text{Tr}(G(E))\} \quad (\text{A2})$$

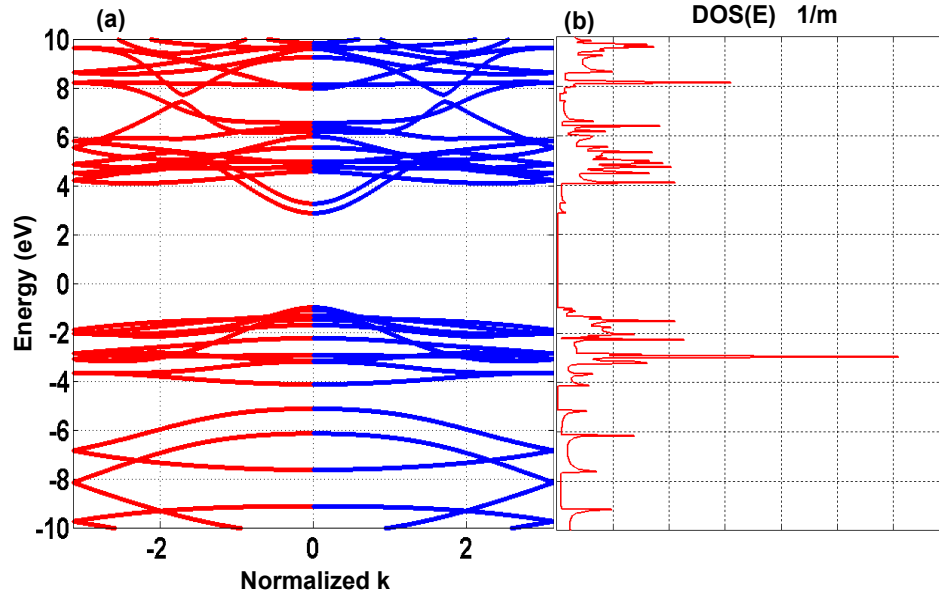


Figure A2 (a) Band structure and (b) DOS of the SiNW as shown in Figure A1.

Figure A2 shows the band structure and density of states of 0.6nm [110] SiNW. As can be seen the DOS has very large values for those parts of the band structure which have higher effective mass (e.g. flat bands). For each energy point along energy axis,  $g_{11}$  and  $g_{33}$  solver is called iteratively. The iteration starts using an initial guess e.g. random number matrix and convergence achieved when the different between left and right hand side of equation A1 is less than a threshold (e.g. 0.01).

## Appendix B: TB calculation of banstrcture of bulk silicon

Following the procedure which is given in [121] we can build the tight binding Hamiltonian of bulk silicon and germanium by finding the unit cell and suitable translation vectors between a unit cell and its neighboring cells. Figure B1 shows the unit cell of Si ( $a = 5.43\text{\AA}$ ). Four atoms in a tetrahedral section of the crystal are numbered as 1 to 4. If the unit cell contains atoms 1 and 2, it has six neighbors as numbered by representative nearest atoms (3 to 8). Translation vectors  $d_{14}$ ,  $d_{13}$ ,  $d_{15}$  are those which connect the Atom1 to its corresponding neighbors in three unit cells (i.e. 3, 4 and 5). Therefore the coordinates of other three neighbors (6,7 and 8) can be found by applying  $-d_{24}$ ,  $-d_{23}$  and  $-d_{25}$  to the Atom1.

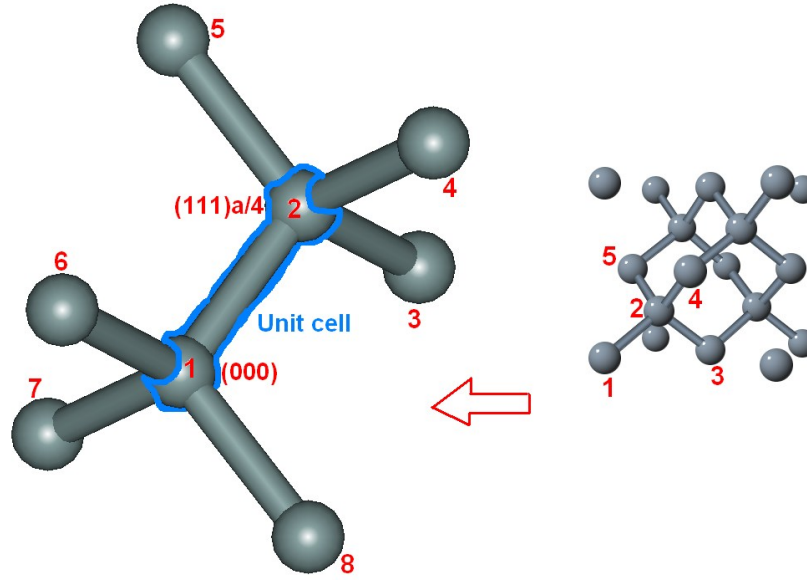


Figure B1 (Right) Crystal structure of bulk silicon (diamond). Atoms 1 and 2 construct a unit cell, surrounded by six neighbors. The atoms (3,4 and 5) and (6,7 and 8) are nearest neighbors of the atoms 2 and 1 respectively (left). Coordinates of atoms 1 to 8 are given in Figure 2.B2.

atom	x	y	z
8			
Si	0	0	0
Si	1.3575	1.3575	1.3575
Si	2.7150	2.7150	0
Si	0	2.7150	2.7150
Si	2.7150	0	2.7150
Si	-1.3575	-1.3575	1.3575
Si	1.3575	-1.3575	-1.3575
Si	-1.3575	1.3575	-1.3575

Figure B2 Coordinate of the eight atoms specified in Figure B1.

Based on Figure B1 and B2, the translation vectors connecting each unit cell to its neighbors are given as:  $\mathbf{d}_{13} = (1/2 \ 1/2 \ 0)$ ,  $\mathbf{d}_{14} = (1/2 \ 0 \ 1/2)$  and  $\mathbf{d}_{15} = (0 \ 1/2 \ 1/2)$ . The total tight-banding Hamiltonian,  $\mathcal{H}_T$  which is a  $20 \times 20$  matrix can be written as:

$$\mathcal{H}_T = \mathcal{H}_0 + \mathcal{H}_{23}e^{ik.d_{13}} + \mathcal{H}_{24}e^{ik.d_{14}} + \mathcal{H}_{25}e^{ik.d_{15}} + \mathcal{H}_{16}e^{-ik.d_{13}} + \mathcal{H}_{17}e^{-ik.d_{14}} + \mathcal{H}_{18}e^{-ik.d_{15}} \quad (\text{B1})$$

where  $\mathcal{H}_0$  is:

$$\mathcal{H}_0 = \begin{pmatrix} H_{11} & H_{12} \\ H_{21} & H_{22} \end{pmatrix} \quad (\text{B2})$$

in which  $10 \times 10$  sub-matrixes are filled using  $\text{sp}^3\text{d}^5\text{s}^*$  Jancu's parameters [110]. For the rest of matrixes we have:

$$\mathcal{H}_{2,j} = \begin{pmatrix} 0 & 0 \\ H_{2,m} & 0 \end{pmatrix} \text{ and } \mathcal{H}_{1,n} = \begin{pmatrix} 0 & H_{1,n} \\ 0 & 0 \end{pmatrix} \quad m = 3, 4, 5 \text{ \& } n = 6, 7, 8 \quad (\text{B3})$$

Equation B1 is solved using the eigenvalue solver in MTALAB<sup>®</sup> giving 20 Eigenvalues and eigenvectors for each point in 3D BZ of bulk silicon or germanium i.e.  $\mathbf{k} = [k_x, k_y, k_z]$ .



## Appendix C: Simplification of the momentum matrix element

For the general case of crystalline bulk solid or nanowires with a few dimensions comparable with the wavelength of light, the momentum matrix element in equation 4.21 of section 4.3 can be calculated as follows. At each point in the BZ e.g.  $\mathbf{K}_i$  or  $\mathbf{K}_f$ , the electronic states can be written as:

$$|a_{i,f}\rangle = \frac{1}{\sqrt{N}} e^{i\mathbf{K}_{i,f} \cdot \mathbf{r}} u_{i,f}(\mathbf{r}) \quad (\text{C1})$$

Where  $i$  and  $f$  stand for initial and final states respectively, and  $\mathbf{K}_{i,f}$  represents the wave vector of electron in initial and final states and  $N$  is the number of unit cells per unit volume. The envelope (Bloch function) is periodic with periodicity of  $\mathbf{a}_m$ , where  $m$  stands for the  $m^{\text{th}}$  unit cell in the lattice as shown in Figure C1.

$$u_{i,f}(\mathbf{r} + \mathbf{a}_m) = u_{i,f}(\mathbf{r}) \quad (\text{C2})$$

Inserting equation C1 into  $\langle a_f | \hat{\mathbf{p}} \cdot \hat{\mathbf{e}}_{k\sigma} e^{-i\mathbf{k} \cdot \mathbf{r}} | a_i \rangle$  and using the definition of momentum operator results:

$$\begin{aligned} \langle a_f | \hat{\mathbf{p}} \cdot \hat{\mathbf{e}}_{k\sigma} e^{-i\mathbf{k} \cdot \mathbf{r}} | a_i \rangle &= \frac{1}{N} \int d^3\mathbf{r} u_f^*(\mathbf{r}) e^{-i\mathbf{K}_f \cdot \mathbf{r}} \hat{\mathbf{p}} \cdot \hat{\mathbf{e}}_{k\sigma} e^{-i\mathbf{k} \cdot \mathbf{r}} u_i(\mathbf{r}) e^{+i\mathbf{K}_i \cdot \mathbf{r}} = \\ &= \frac{1}{N} \int d^3\mathbf{r} u_f^*(\mathbf{r}) e^{-i\mathbf{K}_f \cdot \mathbf{r}} \hat{\mathbf{p}} \cdot \hat{\mathbf{e}}_{k\sigma} e^{+i(\mathbf{K}_i - \mathbf{k}) \cdot \mathbf{r}} u_i(\mathbf{r}) = \\ &= -i\hbar \frac{1}{N} \int d^3\mathbf{r} u_f^*(\mathbf{r}) e^{-i\mathbf{K}_f \cdot \mathbf{r}} \nabla \cdot \hat{\mathbf{e}}_{k\sigma} e^{+i(\mathbf{K}_i - \mathbf{k}) \cdot \mathbf{r}} u_i(\mathbf{r}) = \\ &= -i\hbar \frac{1}{N} \int d^3\mathbf{r} u_f^*(\mathbf{r}) e^{-i\mathbf{K}_f \cdot \mathbf{r}} \hat{\mathbf{e}}_{k\sigma} \cdot \{ e^{+i(\mathbf{K}_i - \mathbf{k}) \cdot \mathbf{r}} \nabla u_i(\mathbf{r}) + i(\mathbf{K}_i - \mathbf{k}) e^{+i(\mathbf{K}_i - \mathbf{k}) \cdot \mathbf{r}} u_i(\mathbf{r}) \} = \\ &= -i\hbar \frac{1}{N} \int d^3\mathbf{r} u_f^*(\mathbf{r}) e^{-i(\mathbf{K}_f + \mathbf{k} - \mathbf{K}_i) \cdot \mathbf{r}} \hat{\mathbf{e}}_{k\sigma} \cdot \{ \nabla u_i(\mathbf{r}) + i(\mathbf{K}_i - \mathbf{k}) u_i(\mathbf{r}) \} \quad (\text{C3}) \end{aligned}$$

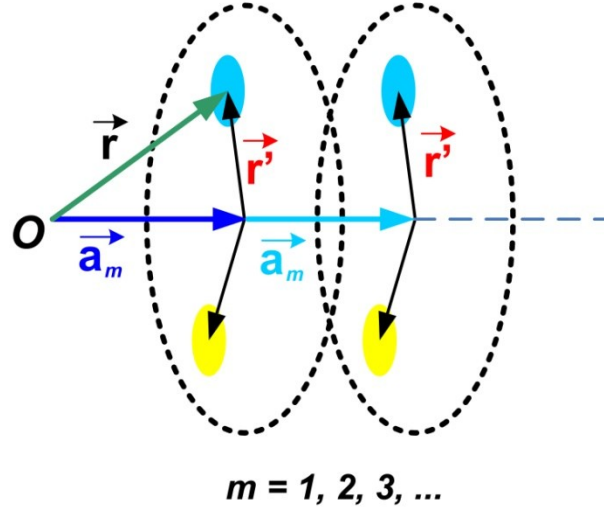


Figure C1 A periodic nanostructure showing two unit cells in  $\mathbf{a}_m$  direction and 2 atoms in each unit cell (unit cell length =  $a_m$ ).

Now the integration in equation C3 is decomposed as a summation over all unit cells ( $m$ 's) in the crystal and an integration within a unit cell as:

$$\int d^3r[\dots] = \sum_m \int_{ucell}[\dots] d^3r \quad , m = 1, 2, 3, \dots \quad (C4)$$

Now the variables can be changed so that integration is performed on the local coordinate of atoms in each unit cell (see Figure C1). Having  $\mathbf{r} = \mathbf{r}' + \mathbf{a}_m$  ,  $d\mathbf{r} = d\mathbf{r}'$  and  $u_{i,f}(\mathbf{r}) = u_{i,f}(\mathbf{r}' + \mathbf{a}_m) = u_{i,f}(\mathbf{r}')$ , equation C3 can be written as:

$$\langle a_f | \hat{\mathbf{p}} \cdot \hat{\mathbf{e}}_{k\sigma} e^{-i\mathbf{k} \cdot \mathbf{r}} | a_i \rangle = \frac{-i\hbar}{N} \sum_m \int_{ucell} u_f^*(\mathbf{r}' + \mathbf{a}_m) e^{-i(K_f + k - K_i) \cdot (\mathbf{r}' + \mathbf{a}_m)} \hat{\mathbf{e}}_{k\sigma} \cdot \{ \nabla u_i(\mathbf{r}' + \mathbf{a}_m) + i(K_i - k) u_i(\mathbf{r}' + \mathbf{a}_m) \} d^3\mathbf{r}' \quad (C5)$$

which gives:

$$\begin{aligned} \langle a_f | \hat{\mathbf{p}} \cdot \hat{\mathbf{e}}_{k\sigma} e^{-i\mathbf{k} \cdot \mathbf{r}} | a_i \rangle = & \frac{1}{N} \sum_m e^{-i(K_f + k - K_i) \cdot \mathbf{a}_m} \times \\ & \left\{ \int_{ucell} e^{-i(K_f + k - K_i) \cdot \mathbf{r}'} u_f^*(\mathbf{r}') \hat{\mathbf{e}}_{k\sigma} \cdot \hat{\mathbf{p}} u_i(\mathbf{r}') d^3\mathbf{r}' + \int_{ucell} -i\hbar e^{-i(K_f + k - K_i) \cdot \mathbf{r}'} u_f^*(\mathbf{r}') \hat{\mathbf{e}}_{k\sigma} \cdot i(K_i - k) u_i(\mathbf{r}') d^3\mathbf{r}' \right\} \end{aligned} \quad (C6)$$

Right hand side of equation C6 can be further simplified because the photon wave vector ( $\mathbf{k}$ ) is small compared to electron wave vectors, hence  $\mathbf{K}_f + \mathbf{k} - \mathbf{K}_i \approx \mathbf{K}_f - \mathbf{K}_i$ . Now the summation over unit cells ( $\mathbf{m}$ ) can be further reduced to Kröneckers delta as follows:

$$\frac{1}{N} \sum_{\mathbf{m}} e^{-i(\mathbf{K}_f + \mathbf{k} - \mathbf{K}_i) \cdot \mathbf{a}_m} = \frac{1}{N} \sum_{\mathbf{m}} e^{i(\mathbf{K}_i - \mathbf{K}_f) \cdot \mathbf{a}_m} = \frac{1}{N} \cdot N \cdot \delta_{\mathbf{K}_i, \mathbf{K}_f} = \delta_{\mathbf{K}_i, \mathbf{K}_f} = \begin{cases} 1 & \mathbf{K}_i = \mathbf{K}_f \\ 0 & o.w \end{cases} \quad (C7)$$

Hence  $\mathbf{K}_i = \mathbf{K}_f$  which allows for direct transition only (momentum conserving) and the term  $e^{-i(\mathbf{K}_f + \mathbf{k} - \mathbf{K}_i) \cdot \mathbf{r}'}$  is equal to 1. The second term in equation C6 is zero due to orthogonality of  $u_i(\mathbf{r})$  and  $u_f(\mathbf{r})$ . Therefore matrix element is given only by the first term in the right hand side of equation C6 which is:

$$\langle a_f | \hat{\mathbf{p}} \cdot \hat{\mathbf{e}}_{\mathbf{k}\sigma} e^{-i\mathbf{k} \cdot \mathbf{r}} | a_i \rangle = \int_{ucell} u_f^*(\mathbf{r}') \hat{\mathbf{P}} \cdot \hat{\mathbf{e}}_{\mathbf{k}\sigma} u_i(\mathbf{r}') d^3\mathbf{r}' = \langle u_f | \hat{\mathbf{p}} \cdot \hat{\mathbf{e}}_{\mathbf{k}\sigma} | u_i \rangle \quad (C8)$$

## Appendix D: Matrix element of $e^{iq \cdot r}$

The simplification of electron-phonon interaction Hamiltonian matrix element is reduced to calculation of terms like  $\langle u_i | e^{iq \cdot r} | f u_f \rangle$ , where  $u_i$  and  $u_f$  represent the Bloch part of initial and final electronic states, respectively. From now on  $i$  and  $f$  represent these states for shorter notation. In this work we chose a direct numerical method to calculate the matrix element which seems different from the method used in [148] in the appearance. However the momentum relaxation rates calculated with our numerical method perfectly matches with the momentum relaxation rates given in [148] for the same set of SiNWs. This proves equality of the matrix elements calculated with either method.

To explain the direct numerical method in a simple manner, without loss of generality we use a quantum dot with three atoms as the nano-system of choice. Each atom is assumed to have two orbitals (s and p) in a simplified exemplar tight binding scheme (Figure D1).

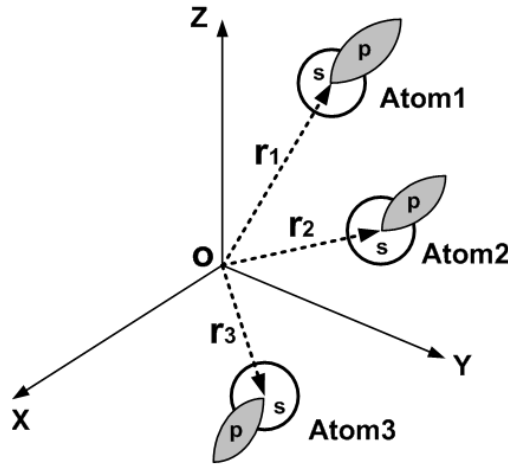


Figure D1 Arrangement of atoms and orbitals in a three atomic quantum dot

In this tight binding scheme the initial and final states can be represented by the following vectors which results directly from the band structure calculation (or Eigen solver):

$$|i\rangle = \alpha_{11}s + \alpha_{12}p + \alpha_{21}s + \alpha_{22}p + \alpha_{31}s + \alpha_{32}p = [\alpha_{11} \ \alpha_{12} \ \alpha_{21} \ \alpha_{22} \ \alpha_{31} \ \alpha_{32}] \quad (D1)$$

$$|f\rangle = \beta_{11}s + \beta_{12}p + \beta_{21}s + \beta_{22}p + \beta_{31}s + \beta_{32}p = [\beta_{11} \ \beta_{12} \ \beta_{21} \ \beta_{22} \ \beta_{31} \ \beta_{32}] \quad (D2)$$

Now these states can be written in closed form after which we use them in the direct definition of matrix element and process analytically.

$$|i\rangle = \sum_{n=1,2} \sum_{m=1,2,3} \alpha_{m,n}^{i*} \varphi_n(\mathbf{r} - \mathbf{r}_m) \quad \& \quad |f\rangle = \sum_{n=1,2} \sum_{m=1,2,3} \beta_{m,n}^f \varphi_n(\mathbf{r} - \mathbf{r}_m) \quad (\text{D3})$$

where  $m$  and  $n$  count the number of atoms and number of orbitals on each atom, respectively. The orbital type is represented by  $\varphi$  (s and p for  $n=1$  and 2, respectively).  $\mathbf{r}_m$  is the position of the  $m$ 'th atom within the quantum dot. Using equation D3 the matrix element can be expanded as:

$$\begin{aligned} \langle i | e^{iq \cdot r} | f \rangle &= \sum_{m,n} \alpha_{m,n}^{i*} \langle \varphi_n(r - r_m) | e^{iq \cdot r} | \sum_{m',n'} \beta_{m',n'}^f \varphi_{n'}(r - r_{m'}) \rangle = \\ &= \sum_{m,n} \sum_{m',n'} \alpha_{m,n}^{i*} \beta_{m',n'}^f \langle \varphi_n(r - r_m) | e^{iq \cdot r} | \varphi_{n'}(r - r_{m'}) \rangle \cdot \delta_{m,m'} \end{aligned} \quad (\text{D4})$$

The Krönecker delta is added to enforce this assumption that orbitals of different atoms have no overlapping and their contribution to matrix element has to be zero. Therefore equation D4 is further simplified as follows. Also it is assumed that different orbitals on the same atom have no interaction.

$$\begin{aligned} \langle i | e^{iq \cdot r} | f \rangle &= \sum_{n,n'} \sum_m \alpha_{m,n}^{i*} \beta_{m,n}^f \langle \varphi_n(r - r_m) | e^{iq \cdot r} | \varphi_{n'}(r - r_m) \rangle \cdot \delta_{n,n'} = \\ &= \sum_n \sum_m \alpha_{m,n}^{i*} \beta_{m,n}^f \langle \varphi_n(r - r_m) | e^{iq \cdot r} | \varphi_n(r - r_m) \rangle \end{aligned} \quad (\text{D5})$$

The variable of  $r - r_m$  can be replaced with  $u$  which results:

$$\begin{aligned} \langle i | e^{iq \cdot r} | f \rangle &= \\ &= \sum_{n=1,2} \sum_{m=1,2,3} \alpha_{m,n}^{i*} \beta_{m,n}^f \langle \varphi_n(u) | e^{iq \cdot (r_m + u)} | \varphi_n(u) \rangle = \\ &= \sum_{n=1,2} \sum_{m=1,2,3} \alpha_{m,n}^{i*} \beta_{m,n}^f e^{iq \cdot r_m} \langle \varphi_n(u) | e^{iq \cdot u} | \varphi_n(u) \rangle \end{aligned} \quad (\text{D6})$$

Temporarily we call the last term of equation D6 to be a constant as  $F(\mathbf{q})$ . Now the second summation (summation over  $m$ ) is expanded.

$$\langle i | e^{iq \cdot r} | f \rangle = \sum_{n=1,2} (\alpha_{1,n}^{i*} \beta_{1,n}^f e^{iq \cdot r_1} + \alpha_{2,n}^{i*} \beta_{2,n}^f e^{iq \cdot r_2} + \alpha_{3,n}^{i*} \beta_{3,n}^f e^{iq \cdot r_3}) F(\mathbf{q}) \quad (\text{D7})$$

Expanding the summation over  $n$  yields:

$$\begin{aligned} \langle i | e^{iq \cdot r} | f \rangle &= (\alpha_{1,1}^{i*} \beta_{1,1}^f e^{iq \cdot r_1} + \alpha_{2,1}^{i*} \beta_{2,1}^f e^{iq \cdot r_2} + \alpha_{3,1}^{i*} \beta_{3,1}^f e^{iq \cdot r_3}) \cdot F(\mathbf{q}) + (\alpha_{1,2}^{i*} \beta_{1,2}^f e^{iq \cdot r_1} + \\ &+ \alpha_{2,2}^{i*} \beta_{2,2}^f e^{iq \cdot r_2} + \alpha_{3,2}^{i*} \beta_{3,2}^f e^{iq \cdot r_3}) \cdot F(\mathbf{q}) \end{aligned} \quad (\text{D8})$$

Since the order of  $\mathbf{q}$  is  $2\pi/a$  ( $a$  is the unit cell length which is much larger than the span of the atomic orbitals,  $u$ ), therefore  $F(\mathbf{q})$  can be reasonably approximated as follows:

$$F(\mathbf{q}) = \langle \varphi_n(u) | e^{i\mathbf{q}\cdot\mathbf{u}} | \varphi_n(u) \rangle \sim \langle \varphi_n(u) | 1 + \mathbf{q}\cdot\mathbf{u} + \dots | \varphi_n(u) \rangle \sim \langle \varphi_n(u) | \varphi_n(u) \rangle = 1 \quad (\text{D9})$$

Rearranging the terms in equation D8 gives the following picture which shows how exactly the matrix element can be evaluated numerically without using the method given in [148].

$$\langle i | e^{i\mathbf{q}\cdot\mathbf{r}} | f \rangle = [\alpha_{1,1}^i \ \alpha_{1,2}^i]^\dagger e^{i\mathbf{q}\cdot\mathbf{r}_1} \begin{pmatrix} \beta_{1,1}^f \\ \beta_{1,2}^f \end{pmatrix} + [\alpha_{2,1}^i \ \alpha_{2,2}^i]^\dagger e^{i\mathbf{q}\cdot\mathbf{r}_2} \begin{pmatrix} \beta_{2,1}^f \\ \beta_{2,2}^f \end{pmatrix} + [\alpha_{3,1}^i \ \alpha_{3,2}^i]^\dagger e^{i\mathbf{q}\cdot\mathbf{r}_3} \begin{pmatrix} \beta_{3,1}^f \\ \beta_{3,2}^f \end{pmatrix} \quad (\text{D10})$$

The final result (as shown in Figure D2) can be multiplied to its own complex conjugate to give the desired quantity of  $|\langle i | e^{i\mathbf{q}\cdot\mathbf{r}} | f \rangle|^2$ .

$$\langle i | e^{i\mathbf{q}\cdot\mathbf{r}} | f \rangle = \underbrace{[\alpha_{1,1}^i \ \alpha_{1,2}^i]}_{\text{Atom1}} \underbrace{[\alpha_{2,1}^i \ \alpha_{2,2}^i]}_{\text{Atom2}} \underbrace{[\alpha_{3,1}^i \ \alpha_{3,2}^i]}_{\text{Atom3}}^\dagger \begin{bmatrix} e^{i\mathbf{q}\cdot\mathbf{r}_1} \\ e^{i\mathbf{q}\cdot\mathbf{r}_1} \\ e^{i\mathbf{q}\cdot\mathbf{r}_2} \\ e^{i\mathbf{q}\cdot\mathbf{r}_2} \\ e^{i\mathbf{q}\cdot\mathbf{r}_3} \\ e^{i\mathbf{q}\cdot\mathbf{r}_3} \end{bmatrix} \begin{bmatrix} \beta_{1,1}^f \\ \beta_{1,2}^f \\ \beta_{2,1}^f \\ \beta_{2,2}^f \\ \beta_{3,1}^f \\ \beta_{3,2}^f \end{bmatrix}$$

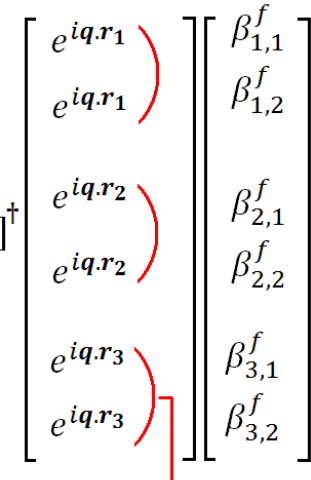

  
**repeated n times**  
**n: number of orbitals**

Figure D2 Arrangement of tight binding based eigenvectors to calculate the matrix element

The semi-analytic method used in [148] starts from equation D6. Assuming  $F(\mathbf{q})=1$  it can be written:

$$\langle i | e^{i\mathbf{q}\cdot\mathbf{r}} | f \rangle = \sum_n \sum_m \alpha_{m,n}^{i*} \beta_{m,n}^f e^{i\mathbf{q}\cdot\mathbf{r}_m} \quad (\text{D11})$$

Now the quantity of  $|\langle i | e^{i\mathbf{q}\cdot\mathbf{r}} | f \rangle|^2$  is evaluated directly using equation D11:

$$\begin{aligned}
|\langle i|e^{iq \cdot r}|f\rangle|^2 &= \langle i|e^{iq \cdot r}|f\rangle (\langle i|e^{iq \cdot r}|f\rangle)^* = \\
&= \left( \sum_n \sum_m \alpha_{m,n}^{i*} \beta_{m,n}^f e^{iq \cdot r_m} \right) \left( \sum_{n'} \sum_{m'} \alpha_{m',n'}^i \beta_{m',n'}^{f*} e^{-iq \cdot r_{m'}} \right) = \\
&= \sum_{m,m'} \sum_{n,n'} \alpha_{m,n}^{i*} \beta_{m,n}^f \alpha_{m',n'}^i \beta_{m',n'}^{f*} e^{iq \cdot (r_m - r_{m'})} \quad (D12)
\end{aligned}$$

Separating out the terms with  $m=m'$  and  $n=n'$  yields:

$$|\langle i|e^{iq \cdot r}|f\rangle|^2 = \sum_{m,n} |\alpha_{m,n}^i|^2 |\beta_{m,n}^f|^2 + \sum_{m \neq m'} \sum_{n \neq n'} \alpha_{m,n}^{i*} \beta_{m,n}^f \alpha_{m',n'}^i \beta_{m',n'}^{f*} e^{iq \cdot (r_m - r_{m'})} \quad (D13)$$

Further simplification of equation D13 results in a quantity as given in equation (15) of [148]. Again it is emphasized that using the numerical scheme of Figure D2 or using the method of equation D13 results in the same values of electron-phonon scattering rates and momentum relaxation rates for the same kind of nanowires.

## Appendix E: Electron-LO phonon scattering rate in Effective Mass

### Approximation

In the calculation of electron-LO phonon scattering rate in section 4.5.2 we encountered a derivative of sub band energy with respect to  $k_z'$  (or  $q_z$ ) (for example equation 4.83). Two following methods are suggested in case we can use effective mass approximation i.e. when the conduction band can be approximated as a parabolic band with the effective mass of  $m_{z'}^*$ :

$$E(k_z') = \frac{\hbar^2 k_{z'}^2}{2m_{z'}^*} + \epsilon_{z'_{min}} \quad (E1)$$

$$\left. \frac{\partial E(k_z')}{\partial k_z'} \right|_{q_z=q_p} = \frac{\hbar^2 k_{z'}}{m_{z'}^*} = \frac{\hbar^2 (k_z \pm q_p)}{m_{z'}^*} \quad (E2)$$

Now the density of state term in equation 4.83 can be replaced with equation E1 to get:

$$W(k_z) = \frac{|D_{op}|^2}{8\pi^2 \rho \omega_0} B_{\pm} (\hbar \omega_0) \sum_{q_p} \int_0^{q_c} U(q_t, q_p) dq_t \cdot \frac{m_{z'}^*}{\hbar^2 (k_z \pm q_p)} \quad (E3)$$

In the second method,  $k_z'$  in equation E2 can be written in terms of energy using equation E1:

$$k_z' = \left[ \frac{2m_{z'}^* (E(k_z') - \epsilon_{z'_{min}})}{\hbar^2} \right]^{\frac{1}{2}} \quad (E4)$$

Therefore the derivative with respect to  $k_z'$  is reduced to:

$$\left. \frac{\partial E(k_z')}{\partial k_z'} \right|_{q_z=q_p} = \frac{\sqrt{2}\hbar}{\sqrt{m_{z'}^*}} \sqrt{E(k_z') - \epsilon_{z'_{min}}} = \frac{\sqrt{2}\hbar}{\sqrt{m_{z'}^*}} \sqrt{E(k_z \pm q_p) - \epsilon_{z'_{min}}} \quad (E5)$$

Inserting equation E5 into equation 4.83 gives the second formulation for electron-LO phonon scattering rate which is:

$$W(k_z) = \frac{|D_{op}|^2}{8\pi^2 \rho \omega_0} B_{\pm} (\hbar \omega_0) \sum_{q_p} \int_0^{q_c} U(q_t, q_p) dq_t \cdot \frac{\sqrt{m_{z'}^*}}{\sqrt{2}\hbar} \frac{1}{\sqrt{E(k_z \pm q_p) - \epsilon_{z'_{min}}}} \quad (E6)$$

This formulation has two advantages: Firstly it can be easily generalized to the case of scattering from indirect conduction sub-band to higher direct conduction sub-bands in which effective mass and minimum energies of the former sub-bands must be known. Secondly the issue of zero slope in BZ center ( $\Gamma$ ) which leads to a singularity, can be avoided by introducing a broadening as:



$$\frac{1}{\sqrt{E(k_z \pm q_p) - \epsilon_{z'_{min}}}} \cong \text{Re} \left( \frac{1}{\sqrt{(E(k_z \pm q_p) - \epsilon_{z'_{min}}) + i\gamma}} \right) = \frac{\sqrt{E(k_z \pm q_p) - \epsilon_{z'_{min}}}}{(E(k_z \pm q_p) - \epsilon_{z'_{min}}) - \gamma^2} \quad (\text{E7})$$

The broadening  $\gamma^2$  can be assumed to be 5meV which is far less than the broadening due to LO phonons i.e.  $E_{LO} = 63\text{meV}$ .

## Permissions

Following is a list of the reused materials in this thesis and the obtained permissions from the publishers.

*Figures 1.4, 1.5 and 1.12, Source: Institute for Electrical and Electronic Engineers (IEEE).*

Rightslink® by Copyright Clearance Center - Google Chrome  
https://s100.copyright.com/AppDispatchServlet#formTop



[Home](#) [Create Account](#) [Help](#)



Requesting permission to reuse content from an IEEE publication

**Title:** Bended Gate-All-Around Nanowire MOSFET: a device with enhanced carrier mobility due to oxidation-induced tensile stress

**Conference Proceedings:** 2007. IEDM 2007. IEEE International

**Author:** Moselund, K.E.; Dobrosz, P.; Olsen, S.; Pott, V.; De Michielis, L.; Tsamados, D.; Bouvet, D.; O'Neill, A.; Ionescu, A.M.

**Publisher:** IEEE

**Date:** 10-12 Dec. 2007

Copyright © 2007, IEEE

User ID

Password

☐ Enable Auto Login

[LOGIN](#)

[Forgot Password/User ID?](#)

If you're a [copyright.com](#) user, you can login to RightsLink using your [copyright.com](#) credentials. Already a RightsLink user or want to [learn more?](#)

### Thesis / Dissertation Reuse

**The IEEE does not require individuals working on a thesis to obtain a formal reuse license, however, you may print out this statement to be used as a permission grant:**

*Requirements to be followed when using any portion (e.g., figure, graph, table, or textual material) of an IEEE copyrighted paper in a thesis:*

- 1) In the case of textual material (e.g., using short quotes or referring to the work within these papers) users must give full credit to the original source (author, paper, publication) followed by the IEEE copyright line © 2011 IEEE.
- 2) In the case of illustrations or tabular material, we require that the copyright line © [Year of original publication] IEEE appear prominently with each reprinted figure and/or table.
- 3) If a substantial portion of the original paper is to be used, and if you are not the senior author, also obtain the senior author's approval.

*Requirements to be followed when using an entire IEEE copyrighted paper in a thesis:*

- 1) The following IEEE copyright/ credit notice should be placed prominently in the references: © [year of original publication] IEEE. Reprinted, with permission, from [author names, paper title, IEEE publication title, and month/year of publication]
- 2) Only the accepted version of an IEEE copyrighted paper can be used when posting the paper or your thesis on-line.
- 3) In placing the thesis on the author's university website, please display the following message in a prominent place on the website: In reference to IEEE copyrighted material which is used with permission in this thesis, the IEEE does not endorse any of [university/educational entity's name goes here]'s products or services. Internal or personal use of this material is permitted. If interested in reprinting/republishing IEEE copyrighted material for advertising or promotional purposes or for creating new collective works for resale or redistribution, please go to [http://www.ieee.org/publications\\_standards/publications/rights/rights\\_link.html](http://www.ieee.org/publications_standards/publications/rights/rights_link.html) to learn how to obtain a License from RightsLink.

If applicable, University Microfilms and/or ProQuest Library, or the Archives of Canada may supply single copies of the dissertation.

[BACK](#)

[CLOSE WINDOW](#)

Copyright © 2012 Copyright Clearance Center, Inc. All Rights Reserved. [Privacy statement](#). Comments? We would like to hear from you. E-mail us at [customercare@copyright.com](mailto:customercare@copyright.com)

Figure 1.6, Source: Nature Publishing Group.

License Number	2994611160507
License date	Sep 23, 2012
Licensed content publisher	Nature Publishing Group
Licensed content publication	Nature Materials
Licensed content title	Highly ordered nanowire arrays on plastic substrates for ultrasensitive flexible chemical sensors
Licensed content author	Michael C. McAlpine , Habib Ahmad , Dunwei Wang and James R. Heath
Licensed content date	May 1, 2007
Volume number	6
Issue number	5
Type of Use	reuse in a thesis/dissertation
Requestor type	academic/educational
Format	print and electronic
Portion	figures/tables/illustrations
Number of figures/tables/illustrations	1
High-res required	no
Figures	Figure 1 Illustration of the steps for transfer printing SNAP nanowires onto plastic substrates
Author of this NPG article	no
Your reference number	
Title of your thesis / dissertation	Electronic and Optical Properties of Silicon Nanowires: Theory and Modelling
Expected completion date	Oct 2012
Estimated size (number of pages)	207
Total	0.00 USD
Terms and Conditions	Terms and Conditions for Permissions

Nature Publishing Group hereby grants you a non-exclusive license to reproduce this material for this purpose, and for no other use, subject to the conditions below:

1. NPG warrants that it has, to the best of its knowledge, the rights to license reuse of this material. However, you should ensure that the material you are requesting is original to Nature Publishing Group and does not carry the copyright of another entity (as credited in the published version). If the credit line on any part of the material you have requested indicates that it was reprinted or adapted by NPG with permission from another source, then you should also seek permission from that source to reuse the material.

Figure 1.7, 1.13, Figures 2.3, 2.4, 2.5, 2.8 (I am the author of these figures) and Figure 6.12, Source: American Institute of Physics (AIP).

License Number	2994590298440
Order Date	Sep 23, 2012
Publisher	American Institute of Physics
Publication	Applied Physics Letters
Article Title	Optical characterization of wurtzite gallium nitride nanowires
Author	M. W. Lee, H. Z. Twu, C.-C. Chen, C.-H. Chen et al.
Online Publication Date	Nov 26, 2001
Volume number	79
Issue number	22
Type of Use	Thesis/Dissertation
Requestor type	Student
Format	Print and electronic
Portion	Figure/Table
Number of figures/tables	1
Title of your thesis / dissertation	Electronic and Optical Properties of Silicon Nanowires: Theory and Modelling
Expected completion date	Oct 2012
Estimated size (number of pages)	207
Total	0.00 USD

#### Terms and Conditions

American Institute of Physics -- Terms and Conditions: Permissions Uses

American Institute of Physics ("AIP") hereby grants to you the non-exclusive right and license to use and/or distribute the Material according to the use specified in your order, on a one-time basis, for the specified term, with a maximum distribution equal to the number that you have ordered. Any links or other content accompanying the Material are not the subject of this license.

1. You agree to include the following copyright and permission notice with the reproduction of the Material: "Reprinted with permission from [FULL CITATION]. Copyright [PUBLICATION YEAR], American Institute of Physics." For an article, the copyright and permission notice must be printed on the first page of the article or book chapter. For photographs, covers, or tables, the copyright and permission notice may appear with the Material, in a footnote, or in the reference list.
2. If you have licensed reuse of a figure, photograph, cover, or table, it is your responsibility to ensure that the material is original to AIP and does not contain the copyright of another entity, and that the copyright notice of the figure, photograph, cover, or table does not indicate that it was reprinted by AIP, with permission, from another source. Under no circumstances does AIP, purport or intend to grant permission to reuse material to which it does not hold copyright.
3. You may not alter or modify the Material in any manner. You may translate the Material into another language only if you have licensed translation rights. You may not use the Material

License Number	2994590446097
Order Date	Sep 23, 2012
Publisher	American Institute of Physics
Publication	Applied Physics Letters
Article Title	Strain induced change of bandgap and effective mass in silicon nanowires
Author	Daryoush Shiri, Yifan Kong, Andrei Buin, M. P. Anantram et al.
Online Publication Date	Aug 22, 2008
Volume number	93
Issue number	7
Type of Use	Thesis/Dissertation
Requestor type	Student
Format	Print and electronic
Portion	Figure/Table
Number of figures/tables	3
Title of your thesis / dissertation	Electronic and Optical Properties of Silicon Nanowires: Theory and Modelling
Expected completion date	Oct 2012
Estimated size (number of pages)	207
Total	0.00 USD

#### Terms and Conditions

American Institute of Physics -- Terms and Conditions: Permissions Uses

American Institute of Physics ("AIP") hereby grants to you the non-exclusive right and license to use and/or distribute the Material according to the use specified in your order, on a one-time basis, for the specified term, with a maximum distribution equal to the number that you have ordered. Any links or other content accompanying the Material are not the subject of this license.

1. You agree to include the following copyright and permission notice with the reproduction of the Material: "Reprinted with permission from [FULL CITATION]. Copyright [PUBLICATION YEAR], American Institute of Physics." For an article, the copyright and permission notice must be printed on the first page of the article or book chapter. For photographs, covers, or tables, the copyright and permission notice may appear with the Material, in a footnote, or in the reference list.
2. If you have licensed reuse of a figure, photograph, cover, or table, it is your responsibility to ensure that the material is original to AIP and does not contain the copyright of another entity, and that the copyright notice of the figure, photograph, cover, or table does not indicate that it was reprinted by AIP, with permission, from another source. Under no circumstances does AIP, purport or intend to grant permission to reuse material to which it does not hold copyright.
3. You may not alter or modify the Material in any manner. You may translate the Material into another language only if you have licensed translation rights. You may not use the Material for promotional purposes. AIP reserves all rights not specifically granted herein.

License Number	2994590650787
Order Date	Sep 23, 2012
Publisher	American Institute of Physics
Publication	Journal of Applied Physics
Article Title	Silicon nanowire n-type metal-oxide-semiconductor field-effect transistors and single-electron transistors at room temperature under uniaxial tensile strain
Author	YeonJoo Jeong, Kousuke Miyaji, Takuya Saraya, Toshiro Hiramoto et al.
Online Publication Date	Apr 24, 2009
Volume number	105
Issue number	8
Type of Use	Thesis/Dissertation
Requestor type	Student
Format	Print and electronic
Portion	Figure/Table
Number of figures/tables	1
Title of your thesis / dissertation	Electronic and Optical Properties of Silicon Nanowires: Theory and Modelling
Expected completion date	Oct 2012
Estimated size (number of pages)	207
Total	0.00 USD

#### Terms and Conditions

American Institute of Physics -- Terms and Conditions: Permissions Uses

American Institute of Physics ("AIP") hereby grants to you the non-exclusive right and license to use and/or distribute the Material according to the use specified in your order, on a one-time basis, for the specified term, with a maximum distribution equal to the number that you have ordered. Any links or other content accompanying the Material are not the subject of this license.

1. You agree to include the following copyright and permission notice with the reproduction of the Material: "Reprinted with permission from [FULL CITATION]. Copyright [PUBLICATION YEAR], American Institute of Physics." For an article, the copyright and permission notice must be printed on the first page of the article or book chapter. For photographs, covers, or tables, the copyright and permission notice may appear with the Material, in a footnote, or in the reference list.
2. If you have licensed reuse of a figure, photograph, cover, or table, it is your responsibility to ensure that the material is original to AIP and does not contain the copyright of another entity, and that the copyright notice of the figure, photograph, cover, or table does not indicate that it was reprinted by AIP, with permission, from another source. Under no circumstances does AIP, purport or intend to grant permission to reuse material to which it does not hold copyright.
3. You may not alter or modify the Material in any manner. You may translate the Material into

License Number	2994590844599
Order Date	Sep 23, 2012
Publisher	American Institute of Physics
Publication	Journal of Applied Physics
Article Title	The structural and luminescence properties of porous silicon
Author	A. G. Cullis, L. T. Canham, P. D. J. Calcott
Online Publication Date	Aug 1, 1997
Volume number	82
Issue number	3
Type of Use	Thesis/Dissertation
Requestor type	Student
Format	Print and electronic
Portion	Figure/Table
Number of figures/tables	1
Title of your thesis / dissertation	Electronic and Optical Properties of Silicon Nanowires: Theory and Modelling
Expected completion date	Oct 2012
Estimated size (number of pages)	207
Total	0.00 USD

#### Terms and Conditions

American Institute of Physics -- Terms and Conditions: Permissions Uses

American Institute of Physics ("AIP") hereby grants to you the non-exclusive right and license to use and/or distribute the Material according to the use specified in your order, on a one-time basis, for the specified term, with a maximum distribution equal to the number that you have ordered. Any links or other content accompanying the Material are not the subject of this license.

1. You agree to include the following copyright and permission notice with the reproduction of the Material: "Reprinted with permission from [FULL CITATION]. Copyright [PUBLICATION YEAR], American Institute of Physics." For an article, the copyright and permission notice must be printed on the first page of the article or book chapter. For photographs, covers, or tables, the copyright and permission notice may appear with the Material, in a footnote, or in the reference list.
2. If you have licensed reuse of a figure, photograph, cover, or table, it is your responsibility to ensure that the material is original to AIP and does not contain the copyright of another entity, and that the copyright notice of the figure, photograph, cover, or table does not indicate that it was reprinted by AIP, with permission, from another source. Under no circumstances does AIP, purport or intend to grant permission to reuse material to which it does not hold copyright.
3. You may not alter or modify the Material in any manner. You may translate the Material into another language only if you have licensed translation rights. You may not use the Material for promotional purposes. AIP reserves all rights not specifically granted herein.
4. The foregoing license shall not take effect unless and until AIP or its agent, Copyright

*Figures 3.2, 3.3.4, 3.5, 3.6 and 3.7 (I am the author of these figures), Source: John Wiley and Sons Ltd.*

License Number	2994610213251
License date	Sep 23, 2012
Licensed content publisher	John Wiley and Sons
Licensed content publication	physica status solidi - Rapid Research Letters
Book title	
Licensed content author	Yifan Kong,Daryoush Shiri,Andrei Buin
Licensed content date	Sep 14, 2009
Start page	281
End page	283
Type of use	Dissertation/Thesis
Requestor type	Author of this Wiley article
Format	Print and electronic
Portion	Figure/table
Number of figures/tables	4
Number of extracts	
Original Wiley figure/table number(s)	Figure 1 Figure 2 Figure 3 Figure 4
Will you be translating?	No
Order reference number	
Total	0.00 USD
Terms and Conditions	

#### TERMS AND CONDITIONS

This copyrighted material is owned by or exclusively licensed to John Wiley & Sons, Inc. or one of its group companies (each a "Wiley Company") or a society for whom a Wiley Company has exclusive publishing rights in relation to a particular journal (collectively WILEY"). By clicking "accept" in connection with completing this licensing transaction, you agree that the following terms and conditions apply to this transaction (along with the billing and payment terms and conditions established by the Copyright Clearance Center Inc., ("CCC's Billing and Payment terms and conditions"), at the time that you opened your Rightslink account (these are available at any time at <http://myaccount.copyright.com>)



#### Terms and Conditions

1. The materials you have requested permission to reproduce (the "Materials") are protected by copyright.


2. You are hereby granted a personal, non-exclusive, non-sublicensable, non-transferable, worldwide, limited license to reproduce the Materials for the purpose specified in the licensing process. This license is for a one-time use only with a maximum distribution equal to the number that you identified in the licensing process. Any form of republication granted by this licence must be completed within two years of the date of the grant of this licence (although copies prepared before may be distributed thereafter). The Materials shall not be used in any other manner or for any other purpose. Permission is granted subject to an appropriate acknowledgement given to the author, title of the material/book/journal and the publisher. You shall also duplicate the copyright notice that appears in the Wiley publication in your use of the Material. Permission is also granted on the understanding that nowhere in the text is a



Figure 1.8, 1.11a, 2.6b, 2.7b, Source: American Chemical Society (ACS)



[Home](#) [Account Info](#) [Help](#)

 **ACS Publications**  
High quality. High impact.

**Title:** Recombination Dynamics of Spatially Confined Electron–Hole System in Luminescent Gold Catalyzed Silicon Nanowires

**Author:** O. Demichel, V. Calvo, N. Pauc, A. Besson, P. Noé, F. Oehler, P. Gentile, and N. Magnea

**Publication:** Nano Letters

**Publisher:** American Chemical Society

**Date:** Jul 1, 2009

Copyright © 2009, American Chemical Society

Logged in as:  
Daryoush Shiri  
Account #: 3000381982

[LOGOUT](#)

#### PERMISSION/LICENSE IS GRANTED FOR YOUR ORDER AT NO CHARGE

This type of permission/license, instead of the standard Terms & Conditions, is sent to you because no fee is being charged for your order. Please note the following:

- Permission is granted for your request in both print and electronic formats, and translations.
- If figures and/or tables were requested, they may be adapted or used in part.
- Please print this page for your records and send a copy of it to your publisher/graduate school.
- Appropriate credit for the requested material should be given as follows: "Reprinted (adapted) with permission from (COMPLETE REFERENCE CITATION). Copyright (YEAR) American Chemical Society." Insert appropriate information in place of the capitalized words.
- One-time permission is granted only for the use specified in your request. No additional uses are granted (such as derivative works or other editions). For any other uses, please submit a new request.

If credit is given to another source for the material you requested, permission must be obtained from that source.

[BACK](#)

[CLOSE WINDOW](#)

Copyright © 2012 [Copyright Clearance Center, Inc.](#) All Rights Reserved. [Privacy statement.](#)  
Comments? We would like to hear from you. E-mail us at [customer@copyright.com](mailto:customer@copyright.com)



**Title:** Tunable Visible and Near-IR  
Emission from Sub-10 nm  
Etched Single-Crystal Si  
Nanopillars

**Author:** Sameer S. Walavalkar, Carrie E.  
Hofmann, Andrew P. Homyk, M.  
David Henry, Harry A. Atwater,  
and Axel Scherer

**Publication:** Nano Letters

**Publisher:** American Chemical Society

**Date:** Nov 1, 2010

Copyright © 2010, American Chemical Society

Logged in as:

Daryoush Shiri

Account #:

3000381982

LOGOUT

### PERMISSION/LICENSE IS GRANTED FOR YOUR ORDER AT NO CHARGE

This type of permission/license, instead of the standard Terms & Conditions, is sent to you because no fee is being charged for your order. Please note the following:

- Permission is granted for your request in both print and electronic formats, and translations.
- If figures and/or tables were requested, they may be adapted or used in part.
- Please print this page for your records and send a copy of it to your publisher/graduate school.
- Appropriate credit for the requested material should be given as follows: "Reprinted (adapted) with permission from (COMPLETE REFERENCE CITATION). Copyright (YEAR) American Chemical Society." Insert appropriate information in place of the capitalized words.
- One-time permission is granted only for the use specified in your request. No additional uses are granted (such as derivative works or other editions). For any other uses, please submit a new request.

If credit is given to another source for the material you requested, permission must be obtained from that source.

BACK

CLOSE WINDOW

ACS Publications  
High quality. High impact.

**Title:** Strain-Driven Electronic Band  
Structure Modulation of Si  
Nanowires

**Author:** Ki-Ha Hong, Jongseob Kim,  
Sung-Hoon Lee, and Jai Kwang  
Shin

**Publication:** Nano Letters

**Publisher:** American Chemical Society

**Date:** May 1, 2008

Copyright © 2008, American Chemical Society

Logged in as:

Daryoush Shiri

Account #:

3000381982

LOGOUT

**PERMISSION/LICENSE IS GRANTED FOR YOUR ORDER AT NO CHARGE**

This type of permission/license, instead of the standard Terms & Conditions, is sent to you because no fee is being charged for your order. Please note the following:

- Permission is granted for your request in both print and electronic formats, and translations.
- If figures and/or tables were requested, they may be adapted or used in part.
- Please print this page for your records and send a copy of it to your publisher/graduate school.
- Appropriate credit for the requested material should be given as follows: "Reprinted (adapted) with permission from (COMPLETE REFERENCE CITATION). Copyright (YEAR) American Chemical Society." Insert appropriate information in place of the capitalized words.
- One-time permission is granted only for the use specified in your request. No additional uses are granted (such as derivative works or other editions). For any other uses, please submit a new request.

If credit is given to another source for the material you requested, permission must be obtained from that source.

BACK

CLOSE WINDOW

Copyright © 2012 [Copyright Clearance Center, Inc.](#) All Rights Reserved. [Privacy statement.](#)  
Comments? We would like to hear from you. E-mail us at [customercare@copyright.com](mailto:customercare@copyright.com)

Adapted reprint of my paper in Chapter 5 Source: Scientific Reports by Nature Publishing Group.



RightsLink®

Home

Create Account

Help



**Title:** Reversible Modulation of Spontaneous Emission by Strain in Silicon Nanowires  
**Author:** Daryoush Shiri, Amit Verma, C. R. Selvakumar, M. P. Anantram  
**Publication:** Scientific Reports  
**Publisher:** Nature Publishing Group  
**Date:** Jun 15, 2012  
Copyright © 2012, Rights Managed by Nature Publishing Group

User ID

Password

☐ Enable Auto Login

LOGIN

[Forgot Password/User ID?](#)

If you're a [copyright.com user](#), you can login to RightsLink using your copyright.com credentials. Already a [RightsLink user](#) or want to [learn more?](#)

### Creative Commons

The request you have made is considered to be non-commercial/educational. As the article you have requested has been distributed under a Creative Commons license (Attribution-Noncommercial 2.5), you may reuse this material for non-commercial/educational purposes without obtaining additional permission from Nature Publishing Group, providing that the author and the original source of publication are fully acknowledged.

For full terms and conditions of the Creative Commons license, please see the attached link <http://creativecommons.org/licenses/by-nc/2.5>

BACK

CLOSE WINDOW

Copyright © 2012 [Copyright Clearance Center, Inc.](#) All Rights Reserved. [Privacy statement.](#)  
Comments? We would like to hear from you. E-mail us at [customercare@copyright.com](mailto:customercare@copyright.com)

Figure 1.3, Source: American Association for the Advancement of Science (AAAS)

License Number	2994610877052
License date	Sep 23, 2012
Licensed content publisher	The American Association for the Advancement of Science
Licensed content publication	Science
Licensed content title	A Laser Ablation Method for the Synthesis of Crystalline Semiconductor Nanowires
Licensed content author	Alfredo M. Morales, Charles M. Lieber
Licensed content date	Jan 9, 1998
Volume number	279
Issue number	5348
Type of Use	Thesis / Dissertation
Requestor type	Scientist/individual at a research institution
Format	Print and electronic
Portion	Figure
Number of figures/tables	1
Order reference number	
Title of your thesis / dissertation	Electronic and Optical Properties of Silicon Nanowires: Theory and Modelling
Expected completion date	Oct 2012
Estimated size(pages)	207
Total	0.00 USD

#### Terms and Conditions

#### American Association for the Advancement of Science TERMS AND CONDITIONS

Regarding your request, we are pleased to grant you non-exclusive, non-transferable permission, to republish the AAAS material identified above in your work identified above, subject to the terms and conditions herein. We must be contacted for permission for any uses other than those specifically identified in your request above.

The following credit line must be printed along with the AAAS material: "From [Full Reference Citation]. Reprinted with permission from AAAS."

All required credit lines and notices must be visible any time a user accesses any part of the AAAS material and must appear on any printed copies and authorized user might make.

This permission does not apply to figures / photos / artwork or any other content or materials included in your work that are credited to non-AAAS sources. If the requested material is sourced to or references non-AAAS sources, you must obtain authorization from that source as well before using that material. You agree to hold harmless and indemnify AAAS against any claims arising from your use of any content in your work that is credited to non-AAAS sources.

*Figures 1.9, 1.11b, 5.19, Table 3.1, Source: American Physical Society (APS)*



AMERICAN PHYSICAL SOCIETY

One Physics Ellipse, College Park, MD 20740 · <http://www.aps.org>

September 26, 2012

Daryoush Shiri  
PhD Candidate, Nanotechnology Program,  
Department of Electrical and Computer Engineering  
University of Waterloo, Waterloo, Ontario N2L 3G1, Canada

**Ref # 21208**

Thank you for your permission request dated September 23, 2012. We are pleased to grant you a non-exclusive, non-transferable permission, English rights, limited to **print and electronic format**, provided you meet the criteria outlined below. Permission is for a one-time use and does not include permission for future editions, updates, databases, translations, or any other matters. Permission must be sought for each additional use. This permission does not include the right to modify APS material.

Please print the required copyright credit line on the first page that the material appears: "Reprinted (abstract/excerpt/figure) with permission from [FULL REFERENCE CITATION] as follows: authors names, journal title, volume number, page number and year of publication. Copyright (YEAR) by the American Physical Society.

The following language must appear somewhere on the website: "Readers may view, browse, and/or download material for temporary copying purposes only, provided these uses are for noncommercial personal purposes. Except as provided by law, this material may not be further reproduced, distributed, transmitted, modified, adapted, performed, displayed, published, or sold in whole or part, without prior written permission from the American Physical Society."

Provide a hyperlink from the reprinted APS material (the hyperlink may be embedded in the copyright credit line). APS's link manager technology makes it convenient and easy to provide links to individual articles in APS journals. For information, see: <http://link.aps.org/>.

You must also obtain permission from at least one of the authors for each separate work, if you haven't done so already. The author's name and address can be found on the first page of the published Article.

Use of the APS material must not imply any endorsement by the American Physical Society.

Permission is granted for use of the following APS material only:

- Figs. 1, 12, Phys. Rev. B 83, 245443 (2011)
- Fig. 4, Phys. Rev. B 78, 235422 (2008)
- Fig. 1, Phys. Rev. Lett. 94, 219701 (2005)
- Tables I, II, Phys. Rev. B 51, 9521–9525 (1995)

Permission is limited to the single title specified of the publication as follows:

A Ph.D. thesis entitled, "Electronic and Optical Properties of Silicon nanowires: Theory and Modelling," to be published by the University of Waterloo

If you have any questions, please refer to the Copyright FAQ at: <http://publish.aps.org/copyrightFAQ.html> or send an email to [assocpub@aps.org](mailto:assocpub@aps.org).

Sincerely,  
Melissa Overton  
Publications Marketing Coordinator

## Bibliography

- [1] J. Xiang, et al., Ge/Si nanowire heterostructures as high-performance field-effect transistors, *Nature* 441, 489 (2006).
- [2] N. Singh, et al., Observation of metal-layer stress on Si nanowires in gate-all-around high- $\kappa$ /metal-gate device structures, *IEEE Electron Device Letters*, 28(7), 558 (2007).
- [3] C. Yang, Z. Zhong, and C. M. Lieber, Encoding electronic properties by synthesis of axial modulation-doped silicon nanowires, *Science* 310, 1304 (2005).
- [4] Q. Li, et al., Silicon nanowire on oxide/nitride/oxide for memory application. *Nanotechnology* 18, 235204 (2007).
- [5] Y. Hu, F. Kuemmeth, C. M. Lieber, and C. M. Marcus, Hole spin relaxation in Ge-Si core-shell nanowire qubits, *Nat. Nanotechnol.* 7, 47 (2012).
- [6] M. McAlpine, H. Ahmad, D. Wang, and K. J. Heath, Highly ordered nanowire arrays on plastic substrates for ultrasensitive flexible chemical sensors. *Nat. Mater.* 6, 379 (2007).
- [7] E. Stern, et al. Label-free immunodetection with CMOS-compatible semiconducting nanowires, *Nature* 445, 519 (2007).
- [8] R. He, and P. Yang, Giant piezoresistance effect in silicon nanowires, *Nat. Nanotechnol.* 1, 42 (2006).
- [9] X. L. Feng, R. He, P. Yang, and M. L. Roukes, Very high frequency silicon nanowire electromechanical resonators, *Nano Lett.* 7(7), 1953 (2007).
- [10] A. I. Hochbaum, et al., Enhanced thermoelectric performance of rough silicon nanowires, *Nature* 451, 163 (2008).
- [11] A. I. Boukai, et al., Silicon nanowires as efficient thermoelectric materials, *Nature* 451, 168 (2008).
- [12] B. Tian, et al., Coaxial silicon nanowires as solar cells and nanoelectronic power sources, *Nature* 449, 885 (2007).
- [13] V. Sivakov, et al., Silicon nanowire-based solar cells on glass: synthesis, optical properties, and cell parameters, *Nano Lett.* 9(4), 1549 (2009).
- [14] Y. Ahn, J. Dunning, and J. Park, Scanning photocurrent imaging and electronic band studies in silicon nanowire field effect transistors. *Nano Lett.* 5(7), 1367 (2005).
- [15] A. Zhang, H. Kim, J. Cheng, and Y. -H. Lo, Ultrahigh responsivity visible and infrared detection using silicon nanowire phototransistors, *Nano Lett.* 10(6), 2117 (2010).
- [16] C. Yang, C. J. Barrelet, F. Capasso, and C. M. Lieber, Single p-type/Intrinsic/n-type silicon nanowires as nanoscale avalanche photodetectors, *Nano Lett.* 6(12), 2929 (2006).
- [17] O. Hayden, R. Agarwal, and C. M. Lieber, Nanoscale avalanche photodiodes for highly sensitive and spatially resolved photon detection, *Nat. Mater.* 5, 352 (2006).
- [18] R. Agarwal and C. M. Lieber, Semiconductor nanowires: optics and optoelectronics, *Appl. Phys. A: Mater. Sci. Proc.* 85, 209 (2006).
- [19] Y. Huang, X. Duan, and C. M. Lieber, Nanowires for integrated multicolor nanophotonics, *Small* 1 (1), 142 (2005).
- [20] O. Hayden, A. B. Greytak, and D. C. Bell, Core-shell nanowire light-emitting diodes, *Adv. Mater.* 17 (6), 701 (2005).
- [21] B. Bhushan (Editor), *Springer Handbook of Nanotechnology*, Chapter 4, (Springer-Verlag, Berlin, Heidelberg, 2007).
- [22] W. Lu, P. Xie, and C. M. Lieber, Nanowire transistor performance limits and applications, *IEEE Transactions on Electron Devices*, 55 (11), (2008).

- [23] A. I. Hochbaum, and P. Yang, Semiconductor nanowires for energy conversion, *Chem. Rev.* 110, 527 (2010).
- [24] R. Rurali, Colloquium: structural, electronic, and transport properties of silicon nanowires, *Rev. Mod. Phys.* 82, 427 (2010).
- [25] Y. Cui, L. J. Lauhon, M. S. Gudisken, J. Wang and C. M. Lieber, Diameter-controlled synthesis of single-crystal silicon nanowires, *Appl. Phys. Lett.* 78, 2214 (2001).
- [26] Y. Wu, Y. Cui, L. Huynh, C. J. Barrelet, D. C. Bell, and C. M. Lieber, Controlled growth and structures of molecular-scale silicon nanowires, *Nano Lett.* 4(3), 433 (2004).
- [27] T. Vo, A. J. Williamson, and G. Galli, First principles simulations of the structural and electronic properties of silicon nanowires, *Phys. Rev. B* 74, 045116 (2006).
- [28] J. Ramanujam, D. Shiri, and A. Verma, Silicon Nanowire Growth and Properties: A Review, *Mater. Express*, Vol. 1, No. 2, 105-126 (2011).
- [29] V. Schmidt, J. V. Wittemann, S. Senz, and U. Gösele, Silicon nanowires: a review on aspects of their growth and their electrical properties, *Adv. Mater.* 21, 2681 (2009).
- [30] A. M. Morales and C. M. Lieber, A laser ablation method for the synthesis of crystalline semiconductor nanowires, *Science* 279, 208 (1998).
- [31] D. D. D. Ma, C. S. Lee, F. C. K. Au, S. Y. Tong, and S. T. Lee, Small-diameter silicon nanowire surfaces, *Science* 299, 1874 (2003).
- [32] N. Wang, Y. F. Zhang, Y. H. Tang, C. S. Lee, and S. T. Lee, SiO<sub>2</sub>-enhanced synthesis of Si nanowires by laser ablation, *Appl. Phys. Lett.* 73, 3902 (1998).
- [33] K. E. Moselund, et al., Bended gate-all-around nanowire MOSFET: a device with enhanced carrier mobility due to oxidation-induced stress, *IEDM digest of technical papers*, IEDM (2007).
- [34] N. Singh, et al., Ultra-narrow silicon nanowire gate-all-around CMOS devices: Impact of diameter, channel-orientation and low temperature on device performance, *IEDM Tech. Dig.* 547 (2006).
- [35] W. I. Park, G. Zheng, X. Jiang, B. Tian and C. M. Lieber, Controlled synthesis of millimeter-long silicon nanowires with uniform electronic properties, *Nano Lett.* 8(9), 3004 (2008).
- [36] N. A. Melosh, et al., Ultrahigh-density nanowire lattices and circuits, *Science* 300, 112 (2003).
- [37] S. S. Walavalkar, C. E. Hofmann, A. P. Homyk, M. D. Henry, H. A. Atwater, and A. Scherer, Tunable visible and near-IR emission from Sub-10 nm etched single-crystal Si nanopillars, *Nano Lett.* 10(11), 4423 (2010).
- [38] H. I. Liu, D. K. Biegelsen, F. A. Ponce, N. M. Johnson, and R. F. W. Pease, Self-limiting oxidation for fabricating sub-5 nm silicon nanowires, *Appl. Phys. Lett.* 64, 1383 (1994).
- [39] M. S. Hybertsen, Absorption and emission of light in nanoscale silicon structures, *Phys. Rev. Lett.* 72, 1514 (1994).
- [40] A. G. Cullis and L. T. Canham, Visible light emission due to quantum size effects in highly porous crystalline silicon, *Nature* 353, 335 (1991).
- [41] V. Lehmann and U. Gösele, Porous silicon formation: A quantum wire effect, *Appl. Phys. Lett.* 58, 856 (1991).
- [42] A. J. Read, R. J. Needs, K. J. Nash, L. T. Canham, P. D. J. Calcott and A. Qteish, First-principles calculations of the electronic properties of silicon quantum wires, *Phys. Rev. Lett.* 69, 1232 (1992).
- [43] P. D. J. Calcott, K. J. Nash, L. T. Canham, M. J. Kane, and D. Brumhead, Identification of radiative transitions in highly porous silicon, *J. Phys: Condens. Matter.* 5, L91 (1993).
- [44] Z. H. Lu, D. J. Lockwood and J.-M. Baribeau, Quantum confinement and light emission in SiO<sub>2</sub>/Si superlattice, *Nature* 378, 258 (1995).
- [45] G. D. Sanders, and Y. -C. Chang, Theory of optical properties of quantum wires in porous silicon, *Phys. Rev. B* 45, 9202 (1992).
- [46] C. Y. Yeh, S. B. Zhang, and A. Zunger, Confinement, surface, and chemisorption effects on the optical properties of Si quantum wires, *Phys. Rev. B* 50, 14405 (1994).



- [47] J. B. Xia, and K. W. Cheah, Quantum confinement effect in thin quantum wires, *Phys. Rev. B* 55, 15688 (1997).
- [48] F. Buda, J. Kohanoff, and M. Parrinello, Optical properties of porous silicon: a first-principles study, *Phys. Rev. Lett.* 69, 1272 (1992).
- [49] M. S. Hybertsen, and M. Needels, First-principles analysis of electronic states in silicon nanoscale quantum wires, *Phys. Rev. B* 48, 4608 (1993).
- [50] A. G. Cullis, L. T. Canham and P. D. J. Calcott, The structural and luminescence of porous silicon, *J. Appl. Phys.* 82, 909(1997).
- [51] M. Gotza, M. Dutoit, and M. Illegems, Fabrication and photoluminescence investigation of silicon nanowires on silicon-on-insulator material, *J. Vac. Sci. Technol. B* 16, 582 (1998).
- [52] D. P. Yu, et al., Nanoscale silicon wires synthesized using simple physical evaporation, *Appl. Phys. Lett.* 72, 3458 (1998); D. P. Yu, et al., Amorphous silica nanowires: intensive blue light emitters, *ibid* 73, 3076 (1998).
- [53] J. Qi, A. M. Belcher, and J. M. White, Spectroscopy of individual silicon nanowires, *Appl. Phys. Lett.* 82, 2616 (2003).
- [54] J. H. He, et al., Synthesis of blue-light-emitting  $\text{Si}_{1-x}\text{Ge}_x$  oxide nanowires, *Appl. Phys. Lett.* 86 (26), 263109 (2005).
- [55] T. K. Sham, et al., Electronic structure and optical properties of silicon nanowires: A study using x-ray excited optical luminescence and x-ray emission spectroscopy, *Phys. Rev. B* 70, 045313 (2004).
- [56] M. Dovrat, N. Arad, X.-H. Zhang, S.-T. Lee, and A. Sa'ar, Optical properties of silicon nanowires from cathodoluminescence imaging and time-resolved photoluminescence spectroscopy, *Phys. Rev. B* 75, 205343 (2007).
- [57] O. Demichel, et al., Recombination dynamics of spatially confined electron-hole system in luminescent gold catalyzed silicon nanowires, *Nano. Lett.* 9 (7), 2575 (2009).
- [58] J. E. Allen, et al., High-resolution detection of Au catalyst atoms in Si nanowires, *Nat. Nanotechnol.*, 3 (3) 168 (2008).
- [59] J. D. Holmes, K. P. Johnston, R. C. Doty, and B. A. Korgel, Control of thickness and orientation of solution-grown silicon nanowires, *Science* 287, 1471 (2000).
- [60] A. I. Hochbaum, D. Gargas, Y. J. Hwang, and P. Yang, Single crystalline mesoporous silicon nanowires, *Nano Lett.* 9(10), 3550 (2009).
- [61] Y. Qu, L. Liao, Y. Li, H. Zhang, Y. Huang, and X. Duan, Electrically conductive and optically active porous silicon nanowires, *Nano Lett.* 9(12), 4539 (2009).
- [62] J. Huo, J. L. Freeouf, and J. R. Carruthers, Electroluminescence from silicon nanowires, *Nanotechnology* 15, 1848 (2004).
- [63] V. A. Sivakov, F. Voigt, A. Berger, G. Bauer, and S. H. Christiansen, Roughness of silicon nanowire sidewalls and room temperature photoluminescence, *Phys. Rev. B* 82, 125446 (2010).
- [64] D. M. Lyons, K. M. Ryan, M. A. Morris, and J. D. Holmes, Tailoring the optical properties of silicon nanowire arrays through strain, *Nano. Lett.* 2 (8), 811 (2002).
- [65] G. Audoit, et al., Strain induced photoluminescence from silicon and germanium nanowire arrays, *J. Mater. Chem.* 15, 4809 (2005).
- [66] A. R. Guichard, R. D. Kekatpure, M. L. Brongersma, and T. I. Kamins, Temperature-dependent Auger recombination dynamics in luminescent silicon nanowires, *Phys. Rev. B* 78, 235422 (2008).
- [67] O. Demichel, et al., Quantum confinement effects and strain-induced band-gap energy shifts in core-shell Si-SiO<sub>2</sub> nanowires, *Phys. Rev. B* 83, 245443 (2011).
- [68] Y. M. Niquet, A. Lherbier, N. H. Quang, M. V. Fernández-Serra, X. Blase and C. Delerue, Electronic structure of semiconductor nanowires, *Phys. Rev. B* 73, 165319 (2006).
- [69] M. Khorasaninejad and S. S. Saini, Bend-waveguides on silicon nanowire optical waveguide (SNOW), *IEEE Photonics Journal*, 3, 696 -702 (2011).

- [70] M. Khorasaninejad, N. Abedzadeh, J. Walia, S. Patchett, and S. S. Saini, Color matrix refractive index sensors using coupled vertical silicon nanowire arrays, *Nano Lett.* 12(8), 4228 (2012).
- [71] L. Tsakalakos, et al., Strong broadband optical absorption in silicon nanowire films, *J. Nanophoton* 1, 13552 (2007).
- [72] L. Hu and G. Chen, Analysis of optical absorption in silicon nanowire arrays for photovoltaic applications, *Nano Lett.* 7(11), 3249 (2007).
- [73] J. Zhu, et al., Optical absorption enhancement in amorphous silicon nanowire and nanocone arrays, *Nano Lett.* 9(1), 279 (2009).
- [74] M. M. Adachi, M. P. Anantram, and K. S. Karim, Optical properties of crystalline-amorphous core-shell silicon nanowires, *Nano Lett.* 10(10), 4093 (2010).
- [75] T. -M. Shih, et al., Supercollimation in photonic crystals composed of silicon rods, *Appl. Phys. Lett.* 93, 131111 (2008).
- [76] A. Zhang, S. You, C. Soci, D. Wang, and Y.-H. Lo, Planar and vertical Si nanowire photodetectors, *Lasers and Electro-Optics, and Conference on Quantum Electronics and Laser Science, CLEO/QELS*, San Jose, California, May (2008).
- [77] Y. Ishikawa, et al., Strain-induced band gap shrinkage in Ge grown on Si substrate, *Appl. Phys. Lett.* 82, 2044 (2003).
- [78] T. Krishnamohan, et al., High performance, uniaxially-strained, silicon and germanium, double-gate p-MOSFETs, *Microelectronics Engineering* 84, 2063 (2007).
- [79] X. Sun, J. Liu, L. C. Kimerling, and J. Michel, Room-temperature direct bandgap electroluminescence from Ge-on-Si light-emitting diodes, *Optics Lett.* 34 (8), 1198 (2009).
- [80] X. Sun, et al., Electrically pumped hybrid evanescent Si/InGaAsP lasers, *Optics Lett.* 34 (9), 1345 (2009).
- [81] R. A. Soref, and L. Friedman, Direct-gap Ge/GeSn/Si and GeSn/Ge/Si heterostructures, *Superlattices Microstruct.* 14 (2-3), 189 (1993).
- [82] J. Menéndez and J. Kouvetakis, Type-I Ge/Ge<sub>1-x-y</sub>Si<sub>x</sub>Sn<sub>y</sub> strained-layer heterostructures with a direct Ge bandgap, *Appl. Phys. Lett.* 85, 1175 (2004).
- [83] I. A. Goldthorpe, A. F. Marshall, and P. C. McIntyre, Synthesis and strain relaxation of Ge-core/Si-shell nanowire arrays, *Nano Lett.* 8(11), 4081 (2008).
- [84] N. Fukata, et al., Phonon confinement and self-limiting oxidation effect of silicon nanowires synthesized by laser ablation, *J. Appl. Phys.* 100, 024311 (2006).
- [85] A. Seike, et al., Strain-induced transconductance enhancement by pattern dependent oxidation in silicon nanowire field-effect transistors, *Appl. Phys. Lett.*, 91, 202117 (2007).
- [86] V. Pott, et al., Fabrication and characterization of gate-all-around silicon nanowires on bulk silicon, *IEEE Transactions on Nanotechnology*, 7 (6), November 2008.
- [87] R. S. Jacobsen, et al., Strained silicon as a new electro-optic material, *Nature* 441, 199 (2006).
- [88] M. Cazzanelli, et al., Second-harmonic generation in silicon waveguides strained by silicon nitride, *Nat. Mater* 11, 148 (2011).
- [89] L. Yang, M. P. Anantram, J. Han, and J. P. Lu, Band-gap change of carbon nanotubes: effect of small uniaxial and torsional strain, *Phys. Rev. B* 60, 13874 (1999).
- [90] E. D. Minot, et al., Tuning carbon nanotube band gaps with strain, *Phys. Rev. Lett.* 90, 156401 (2003).
- [91] J. Cao, Q. Wang, and H. Dai, Electromechanical properties of metallic, quasimetallic, and semiconducting carbon nanotubes under stretching. *Phys. Rev. Lett.* 90, 157601 (2003).
- [92] T. W. Tombler, et al., Reversible electromechanical characteristics of carbon nanotubes under local-probe manipulation, *Nature* 405, 769 (2000).
- [93] A. San Paulo, et al., Mechanical elasticity of single and double clamped silicon nanobeams fabricated by the vapor-liquid-solid method, *Appl. Phys. Lett.* 87, 053111 (2005).

- [94] H. Maki, et al., Direct observation of the deformation and the band gap change from an individual single-walled carbon nanotube under uniaxial strain. *Nano Lett.* 7(4), 890 (2007).
- [95] S. M. Kaniber, L. Song, J. P. Kotthaus, and A. W. Holleitner, Photocurrent properties of freely suspended carbon nanotubes under uniaxial strain, *Appl. Phys. Lett.* 94, 261106 (2009).
- [96] C. Stampfer, et al., Fabrication of Single-Walled Carbon-Nanotube-Based Pressure Sensors, *Nano Lett.* 6(2), 233 (2006).
- [97] S. Y. Ryu, et al., Lateral buckling mechanics in silicon nanowires on elastomeric substrates, *Nano Lett.* 9(9), 3214 (2009).
- [98] A. Lugstein, et al., Scalable approach for vertical device integration of epitaxial nanowires, *Nano Lett.* 9(5), 1830 (2009).
- [99] Y. J. Jeong, K. Miyaji, T. Saraya, and T. Hiramoto, Silicon nanowire n-type metal-oxide-semiconductor field-effect transistors and single-electron transistors at room temperature under uniaxial tensile strain, *J. Appl. Phys.* 105, 084514 (2009).
- [100] A. R. Hall, M. R. Falvo, R. Superfine, S. and Washburn, Electromechanical response of single-walled carbon nanotubes to torsional strain in a self-contained device, *Nat. Nanotechnol.* 2, 413 (2007).
- [101] T. Mirfakhrai, et al., Mechano-electrical force sensors using twisted yarns of carbon nanotubes. *IEEE/ASME Trans. Mechatronics.* 16, 90 (2011).
- [102] L. Dreher, et al., Electroelastic hyperfine tuning of phosphorus donors in silicon, *Phys. Rev. Lett.* 106, 037601 (2011).
- [103] C. Brüggemann, et al., Laser mode feeding by shaking quantum dots in a planar microcavity, *Nat. Photon.* 6, 30 (2012).
- [104] M. Khorasaninejad, M. M. Adachi, J. Walia, K. S. Karim and S. S. Saini, Raman spectrum of core/shell silicon nanowires on different substrates, *Phys. Stat. Sol. (a)*, Revised.
- [105] V. Poborchii, T. Tada, K. Usuda, and T. Kanayama, Polarized Raman microscopy of anisotropic stress relaxation in strained-Si-on-insulator stripes, *Appl. Phys. Lett.* 99, 191911 (2011).
- [106] A. Torres, et al., Micro-Raman spectroscopy of Si nanowires: Influence of diameter and temperature, *Appl. Phys. Lett.* 96, 011904 (2010).
- [107] M. Hÿtch, F. Houdellier, F. Hÿe, and E. Snoeck, Nanoscale holographic interferometry for strain measurements in electronic devices, *Nature* 453, 1086-1089 (2008).
- [108] N. -K. Chang, C. -C. Su, and S. -H. Chang, Fabrication of single-walled carbon nanotube flexible strain sensors with high sensitivity, *Appl. Phys. Lett.* 92, 063501 (2008).
- [109] T. Kizuka, Y. Takatani, K. Asaka, and R. Yoshizaki, Measurements of the atomistic mechanics of single crystalline silicon wires of nanometer width, *Phys. Rev. B* 72, 035333 (2005).
- [110] J. -M. Jancu, R. Scholz, F. Beltram, and F. Bassani, Empirical sp<sup>3</sup>s tight-binding calculation for cubic semiconductors: general method and material parameters, *Phys. Rev. B* 57, 6493 (1998).
- [111] P. W. Leu, A. Svizhenko, and K. Cho, Ab initio calculations of the mechanical and electronic properties of strained Si nanowires. *Phys. Rev. B* 77, 235305 (2008).
- [112] J. -A. Yan, L. Yang, and M. Y. Chou, Size and orientation dependence in the electronic properties of silicon nanowires, *Phys. Rev. B* 76, 115319 (2007).
- [113] N. Morioka, H. Yoshioka, J. Suda, and T. Kimoto, Quantum-confinement effect on holes in silicon nanowires: Relationship between wave function and band structure, *J. Appl. Phys.* 109, 064318 (2011).
- [114] J. Tersoff, New empirical approach for the structure and energy of covalent systems, *Phys. Rev. B.* 37, 6991 (1988).
- [115] J. D. Gale, and A. L. Rohl, The General Utility Lattice Program (GULP), *Mol. Simul.* 29 (5), 291 (2003).
- [116] R. D. Menezes, J. F. Justo, and L. V. C. Assali, Energetics of silicon nanowires: a molecular dynamics investigation, *Phys. Stat. Sol. (a)* 204 (4), 951 (2007).

- [117] D. Shiri, Y. Kong, A. K. Buin, and M. P. Anantram, Strain induced change of bandgap and effective mass in silicon nanowires. *Appl. Phys. Lett.* 93, 073114 (2008).
- [118] K. -H. Hong, J. Kim, S. -H. Lee and J. K. Shin, Strain-driven electronic band structure modulation of Si nanowires, *Nano Lett.* 8(5), 1335 (2008).
- [119] Physical Properties of semiconductors at Ioffe Physical Technical Institute website: <http://www.ioffe.ru/SVA/NSM/Semicond/index.html>
- [120] M. P. Anantram, M. Lundstrom, and D. E. Nikonov, Modeling of nanoscale devices, *Proceedings of the IEEE*, 96 (9), 1511–1550 (2008).
- [121] S. Datta, *Quantum Transport: Atom to Transistor*, Chapter 5, (Cambridge University Press, Cambridge, 2005).
- [122] X. Sun, G. Calebotta, B. Yu, G. Selvaduray, and M. Meyyappan, Synthesis of germanium nanowires on insulator catalyzed by indium or antimony, *J. Vac. Sci. Tech. B* 25 (2), 415 (2007).
- [123] P. Nguyen, T. H. Ng, and M. Meyyappan, Growth of individual vertical germanium nanowires, *Adv. Mater.* 17 (5), 549 (2005).
- [124] M. d’Avezac, J.-W. Luo, T. Chanier, and A. Zunger, Genetic-algorithm discovery of a direct-gap and optically allowed superstructure from indirect-gap Si and Ge semiconductors, *Phys. Rev. Lett.* 108, 027401 (2012).
- [125] <http://www.castep.org/>
- [126] J. P. Perdew, and Y. Wang, Accurate and simple analytic representation of the electron-gas correlation energy, *Phys. Rev. B* 45, 13244 (1992).
- [127] <http://www.cmt.york.ac.uk/cmd/>
- [128] C. Harris, and E. P. O’Reilly, Nature of the band gap of silicon and germanium nanowires, *Physica E* 32(1-2), 341 (2006).
- [129] J. Wang, A. Rahman, G. Klimeck, and M. Lundstrom, Bandstructure and orientation effects in ballistic Si and Ge nanowire FETs, *IEEE International Electron Devices Meeting Technical Digest*, DOI: 10.1109/IEDM.2005.1609399, pages.4pp-533 (2005).
- [130] Y. Kong, D. Shiri, and A. K. Buin, First-principle investigation of strain effects on the electronic properties of germanium nanowires, *Phys. Stat. Sol. (RRL)*, 3 (9), 281, (2009).
- [131] V. Fiorentini, and A. Baldereschi, Dielectric scaling of the self-energy scissor operator in semiconductors and insulators, *Phys. Rev. B* 51, 17196 (1995).
- [132] Y. -M. Juan, and E. Kaxiras, Use of the generalized gradient approximation in pseudopotential calculations of solids, *Phys. Rev. B* 51, 9521 (1995).
- [133] J. Kohanoff, *Electronic Structure Calculations for Solids and Molecules: Theory and Computational Methods*, Chapter 5, (Cambridge University Press, Cambridge, 2006).
- [134] Z. Wu, J. B. Neaton, and C. Grossman, Charge separation via strain in silicon nanowires, *Nano Lett.* 9(6), 2418 (2009).
- [135] L. Zhang, M. d’Avezac, J.-W. Luo, and A. Zunger, Genomic design of strong direct-gap optical transition in Si/Ge core/multishell nanowires, *Nano Lett.* 12(2), 984 (2012).
- [136] SIESTA (Spanish Initiative for Electronic Simulations with Thousands of Atoms) software webpage: <http://icamb.cat/leem/siesta/>
- [137] P. Vogl, H. P. Hjalmarson, and J. D. Dow, A semi-empirical tight binding theory of the electronic structure of semiconductors, *J. Phys. Chem. Solids* 44 (5), 356-378(1983).
- [138] L. C. Lew Yan Voon, and L. R. Ram-Mohan, Tight-binding representation of the optical matrix elements: theory and applications, *Phys. Rev. B* 47, 15500 (1993).
- [139] Y.-C. Chng and D. E. Aspnes, Theory of dielectric-function anisotropies of (001) GaAs (2×1) surfaces, *Phys. Rev. B* 41, 12002 (1990).
- [140] T. B. Boykin and P. Vogl, Dielectric response of molecules in empirical tight-binding theory, *Phys. Rev. B* 65, 035202 (2001).

- [141] W. Greiner, *Quantum Mechanics: Special Chapters*, (Springer-Verlag, Berlin, Heidelberg, 1998).
- [142] J. C. Slater, Atomic shielding constants, *Phys. Rev.* 36, 57 (1930).
- [143] N. A. Hill, and K. B. Whaley, Two-particle calculation of excitonic effects in semiconductor nanocrystals, *Chem. Phys.* 210, 117 (1996).
- [144] S. Lee, J. Kim, L. Jönsson, J. W. Wilkins, G.W. Bryant, and G. Klimeck, Many-body levels of optically excited and multiply charged InAs nanocrystals modeled by semiempirical tight binding, *Phys. Rev. B* 66, 235307 (2002).
- [145] J. Stöhr, and H.C. Siegmann, *Magnetism from fundamentals to nanoscale dynamics*, (Springer-Verlag, Berlin, Heidelberg, 2006).
- [146] A. Anselm, *Introduction to Semiconductor Theory*, (Mir Publishers, Moscow, 1981).
- [147] M. Lundstrom, *Fundamentals of Carrier Transport*, (Cambridge University Press, Cambridge, 2000).
- [148] A. K. Buin, A. Verma, and M. P. Anantram, Carrier-phonon interaction in small cross-sectional silicon nanowires. *J. Appl. Phys.* 104, 053716, (2008);
- [149] Web page of Professor Amit Verma at Texas A&M University-Kingsville, <http://www.engineer.tamuk.edu/departments/eecs/eeen/faculty/verma.htm>
- [150] T. Maegawa, T. Hara, T. Yamauchi, H. Tsuchiya, and M. Ogawa, Strain effects on electronic band structures in nano-scaled silicon: from bulk to nanowire, *IEEE Transactions on Electron Devices*, 56, 553 (2009).
- [151] D. Shiri, Y. Kong, A. K. Buin, and M. P. Anantram, Electromechanical response of silicon nanowires: bandgap and effective mass, *Proceedings of International Semiconductor Device Research Symposium*, College Park, MD, 12–14 December 2007, IEEE, Piscataway, NJ, pp. 1–2.
- [152] R. N. Sajjad, and K. Alam, Electronic properties of a strained  $\langle 100 \rangle$  silicon nanowire, *J. Appl. Phys.* 105, 044307 (2009).
- [153] A. J. Lu, R. Q. Zhang, and S. T. Lee, Stress-induced band gap tuning in  $\langle 112 \rangle$  silicon nanowires, *Appl. Phys. Lett.* 91, 263107 (2007).
- [154] Ö. O. Soykal, R. Ruskov, and C. Tahan, Sound-Based analogue of cavity quantum electrodynamics in silicon, *Phys. Rev. Lett.* 107, 235502 (2011).
- [155] Bruneval, F., Botti, S., and Reining, L. Comment on “quantum confinement and electronic properties of silicon nanowires”. *Phys. Rev. Lett.* 94, 219701 (2005).
- [156] J. G. Vilhena, S. Botti, and M. A. L. Marques, Excitonic effects in the optical properties of CdSe nanowires. *Appl. Phys. Lett.* 96, 123106 (2010).
- [157] A. K. Buin, A. Verma, A. Svizhenko, and M. P. Anantram, Significant enhancement of hole mobility in  $[110]$  silicon nanowires compared to electrons and bulk Silicon. *Nano Lett.* 8(2), 760 (2008).
- [158] M. A. Osman, and D. K. Ferry, Monte Carlo investigation of the electron-hole-interaction effects on the ultrafast relaxation of hot photoexcited carriers in GaAs. *Phys. Rev. B* 36, 6018 (1987).
- [159] A. Verma, M. Z. Kauser, and P. P. Ruden, Ensemble Monte Carlo transport simulations for semiconducting carbon nanotubes. *J. Appl. Phys.* 97, 114319 (2005).
- [160] A. Verma, A. K. Buin, and M. P. Anantram, High-field hole transport in silicon nanowires, *J. Appl. Phys.* 106, 113713 (2009).
- [161] Q. Yang, W. Wang, S. Xu, and Z. L. Wang, Enhancing light emission of ZnO microwire-based diodes by piezo-phototronic effect, *Nano Lett.* 11(9), 4012, (2011).
- [162] M. Nawaz, J. P. Leburton, and J. Jin, Hole scattering by confined optical phonons in silicon nanowires. *Appl. Phys. Lett.* 90, 183505 (2007).

- [163] E. B. Ramayya, D. Vasileska, S. M. Goodnick, and I. Knezevic, Electron transport in silicon nanowires: The role of acoustic phonon confinement and surface roughness scattering, *J. Appl. Phys.* 104, 063711 (2008).
- [164] X. Zhao, C. M. Wei, L. Yang, and M. Y. Chou, Quantum confinement and electronic properties of silicon nanowires, *Phys. Rev. Lett.* 92, 236805 (2004).
- [165] J. Wang, M. S. Gudiksen, X. Duan, Y. Cui, and C. M. Lieber, Highly polarized photoluminescence and photodetection from single indium phosphide nanowires, *Science* 293, 1455 (2001).
- [166] M. Bruno, M. Palummo, A. Marini, R. Del Sole, and S. Ossicini, From Si nanowires to porous silicon: the role of excitonic effects, *Phys. Rev. Lett.* 98, 036807 (2007).
- [167] C. Delerue, and M. Lannoo, *Nanostructures Theory and Modeling*, (Springer-Verlag, Berlin, Heidelberg, 2004).
- [168] L. Zhang, et al., Excitons and excitonic fine structures in Si nanowires: prediction of an electronic state crossover with diameter changes, *Phys. Rev. B* 84, 075404 (2011).
- [169] E. Rosencher, and B. Vinter, *Optoelectronics*, (Cambridge University Press, Cambridge, 2002).
- [170] G. Sallen, et al., Sub nanosecond spectral diffusion of a single quantum dot in a nanowire, *Phys. Rev. B* 84, 041405(R) (2011).
- [171] F. D. Stefani, J. P. Hoogenboom, and E. Barkai, Beyond quantum jumps: Blinking nano-scale light emitters, *Physcis Today*, 62 (3), 34-39 (2009).
- [172] B. K. Ridley, *Quantum Processes in Semiconductors*, Fourth Edition, (Oxford University press, Oxford, 1999).
- [173] M. -F. Li, *Modern Semiconductor Quantum Physics*, (World Scientific, Singapore, 1994).
- [174] C. Hamaguchi, *Basic Semiconductor Physics*, (Springer-Verlag, Berlin, Heidelberg, 2001).
- [175] J. Noffsinger, E. Kioupakis, C. G. Van de Walle, S. G. Louie and M. L. Cohen, Phonon assisted optical absorption in silicon from first principles, *Phys. Rev. Lett* 108, 167402 (2012).
- [176] P. Nozières, and D. Pines, Electron interaction in solids; characteristic energy loss spectrum, *Phys. Rev.* 113, 1254 (1959).
- [177] E. Eherenreich, and M. H. Cohen, Self-consistent field approach to the many-electron problem, *Phys. Rev.* 115, 786 (1959).
- [178] S. L. Adler, Quantum theory of the dielectric constant in real solids, *Phys. Rev.* 126, 413 (1962).
- [179] A. Marini, *Optical and electronic properties of Copper and Silver: from Density Functional Theory to Many Body Effects*, PhD Dissertation, University of Rome - Tor Vergata (2001).
- [180] F. Trani, *Electronic and Optical Properties of Silicon Nanocrystals: a Tight Binding Study*, PhD Dissertation, Università di Napoli “Federico II” (2004).
- [181] H. Yoshioka, *Fundamental Study on Si Nanowires for Advanced MOSFETs and Light-Emitting Devices*, PhD Dissertation, Kyoto University, 2010.
- [182] V. Lucarini, J.J. Saarinen, K.-E. Peiponen, and E.M. Vartiainen, *Kramers–Krönig Relations in Optical Materials Research*, (Springer-Verlag, Berlin, Heidelberg, 2005).
- [183] F. Szmulowicz, and J. K. Wendeln, Tetrahedral subdivision of the irreducible wedge for Brillouin zones of cubic lattices, *Phys. Rev. B* 25, 2428 (1982).
- [184] M. A. Green, and M. J. Keevers, Optical properties of intrinsic silicon at 300K, *Progress in Photovoltaics: Research and Applications*, 3 (3), 189 – 192 (1995).
- [185] O. Madelung (Editor), *Semiconductor-Basic Data*, 2<sup>nd</sup> Edition, (Springer-Verlag, Berlin, Heidelberg, 1996).
- [186] M. R. Black, Y.-M. Lin, S. B. Cronin, O. Rabin, and M. S. Dresselhaus, Infrared absorption in bismuth nanowires resulting from quantum confinement, *Phys. Rev. B* 65, 195417 (2002).

- [187] M. W. Lee, H. Z. Twu, C.-C. Chen, and C.-H. Chen, Optical characterization of wurtzite gallium nitride nanowires, *Appl. Phys. Lett.* 79, 3693 (2001).
- [188] D. Shiri, A. Verma, C. R. Selvakumar, and M. P. Anantram, Reversible modulation of spontaneous emission by strain in silicon nanowires, *Sci. Rep.* 2, 461; DOI:10.1038/srep00461 (2012).
- [189] M. P. Anantram, and D. Shiri, Strain modulated nanostructures for optoelectronic devices and associated systems and methods, US Patent Application, Number: 20100290217, Date: 2010-11-18.
- [190] P. T. Landsberg, *Recombination in semiconductors*, (Cambridge University Press, Cambridge, 1991).
- [191] M. Heinemann, and C. Heiliger, Auger recombination rates in ZnMgO from first principles, *J. Appl. Phys.* 110, 083103 (2011).
- [192] M. Govoni, I. Marri and S. Ossicini, Auger recombination in Si and GaAs semiconductors: Ab initio results, *Phys. Rev. B* 84, 075215 (2011).
- [193] M. Takeshima, Simple method of calculating phonon-assisted Auger recombination rate in direct-gap semiconductors, *Jpn. J. Appl. Phys.* 22, 491 (1983).
- [194] A. Haug, Non-radiative recombination of electron-hole drops by means of phonon-assisted Auger recombination, *J. Lumin.* 20 (2), 173 (1979).
- [195] W. Guo, et al., Auger recombination in III-nitride nanowires and its effect on nanowire light-emitting diode characteristics, *Nano Lett.* 11(4), 1434 (2011).
- [196] M. Sheik-Bahai, D. C. Hutchings, D. J. Hagan, and E. W. Van Stryland, Dispersion of Bound electronic nonlinear refraction in solids, *IEEE Jour. Quant. Elect.* 27(6), 1296 (1991).
- [197] G. W. Bryant, Two-photon absorption in Ge: band effects, *Phys. Rev. B* 22 (4), 1992 (1980).
- [198] Y.-C. Chang, A. E. Chiou, and M. Khoshnevisan, Linear and two-photon absorptions of Si-Ge strained-layer superlattices, *J. Appl. Phys.* 71, 1349 (1992).
- [199] J. M. An, A. Franceschetti, S. V. Dudy, and A. Zunger, The peculiar electronic structure of PbSe quantum dots, *Nano. Lett.* 6 (12), 2728 (2006).
- [200] T. Iitaka, and T. Ebisuzaki, Efficient algorithm for calculating two-photon absorption spectra, *Phys. Rev. E* 60 (2), R1178 (1999).
- [201] A. Hayat, P. Ginzburg, and M. Orenstein, Infrared single-photon detection by two-photon absorption in silicon, *Phys. Rev. B* 77, 125219 (2008).
- [202] B. M. Van Der Ende, L. Aarts, and A. Meijerink. Lanthanide ions as spectral converters for solar cells. *Physical Chemistry Chemical Physics*, 11(47), 11081 (2009).
- [203] R.W. Boyd, *Nonlinear Optics*, Chapters 4 and 9, Third Edition, (Academic Press, London, 2008).
- [204] M. Murayama, and T. Nakayama, Two-photon-absorption spectra originating from higher-energy transitions, *Phys. Rev. B* 49, 5737 (1994).
- [205] Y. Takimoto, F. D. Villa and J. J. Rehr, Real-time time-dependent density functional theory approach for frequency-dependent nonlinear optical response in photonic molecules, *J. Chem. Phys.* 127 (15), 154114 (2007).
- [206] J. M. Soler, et al., The SIESTA method for ab initio order-N materials simulation, *J. Phys.: Condens. Matter.* 14, 2745 (2002).
- [207] N. Berkaine, E. Orhan, O. Masson, P. Thomas and J. Junquera, Nonlinear optical properties of TeO<sub>2</sub> crystalline phases from first principles, *Phys. Rev. B* 83, 245205 (2011).
- [208] H. Garcia, and R. Kalyanaraman, Phonon-assisted two-photon absorption in the presence of a dc-field: the nonlinear Franz-Keldysh effect in indirect gap semiconductors, *J. Phys. B: At. Mol. Opt. Phys.* 39, 2737-2746 (2006)
- [209] H. D. Jones, and H. R. Reiss, Intense-field effects in solids, *Phys. Rev. B* 16, 2466 (1977).